

# **Adsorptive Properties of Vanadium Substituted ETS-10**

by

Farnaz Mani

A thesis submitted in partial fulfillment of the requirements for the degree of

Doctor of Philosophy

in

Chemical Engineering

Department of Chemical and Materials Engineering  
University of Alberta

© Farnaz Mani, 2015

# Abstract

High purity microporous vanadosilicate (EVS-10/AM-6) has been hydrothermally synthesized by a simple template-free, reducing agent-free method in the absence of titanasilicate ETS-10 seeds. Direct comparison between EVS-10 and ETS-10 showed successful isomorphous substitution of titanium with vanadium in the framework. The existence of vanadium is confirmed by energy dispersive X-ray spectroscopy and inductively coupled plasma mass spectrometry. The scan electron microscopy and the X-ray diffractometer show similar crystal morphology and structure. The structural and adsorptive characteristics of EVS-10 with ETS-10 have been compared. The Henry Law constants and heats of adsorption were calculated for both adsorbents from low pressure adsorption data using CH<sub>4</sub>, C<sub>2</sub>H<sub>6</sub>, C<sub>2</sub>H<sub>4</sub>, N<sub>2</sub>, O<sub>2</sub>, and CO<sub>2</sub> for pressures up to 100 kPa and temperatures of 303, 323, and 343 K. The adsorption data were fit using Langmuir, Toth, and Redlich-Peterson isotherms. The best model was selected based on the quality of fit to the data and how closely the model predicted the saturation concentration. The structural properties for EVS-10 are almost indistinguishable from ETS-10. The adsorption data reflects this similarity in that both adsorbents have similar heats of adsorption and selectivities for a wide range of gases. These results suggest that heteroatom substitution in ETS-10 does not necessarily affect its adsorption properties if the framework dimensions and composition remain similar.

A proposal for the differences in the adsorption characteristic for ETS-10 is created by contrasting the adsorption properties of as-synthesized ETS-10 with 13X and high siliceous ZSM-5. To determine whether adsorption on Na-ETS-10 is driven predominately by cationic or van der Waals effects, the adsorption affinity for several gases was measured on all three adsorbents. The

adsorption mechanism was probed by using the isotherms to calculate both the enthalpy and entropy of adsorption as a function of loading and by contrasting the behaviour of ETS-10 against both 13X and ZSM-5. The results of the analysis indicate that ETS-10 has, simultaneously, a high affinity for molecules both with and without strong quadrupole moments. This behaviour is believed to result from a sparse number of highly deshielded cations that exist in the otherwise non-polar channels.

The phenomenon associated with the ion-exchange of silver ions into the microporous vanadosilicate EVS-10 is explored. The divalent charge on the vanadium is offset by mobile and exchangeable cationic counter-ions. It was found that silver replaces sodium quantitatively and that, unexpectedly, the silver ions are spontaneously reduced to silver metal which appear as nano-scale metal clusters in the TEM images. The reduction of the silver ions is accompanied by an oxidation of the framework vanadium and this redox pair is established through XPS and Raman spectroscopy. The mechanism for this unique behaviour is believed to be explained by a galvanic reaction between the incoming  $\text{Ag}^+$  and the framework  $\text{V}^{4+}$ .

Separation of ethane from methane from a binary gas mixture was conducted by adsorption on EVS-10. In this study a feed consisted of 80% methane and 20% ethane was used. The bed selectivity resulted from adsorptive separation on EVS-10 was 36 at room temperature and atmospheric pressure. This study suggested that EVS-10 could be an effective candidate for separation of ethane from the gas streams highly enriched in methane. In other words, EVS-10 could be potentially used in cases such as natural gas purification.

# Preface

The Materials presented in the current thesis are part of the research project under supervision of Dr. Steven M. Kuznicki, which has been funded by Natural Sciences and Engineering Research Council (NSERC) of Canada and Industrial Research Chair in Molecular Sieve Separations Technology and Helmholtz-Alberta Initiative.

Chapter 3 of this work is accepted as Mani, F., Wu, L., Kuznicki S.M., 2013. “A Simplified Method to Synthesis Pure Vanadium Silicate Analogue of ETS-10” in Journal of Microporous and Mesoporous Materials.

Chapter 4 of this work is accepted as Mani, F., Sawada, J.A., Kuznicki S.M., 2015. “Comparative Adsorption Study of EVS-10 and ETS-10” in Journal of Microporous and Mesoporous Materials. Dr. Tetyana Kuznicki helped in editing with the manuscript.

Chapter 5 of this work is submitted as Mani, F., Sawada, J.A., Kuznicki S.M., 2015. “The Adsorptive Behaviour of ETS-10, 13X, and Highly Siliceous ZSM-5” in Journal of Microporous and Mesoporous Materials. Dr. James Sawada helped with the Crystallography part of the study. Dr. Tetyana Kuznicki and Dr. James Sawada helped in editing with the manuscript.

Chapter 6 of this work is submitted as Mani, F., Sawada, J.A., Kuznicki S.M., 2015. “Spontaneous Formation of Silver Nanoparticles on the Vanadium Silicate EVS-10” in Journal of Microporous and Mesoporous Materials. Dr. James Sawada helped with the Crystallography, Raman spectroscopy, and the silver-Vanadium Redox Chemistry of the study.

All of the X-ray diffraction (XRD) and energy-dispersive X-ray (EDX) measurements were ran by Diane Caird and Nathan Gerein, respectively at department of Earth and Atomosperic sciences. The transmission electron microscopy (TEM) images and Raman Spectroscopy data were ran by Jian Chen and Xia Mike, respectively at National Institute

for Nanotechnology (NINT), Canada National Research Council at university of Alberta.  
The X-ray photoelectron spectroscopy (XPS) were ran by Dimitre Karpuzov at the  
Alberta Centre for Surface Engineering and Science (ACSES), University of Alberta.

*To my Love and my beloved parents,  
for their unconditional love, invaluable advice and support.*

# Acknowledgements

This dissertation would not have been possible without the assistance of several individuals. I am most indebted to my advisor Dr. Steven M. Kuznicki for his encouragement and guidance throughout my studies at the University of Alberta. It was a great pleasure to work under his supervision.

I am most grateful to Dr. James Sawada. His invaluable kindness, guidance and comments allowed me to develop my personality and knowledge. I would like to thank him for his extensive discussions related to most part of my research. He has been a great assistant and friend.

I would like to extend my appreciation to Albana Zeko and Dr. Tetyana Kuznicki for their patience and continuous support in manuscript development.

I would like to express my gratitude to a number of technicians and research assistants for their valuable support and assistance toward my research: Tong Qui, Lan Wu, An Weizhu, Diane Caird, Nathan Gerein, Jian Chen, Dimitre Karpuzov, Xia Mike.

I would like to acknowledge the Natural Sciences and Engineering Research Council (NSERC) of Canada and Industrial Research Chair in Molecular Sieve Separations Technology and Helmholtz-Alberta Initiative for their support.

I am also thankful to my amazing friends whose presence brings joy and laughter to my life in Canada: Fatemeh, Abolfazl, Solmaz, Behnam, Masoud, Mitra, Tina, Somaye, Ali, Ehsan, Pegah, Nayef, Roshanak, Ali, Mehrdad, Niousha, Babak, Nima, Ata, Elahe, Reza, Mohammad, Siyavash, Behdokht, Arash, Marjan, Parastoo, Maryam, Reza.

Last but not least, I would like to express my heartfelt gratitude to my love, Arash, my parents, my brother, Farzad, my sister, Farnoosh, without whose extreme patient, support, love, encouragement and blessing I could not have achieved what I have today.

# Contents

<b>Chapter 1</b>	1
<b>Introduction</b>	1
1 Overview	1
1.1 Classical Zeolite Molecular Sieves	1
1.2 Mixed Coordination Molecular Sieves	2
1.2.1 Systematic Pore Shrinkage with Structural Dehydration:	5
1.2.2 Pore Tuning by Anions	6
1.2.3 Possibility of Framework Atom Substitution	7
1.3 Ion-exchange property of mixed coordination molecular sieves	11
1.4 Research Objectives	14
1.5 Commercial Gas Separation Technique	15
1.5.1 Adsorption Process	16
1.6 Thesis Outline	18
References	20
<b>Chapter 2</b>	23
<b>Fundamental of Adsorption</b>	23
2.1 Adsorption Principles	23
2.2 Forces and Energies of Adsorption	24
2.3 Heat of Adsorption	26
2.4 Selectivity	28
2.5 Effects of Adsorbate Properties on Adsorption: Polarizability ( $\alpha$ ), Dipole Moment ( $\mu$ ) and Quadrupole moment ( $Q$ )	29
2.6 Adsorption Isotherm	31
2.6.1 Equilibrium Adsorption of Pure Gas	33
2.6.1.1 Langmuir Isotherm	33
2.6.1.2 The BET Isotherm	34

2.6.2	Equilibrium Adsorption of Gas Mixtures	36
2.6.2.1	Extended Langmuir Isotherm	36
2.6.2.2	Ideal Adsorbed Solution Theory (IAST)	37
	References	40
	<b>Chapter 3</b>	41
	<b>A Simplified Method to Synthesize Pure Vanadium Silicate Analogue of ETS-10</b>	41
3.1	Introduction	41
3.2	Experimental	44
3.3	Result and Discussion	47
3.4	Conclusion	54
	References	55
	<b>Chapter 4</b>	57
	<b>Comparative Adsorption Study of EVS-10 and ETS-10</b>	57
4.1	Introduction	57
4.2	Theoretical Background	59
4.3	Experimental	61
4.4	Result and Discussion	63
4.4.1	Characterization	63
4.4.2	Single Component Adsorption Isotherm	68
4.4.3	Henry Constant, Heat of Adsorption	72
4.4.4	Ideal/Henry Selectivity	74
4.5	Conclusion	75
	References	76
	<b>Chapter 5</b>	79
	<b>A Proposed Adsorption Mechanism for Na-ETS-10</b>	79
5.1	Introduction	79
5.2	Theoretical Background	83
5.2.1	Isotherm models	83
5.2.2	Gibbs Energy and Entropy of Adsorption	84
5.3	Experimental	87

5.3.1	Materials	87
5.3.2	Isotherm Measurements	87
5.4	Results and Discussion	88
5.4.1	Single-Component Adsorption Isotherms	88
5.4.2	Limiting Heat of Adsorption and Polarizability	89
5.4.3	Variation of Adsorbate Heat of Adsorption with Loading	93
5.4.4	Change of Adsorption Entropy with Loading	96
5.4.5	ETS-10 Crystal Structure	99
5.5	Conclusion	103
	References	105
	<b>Chapter 6</b>	110
	<b>Spontaneous Formation of Silver Nanoparticles on the Vanadium Silicate</b>	
	<b>EVS-10</b>	110
6.1	Introduction	110
6.2	Experimental	111
6.2.1	Synthesis	111
6.2.2	Ion exchange	112
6.2.3	EDX	112
6.2.4	XRD	113
6.2.5	TEM	113
6.2.6	XPS	113
6.2.7	Raman Spectroscopy	114
6.3	Results and discussion	114
6.3.1	EDX	114
6.3.2	XRD	115
6.3.3	TEM	120
6.3.4	XPS	121
6.3.5	Raman Spectroscopy	128
6.3.6	Silver-Vanadium Redox Chemistry	132
6.4	Conclusions	135
	References	136

<b>Chapter 7</b>	140
<b>Separation Studies of Ethane/Methane Binary Mixture by Adsorption on EVS-10</b>	140
7.1 Introduction	140
7.2 Experimental	141
7.2.1 Sample Preparation	141
7.2.2 Low Pressure Isotherms	142
7.2.3 Inverse Gas Chromatography	143
7.2.4 Bench-scale multicomponent Adsorption	143
7.2.4.1 Mass flow meter calibration	146
7.2.4.2 Dead volume measurement	147
7.3 Theoretical Background	149
7.3.1 Pure gas isotherms	149
7.3.2 Mixed-gas Adsorption Model	150
7.3.3 Henry's constant, Limiting Selectivity and Isothermic Heats of Adsorption	152
7.4 Results and Discussion	154
7.4.1 Single component adsorption	154
7.4.2 Heat of Adsorption	157
7.4.3 Equilibrium Binary Selectivity	159
7.4.4 Inverse Gas Chromatography	160
7.4.5 Bench Scale Multicomponent Adsorption	162
7.4.6 Desorption	165
7.5 Conclusion	167
References	168
<b>Chapter 8</b>	170
<b>Summary, Conclusion and Future Suggestions</b>	170
8.1 Summary and Conclusion	170
8.2 Future Work	176
References	178
<b>Bibliography</b>	179

<b>Appendix</b>	190
Appendix A: Unconstrained Optimization Parameter for the most accurate fit on ETS-10, 13X and high silicalite ZSM-5	190
Appendix B: Values of Entropy, Gibbs free energy and Adsorbate Entropy on high silicalite ZSM-5, ETS-10 and 13X at 343K at different loadings	193
Appendix C: Isotherm Raw Data	212
Appendix C.I: Isotherm Raw Data of CH <sub>4</sub> , C <sub>2</sub> H <sub>6</sub> , C <sub>2</sub> H <sub>4</sub> , and CO <sub>2</sub> on ETS-10 at 303-323-343K	212
Appendix C.II: Isotherm Raw Data of CH <sub>4</sub> , C <sub>2</sub> H <sub>6</sub> , C <sub>2</sub> H <sub>4</sub> , and CO <sub>2</sub> on high siliceous ZSM-5 at 303-323-343K	219
Appendix C.III: Isotherm Raw Data of CH <sub>4</sub> , C <sub>2</sub> H <sub>6</sub> , C <sub>2</sub> H <sub>4</sub> , and CO <sub>2</sub> on 13X at 303-323-343K	223

# List of Tables

2.1	Comparison between Physisorption and Chemisorption (Ruthven, D. M., 1984)	24
2.2	Contribution to near zero loading heat of adsorption. * Permanent dipole moments ( $\mu$ ): $\text{H}_2\text{O} > \text{NH}_3 > \text{N}_2\text{O}$ and Quadropole moments (Q): $\text{CO}_2 > \text{N}_2\text{O} > \text{N}_2 > \text{NH}_3$ . **For graphite carbon $\Phi_{ind}=0$	30
3.1	A Comparison between ETS-10, and the new material (EVS-10) surface area and pore size. Using nitrogen as a probe gas. In all cases, the sample was outgassed at 150°C	52
3.2	A Comparison between ETS-10, and seed-free, template-free, reducing agent-free EV S-10 compensating ions ratio to structural atoms, titanium and vanadium, respectively. The sample was outgassed at 150° C. All the values are average of 5 measurements	54
4.1	Micropore analysis under cryogenic conditions for EVS-10 and ETS-10. Samples were outgassed overnight under vacuum at 0.5 Pa and 523 K. Argon was used as the probe gas and liquid argon was used as the cryogen bath	66
4.2	Mol equivalents of each element in the molecular structure of EVS-10 and ETS-10 from EDX analysis	68
4.3	Theoretical saturation concentrations calculated from Eq. 4.4 at 303K and predicted saturation concentrations from the fit of the best models on the isotherm data at 303K	69
4.4	Unconstrained Optimization Parameter for the Best Model on ETS-10	71
4.5	Unconstrained Optimization Parameter for the Best Model on EVS-10	72

4.6	Comparison of Henry's constants ( $\text{mol kg}^{-1} \text{kPa}^{-1}$ ) and heats of adsorption ( $\text{kJ mol}^{-1}$ ) from Langmuir isotherm at 298K	73
4.7	Comparison of Ideal/Henry's selectivities ( $\alpha$ ) at 298 K	75
5.1	A comparison of the Heat of Adsorption ( $\text{kJ.mol}^{-1}$ ) on silicalite, 13X and ETS-10 between the reported value in the literature and values calculated from the Langmuir isotherm at 298K. High siliceous ZSM-5 is comparable to silicalite in the literature	91
5.2	Properties of adsorbate gas, Sircar et al., 2003	92
6.1	EDX results on the silver exchanged EVS-10 series expressed as mole ratios to vanadium	114
6.2	Mean peak positions of the bands deconvoluted from and Ag 3d <sub>3/2</sub> XPS spectra	122
6.3	Mean peak positions of the bands deconvoluted from and V 2p <sub>3/2</sub> XPS spectra	126
7.1	Summarizing values for rotameter calibration with Coriolis mass flow meter	146
7.2	Fitting Parameters of ethane, methane after fitting the isotherm to Dual Site Langmuir model and Langmuir model at 298K	155
7.3	Fitting Parameters of ethane, methane after fitting the isotherm to Dual Site Langmuir model and Langmuir model at 323K	155
7.4	Fitting Parameters of ethane, methane after fitting the isotherm to Dual Site Langmuir model and Langmuir model at 343K	155
7.5	Adsorption Parameters for methane and ethane on EVS-10 at 298K fit to Dual site Langmuir adsorption model	158
7.6	A comparison between the predicted and the experimental breakthrough time	164

# List of Figures

- 1.1 The framework structure of ETS-10. Chains of  $TiO_6$  octahedra runs in two perpendicular directions and isolated by rings of  $SiO_4$  tetrahedra a) single element of the chain; b) single chain; c) three-dimensional view (Lamberti, C., 1999) 3
- 1.2 Presence of large defects such as twin-pores due to random stacking during crystallization (Rocha et al., 2000) 4
- 1.3 ETS-10 High Resolution Electron Micrograph (Rocha et al., 2000 ) 5
- 1.4 The five suggested cation sites for ETS-10 (adapted from Anderson et al., 1999) 14
- 2.1 Five types of adsorption isotherms, adopted from Thomos et al., 1998 31
- 3.1 It is shown the XRD pattern of ETS-10 as explained in the patent by Kuznicki et al., 1991 (dashed line) and the XRD pattern of EVS-10 at 503 K from mixture with  $1.44Na_2O:0.19K_2O:2.2SiO_2:0.11V_2O_5:35H_2O:0.34F$  (solid line) and. Both XRD patterns are similar which proves the analogous molecular structure for the two materials 47
- 3.2 The XRD pattern of EVS-10 at 503 K from mixture with molar composition of  $1.44Na_2O:0.19K_2O:2.2SiO_2:0.11V_2O_5:35H_2O:0.34F$  asterisk referred to quartz impurity (a) as-synthesized product without aging (b) after 1 day aging at room temperature, (c) after 2 days aging at room temperature 48
- 3.3 The asterisks represent the main EVS-10 peaks. As pH decreased the main peaks became more pronounced (a) It is form a mixture with pH  $\sim 12.5$ , (b) pH  $\sim 11.7$ , (c) pH  $\sim 11.0$  (d) pH  $\sim 10.5$ , (e) pH  $\sim 10.2$  49
- 3.4 (a) shows substantial amount of quartz in the synthesis mixture in the absence of fluoride ions (b) quartz impurities are dissolved as a result of the use of fluoride ions 50
- 3.5 The SEM image on the seedless, template-free, reducing agent-free vanadium silicate. Similar to ETS-10 crystals the EVS-10 crystals are also cubic-forms 51

3.6 The TEM images on the seedless, template-free, reducing agent-free vanadium silicate. The microporous structure of the new material, EVS-10, is clearly shown

51

3.7 (a) EVS-10 products synthesized at 230° C from mixture with molar composition of 1.44Na<sub>2</sub>O:0.19K<sub>2</sub>O:2.2SiO<sub>2</sub>:0.11V<sub>2</sub>O<sub>5</sub>:35H<sub>2</sub>O:0.34F (dashed line) (b) ETS-10 products synthesized at 230°C as explained in the patent by Kuznicki et al., 1991 (solid line)

53

4.1 XRD patterns of EVS-10 synthesised at 503K (solid line) and ETS-10 synthesized at 488K (dashed line) Mani et al., 2013

64

4.2 Right: SEM image of the seedless, template-free and reducing agent free vanadium silicate EVS-10. Left: SEM image of ETS-10

64

4.3 Left: TEM image on the seedless, template-free, reducing agent-free vanadium silicate crystals. The microporous structure of the new material, EVS-10, is clearly shown. Right: TEM image of ETS-10 crystal adopted from (Casado et al., 2009)

65

4.4 Horvath-Kawazoe differential pore volume plot: solid line represents EVS-10 and dashed line - ETS-10

67

4.5 Fit of (a) Langmuir model to methane isotherm, (b) Toth model to ethylene isotherm, (c) Toth model to ethane isotherm and (d) Fit Toth model to CO<sub>2</sub> isotherm. All the adsorption data are on vanadosilicate EVS-10: ▲ - 303K, ▼ - 323K and ● - 343K

70

4.6 Fit of (a) Langmuir model to methane isotherm, (b) Toth model to ethylene isotherm, (c) Toth model to ethane isotherm and (d) Fit Toth model to CO<sub>2</sub> isotherm. All the adsorption data are on titanosilicate ETS-10 at: ▲ - 303K, ▼ - 323K and ● - 343K

70

4.7 Fit of Langmuir model to the isotherms of (a) N<sub>2</sub> and (b) O<sub>2</sub> on ETS-10; (c) N<sub>2</sub> and (d) O<sub>2</sub> on EVS-10 at: ▲ - 303K, ▼ - 323K and ● - 343K

71

4.8 Van Hoff 's plot of Henry's constant values from experimental data at 303, 323, and 343K: ○ - C<sub>2</sub>H<sub>4</sub>, □ - C<sub>2</sub>H<sub>6</sub>, ▽ - CH<sub>4</sub>, Δ - CO<sub>2</sub>; ◁ - N<sub>2</sub>, ▷ - O<sub>2</sub>. Void symbols represent EVS-10 and solid symbols represent ETS-10. The solid lines represent the regression lines

74

5.1	Fit of the models with the most precise fit to the isotherm: (a) CO <sub>2</sub> and (b) C <sub>2</sub> H <sub>4</sub> both fit to langmuir on ZSM-5, to Redlich Peterson on ETS-10 and to Toth on 13X (c) C <sub>2</sub> H <sub>6</sub> fits to Langmuir on 13X and ZSM-5 and to Redlich Peterson on ETS-10 (d) CH <sub>4</sub> fits to Langmuir in all the three adsorbents. All the adsorption data are at 303K	89
5.2	Isosteric heat of adsorption as a function of adsorbate polarizability: ● represents high siliceous ZSM-5, ■ represents 13X, ▲ represents ETS-10	93
5.3	Comparison of the variation of isosteric heat of adsorption (-ΔH) at different adsorbate loading in the adsorption of CO <sub>2</sub> , C <sub>2</sub> H <sub>4</sub> , C <sub>2</sub> H <sub>6</sub> , CH <sub>4</sub> on 13X, ETS-10 and high siliceous ZSM-5	95
5.4	Comparison of the corrected entropy change (-ΔS <sub>m</sub> ) at different adsorbate loading with the theoretical entropy change (ΔS <sub>t</sub> ) in the adsorption of CO <sub>2</sub> , C <sub>2</sub> H <sub>4</sub> , C <sub>2</sub> H <sub>6</sub> , CH <sub>4</sub> on 13X, ETS-10 and high siliceous ZSM-5. All the entropy change data are at 343 K	99
5.5	ETS structure visualized in Mercury combines both the framework and non-framework ions using the atomic coordinates and unit cell dimensions provided by Anderson et al., 1994 with the atomic positions for the Na and K cations provided by Grillo et al., 1996 Representation of 12-ring pore structure viewed down the 110 plane. Titanium atoms are grey, silicon is blue, oxygen is red, potassium is violet, and sodium is orange	102
6.1	Powder XRD profiles for the as-synthesized EVS-10 and silver exchanged EVS-10 samples	116
6.2	Framework representation of the EVS-10 structure adopted from the crystallographic data reported by Anderson <sup>29</sup> and the coordinate information for the cations published by Grillo et al., 1996. Red, blue, and violet represent oxygen, silicon and vanadium respectively. The cation positions are grey and orange	117
6.3	The simulated and experimental differences in relative, normalized intensity for the 50%Ag and EVS-10 powder patterns	118
6.4	The angular shift in the experimental powder XRD patterns as a function of silver exchange	119

6.5	TEM images of for the silver-exchanged EVS-10 samples. a) 1%Ag b)5%Ag c)10%Ag d)25%Ag e)50%Ag	121
6.6	Silver 3d <sub>3/2</sub> XPS results for silver-exchanged EVS-10	122
6.7	The proportion of each silver band deconvoluted from the Ag 3d <sub>3/2</sub> spectra for the silver-exchanged samples. Binding energies characteristic of Ag <sub>2</sub> O are labelled as Ag <sup>+</sup> while those for silver metal and zeolite-bound silver ions are labelled Ag <sup>(0)</sup> and Ag <sub>Z</sub> , respectively	124
6.8	Vanadium 2p <sub>3/2</sub> XPS spectra for EVS-10 and the silver-exchanged forms of EVS-10	125
6.9	The proportion of each vanadium band deconvoluted from the V 2p <sub>3/2</sub> spectra for EVS-10 and the silver-exchanged EVS-10 samples. The 0% sample represents as-synthesized EVS-10 while the remaining labels specify the silver loading. The solid bars are binding energies characteristic of V <sup>4+</sup> while the shaded bars are binding energies characteristic of V <sup>5+</sup>	127
6.10	spectra for EVS-10 and the silver-exchanged EVS-10 samples	128
6.11	Pourbaix diagram for vanadium speciation in water having an ionic strength of zero (Al-Kharafi et al., 1997)	133
7.1	Multicomponent Adsorption/Desorption Schematic	145
7.2	Multicomponent Adsorption/Desorption test stand. Left picture shows front of the set-up and right one displays the rear of the set-up	145
7.3	Calibration curve for rotameter	147
7.4	Gas Pycnometer	149
7.5	a) Methane and b) Ethane low pressure isotherms on EVS-10. ‘■’, ‘●’ and ‘▲’ represent experimental data at 298, 323, 343 K, respectively. Solid line is from the dual site adsorption model	156
7.6	a) Methane and b) Ethane low pressure isotherms on EVS-10. ‘■’, ‘●’ and ‘▲’ represent experimental data at 303, 323, 343 K, respectively. Solid line is from the langmuir adsorption model	156

7.7	Van't Hoff plot of Henry constants values fit to Langmuir dual site at 298, 323, 343 K: '■' and '●' represents methane and ethane on EVS-10, respectively	158
7.8	Variation of isosteric heat of adsorption at different adsorbate loading on EVS-10. The experimental isotherm data were fitted to Dual site Langmuir adsorption. Symbol '□' represents Ethane and, '○' represents methane	159
7.9	C <sub>2</sub> H <sub>6</sub> /CH <sub>4</sub> (80/20) equilibrium selectivity (binary selectivity) at ambient temperature and pressure predicted by IAST using dual site Langmuir for pure-gas isotherm	160
7.10	Inverse Gas Chromatography from Pure stream of a) methane and b) ethane at 150°C on EVS-10	161
7.11	Inverse Gas Chromatography of a feed with composition of 80% methane and 20% ethane on EVS-10	161
7.12	C <sub>2</sub> H <sub>6</sub> /CH <sub>4</sub> Breakthrough curve on EVS-10 at room temperature. Feed gas: 80% CH <sub>4</sub> and 20% C <sub>2</sub> H <sub>6</sub> at 170 ml/min flow rate	163
7.13	C <sub>2</sub> H <sub>6</sub> /CH <sub>4</sub> Breakthrough curve on EVS-10 at room temperature in terms of equivalent bed volume. With 170 ml/min feed flow rate and a bed volume of 45ml, CH <sub>4</sub> breakthrough occurs at approximately 18 BV and C <sub>2</sub> H <sub>6</sub> breakthrough occurs at approximately 104 BV	164
7.14	The gas tank connected to set up filled with water in order to collect the desorbed gas	166
7.15	Gas Chromatography results on a) desorbed gas: 10% methane and 90% ethane, b) feed gas: 80% methane and 20% ethane	167

# Chapter 1

## Introduction

### 1 Overview

Stable microporous materials such as molecular sieves have many applications in catalysis, adsorption, ion exchange, gas separation and liquid separation. Due to their great potential, people have studied them over decades to improve their functions and extend their applications. Classical zeolites and mixed coordination materials are among the most applicable molecular sieves in the above mentioned fields. They are part of the inorganic crystalline molecular sieves. The term "molecular sieve" was initially used by J.W. Mc Bain to describe the sieve-like property of the porous solid materials on a molecular scale <sup>1</sup>.

#### 1.1 Classical Zeolite Molecular Sieves

Classical zeolites are comprised of four coordinated aluminum and silicon chains in the form of  $\text{AlO}_4$  and  $\text{SiO}_4$  tetrahedra units. Silica units are uncharged, while one negative charge is associated with aluminum units; therefore, in order to maintain electron neutrality they are surrounded by charge-compensating cations. The zeolite structural formula is best expressed as  $\text{M}_{x/n}[(\text{AlO}_2)_x(\text{SiO}_2)_y] \cdot w \text{H}_2\text{O}$ . Where M denoted the cation of valence n, w is the number of water molecules and the ratio y/x has values of 1–5 depending on the structure. They have uniform pore size distribution from 3 Å to 10 Å which are exclusively identified by the crystal unit structure. Classical zeolites all have a

significant internal surface area accessible for adsorption; this is attributed to the channels or pores that are uniformly distributed in the entire volume.

Some classical zeolites that are commercially used for different applications are: Zeolite A, Zeolite X and Zeolite Y. Zeolite A is used as desiccant to substitute the current refrigerant drying used in industry<sup>3</sup>. It is the first synthetic zeolite to commercially separate oxygen from argon at a Union Carbide plant<sup>3</sup>. Zeolite type A and X are used for gas drying<sup>4</sup>. Zeolite Y is mostly used as catalyst for petroleum cracking<sup>2,5</sup>.

## 1.2 Mixed Coordination Molecular Sieves

The microporous framework in mixed coordination molecular sieves is consisted of interlinked octahedral and tetrahedra. They contain rings of 4 coordinated tetrahedral silicon atoms connected to parallel chains of 6 coordinated octahedral titanium atoms. The corner-sharing titania octahedra make up the chains are associated with  $-2$  charges and silica units are uncharged. Mixed coordination molecular sieves are exemplified by titanium silicates so called as ETS-10 (Engelhard Titanium Silicate)<sup>6</sup>. The detailed elements of the ETS-10 structure is shown in Figure 1.1; the most important properties of ETS-10 is that the  $\text{TiO}_6$  octahedra are connected together with formation of linear  $\text{—O—Ti—O—Ti—O—Ti—O—}$  chains in the plane perpendicular to four silicon atoms through oxygen bridges<sup>7</sup>. The synthesis of ETS-10 was first reported by Kuznicki et al.<sup>6</sup> ETS-10 is the one of a kind in tetrahedral / octahedral framework microporous titanosilicate synthesized; this is attributed to its wide pore size range and high thermal stability. The most interesting characteristics of ETS-10 is that infinite  $\text{-O-Ti-O-Ti-O-}$  chains in the structure are surrounded by a silicate ring structure; this behavior leads up to the formation of a rod which imparts some of the fascinating properties of ETS-10. Adjacent

layers of rod attached orthogonal to each other<sup>8</sup> form a polymorph of ETS-10. The stacking sequence of the polymorphs are random probably due to mechanism of the crystal growth; This would results in line defects in ETS-10 which creates twin-pores<sup>8-10</sup> (see Figure 1.2). ETS-10 has a three dimensional 12-ring pore structure with a Si/Ti ratio approaching 5. Its porous structure is composed of a network of connected 7 by 5 Å channels formed by 12-membered silica ring. A typical gel composition of ETS-10 is:  $4.7\text{Na}_2\text{O}:1.5\text{K}_2\text{O}:\text{TiO}_2:5.5\text{SiO}_2:122\text{H}_2\text{O}$ <sup>11</sup>.

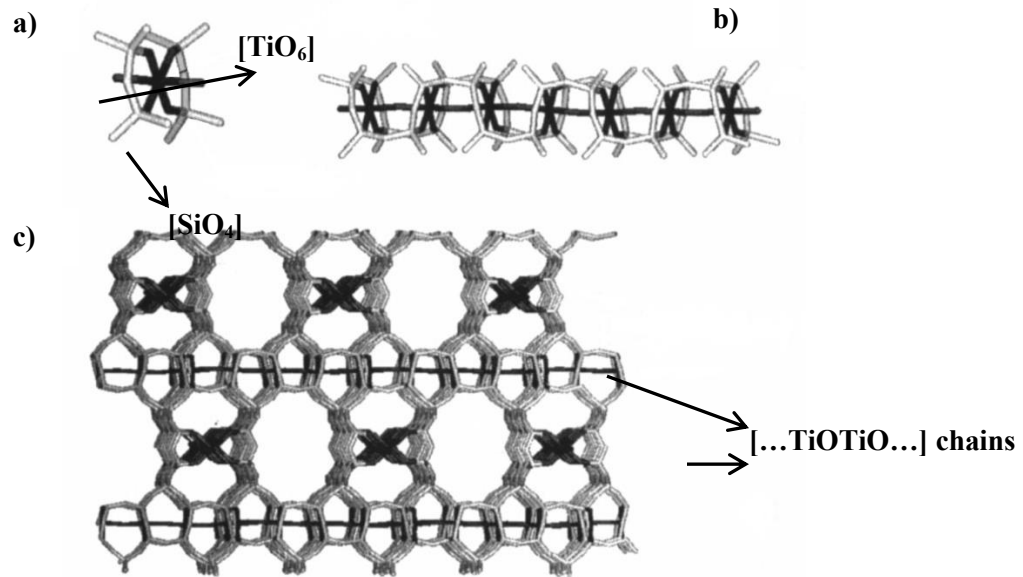


**Figure 1.1:** The framework structure of ETS-10. Chains of TiO<sub>6</sub> octahedra runs in two perpendicular directions and isolated by rings of SiO<sub>4</sub> tetrahedra a) single element of the chain; b) single chain; c) three-dimensional view<sup>7</sup>.

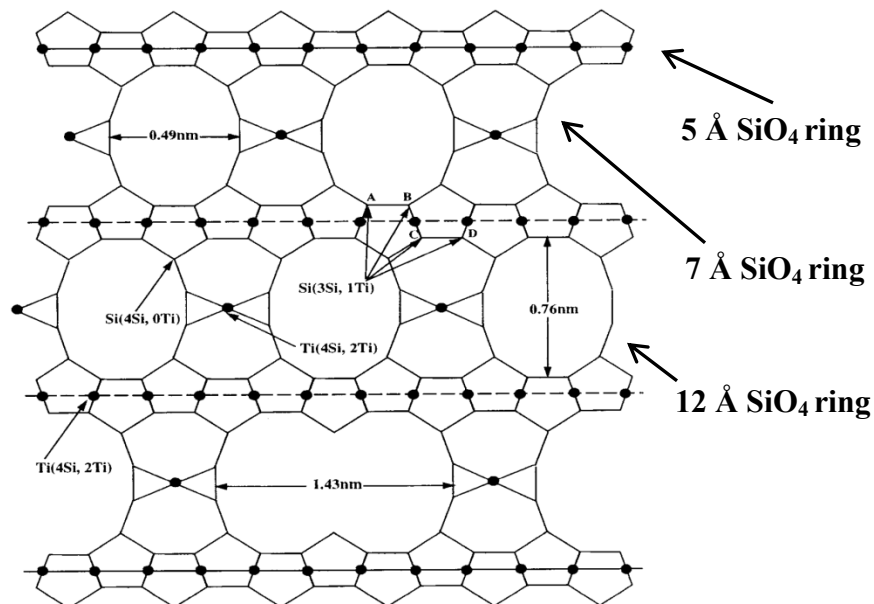


**Figure 1.2: Presence of large defects such as twin-pores due to random stacking during crystallization (Rocha et al.<sup>8</sup>)**

The synthesis of ETS-10 usually needs the presence of both  $\text{Na}^+$  and  $\text{K}^+$  in the parent gel. There has been report of the use of organic template molecules in the synthesis of ETS-10. The templates reported to use are tetramethylammonium chloride, pyrrolidine, tetraethylammonium chloride<sup>12,13</sup>, tetrapropylammonium bromide, 1,2-diaminoethane<sup>12</sup>, choline chloride, and the bromide salt of hexaethyl diquat-5<sup>14</sup>. However use of template is not beneficial when it comes to large industrial synthesis scale. Since the templating agents are expensive. Besides, the occluded templates have to be removed in order to provide microporosity; this procedure can be both costly and potentially damaging to the framework<sup>8</sup>. The structure of ETS-10 is inherently disordered<sup>10</sup>. The details of this inborn disorder and the pore structure are clearly shown in the high resolution electron micrograph (Figure 1.3). The large 12-ring pores are clearly visible in the structure and as it is shown they stack randomly in the structure.

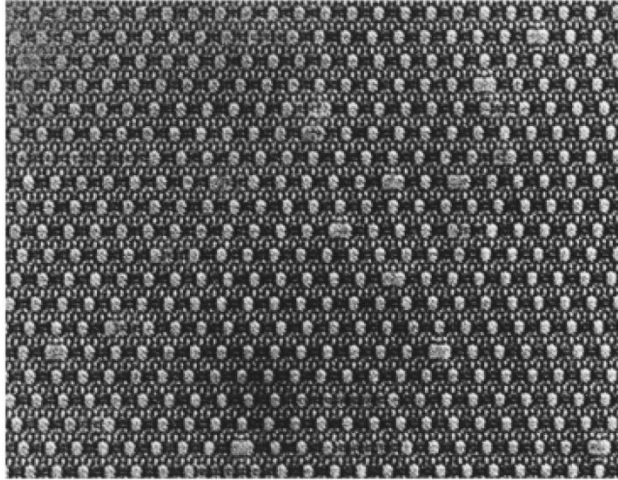


**Figure 1.3: ETS-10 High Resolution Electron Micrograph (Rocha et al.<sup>8</sup>)**

Mixed coordination molecular sieves have many similar characteristics to classical zeolites such as crystalline structure, uniform pores; both consist of cages and channels with a lot of sites for adsorption, ion exchange and catalysis. In addition to their many similarities to classical zeolites, they possessed some distinguished properties which are going to be discussed in the following section.

### **1.2.1 Systematic Pore Shrinkage with Structural Dehydration:**

The mixed coordination sieves have flexible chains that twist with water loss in oppose to rigid structure of classical zeolites. The octahedral chain can lose structural water upon calcination. As a result they twist and push the ring down and therefore the pore size is changed. This phenomenon is called Molecular Gate effect in which the degree of change in pore size depends on the temperature of calcination. For instance, in most cation forms, the crystal lattice of ETS -4, the first synthetic analogue of the mineral zorite<sup>1</sup>, systematically contracts upon structural dehydration at elevated temperature and via this phenomena, the lattice sizes and; therefore, the channels apertures of ETS- 4 can be

controlled to "tune" the effective size of the pores. This phenomenon is used in natural gas purification<sup>15,16</sup>. ETS-4 framework contains six coordinated and five coordinated titanium units along with four coordinated silicate units. The pore size is about 3.8 Å when activated at 200°C while it decreases to 3.4Å when activated at 340°C. This way of controlling the pore size has a negative effect; it inevitably damages the ETS-4 framework and causes some defects in the lattice and eliminates some pore volume and decreases the adsorbent capacity. Consequently, only some cation exchanged forms of ETS-4 based adsorbents such as Ba-ETS-4 are stable under thermal activation; this restricts the practical usage of the Molecular Gate technology in modifying this class of molecular sieves.

### **1.2.2 Pore Tuning by Anions:**

Unlike classical zeolites, mixed coordination materials have anions as well as cations associated with titanium chains in the structure; the anions come from the synthesis mixture. They protrude into the channels and cages and as a result affect the pore size. They are not exchangeable in the same way that cations are; however, the quantity of them can be controlled through controlling synthesis mixture. Tailoring the pore size by controlling the anions in the structure is called anion pore tuning, the anion usually is hydroxyl groups ( $\text{OH}^-$ ), but it can also be any of the halogens such as  $\text{F}^-$ ,  $\text{Cl}^-$ ,  $\text{Br}^-$ ,  $\text{I}^-$ . Lin et al reported substitution of large halogens such as  $\text{Cl}^-$  and  $\text{I}^-$  with hydroxyl groups that leads to effectively reduction of the pore size of titanium silicate zirconite analogues; this is attributed to creation of a steric effect when these substituted anions protrude into the framework. The halogen atoms act as a physical barrier and decrease the channel availability for adsorbate molecules. Therefore the pore size reduces upon increasing the

number of halogens in the framework<sup>17</sup>. In this method, the size of the channels is manipulated by controlling the size and the number of the anions protruding into the channels without relying on the structural shrinkage; it has potential application in size-based separation areas including permanent gas separation and purification of light hydrocarbons.

### **1.2.3 Possibility of Framework Atom Substitution:**

Upon complete or partial infinite substitution of octahedral and tetrahedral atoms into the titanium silicate framework, a new molecular sieve can be synthesized born with similar structure to ETS-10. Titanium in the structure can be replaced by arsenic, cobalt, chromium, copper, iron, germanium, magnesium, manganese, molybdenum, niobium, nickel, vanadium, yttrium, the actinides such as uranium, the lanthanides such as cerium, zinc, zirconium<sup>18</sup>. There are also many different substitution atoms for silicon such as aluminum, arsenic, bismuth, boron, beryllium, cobalt, chromium, copper, iron, gallium, germanium, indium, lead, magnesium, manganese, molybdenum, niobium, nickel, antimony, tin, vanadium, tungsten, zinc<sup>18</sup>. Possibility of introducing different metals into the titanium silicate framework leads to formation of novel microporous materials; they are not only applicable in the areas associated with zeolites such as adsorption, gas separation, catalysis but also applicable in some new fields such as optoelectronics, batteries and sensors<sup>8</sup>.

Many attempts have been reported in the literature to substitute either titanium or silicon in the titanium silicate molecular sieves. Upon this characteristic, new generations of mixed coordination family have been synthesized born. Below I have summarized some of the reported studied in the literature.

### ***1.2.3.1 Zirconosilicates***

Similar to titanium, zirconium can form different silicate minerals with zirconium in octahedral coordination. In all the cases in the literature, zirconium chloride is reported as the source of zirconium. The synthesis of zirconium silicates has been studied under hydrothermal conditions from 300 to 700°C and pressure of up to 700 bar<sup>19</sup>. Unlike ETS-10, the key component in the synthesis of most of the zirconium silicates so far have been different kinds of ammonium; these have been used as templates to direct what structure is formed and to increase the Zr to Si ratio. Besides the cost of templating agents, removing them from the frameworks is expensive and damaging to the structure. Jale et al reported using tetramethylammonium bromide as the template in zirconium silicate synthesis<sup>20</sup>. In another attempt, Lin et al also reported synthesis of a zirconium silicate that is analogue of petarasite, a microporous natural zirconium silicate, in the presence of a template. Zirconium in this rare mineral just like titanium in ETS-10 is in octahedral coordination i.e. it is surrounded by six oxygen ( $ZrO_6$ ) and silicon is in tetrahedral coordination ( $SiO_4$ )<sup>21</sup>. Rocha et al reported synthesis of a microporous zirconosilicates so called as AV-3 in the absence of any template. Its crystal showed an open three dimensional structure consisting of six membered silicate rings of four coordinated silicon and six coordinated zirconium ( $ZrO_6$ ). According to the authors, it has a potential application in the field of catalysis<sup>22</sup>.

### ***1.2.3.2 Niobosilicate***

Rocha et al carried out a study on synthesis of niobium silicates so called as AM-11 (Aveiro- Manchester). They carried out their synthesis in two parts and used

templates. The first part was consisted of an alkaline solution containing tetraethylorthosilicate, ethanol, water, sodium hydroxide, sodium fluoride. The second one contained water, oxalic acid, and niobium oxalate (as the source of niobium). These two solutions were mixed and seed of ETS- 4 was added. The pH was adjusted to 10.2 by adding an ammonia solution. The synthesis occurred in 15 days at 200°C in Teflon-lined autoclaves. The authors reported incorporation of hexa-coordinated niobium in the framework. A series of adsorption tests suggested a small pore size for these materials. Further characterization tests on acid-base properties of this synthetic niobosilicate showed a catalytic property having both acidic and basic active sites. It has been reported as a potential catalyst for alcohol dehydration<sup>23</sup>.

### ***1.2.3.3 Stannosilicate***

Corcoran et al has pioneered the synthesis of microporous structure of stannosilicates under hydrothermal conditions. They reported synthesis of two compounds with composition of  $\text{Na}_8\text{Sn}_3\text{Si}_{12}\text{O}_{34}\cdot n\text{H}_2\text{O}$  and  $\text{Na}_4\text{SnSi}_4\text{O}_{12}\cdot n\text{H}_2\text{O}$  in which stannum is in octahedral coordination position and silicon is in tetrahedral coordination position. Both compounds showed reversible water loss and high capacity ion exchanger property<sup>8,24,25</sup>. In another study, Rocha et al reported another hydrothermally synthesized stannosilicates with the chemical composition of  $\text{Na}_2\text{SnSi}_3\text{O}_9\cdot 2\text{H}_2\text{O}$ . The synthesis mixture did not contain any templates; it consisted of sodium silicate, sodium hydroxide, sodium chloride and water along with stannum chloride ( $\text{SnCl}_4\cdot 5\text{H}_2\text{O}$ ) as the source of stannum. The structure was comprised of a three dimensional framework having six coordinated stannum

(SnO<sub>6</sub>) in each corner along with four coordinated silicon atoms (SiO<sub>4</sub>). In the structure, the SnO<sub>6</sub> units interconnect with SiO<sub>4</sub> units, and no linkages of Sn—O—Sn— were observed in the framework<sup>26</sup>.

#### **1.2.3.4 Vanadosilicate**

Microporous vanadium silicates belong to mixed coordination category of molecular sieves with great potential for different applications such as acid catalysts and sorbate<sup>27,28</sup>.

The first large pore vanadosilicate material has been reported by Rocha et al denoted as AM-6. In this study, the authors used vanadium sulfate as a source of vanadium and used seed<sup>1</sup> of ETS-10. The synthesis was conducted under hydrothermal conditions in autoclave for 3 days. The Si to V ratio was adjusted to 5. They obtained a pale green product with similar XRD pattern and similar structure to ETS-10, i.e. having six-coordinated vanadium and four-coordinated silicon. As a result of stoichiometric amounts of vanadium in the AM-6 structure, it could be used as a catalyst or a sorbate<sup>27</sup>.

Another study have been conducted by Brandao et al on synthesis of two large pore sodium vanadium silicates with framework composition Na<sub>6</sub>Si<sub>14</sub>V<sub>4</sub>O<sub>39</sub> and Na<sub>4</sub>CaSi<sub>10</sub>V<sub>2</sub>O<sub>27</sub>, denoted AM -15 and AM-17, respectively. The former contains both V<sup>4+</sup> in a pyramidal coordination and V<sup>5+</sup> in a tetrahedral coordination, while the latter contains mostly octahedral V<sup>IV</sup>. They both have a good thermal stability in the air (i.e. 380°C for AM-15 and 450°C for AM-17). The nitrogen adsorption isotherm suggests a narrow pore size distribution with 7.3 and 8 Å width for AM-17 and AM-15, respectively. Several adsorption tests indicate that they both are

---

<sup>1</sup> A small quantity of crystalline sieve used to direct the crystallization toward the same product.

capable of adsorbing benzene (6.8 Å), m-xylene (7.4 Å), mesitylene (8.4 Å); this indicates large accessible pores with 7-8 Å width. AM-17 is reported as an interesting catalyst for dehydrogenation reactions<sup>29</sup>.

### **1.3 Ion-exchange property of mixed coordination molecular sieves**

In addition to the above mentioned characteristics which are exclusive to the mixed coordination class, cation substitution is another approach in order to monitor and modify the pore size. The ion exchange property is a characteristic that is common between the mixed coordination zeolites and the classical zeolites. Depending on the size and charge density of the cations after ion exchange the pore size can be decreased or increased. For instance, the pore size of zeolite 4A—pore size of about 4Å—which is sodium based increases to 4.9 Å upon ion exchange with calcium so called as zeolite 5A. Divalent charges are tucked away from the pore mouth and therefore remove the steric hindrance that the monovalent ions provide; this would cause the bigger pores on zeolite CaA(5A) than NaA (4A). On the other hand the pore of zeolite 4A reduces to 2.8 Å upon ion exchanging with potassium so called as zeolite 3A. This is attributed to the larger atomic radius of potassium compared to sodium. In summary in zeolite A pore size decreases on the order of CaA>NaA>KA. Similar pore size modification can be observed in zeolite NaX (13X)—with the pore size of about 7.8 Å—after exchanging with calcium which increases the pore size to 10 Å. Ion-exchange capability in molecular sieves largely extends their application. For instance zeolite 3A is being used for purification of ethanol and methanol (kinetic radius of 4.46, 3.6 Å, respectively) from water (kinetic radius of 2.75 Å) and Zeolite 3A and 13X is being used for removal of CO<sub>2</sub> and ammonia (kinetic radius of 3.3, 3.57 Å, respectively) from natural gas streams. Zeolite 4A is also used for

separating the straight chain hydrocarbons (about 4.3 Å) from branched chain hydrocarbons (kinetic radius of at least 5 Å).

As it is mentioned earlier both classical zeolites and mixed coordination family possess ion-exchange capability. The position of the cations are different in the two class of sieves and are determined by the location of the non-silicon atoms in the framework. The cations in the classical sieves are present inside silica and alumina rings close to aluminum. However the position of the cations in the structure due to the complexity of the structure compared to classical zeolites is not as simple for mixed coordination. It was only in 1994 that the possible location of the cations in ETS-10 got determined for the first time by a combination of experimental and simulation techniques. ETS-10 possesses inherent disorder. There are two ordered polymorph of ETS-10: Polymorph A which possesses a zigzag arrangement of 12-ring pores and polymorph B which possesses a diagonal arrangement of 12-ring pores. In both ETS-10 polymorphs, titanate chains are running orthogonally through the structure. The alkali metal cation locations are largely likely to be near the titanate chains. Up to date there are four studies that investigated the position of alkali metal cations in ETS-10<sup>30-33</sup>. Sankar et al. , Grillo et al. and Ching et al. have found out four cation sites distributed along the titanium-oxygen chains<sup>31-33</sup>. They reported site I and II close to silicon five-ring and site III is next to the 12-ring pore and site IV is close to the orthogonal titanium-oxygen chains. It has been reported that sodium cations favour sites I and III while potassium cations preferentially lower the energy of site III and IV<sup>31,32</sup>. On the other hand, Ching et al. determined that cations are not likely to site either inside the 12-ring pore because of the distance from the titanate chains or in the three-rings due to sterical limitation, the 3-rings are too small to

accommodate the ion. They reported the seven-rings pore are the location of the four possible spots that the cations might be present since these pores are at the intermediate distances from the titanium atoms<sup>33</sup>. Anderson et al. studied ETS-10 structure which was synthesized from different source for example ETS-10 synthesized from only sodium, from sodium and potassium and from template. Their studies also extend to hydrated and dehydrated ETS-10 to accurately determine the cation location in absence or presence of water. Their findings from ETS-10 synthesized with both sodium and potassium cations showed presence of the two Na sites—site I and site II (see Figure 1.4)—outside the 12-ring pore. The reason is that the signal from those two sites is consistently strong regardless of the presence of water in the structure. They assigned site III and V to the position in the proximity of water molecules inside the 12-ring pore near the titanate chains. This is attributed to the change of the position of the signal after and before removing water molecules. By comparing the spectrum of ETS-10 in the form of only sodium cations in its hydrated format with ETS-10 sample containing both sodium and potassium cations, they noted the total absence of a strong signal which was present in the ETS-10 with only sodium cation from the ETS-10 with both sodium and potassium; this would suggest a preferred potassium sitting site. It should be noted that the vanished signal was still present in the spectrum of the dehydrated ETS-10 sample containing only sodium. Site IV is located inside the 7-ring pore at the closest vicinity of the titanate chains. It is observed that the signal disappeared in the ETS-10 sample containing both potassium and sodium; this suggests that this site is favoured by potassium cations. The modeling indicated that the rest of the potassium cations will sit in site V.

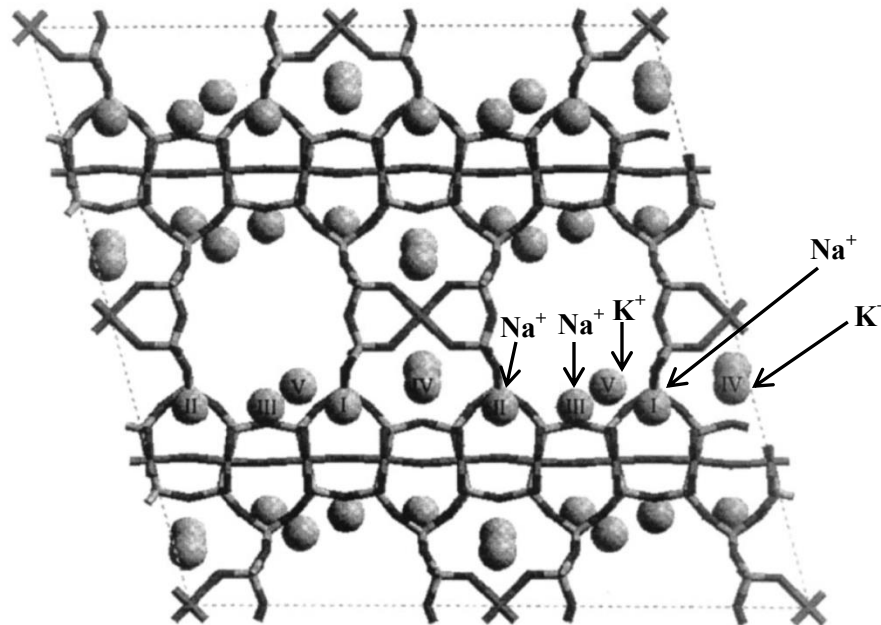


**Figure 1.4: The five suggested cation sites for ETS-10 (adapted from Anderson et al.<sup>30</sup>)**

## 1.4 Research Objectives

The focus of our study is to make a new molecular sieve by use of the framework atom substitution properties of mixed coordination family of molecular sieves. A mixed coordination sieve combines the chemically passive characteristics of de-aluminated classical zeolite with the ion exchange capability of aluminosilicate zeolite. The presence of the silica rings in the ETS-10 structure—a prime example of mixed coordination family—increases the thermal stability of the structure compared to aluminosilicate (classical zeolites) besides the compensating ions in structure provides adsorption sites. It is due to these interesting properties that this study focuses on synthesizing a new molecular sieve with similar structure to ETS-10 without using any ETS-10 seed, template or reducing agent.

All the above-mentioned features allow for the ability to tailor the mixed coordination family adsorbents with precise control for different adsorption purposes; this largely extends the scope of the molecular sieves applications.

## 1.5 Commercial Gas Separation Technique

The most common gas separation techniques are summarized into three processes as follows:

1. ***Cryogenic Distillation:*** The underlying basic of this technique is based on the relative volatilities of the two components. It is particularly more suited for large scale production of high purity gases. Whereas, owing to transportation cost of the cryogenic products and power consumption, it considers less efficient at low to medium-scale production. For instance, for over 70 years, cryogenic distillation has been applied for air separations as well as olefin/paraffin separations from olefin plants, refinery gas streams and other sources<sup>34</sup>.
2. ***Membrane Separation:*** This technique is based on the difference in solubility or diffusivity of the two components in the membrane material. . For air separation, this technique is restricted to a single stage process which leads to maximum 50% nitrogen purity.
3. ***Adsorption Process:*** This technique is more applicable for on-site production, i.e. medium to large scale. Adsorption processes are generally more preferable to distillation and absorption methods due to the costly and energy-intensive characteristics of the latter techniques; they are economically more viable due to the adaptability of the adsorbents, in particular molecular sieves. Among the above mentioned methods, adsorption is the best technique due to its energy

efficient characteristic and feasibility of tailoring the adsorbents to the specific application; it is also not restricted to a single stage process.

### 1.5.1 Adsorption Process:

Pressure swing adsorption (PSA) and vacuum swing adsorption (VSA) are well-established commercial processes for both oxygen production and hydrocarbon separation for at least the past two decades. A relatively high selectivity can be expected with PSA or VSA systems even in one bed due to the fast separation performance. Before 1980, the adsorption and desorption pressures in PSA systems were above atmospheric; they had low capital cost owing to simplicity but high power usage because the feed components should be compressed. Later, the possibility of improving the sorbents and lower expense of the vacuum equipment resulted in development of VPSA systems; they normally perform at adsorption pressure slightly above atmospheric and desorption pressure of about 0.2 atm<sup>34</sup>. With molecular sieves as adsorbents, adsorption separations are classified into three categories as follows.

- ***Thermodynamic Separation (Equilibrium Separation):*** This is the most common type of separation in molecular sieves. There is a preference or selectivity for one molecule over another which results from difference in adsorption strengths. Here, separation is gained based on the difference in the heat of adsorption of the competing species. This mechanism is equilibrium driven with two controlling factor, namely, adsorbate polarizability, and exposure of active sites. Oxygen production on Li-LSX is an example of this type of separation. At equilibrium nitrogen has higher affinity on Li-LSX than oxygen which leads to adsorption of nitrogen streams while oxygen streams breakthrough from the outlet<sup>35,36</sup>.

- ***Kinetic Separation:*** It is a transient process based on the differences in the relative adsorption rates of competing species to get into the adsorbent pores. Therefore, by controlling the exposure time of the gaseous species to the adsorbent, the faster diffusing molecule would be selectively adsorbed on the adsorbent surface. In kinetic separation the difference in the rate of adsorption can be used to design a separation system. The best example of this class of molecular sieves is carbon molecular sieves (CMS). Their pore size distribution allows them to benefit from diffusion of different gases at different rate. Nitrogen production from air is a commercial example of kinetic separation using CMS<sup>36</sup>. Oxygen can diffuse much faster than nitrogen which is believed to be as a result of smaller kinetic diameter of oxygen compared to nitrogen. Therefore, although CMS has a smaller capacity compared to most of the other zeolites, it is more efficient to use CMS for nitrogen generation from air.
- ***Molecular Exclusion Separation (Steric Separation):*** It is a sized-based separation and considered a quasi-equilibrium process. Molecular sieving property of the zeolites accounts for steric separation. In other words, in the steric separation, the porous adsorbent has pores with critical dimension such that it allows only small and properly-shaped molecules to enter, while prevents other molecules which do not fit the pores. Steric separation is restricted to the zeolites owing to their unique characteristics of having uniform micropores in their crystalline structures. One of the methods to control the aperture dimension is to exchange the cations in the zeolitic framework. For instance, zeolites 3A, 4A, and 5A have distinct pore sizes which allow them to adsorb molecules with effective diameters smaller than 3, 4 and 5 Å, respectively. Drying with 3A zeolite and the separation of normal paraffins from iso-

paraffins and cyclic hydrocarbons using 5A are the two largest applications of steric separation<sup>35,36</sup>.

Having chosen adsorption as the separation method, it is important to investigate the underlying thermodynamics behind this technique.

## **1.6 Thesis Outline**

The study presented in this thesis is focused on synthesizing a new molecular sieve with characteristics similar to ETS-10, its ion-exchange property, its underlying adsorption mechanism and subsequently its application toward hydrocarbon separation.

Chapter Two provides background information on the fundamental properties of adsorption. Chapter Three introduces a simple method to synthesize, for the first time, microporous vanadium silicate analogue to ETS-10 without using ETS-10 seed, template or reducing agent. Chapter Four is comprised of a detailed comparative study between the new synthesized adsorbent, vanadium silicate, with its titanium analogue ETS-10. Chapter Five is dedicated to the understanding of the adsorption mechanism on the vanadium silicate so called as EVS-10. In this chapter we have proposed an adsorption mechanism through a detailed thermodynamic study of ETS-10, analogue of EVS-10, compared to two other structurally different zeolites, ZSM-5 and 13X. Chapter six focuses on behaviour of EVS-10 after introducing silver to the EVS-10 framework. Despite all the similarities between ETS-10 and EVS-10, it turns out the silver exchange EVS-10 does not behave similar to the silver exchange ETS-10. A detailed study comprised of different characteristic analysis of Ag-EVS-10 and as-synthesized EVS-10 is carried out in this chapter. Chapter seven focuses on application of the new synthesized molecular sieve, vanadium silicate. This chapter describes an adsorptive separation of a

binary gas mixture of ethane and methane on vanadium silicate EVS-10 using a laboratory-scale unit. At the end, chapter eight summarizes and concludes the Thesis.

## References

- (1) Milton, R. M. Molecular Sieve Adsorbents. 2,882,244, April 1959.
- (2) Breck, D. W. *Zeolite Molecular Sieves: Structure, Chemistry, and Use*; John Wiley & Sons, Inc., 1974.
- (3) Sherman, J. D. Synthetic Zeolites and Other Microporous Oxide Molecular Sieves. 1999, *96*, 3471–3478.
- (4) Sircar, S.; A., M. L. Chapter 22: Gas Separation by Zeolites. In *Hand book of Zeolite Science and Technology*; Auerbach, M. S.; Carrado, A. K.; Dutta, K. P., Eds.; Marcel Dekker, Inc., 2003; Vol. 10.
- (5) Song, C.; Yan, Z. *Characterization and Cracking of the Modified USY Zeolites with Mixed Organic Acid*; Dongying, China.
- (6) Kuznicki, S. M. Large-Pored Crystalline Titanium Molecular Sieve Zeolites. 5011591, 1991.
- (7) Lamberti, C. Electron-Hole Reduced Effective Mass in Monoatomic ...-O-Ti-O-Ti-O-... Quantum Wires Embedded in the Siliceous Crystalline Matrix of ETS-10. *Micropor. Mesopor. Mat.* 1999, *30*, 155–163.
- (8) Rocha, J.; Anderson, M. W. Microporous Titanosilicates and Other Novel Mixed Octahedral-Tetrahedral Framework Oxides. *Inorg. Chem.* 2000, 801–818.
- (9) Anderson, M. W.; Terasaki, O.; Ohsuna, T.; Philippou, A.; MacKay, S. P.; Ferreira, A.; Rocha, J.; Lidin, S. Structure of the Microporous Titanosilicate ETS-10. *Nature* 1994, *367*, 347–351.
- (10) Anderson, M. W.; Terasaki, O.; Ohsuna, T.; Philippou, A.; MacKay, S. P.; Ferreira, A.; Rocha, J.; Lidin, S. Structure of the Microporous Titanosilicate ETS-10. *Stud. Surf. Sci. Catal.* 1995, *98*, 258–259.
- (11) Rocha, J.; Ferreira, A.; Lin, Z.; Anderson, M. W. Synthesis of Microporous Titanosilicate ETS-10 from TiCl<sub>3</sub> and TiO<sub>2</sub>: A Comprehensive Study. *Micropor. Mesopor. Mat.* 1998, *23*, 253–263.
- (12) Valtchev, V. P. Influence of Different Organic Bases on the Crystallization of Titanium Silicate ETS-10. *J. Chem. Soc. Chem. Commun.* 1994, 261.
- (13) Valtchev, V.; Mintova, S. Synthesis of Titanium Silicate ETS-10: The Effect of Tetrametylammonium on the Crystallization Kinetics. *Zeolites* 1994, *14*, 697–700.

- (14) T.P. Das, A.J. Chandwadkar, A.P. Budhkar, S. S. Studies on the Synthesis of ETS-10 II. Use of Organic Templates. *Microporous Mater.* 1996, 5, 401–410.
- (15) Kuznicki, S. Small-Pored Crystalline Titanium Molecular Sieve Zeolites and Their Use in Gas Separation Processes, May 2000.
- (16) Ferdov, S. Temperature- and Vacuum-Induced Framework Contraction of Na-ETS-4. *Langmuir* 2010, 26, 2684–2687.
- (17) Lin, C. C. H.; Sawada, J. A.; Wu, L.; Haastrup, T.; Kuznicki, S. M. Anion-Controlled Pore Size of Titanium Silicate Molecular Sieves. *J. Am. Chem. Soc.* 2009, 131, 609–614.
- (18) Kuznicki, S. M.; Thrush, K. A. Large Pored Molecular Sieves with Charged Octahedral Titanium and Charged Tetrahedral Aluminum Sites. US5244650, October 1993.
- (19) Baussy, G.; Caruba, R.; Baumer, A.; Turco, G. Mineralogie Experimentale Dans Le System ZrO<sub>2</sub>-SiO<sub>2</sub>-Na<sub>2</sub>O-H<sub>2</sub>O. Correlations Petrogenetiques. *Bull. Soc. Miner. Crystallogr.* 1974, 97, 433–444.
- (20) Jale, S. R.; Ojo, A.; Fitch, F. R. Synthesis of Microporous Zirconosilicates Containing ZrO<sub>6</sub> Octahedra and SiO<sub>4</sub> Tetrahedra. *Chem Commun.* 1999, 411–412.
- (21) Lin, Z.; Rocha, J.; Ferreira, P.; Thursfield, A.; Agger, J. R.; Anderson, M. W. Synthesis and Structural Characterization of Microporous Framework Zirconium Silicate. *J. Phys. Chem. B* 1999, 103, 957–963.
- (22) Rocha, J.; Ferreira, P.; Lin, Z.; R. Agger, J.; W. Anderson, M.; J., R. A.; M., W. A. Synthesis and Characterisation of a Microporous Zirconium Silicate with the Structure of Petarasite. *Chem. Commun.* 1998, 1269–1270.
- (23) Rocha, J.; Brandão, P.; Phillippou, A.; Anderson, M. W. Synthesis and Characterisation of a Novel Microporous Niobium Silicate Catalyst. *Chem. Commun.* 1998, 2687–2688.
- (24) CORCORANJR, E.; VAUGHAN, D. Hydrothermal Synthesis of Mixed Octahedral-Tetrahedral Oxides: Synthesis and Characterization of Sodium Stannosilicates. *Solid State Ionics* 1989, 32-33, 423–429.
- (25) W., C. E.; M., N. J.; E., K. H.; W., V. D. E. Phase Identification of Hydrothermal Crystallization Products from M<sub>2</sub>O-SiO<sub>2</sub>-SnO<sub>2</sub>-H<sub>2</sub>O Gels or Solutions. In *Zeolite Synthesis*; pp. 603–616.

- (26) Ferreira, A.; Lin, Z.; Rocha, J.; Morais, C. M.; Lopes, M.; Fernandez, C. Ab Initio Structure Determination of a Small-Pore Framework Sodium Stannosilicate. *J. Inorg. Chem.* 2001, *14*, 3330–3335.
- (27) Rocha, J.; Brandão, P.; Lin, Z.; Anderson, M. W.; Alfredsson, V.; Terasaki, O. The First Large-Pore Vanadosilicate Framework Containing Hexacoordinated Vanadium. *Angew. Chem. Int. Ed. Engl.* 1997, *36*, 100–102.
- (28) Rao, P. R. H.; Belhekar, A. A.; Hedge, S. G.; Ramaswamy, A. V.; Ratnasamy, P. Studies on Crystalline Microporous Vanadium Silicates. II. FTIR, NMR, and ESR Spectroscopy and Catalytic Oxidation of Alkylaromatics over VS-2. *J. Catal.* 1993, *141*, 595–603.
- (29) Brandao, P.; Valente, A.; ad Artur Ferreira and Michael W. Anderson, A. P.; Rocha, J. Hydrothermal Synthesis and Characterisation of Two Novel Large-Pore Framework Vanadium Silicates. *Eur. J. Inorg. Chem.* 2003, 1175–1180.
- (30) Anderson, M. W.; Agger, J. R.; Luigi, D.-P.; Baggaley, A. K.; Rocha, J. Cation Sites in ETS-10:  $^{23}\text{Na}$   $3\text{Q}$  MAS NMR and Lattice Energy Minimisation Calculations. *Phys. Chem. Chem. Phys.* 1999, *1*, 2287–2292.
- (31) Grillo, M. E.; Carrazza, J. Computational Modeling of the Nonframework Cation Location and Distribution in Microporous Titanosilicate ETS-10. *J. Phys. Chem.* 1996, *100*, 12261–12264.
- (32) Sankar, G.; Bell, R. G.; Thomas, J. M.; Anderson, M. W.; Wright, P. A.; Rocha, J. Determination of the Structure of Distorted  $\text{TiO}_6$  Units in the Titanosilicate ETS-10 by a Combination of X-Ray Absorption Spectroscopy and Computer Modeling. *J. Phys. Chem.* 1996, *100*, 449–452.
- (33) Ching, W. Y.; Xu, Y. N.; Gu, Z. Q. Structure and Properties of Microporous Titanosilicate Determined by First-Principles Calculations. *Phys. Rev. B - Condens. Matter Mater. Phys.* 1996, *54*.
- (34) Ruthven, D. M. *Principles of Adsorption and Adsorption Processes*; John Wiley & Sons, Inc. , 1984.
- (35) Yang, R. T. *Adsorbents, Fundamentals and Applications*; John Wiley & Sons, Inc.: Hoboken, New Jersey, 2003; p. 410.
- (36) Yang, R. T. *Gas Separation by Adsorption Process*; Butterworth, Boston, 1987.

# Chapter 2

## Fundamental of Adsorption

### 2.1 Adsorption Principles

Adsorption is defined as adhesion of layer of atoms, ions or molecules (as of gases, liquid or solutes) to a surface. It occurs when the total interaction energy  $\phi$  is equal to the work done to bring a gas molecule to the adsorbed state. It is assumed that adsorbed state is at the saturated vapor pressure (see Equation 2.1) <sup>1</sup>.

$$-\phi = -\Delta G = \int_P^{P_0} VdP = RT \ln \frac{P_0}{P} \quad (2.1)$$

where,  $\Delta G$  is the free energy change and  $P_0$  is the saturated vapor pressure,  $P$  is the pressure at which adsorption happens. There are two kinds of adsorption, namely, physical adsorption and chemical adsorption. Former deals with weak intermolecular forces whereas latter involves with formation of chemical bond between the molecule of sorbate and surface of adsorbent, which is a much stronger interaction. Sometimes adsorption is a physical adsorption but the heat of adsorption is as high as if it were chemisorption. For example, adsorption of molecules such as water and ammonia with small dipolar molecules on zeolite adsorbents is strongly favoured which leads to the high heat of adsorption as high as if it were chemisorption. Although this adsorption is considered physisorption and there is no chemical bonding; however the heat of adsorption is of a magnitude corresponds to chemisorption<sup>2</sup>. The general features of physical and

chemical adsorption are compared in Table 2.1 Most of the adsorptive separation processes are based on physical adsorption<sup>3</sup>.

**Table 2.1: Comparison between Physisorption and Chemisorption<sup>3</sup>**

Physical Adsorption	Chemisorption
Low heat of adsorption (less than 2 or 3 times latent heat of evaporation.) Monolayer or multilayer.	High heat of adsorption (greater than 2 or 3 times latent heat of evaporation.) Monolayer only.
No dissociation of adsorbed species. Only significantly happens at relatively low temperatures.	May involve dissociation. It is possible over a wide range of temperature.
Rapid, non-activated reversible. No bonding; thus no electron transfer although polarization of sorbate might occur.	Activated, possibly slow and irreversible. Involves bonding so electron transfer happens between sorbate and sorbent.

## 2.2 Forces and Energies of Adsorption

The total potential between the adsorbent and the adsorbate molecules is the sum of the total adsorbate-adsorbate and the adsorbate-adsorbent interaction potentials:

$$\phi_{total} = \phi_{adsorbate-adsorbate} + \phi_{adsorbate-adsorbent} \quad (2.2)$$

Adsorbate-adsorbent interaction has a primary effect on the adsorbate-adsorbate interaction. From here on the adsorbate-adsorbent interaction will be referred as  $\phi$ . Generally, there are three types of potential that contributes to the adsorbate-adsorbent interactions: dispersion, electrostatic, and chemical bond. The forces engage in physisorption are comprised of both van der Waals forces (dispersion and repulsion) and electrostatic interactions which include polarization, dipole and quadrupole interactions and as it has been mentioned earlier physisorption does not involve with any chemical bonding<sup>1</sup>.

$$\phi = \phi_D + \phi_R + \phi_{ind} + \phi_{F\mu} + \phi_{FQ} \quad (2.3)$$

where  $\phi_D$  = dispersion energy,  $\phi_R$  = close range repulsion energy,  $\phi_{ind}$  = induction energy (interaction between an induced dipole and electric field),  $\phi_{F\mu}$  = interaction between electric field ( $F$ ) and a permanent dipole ( $\mu$ ),  $\phi_{FQ}$  = interaction between field gradient ( $\dot{F}$ ) and a quadrupole (with quadrupole moment  $Q$ ).

The first two potential are from van der Waals forces which, regardless of the type of adsorbent, are always present. Whereas, the last three terms are contributions from charges on the solid surface that create electric fields. The resulting electrostatic forces is most noticeable in the presence of adsorbents such as zeolites with ionic structure due to the electrostatic field caused by the presence of the ions in the structure<sup>3</sup>. All the above potentials are defined below. The interactions are between an atom or a charge on the surface and the adsorbate molecule<sup>1</sup>.

Dispersion:

$$\phi_D = -\frac{A}{r^6} \quad (2.4)$$

Repulsion:

$$\phi_R = +\frac{B}{r^{12}} \quad (2.5)$$

Field of an ion and induced point dipole:

$$\phi_{ind} = -\frac{1}{2} \alpha F^2 = -\frac{\alpha q^2}{2r^4 (4\pi\epsilon_0)^2} \quad (2.6)$$

Field of an ion and point dipole:

$$\phi_{F\mu} = -F\mu \cos \theta = -\frac{q\mu \cos \theta}{r^2 (4\pi\epsilon_0)} \quad (2.7)$$

Field gradient and linear point quadrupole:

$$\phi_{FQ} = \frac{1}{2} Q F = p \frac{Qq(3 \cos^2 \theta - 1)}{4r^3(4\pi\epsilon_0)} \quad (2.8)$$

where A and B are constants,  $\alpha$  = polarizability,  $F$  = electric field,  $q$  = electronic charge of ion on the surface,  $\epsilon_0$  = Permittivity of a vacuum,  $\mu$  = permanent dipole moment,  $\theta$  = angle between the direction of the field or field gradient and the axis of the dipole or linear quadrupole,  $Q$  = linear quadrupole moment (+ or -). The important parameter,  $r$ , is the distance between the centres of the interacting molecules<sup>1</sup>.

### 2.3 Heat of Adsorption

It is known that the isosteric heat of adsorption at low coverage corresponds to the adsorbate-adsorbent interaction potential ( $\phi$ ) by:

$$\Delta H = \phi - RT + F(T) \quad (2.9)$$

where vibrational and translational energies of the adsorbate molecules accounts for  $F(T)$ .

It has been suggested that at ambient temperature the isosteric heat of adsorption is approximately equal to the total interaction potential, i.e.  $\Delta H \approx \phi$ .

Physical adsorption processes are all exothermic; therefore, all have negative enthalpy ( $\Delta H < 0$ )<sup>3</sup>.

There are three terms referring to the heat of adsorption, including:

1. The isothermal integral heat of adsorption. This is the total heat released when the adsorbate loading is increased from zero to some final value at isothermal conditions.

2. The differential heat of adsorption,  $\Delta\bar{H}_1$ . This is the change in the integral heat of adsorption with a change in adsorbate loading. It may be defined by the following equation:  $\Delta\bar{H}_1 = (\bar{H}_1 - \tilde{H}_g)$

where,  $\tilde{H}_g$  and  $\bar{H}_1$  are molar enthalpy and partial molar enthalpy of the gaseous adsorbate, respectively. The differential heat of adsorption depends on pressure, temperature and adsorbate coverage between two points on the isotherm.

3. The isosteric heat of adsorption is derived from adsorption isosteres—lines of constant adsorbate loading—it is achieved through the Clausius-Clapeyron equation from the slopes of the adsorption isosteres drawn on the plot of the  $\ln P$  vs.  $1/T$ .

$$\frac{d \ln P}{d(1/T)} = -\frac{\Delta\bar{H}_1}{R} = \frac{q_{iso}}{R} \quad (2.10)$$

where  $R$  is the gas constant,  $P$  refers to the adsorbate absolute pressure, and  $T$  is the absolute temperature in Kelvin. The isosteric heat of adsorption is related to the differential heat of adsorption:

$$q_{iso} = -\Delta\bar{H}_1 \quad (2.11)$$

It can be implied that the isosteric and differential heats are identical. It is possible to calculate the integral heat of adsorption from isosteric heats. In most of the zeolites, at low loadings, isosteric heat of adsorption progressively drops as loading is increased. This supports the theory that the adsorbent surface is energetically heterogeneous which means some of the adsorption sites interact more strongly with adsorbate molecules. The most energetic sites are filled first so that adsorption of additional molecules involves progressively lower heats of adsorption. All adsorbents have surfaces that are heterogeneous both energetically and geometrically (not all pores have uniform and

constant dimensions). The degree of heterogeneity differs substantially from one adsorbent type to another<sup>1,3</sup>.

## 2.4 Selectivity

The selectivity or separation factor describes the preference of the adsorbent toward one adsorbate over another. The selectivity is influenced by pressure and temperature. For a given adsorbent, the relative strength of the adsorption of different adsorbates depends on the relative magnitudes of the polarizability, dipole moment, and quadrupole moment of each species. Similarly, for a given adsorbate, the relative strength of adsorption is subject to the relative polarizability and electrostatic field strengths of adsorbent surface. Selectivity ( $\alpha$ ) of a binary gasmixture consisting of gas  $A$  and gas  $B$  can be defined in terms of the isosteric heat of adsorption as follows:

$$\alpha_B^A = K \exp \frac{q_{isoB}^A}{RT} \quad (2.12)$$

In zeolites, selectivity shown towards particular adsorbate molecules may be modified by methods which change energy of interaction terms. Three methods are known for changing the adsorption selectivity:

1. By preloading or introducing small amounts of a polar adsorbate such as water; which means water will preferentially adsorb on the most energetic sites in the zeolite strongly enough that it may not let other less selective adsorbate molecules replace it.
2. By cation exchange; cation exchange not only can change the pore size, but also it can affect the local electric field as well as adsorbate polarization.

3. Decationization; by removing all the cations present in the zeolite framework, the local electric field and field gradients will change. Consequently, any interaction with a molecule with a permanent electric moment will be reduced.

All the above mentioned forces contribute to the total interaction energy, which effect on the isosteric heat of adsorption between an adsorbent and adsorbate; however, depending on the type of adsorbent and adsorbate, some may have significant effect and some may be negligible. In the next section, the effects of the adsorbate properties on adsorption is discussed.

## **2.5 Effects of Adsorbate Properties on Adsorption: Polatrizability ( $\alpha$ ), Dipole Moment ( $\mu$ ) and Quadrupole moment ( $Q$ )**

Properties of the adsorbate have the primary effect on the adsorbate-adsorbent interaction for a given adsorbent. Polarizability is the most important property which determines interactions contributes from repulsion, dispersion and induction. On a surface without charges such as silicalite the induction potential is zero. Polarizability rises with molecular weight since more electrons would be accessible for polarization. On zeolites with charges in the structure, the permanent dipole and quadrupole moment can make major contributions toward the total potential<sup>4</sup>. In Table 2.2, two types of adsorbent are included and have been compared for different types of adsorbate with different properties. As it is shown in Table 2.2, nitrogen which has a moderately strong quadrupole moment, but no permanent dipole, the potential from  $\phi_{F\mu}$  is zero unlike the potential from the quadrupole moment  $\phi_{FQ}$ . It has been indicated that on chabazite the  $\phi_{FQ}$  contribution is one third of the total interaction in that Si/Al ratio is close to one; therefore, it has a lot of charges to interact with the quadrupole moment in nitrogen. NaX (zeolite 13X) has Si/Al ratio lower than chabazite which means there are more charges in the structure therefore

$\phi_{FQ}$  accounts for half of the total energy on zeolite 13X. For the molecules with strong dipoles and quadrupoles or with both the interaction from  $\phi_{F\mu} + \phi_{FQ}$  dominate the total energy. This table shows a brief study on a non-ionic adsorbent and two ionic adsorbents in the presence of different molecules with different polarizability. A more detailed study is conducted in Chapter 4 regarding the effect of polarizability in mixed-coordination molecular sieve with a combined structure having both ionic and non-ionic characteristics.

Heat of adsorption is a way to qualitatively estimate the strength of the interactions between the adsorbent and adsorbate. In fact, an important factor in selecting a proper adsorbent for a targeted adsorbate depends on the adsorption isotherm, which is discussed in the following section. The shapes of the isotherm are influenced by the strength of adsorbate-adsorbent interaction as in heat of adsorption.

**Table 2.2: Contribution to near zero loading heat of adsorption. \* Permanent dipole moments ( $\mu$ ):  $H_2O > NH_3 > N_2O$  and Quadrupole moments ( $Q$ ):  $CO_2 > N_2O > N_2 > NH_3$ . \*\* For graphite carbon  $\phi_{Ind} = 0$ .**

Adsorbent	Adsorbate *	$\alpha \times 10^{24}$ $cm^3/molec.$	$\Delta H$ $(kJ/mol)$	$-(\phi_D + \phi_R + \phi_{Ind})$	$-(\phi_{F\mu} + \phi_{FQ})$
Graphite Carbon **	Kr	2.48	12	2.48	0
	Xe	4.04	15.5	3.1	0
	N <sub>2</sub>	1.74	37.6	6.45	2.55
Chabazite Si/Al=1.6-3.0	N <sub>2</sub> O	3.03	64	9.07	6.18
	NH <sub>3</sub>	2.2	131.8	7.5	23.8
	N <sub>2</sub>	1.74	27.2	3.10	3.4
Na-X Si/Al=1.0-1.5	CO <sub>2</sub>	2.91	51	4.20	7.98
	NH <sub>3</sub>	2.2	74.9	3.75	14.2
	H <sub>2</sub> O	1.45	142	2.65	31.3

## 2.6 Adsorption Isotherm

Adsorption can be defined in terms of adsorption isotherm; it is the quantity of adsorbate on a surface of adsorbent at equilibrium over a range of relative pressure and at constant temperature. The first systematic attempt to interpret adsorption isotherms for gas/solid equilibria was initiated by Brunauer et al (known as BDDT ) in 1940<sup>5</sup>. They categorized adsorption isotherms into five types. The BDDT classification was adapted as the IUPAC classification of adsorption isotherm as shown in Figure 2.1

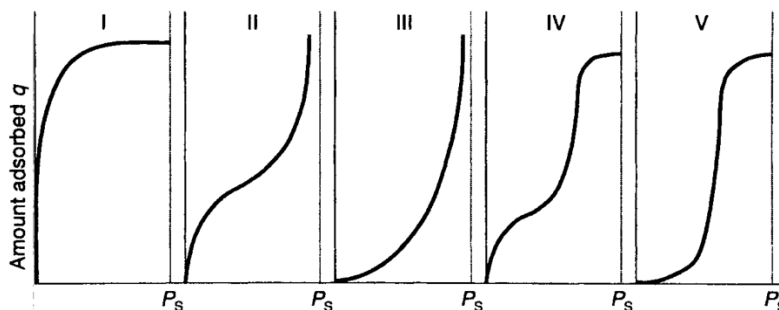


**Figure 2.1: Five types of adsorption isotherms, adopted from Thomos et al.<sup>6</sup>**

Type I isotherm approaches a limiting value and usually is used to describe adsorption on microporous adsorbents like adsorption of  $N_2$  on clinoptilolite<sup>2</sup> at 25°C. The isotherms for the microporous adsorbents in which the pore size is not very much larger than the molecular diameter of the adsorbate are normally of Type I. Since with such adsorbents there is a definite saturation limit due to complete filling of the micropores. Type II describes adsorption on macroporous adsorbents with strong adsorbate-adsorbent interactions; it represents a BET adsorption mechanism. Type III depicts adsorption on macroporous adsorbents with weak adsorbate-adsorbent interactions; it is a typical adsorption isotherm of water on a hydrophobic surface. Type II and III are generally occurs only when adsorbents have wide distribution of pore

<sup>2</sup> It is a natural zeolite comprises of tetrahedral silica and alumina units. It has the complex formula:  $(Na,K,Ca)_{23}Al_3(Al,Si)_2Si_{13}O_{36} \cdot 12H_2O$

sizes. As a result there is a continuous rise with increasing loading from monolayer to multilayer adsorption and finally to capillary condensation. The increase in capacity at elevated pressures is attributed to the capillary condensation happening in pores of larger diameter as the pressure increased. Type IV and type V are similar to type II and type III, with the exception that as  $P$  approaches  $P_0$ , the amount adsorbed approaches a finite limit; this is attributed to the finite pore volume of porous solids. Isotherm of Type IV suggests the formation of two layers on a plane surface or on the wall of a pore very much larger than the adsorbate molecular diameter. Type V happens when the intermolecular attraction forces are larger than the interaction of the adsorbate with the surface of adsorbent.

The great majority of the isotherms models are established based on three different approaches:

*The Langmuir Approach:* Langmuir approach which is proposed by Langmuir (1918) is based on kinetic adsorption and assumes that adsorption system is in dynamic equilibrium, and the evaporation rate (desorption) is equal to that of condensation (adsorption). Langmuir approach is the most practical method in data correlation in separation processes<sup>3</sup>.

*The Gibbs Approach:* Gibbs (1928), supposed that adsorbent is thermodynamically inert at equilibrium. Gibbs adsorption isotherm equation is applied in this approach which assumes a two-dimensional equation of state of the adsorbed film, relating  $\pi - A - T$ <sup>3</sup>:

$$-Ad\pi + nd\mu = 0 \quad (2.13)$$

Where,  $\pi$  is the spreading pressure,  $A$  is surface area,  $n$  and  $\mu$  are the number of moles and the chemical potential, respectively. An intergration of the above equation leads to the desired isotherm. There are as many isotherms as the number of assumed equations of state, ranging from the ideal gas law to virial equations.

Both of the above mentioned approaches have been used to derive different isotherm models for both pure and gas mixtures.

## 2.6.1 Equilibrium Adsorption of Pure Gas

### 2.6.1.1 Langmuir Isotherm:

This isotherm model is the simplest and the most practical one and can be employed for both physical and chemical adsorption processes. The primary assumptions on which the models are formed are<sup>3,7</sup>:

1. Adsorbate molecules are adsorbed at a finite number of well-defined localized sites.
2. Each molecule is adsorbed only on to one site.
3. All sites are homogeneous which means they are energetically equivalent.
4. There is no interaction between the adsorbed molecules with the neighbouring sites. This implies that the heat of adsorption is independent of coverage.

The Langmuir isotherm can be derived based on Langmuir approach as follows:

$$\text{Rate of adsorption} = k_a p (1 - \theta)$$

$$\text{Rate of desorption} = k_d \theta$$

Where  $q_s$  is the total number of sites per unit weight or volume of the adsorbent and  $\theta = q/q_s$  is the fractional coverage. At equilibrium the rates of adsorption and desorption are equal:

$$\frac{\theta}{1 - \theta} = \frac{k_a}{k_d} p = bp \rightarrow \theta = \frac{q}{q_s} = \frac{bp}{1 + bp} \quad (2.14)$$

where  $b = k_a/k_d$  ( $k_a$  adsorption constant and  $k_d$  desorption constant) is the adsorption equilibrium constant,  $q_s$  in Langmuir model is supposed to denote to a fixed number of sites thus it should be a temperature-independent constant while the equilibrium constant  $b$  is a temperature dependant variable. Since  $\Delta H$  is negative,  $b$  decreases with increasing temperature<sup>3</sup>.

$$b = b_0 \exp\left(\frac{-\Delta H_0}{RT}\right) \quad (2.15)$$

### 2.6.1.2 The BET Isotherm

The BET isotherm is the key factor to characterize the specific surface area of a porous adsorbent. The specific surface area of microporous materials is on the order of several hundred square meters per gram. The physical adsorption undergoes multilayer adsorption. Unlike other models, the BET model requires multilayer adsorption. The formation of the second and subsequent layers starts at pressures well below the pressure at which the monolayer formation completes. Therefore it is not simple to extract the monolayer capacity from the experimental isotherm. In 1938 Brunauer, Emmett, and Teller (BET)<sup>8</sup> suggested a simple model to account for multilayer adsorption and discount the monolayer capacity by use of this model and therefore extract the specific surface area<sup>3</sup>. According to the BET, molecules adsorbed in one layer are considered as adsorption sites in the next layer, consequently a large number of the layers can be adsorbed on the surface and leads to the conception of a statistical monolayer. Besides all the Langmuir assumptions, BET models assumes that the characteristics of the second and following layers are the same as that of the bulk phase<sup>3,8</sup>.

In the BET model, the non-mobile adsorbate molecules, which are the molecules that are strongly favored by the surface of the adsorbent, can be adsorbed on to one site. On the first

layer, the rate of condensation on the vacant sites is equal to the rate of evaporation from the sites which are covered by only one adsorbate. The important assumption in this model is that the heat of adsorption of all the layers is assumed to be constant and equal to the heat of liquefaction except for the first layer. Furthermore, the adsorption to desorption constant ratio ( $\alpha/\beta$ ) is assumed to remain unchanged for all the second layers on. Hence, the BET equation is achieved by summing over all the layers:

$$\frac{P}{v(P_0 - P)} = \frac{1}{v_m c} + \frac{c-1}{v_m c} \left(\frac{P}{P_0}\right) \quad (2.16)$$

$$c = \frac{\alpha_1 \beta_2}{\alpha_2 \beta_1} \exp\left(\frac{Q_1 - Q_L}{RT}\right) \cong \exp\left(\frac{Q_1 - Q_L}{RT}\right) \quad (2.17)$$

In the above equation subscripts denotes to the number of layers, and L refers to liquefaction. The values of  $c$  and  $v_m$  are determined experimentally. The constant of  $c$  is usually large and greater than one. By plotting the left side of equ. (2.16) versus the relative pressure ( $P/P_0$ ) when  $P/P_0$  is in the range of 0.05-0.3, then the values of  $c$  and  $v_m$  are obtained from the intercept and the slope of the plot. By knowing the molecular area of the adsorbed molecule, typically  $16.2 \text{ \AA}^2$  per molecule of nitrogen at 77 K, the amount of the surface area can be found directly from  $v_m$ .

$$A = v_m \times N_A \times 16.2 \quad (2.18)$$

where A is the surface area in unit of  $\text{Å}^2$  and  $N_A$  is the Avogadro number.

BET model is valid for temperature below the critical temperature.

## 2.6.2 Equilibrium Adsorption of Gas Mixtures:

Finding right models or correlations for gaseous mixtures is of high importance due to their major role in the design of adsorptive gas separation processes. These models should be able to predict the adsorption properties of a multicomponent gaseous mixture equilibrium employing single-component adsorption data in a given ranges of operating temperature and total pressure. The methods used to obtain single-component experimental isotherms may also be employed to collect data for multicomponent isotherms with an additional assumption. Correlations based on the Langmuir, and Gibbs approaches for single gases adsorption has been applied for multicomponent gaseous mixtures and different isotherm models using these approaches have emerged<sup>3,9</sup>.

### 2.6.2.1 Extended Langmuir Isotherm

Langmuir isotherm can be simply extended to a relation for a multicomponent gaseous mixture only by adding one more assumption to those mentioned for single-gas component Langmuir isotherm. The assumption would be that for every gaseous component there is equilibrium between the amount adsorbed at the adsorbent surface and its partial pressure in the gas phase. Fractional coverage  $\theta_i$  and partial pressure  $p_i$  represents each of the components in the adsorbed and gaseous phase, respectively. The total surface coverage is sum of the coverage of the individual component. The resulting Langmuir isotherm so called as extended Langmuir isotherm for component i can be defined as:

$$\theta_i = \frac{q_i}{q_{mi}} = \frac{b_i p_i}{1 + \sum_1^n b_i p_i} \quad (2.19)$$

Where,  $q_{mi}$  is the maximum capacity of component I (monolayer) from a gaseous mixture adsorbed on the adsorbent. The total surface coverage is the sum of the fractional coverage of each component.

$$\theta_{total} = \sum_{i=1}^n \theta_i \quad (2.20)$$

Extended Langmuir isotherm is vastly used for modeling of Pressure swing adsorption processes mostly due to its simplicity. This model is most accurate at low loading ( $q/q_s < 0.5$ ). Therefore another isotherm such as Ideal Adsorbed Solution Theory (IAST) was proposed to compensate the deficiency of the extended Langmuir model.

### 2.6.2.2 Ideal Adsorbed Solution Theory (IAST)

Ideal Adsorbed Solution Theory (IAST) is based on the assumption that the adsorbed phase is thermodynamically ideal and in equilibrium where the chemical potentials of both adsorbed phase and gas phase must be equal<sup>3,6,10</sup>. The partial pressure exerted by component  $i$  in the gaseous mixture can be defined as:

$$p_i = p_i^0(\pi) x_i \quad (2.21)$$

where,  $p_i^0(\pi)$  is the saturated vapour pressure of component  $i$  in its pure state at the same spreading pressure of the adsorbed phase ( $\pi$ ) and same temperature, and  $x_i$  stands for the mole fraction of species  $i$  in the adsorbed phase. Equation (2.21) is equivalent to Raoult's law for ideal liquid-vapour systems. For a case where the mole fraction of species  $i$  in the gas phase is  $y_i$  and total pressure of the system is  $p$ , in equilibrium the relation between gas phase and adsorbed phase becomes:

$$y_i p = p_i^0(\pi) x_i \quad (2.22)$$

Therefore, in case of equal spreading pressures in a mixture, the condition must be obeyed. Now to relate spreading pressure to moles adsorbed we need to use equation (2.13) from Gibbs approach and by substituting the classic thermodynamic relation for the gas phase at pressure  $p$ ,

$$d\mu = R_g T d \ln p \quad (2.23)$$

In which,  $p$  is the partial pressure of the adsorbate, and then by substituting equation (2.23) in (2.13), we will have:

$$A d\pi = n R_g T d \ln p \quad (2.24)$$

This equation is the differential form of the Gibbs equation isotherm which in its integral form becomes:

$$\pi = R_g T \int_0^{p_s} (n/A) d \ln p \quad (2.25)$$

Using equation (2.25) for a mixture composed of components  $i$  and  $j$ :

$$\pi A / R_g T = \int_0^{p_i^0} n_i^0(p) d \ln p + \int_0^{p_j^0} n_j^0(p) d \ln p \quad (2.26)$$

Where,  $n_i^0(p)$  and  $n_j^0(p)$  are the isotherms for the pure component  $i$  and pure component  $j$ , respectively. Worth to mention that in all above equations, the following relation between mole fractions of components in both adsorbed and gas phase is valid:

$$\sum x_i = \sum y_i = 1 \quad (2.27)$$

Assuming the total pressure,  $P$ , and mole fraction of the component  $i$  in the gas phase,  $y_i$ , are known, then the calculation procedure for the binary mixture would be to find  $p_1^0$ ,  $p_2^0$  and  $x_1$  from the three equations (2.21), (2.22), and (2.27). Once values for  $p_1^0$ ,  $p_2^0$  and  $x_1$  have been found

$n_1$  and  $n_2$  may be calculated. The similar procedure would be followed for multicomponent mixtures<sup>3,6</sup>.

## References

- (1) Yang, R. T. *Adsorbents, Fundamentals and Applications*; John Wiley & Sons, Inc.: Hoboken, New Jersey, 2003; p. 410.
- (2) Breck, D. W. *Zeolite Molecular Sieves: Structure, Chemistry, and Use*; John Wiley & Sons, Inc., 1974.
- (3) Ruthven, D. M. *Principles of Adsorption and Adsorption Processes*; John Wiley & Sons, Inc., 1984.
- (4) Sircar, S.; A., M. L. Chapter 22: Gas Separation by Zeolites. In *Hand book of Zeolite Science and Technology*; Auerbach, M. S.; Carrado, A. K.; Dutta, K. P., Eds.; Marcel Dekker, Inc., 2003; Vol. 10.
- (5) Brunauer, S.; Deming, L. S.; Deming, W. E.; Teller, E. On a Theory of the van Der Waals Adsorption of Gases. *J. Am. Chem. Soc.* 1940, *62*, 1723–1732.
- (6) Thomos, W. J.; Crittenden, B. *Adsorption Technology and Design*; Elsevier Science Technology Books, 1998.
- (7) Masel, R. I. *Principles of Adsorption and Reaction on Solid Surfaces*; A Wley-Interscience Puplication, 1996; p. 998.
- (8) Emmett, P. H.; Brunauer, S. The Use of Low Temperature van Der Waals Adsorption Isotherms in Determining the Surface Area of Iron Synthetic Ammonia Catalysts. *J.Am.Chem.Soc.* 1937, *59*, 1553–1564.
- (9) Do, D. D. *Adsorption Analysis: Equilibria and Kinetics*; Imperial College Press, 1998; p. 892.
- (10) Flor R. Siperstein, A. L. M. Mixed-Gas Adsorption. *AIChE J.* 2001, *47*, 1141–1159.

# Chapter 3

## A Simplified Method to Synthesize Pure Vanadium Silicate Analogue of ETS-10

### 3.1 Introduction

Stable microporous materials such as molecular sieves have many applications in catalysis<sup>1,2</sup>, adsorption<sup>3-5</sup>, ion exchange<sup>6,7</sup>, liquid separation and gas separation<sup>8-12</sup>. In addition to these traditional uses Engelhard Titanium Silicate (ETS)-type molecular sieves have shown potential in electronic applications such as quantum wires, where they act as semiconductors in photocatalysis<sup>13</sup>. Among mixed coordination molecular sieves, the best-characterized example is ETS-10, a microporous titanosilicate with a tetrahedral/octahedral framework with a wide pore size range and high thermal stability<sup>14</sup>. ETS-10 framework consists of infinite chains of six-coordinated titanium and four-coordinated rings of silicon linked by corner-sharing atoms of oxygen. Titanium chains carry two negative charges, which are balanced by sodium and potassium cations; this leads to a high cation-exchange capacity. The infinite—O—Ti—O—Ti—O— chains are surrounded by a silicate ring structure; this leads up to the formation of diffused charged rods that impart some of the interesting properties of the mixed coordination molecular sieves. There are no point charges available in the structure; instead, the guest molecules

are exposed to a rod full of diffused charges. ETS-10 structure allows for framework atom substitution; replacement of titanium with other atoms such as vanadium, copper, iron. A novel application of ETS-10 is as a semiconductor in quantum wires, due to the presence of oxygen-titanium chains in its structure<sup>15,16</sup>. Quantum wires are an electrically conducting wire in which the effect of quantum dominates the transport properties. Among them, the semiconductor quantum wires are the most widely used. Due to the similarities between ETS-10 and EVS-10 structure, it is predicted that pure vanadosilicate (EVS-10) can also be used as a semiconductor in electronics. The properties of materials such as EVS-10 and ETS-10 can be manipulated by the addition of impurities that modulate the electrical behaviour of the material.

Kuznicki et al. was the first to demonstrate that many types of octahedral and tetrahedral atoms could be easily integrated into the ETS-10 type structure<sup>14</sup>. These materials are dubbed EXS. Rocha et al.<sup>17</sup> was the first to report complete substitution of vanadium into an ETS-10 structure. The material was dubbed as AM-6. Their synthesis method involved the use of ETS-10 seeds in order to induce a similar structure to ETS-10. The structure contains hexacoordinated vanadium and titanium chains surrounded by tetrahedral silicate rings. AM-6 has been synthesized from ETS-10 seed crystals, which affect the purity of the product and might restrict its application and complicate its characterization. Generally, it is common to use the seed crystals of the desired material in order to direct the structure towards the favorite zeolite phase. The particle size distribution of the product can be manipulated to some degree by adjusting the seed concentration<sup>18,19</sup>. Since the mechanism of crystal formation during synthesis of the seeded AM-6 is still unknown, its particle size distribution cannot be controlled.

Using ETS-10 seeds in the AM-6 synthesis has also compromised the ability to control the final product characteristics due to the existence of titanium atoms in AM-6. It is therefore useful to produce seed-free products.

The first synthesis of unseeded vanadosilicate was reported by Ismail et al.<sup>20</sup> using a structure-directing agent. These authors used tetramethylammonium hydroxide (TMAOH) or tetramethylammonium bromide (TMABr) as templates. The use of templates has the advantage of directing the structure formation but they are costly. In addition, removing them from the frameworks is expensive and damaging to the structure. These disadvantages limit their use making template-free synthesis another requirement for fundamental studies. Shuvo Jit Datta et al.<sup>21</sup> reported the synthesis of an unseeded AM-6 using ethanol as a reducing agent. As the source of vanadium, the authors used vanadium pentoxide  $V_2O_5$  which is toxic and not commonly used in the laboratory<sup>22</sup>. In addition, vanadium pentoxide is practically insoluble in water (solubility around 0.8%), which will cause inhomogeneity in the parent gel and will effect on the uniformity of the final product<sup>22</sup>.

Here, we are reporting the first unseeded, template-free, reducing agent-free vanadosilicate analogue of ETS-10, dubbed as EVS-10. The as-synthesized material has been developed through a simplified hydrothermal synthesis method using vanadyl sulphate, the most common type of vanadium salt, as the vanadium source. The most important advantage of vanadyl sulfate over vanadium pentoxide is its 100% water-solubility, which results in a homogenous parent gel leading to the formation of more uniform crystals. In order to lower the synthesis cost, we have checked the sensitivity of our method to various degrees of vanadium purity form 17% to 99.9%. Previous

methods simultaneously produce substantial amount of quartz, whereas following our simplified synthesis method the amount of quartz has been significantly reduced.

## 3.2 Experimental

About 300-600-nm-sized vanadium silicate analogue of ETS-10 crystals were prepared by hydrothermal synthesis using vanadyl sulfate as vanadium source. The gel was obtained in two steps. In the first step sodium silicate solution (28.8wt% SiO<sub>2</sub>, 9.14wt% Na<sub>2</sub>O, Fisher Scientific) was mixed with distilled water and stirred to homogenize. Sodium hydroxide (99wt%, Fisher Scientific), potassium chloride (99wt%, Fisher Scientific), sodium fluoride (99wt%, Fisher Scientific), and sodium chloride (99wt%, Fisher Scientific) were added to the mixture. In the second step, a solution containing vanadyl (IV) sulfate hydrate was obtained from Acros. Organics and distilled water were mixed together under strong stirring to obtain a green gel. At the end, the gel with molar compositions of  $x\text{Na}_2\text{O}:y\text{K}_2\text{O}:z\text{SiO}_2:0.05\text{V}_2\text{O}_5:w\text{H}_2\text{O}:n\text{F}$ , where  $x=0.7-2.2$ ,  $y=0.1-0.4$ ,  $z=1.0-2.5$ ,  $w=30-40$ , and  $n=0.1-0.5$  was stirred to homogenize for 2 hours. The final product is EVS-10 along with quartz and some other impurities. In order to get the purest vanadium silicate, we added 32g Na<sub>2</sub>SiO<sub>3</sub>, 12g H<sub>2</sub>O, 0.5 g NaOH, 2.0g KCl, 1g NaF, 4.1g NaCl to 3.06g VOSO<sub>4</sub>×H<sub>2</sub>O, 12g H<sub>2</sub>O. This results in a gel with molar composition of 1.44Na<sub>2</sub>O:0.19K<sub>2</sub>O:2.2SiO<sub>2</sub>:0.11V<sub>2</sub>O<sub>5</sub>:35H<sub>2</sub>O:0.34F. The initial pH of the mixture was between 10.2-10.4 as measured using a Fisher scientific pH meter model 720 A (accuracy 0.02 pH units). Following this step, the gel was left to age under static condition at room temperature for 2-4 days depending on the sodium silicate amount in the parent gel. Syntheses were carried out in 700 ml Teflon-lined stainless steel autoclaves under autogenous pressure at 200-230 °C for 7-10 days. Then the

autoclave was removed from the oven and quenched at room temperature with cold water. Then the product with the purple color was washed with distilled water several times and dried at 80 °C overnight.

In order to investigate the impact of vanadium purity on the structure and lower the synthesis cost, we used vanadyl sulfate with different degrees of purity (i.e. 17-23%, 96%, 99.9% vanadium). We also studied the effect of ETS-10 seed crystals and the effect of aging on the molecular structure of the as-synthesized material.

X-ray powder diffraction (XRD) patterns were acquired by a Rigaku Ultima IV unit equipped with a D/Tex detector, with Fe filter. The results were obtained with Co K wavelength with the average wavelength of 1.790260 Å (Cobalt tube 38 kV, 38 mA). Samples were run from 5 to 90 degrees on a continuous scan using a top-pack mount at a speed of 2 degrees 2- $\theta$  per minute with a step size of 0.02 degrees. The data interpretation is done using JADE 9.1 equipped with 2011 ICDD database.

Field emission scanning electron microscope (FE-SEM) images were captured using JEOL 6301F with the accelerating voltage of 5.0 kV, beam current of 20 A, and working distance of 6 or 10 mm. In order to consider a sample for Beam Microscopy, they must be electrically continuous. Therefore all the samples had been grounded to the stub with a graphite sticky pad and carbon paint, then had been gold coated with 2-5 nm ( $< 50$  Å) using a Nanotech SEM Prep 2DC sputter coater to prevent charging and distortion.

Energy dispersive X-ray spectroscopy (EDX) measurements were obtained on a Zeiss EVO MA 15LaB6 filament scanning electron microscope that is equipped with an EDX

system. EDX acquired with a peltier-cooled 10 mm<sup>2</sup> Bruker Quantax 200 Silicon drift detector with 123 eV resolution.

Thermogravimetric analysis (TGA) was conducted using a TA Q50 TGA. Samples were heated at 100 °C at 10 °C/min under nitrogen flow (40 mL/min) then held isothermally for 15 min to allow moisture removal, and finally heated to 350 °C at 5 °C/min. Isothermal mode allows to distinguish the mass loss due to the surface water.

The particle size distributions were measured on a Quantachrome Autosorb-1 instrument. In order to calculate the particle size distribution, the average density of the EVS-10 crystals was measured to be 679 kg/m<sup>3</sup>. The nitrogen adsorption and desorption measurements were carried out at 77 K using a Quantachrome Autosorb-1 instrument. The Autosorb-1 has the capability of measuring the adsorbed and desorbed volumes of nitrogen at relative pressures in the range 0.001 to slightly under 1.0. The internal and external surface area and the pore size distribution of the as-synthesized material were measured by Quantachrome Autosorb-1 instrument.

The inductively coupled plasma mass spectrometry (ICP) was run on Perkin Elmer's ICP 6000 with ICP RF power of 1300 W under auto lens and dual detector mode. The instrument was set on 4 points calibration curves (0, 0.25, 0.5, 1.00 ppm for Na, K; 0, 0.005, 0.010, 0.020 ppm for V) and the measurement units were cps (counts per sec). The samples were run under 1 mL/min flow rate using 35 Sweeps/Reading, 1 Reading/Replicate and 3 Replicates; "Dwell times" were 10 ms for Na and 20 ms for K and V. The integration time is equal to "Dwell times" multiplied by a number of sweeps; i.e. 35×10=350 ms for Na, and 70×10=700 for K and V. The final results were the

average of 3 replicates. Since the sample was in powder form it had to be liquefied prior to the ICP analysis. The sample was liquefied using hydrogen fluoride (HF) and nitric acid (HNO<sub>3</sub>) and hydrogen chloride (HCl).

### 3.3 Result and Discussion

Both EVS-10 and ETS-10 are found to have the same molecular structure owing to their nearly identical XRD patterns (Figure 3.1). Aging, or leaving the reaction mixture for a prolonged time at low temperature, plays an important role in the synthesis. Figure 3.2 shows that without aging, the product has a substantial fraction of quartz impurity. Aging time on the other hand increases the fraction of EVS-10 in the product while reducing the fraction of quartz impurity. The peak with the asterisk represents the quartz peak, which completely vanishes after 3 days of aging at room temperature.

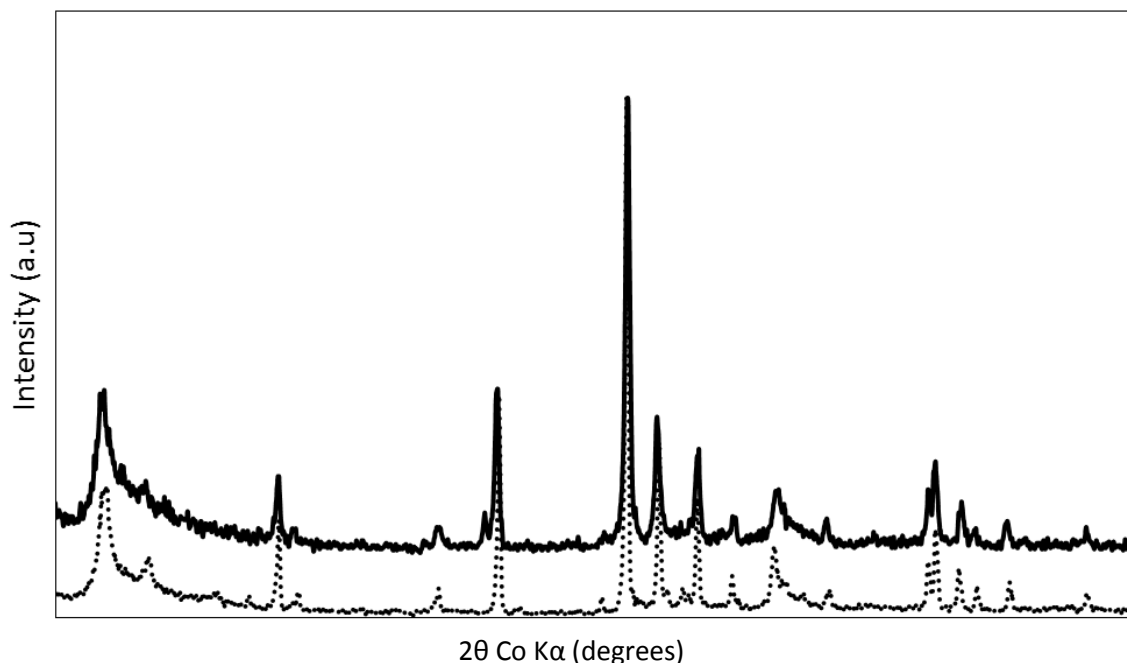
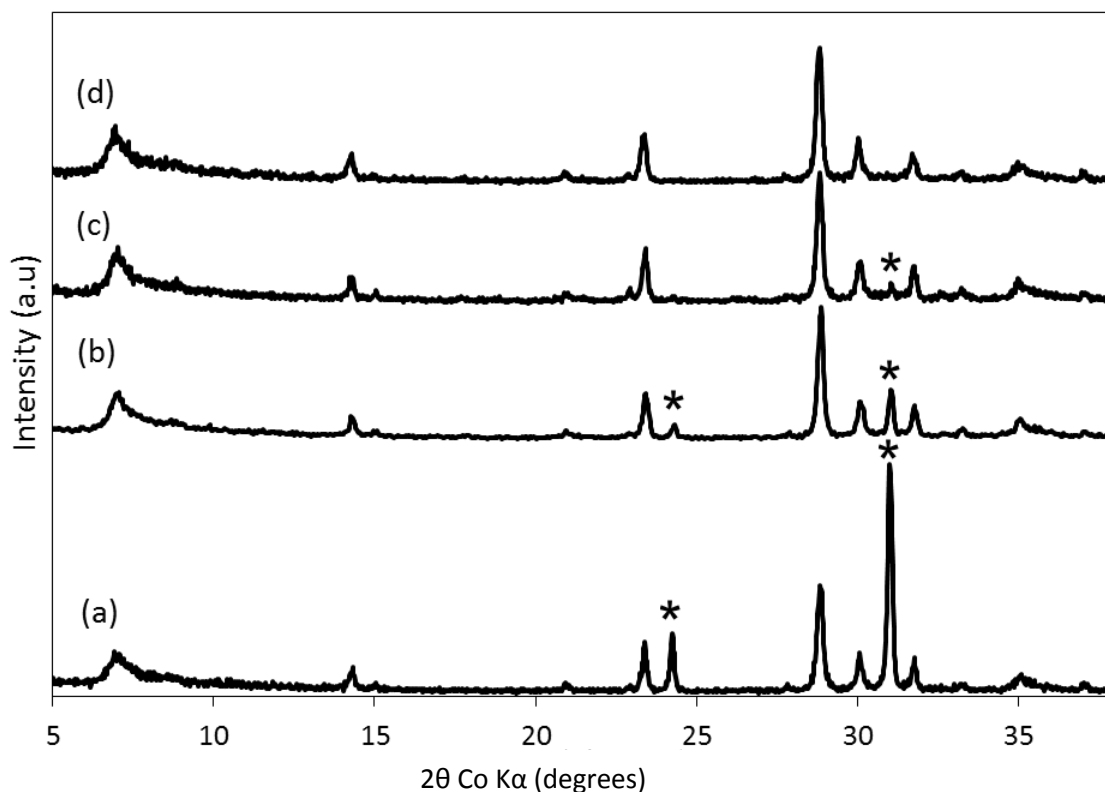


Figure 3.1: It is shown the XRD pattern of ETS-10 as explained in the patent by Kuznicki et al.<sup>14</sup>(dashed line) and the XRD pattern of EVS-10 at 503 K from mixture with

$1.44\text{Na}_2\text{O}:0.19\text{K}_2\text{O}:2.2\text{SiO}_2:0.11\text{V}_2\text{O}_5:35\text{H}_2\text{O}:0.34\text{F}$  (solid line) and. Both XRD patterns are similar which proves the analogous molecular structure for the two materials.



**Figure 3.2:** The XRD pattern of EVS-10 at 503 K from mixture with molar composition of  $1.44\text{Na}_2\text{O}:0.19\text{K}_2\text{O}:2.2\text{SiO}_2:0.11\text{V}_2\text{O}_5:35\text{H}_2\text{O}:0.34\text{F}$  asterisk referred to quartz impurity (a) as-synthesized product without aging (b) after 1 day aging at room temperature, (c) after 2 days aging at room temperature.

The initial pH of the parent gel proved to be very critical. Concentration of sodium hydroxide in the synthesis mixture affected nucleation of EVS-10. Typically at  $230\text{ }^\circ\text{C}$  with  $x \geq 2.0$ , and pH between 10.5-12.5, the mixtures resulted in EVS-10 products of low purity (Figure 3.3a-c). The impurities of the products observed by FE-SEM varied from needles to hexagonal plates. As the pH is decreased, the products became purer as a result of nucleation of more EVS-10 crystals (Figure 3.3d-e). The peaks with asterisks refer to the main peaks of EVS-10; the higher they are the purer the EVS-10 products.

The good quality EVS-10 crystals (i.e. high purity and crystallinity, uniform size of crystals and morphology) are grown from mixtures with a pH between 10-10.5.

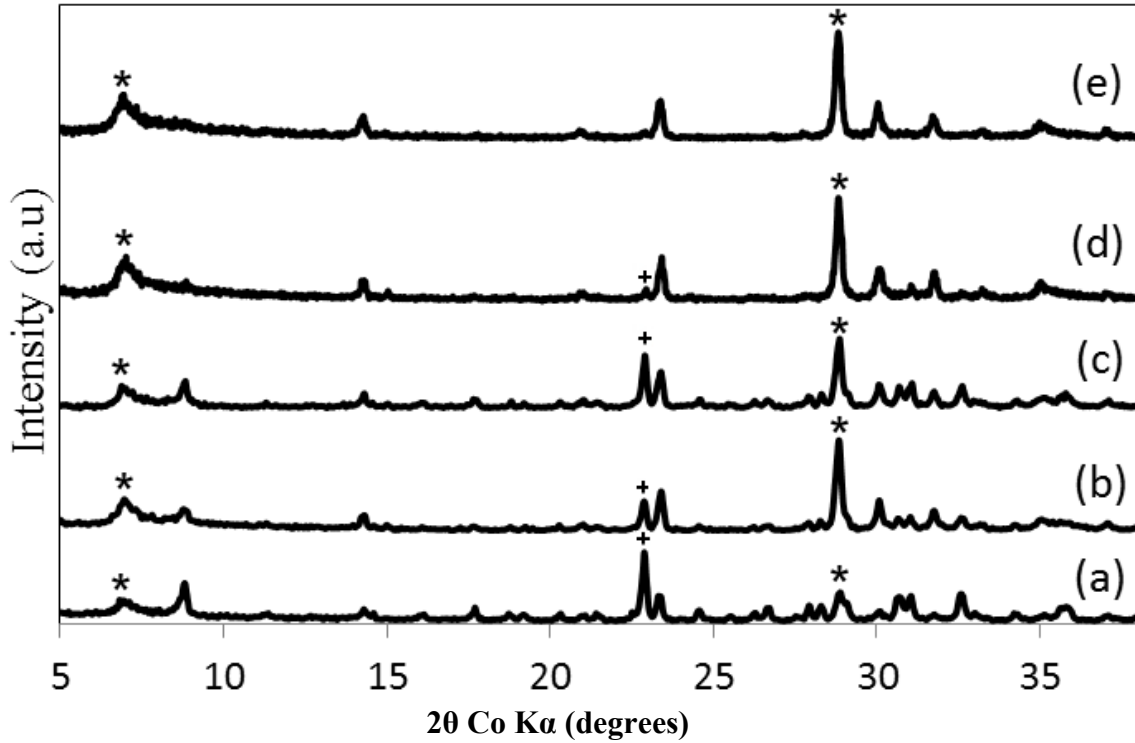


**Figure 3.3:** The asterisks represent the main EVS-10 peaks. As pH decreased the main peaks became more pronounced (a) It is form a mixture with pH ~12.5, (b) pH ~11.7, (c) pH ~11.0 (d) pH ~10.5, (e) pH ~10.2.

Fluoride ions were introduced into the mixture to substantially reduce the amount of quartz impurities. These ions acted as a mineralizer and promoted crystallization of the EVS-10 products. It is shown in Figure 3.4a that synthesis of EVS-10 products in the absence of fluoride ions, results in the formation of a substantial amount of quartz. However, when 0.34 mol fluoride ions per 2.2 moles of SiO<sub>2</sub> were added to the mixture the amount of quartz impurity reduced significantly. In addition, the main EVS-10 peaks became sharper, which resulted in the purer, quartz-free final product (Figure 3.4b).

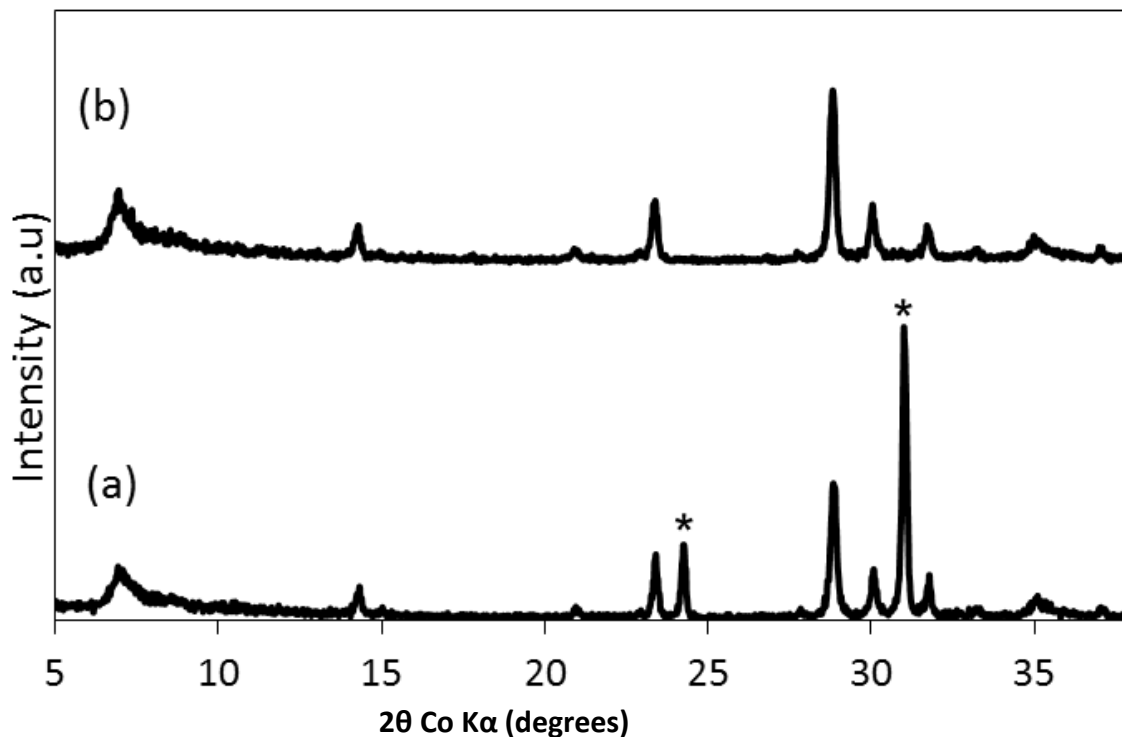


**Figure 3.4: (a) shows substantial amount of quartz in the synthesis mixture in the absence of fluoride ions (b) quartz impurities are dissolved as a result of the use of fluoride ions.**

Scanning electron microscopy (JEOL 6400) images were taken on gold-coated specimens at 20 kV. The images show several nano-sized, cubic-form structures. The morphology of the EVS-10 crystals is similar to its titanium analogue, ETS-10 crystals (Figure 3.5).

The final product, EVS-10, was also analyzed by transmission electron microscopy (TEM) as shown in Figure 3.6. TEM analysis provides better insights on single nanometer- size crystals<sup>23,24</sup>. In Figure 3.6, the c-axis of the square shape particle is oriented perpendicular with the image plane. The straight lines clearly seen in Figure 3.6 may correspond to the two channels that linked together during crystallization of the EVS-10 structure.

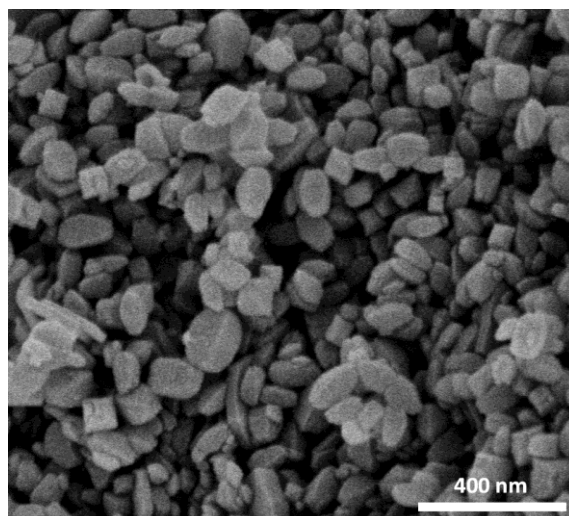


**Figure 3.5:** The SEM image on the seedless, template-free, reducing agent-free vanadium silicate. Similar to ETS-10 crystals the EVS-10 crystals are also cubic-forms.

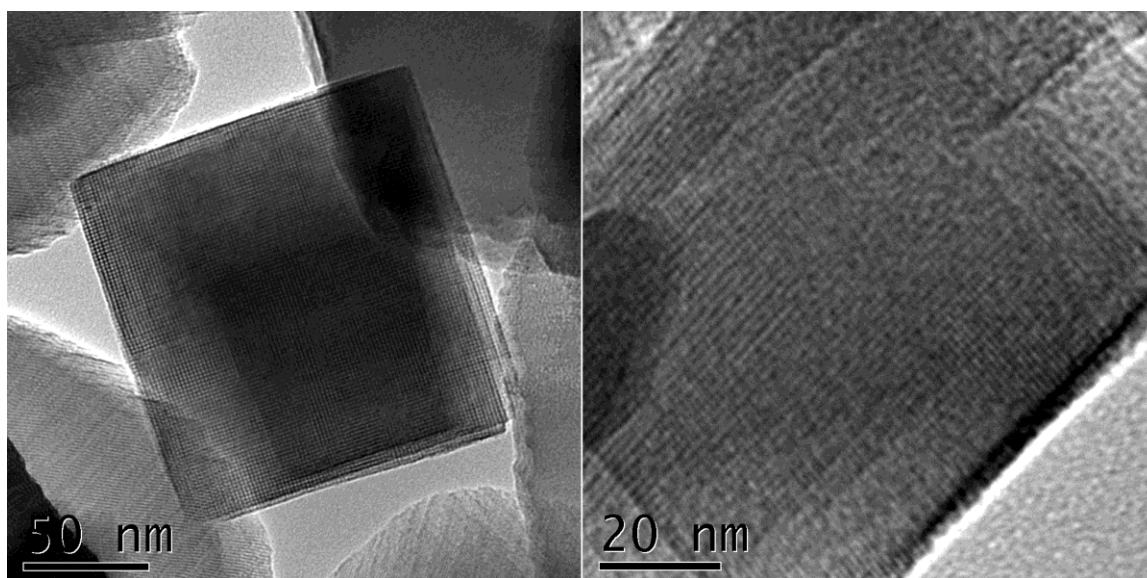


**Figure 3.6:** The TEM images on the seedless, template-free, reducing agent-free vanadium silicate. The microporous structure of the new material, EVS-10, is clearly shown.

The surface area, nitrogen adsorption isotherm and pore size distribution of the as-synthesized material were obtained by Quantochrome (see Table 3.1). The higher external surface area in the new material is attributed to their smaller particle size. As it is shown

in the Table 3.1 the new material has a bigger pore size that could potentially extend the applications of the new synthesized EVS-10 material.

**Table 3.1: A Comparison between ETS-10, and the new material (EVS-10) surface area and pore size. Using nitrogen as a probe gas. In all cases, the sample was outgassed at 150° C.**

Parameter	EVS-10	ETS-10
Total Surface Area (m <sup>2</sup> /g)	345.7	355.5
External Surface Area (m <sup>2</sup> /g)	44.78	26.24
Micro Pore Area (m <sup>2</sup> /g)	300.9	329.2
Pore Size (Å)	9.8	8.4

The amount of surface water and structural water was determined by TGA. Since surface water is more accessible compared to structural water (intercrystalline water), it will boil off from the surface at 100 °C whereas structural water will be removed at higher temperatures. As shown in Figure 3.7, the TGA profiles for both ETS-10 and EVS-10 showed similar trends. When heated from 25 °C to 100 °C, both samples lose about 8wt% water, which is attributed mostly to surface water. During heating from 100 °C to 200 °C both samples lose additional 3wt% water but this is attributed to structural water. The water content for both samples levels off at about 250 °C. In total, both ETS-10 and its vanadium analogue lost about 11 wt% of their total weight due to the moisture loss when heated up to 250 °C.

Similar to EDX, the ICP results show that the ratio of sodium-potassium to vanadium is approximately 2 which corresponds to V<sup>4+</sup> in the molecular framework. Similar to its titanium analogue, the framework of EVS-10 contains monoatomic -O-V-O-V-O- chains made of corner sharing VO<sub>6</sub> octahedra. This means that six oxygen atoms surround every vanadium in the framework. Each corner sharing octahedrally

coordinated  $\text{VO}_6/2$  unit links through the apical oxygen atoms, forming linear chains. Each oxygen atom is shared between two vanadium atoms resulting in three oxygens for every vanadium ( $\text{VO}_3$ )<sup>-2</sup>. Therefore there are two negative charges associated with each vanadium atom; this makes the oxidation state of  $\text{V}^{4+}$  (see Table 3.2). This is confirmed by both EDX and ICP results and strongly suggests that the as-synthesized material most likely contains  $\text{V}^{4+}$  in its framework.

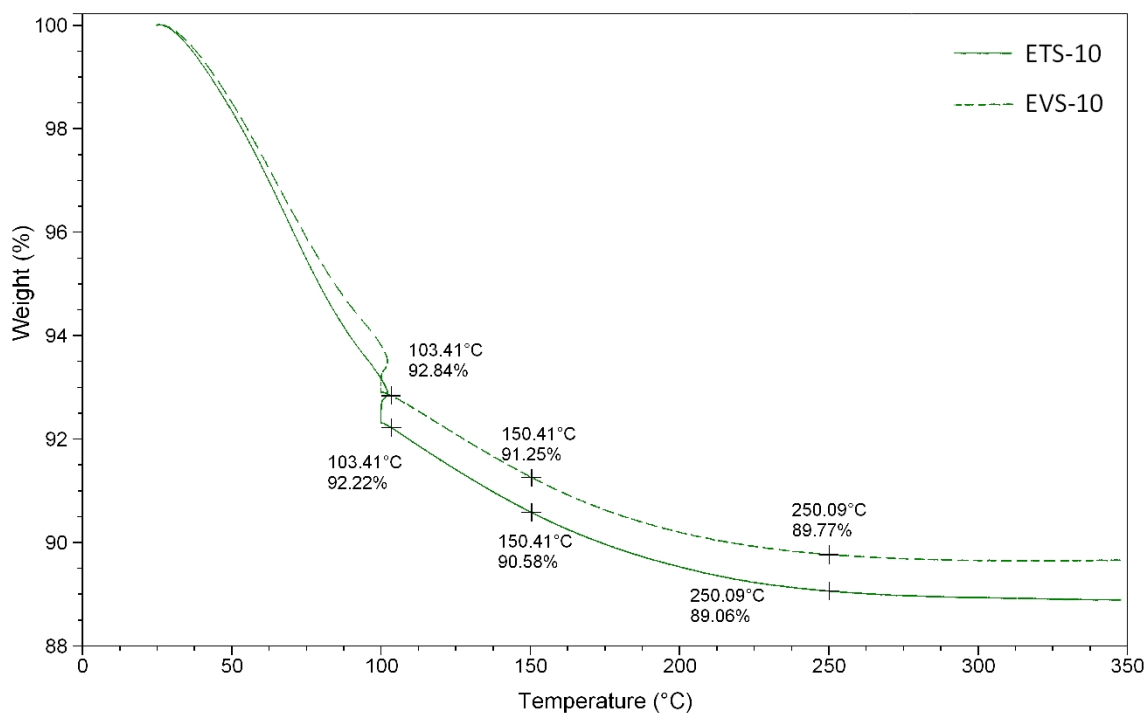


**Figure 3.7:** TGA analysis of: (a) EVS-10 products synthesized at 230° C from mixture with molar composition of  $1.44\text{Na}_2\text{O}:0.19\text{K}_2\text{O}:2.2\text{SiO}_2:0.11\text{V}_2\text{O}_5:35\text{H}_2\text{O}:0.34\text{F}$  (dashed line) (b) ETS-10 products synthesized at 230°C as explained in the patent by Kuznicki et al.<sup>14</sup> (solid line).

**Table 3.2: A Comparison between ETS-10, and seed-free, template-free, reducing agent-free EV S-10 compensating ions ratio to structural atoms, titanium and vanadium, respectively. The sample was outgassed at 150° C. All the values are average of 5 measurements.**

Sample (mol%)	EDX	ICP
EVS-10 (Na+K/V)	2.0	2.3
ETS-10 (Na+K/Ti)	1.99	2.1

### **3.4 Conclusion**

A new simplified method has been developed to synthesize the first seed-free, template-free and reducing agent- free pure vanadosilicate, an analog of titanosilicate ETS-10, dubbed EVS-10. With this new method high purity crystalline vanadosilicate, with very little contamination, is produced. Synthesizing in the absence of template eliminates potential damages due to the harsh conditions needed for template removal. Synthesizing pure vanadosilicate free of titanosilicate seeds allows more control over the characteristics of the final product such as size, morphology and purity. This new simplified synthesis method may allow the economical production of EVS-10 / AM-6 for electronic applications such as quantum wire and semiconductors.

## References

- (1) Perego, C.; Carati, A.; Ingallina, P.; Mantegazza, M. A.; Bellussi, G. Production of Titanium Containing Molecular Sieves and Their Application in Catalysis. *Appl. Catal. A-Gen.* 2001, *221*, 63–72.
- (2) Corma, A. From Microporous to Mesoporous Molecular Sieve Materials and Their Use in Catalysis. *Chem. Rev.* 1997, *97*, 2373–2419.
- (3) Anson, A.; Kuznicki, S. M.; Kuznicki, T.; Haastrup, T.; Wang, Y.; Lin, C. C. H.; Sawada, J. A.; Eyring, E. M.; Hunter, D. Adsorption of Argon, Oxygen, and Nitrogen on Silver Exchanged ETS-10 Molecular Sieve. *Micropor. Mesopor. Mat.* 2008, *109*, 577–580.
- (4) Anson, A.; Wang, Y.; Lin, C. C. H.; Kuznicki, T. M.; Kuznicki, S. M. Adsorption of Ethane and Ethylene on Modified ETS-10. *Chem. Eng. Sci.* 2008, *63*, 4171–4175.
- (5) Anson, A.; Lin, C. C. H.; Kuznicki, S. M.; Sawada, J. a. Adsorption of Carbon Dioxide, Ethane, and Methane on Titanosilicate Type Molecular Sieves. *Chem. Eng. Sci.* 2009, *64*, 3683–3687.
- (6) Kuznicki, S. M.; Thrush, K. A. Removal of Heavy Metals, Especially Lead, from Aqueous Systems Containing Competing Ions Utilizing Wide-Pored Molecular Sieves of the ETS-10 Type, 1991.
- (7) Breck, D. W. *Zeolite Molecular Sieves: Structure, Chemistry, and Use*; John Wiley & Sons, Inc., 1974.
- (8) J.Smolarek, M. W. A. F. N. Recover Industrial Gas via Adsorption. *Chem. Eng.* 1999, *106*, 104–108.
- (9) Ackley, M. W.; Rege, S. U.; Saxena, H. Application of Natural Zeolites in the Purification and Separation of Gases (A Review). *Micropor. Mesopor. Mat.* 2003, *61*, 25–42.
- (10) Knaebel, K. S.; Farooq, S.; Ruthven, D. M. *Pressure Swing Adsorption*; Wiley-VCH, New York, 1994.
- (11) Chue, K. T.; Kim, J. N.; Yoo, Y. J.; Cho, S. H.; Yang, R. T. Comparison of Activated Carbon and Zeolite 13X for CO<sub>2</sub> Recovery from Flue Gas by Pressure Swing Adsorption. *Ind. Eng. Chem. Res.* 1995, *34*, 591–598.
- (12) Xu, J.; Malek, A.; Farooq, S. Production of Argon from an Oxygen-Argon Mixture by Pressure Swing Adsorption. *Ind. Eng. Chem. Res.* 2006, *45*, 5775–5787.

- (13) Krisnandi, Y. K.; Southon, P. D.; Adesina, A. A.; Howe, R. F. ETS-10 as a Photocatalyst. *Int.J.Photoenergy* 2003, 5, 131–140.
- (14) Kuznicki, S.; Madon, R. J.; Koermer, G. S.; Thrush, K. A. Large-Pored Molecular Sieves and Their Use as Catalysts and Ion Exchangers. 0405978B1, 1991.
- (15) Yilmaz, B.; Deng, J.; Jr., A. S. Electrical Transport Through Monoatomic Titania Chains. *Appl. Phys. Lett.* 2007, 90, 152101–152103.
- (16) Jeong, N. C.; Lee, M. H.; Yoon, K. B. No Title. *Angew.Chem.Int.Edit.* 2007, 46, 5868–5872.
- (17) Rocha, J.; Brandao, P.; Lin, Z.; Anderson, M. W.; Alfredsson, V.; Terasaki, O. The First Large-Pore Vanadosilicate Framework Containing Hexacoordinated Vanadium. *Angew. Chem. Int. Ed. Engl.* 1997, 36, 100–102.
- (18) Ji, Z.; Warzywoda, J.; Jr., A. S. Competitive Nucleation and Growth in Seeded Batch Crystallization of Titanosilicate ETS-10 Using  $Ti(SO_4)_2$ . *Micropor. Mesopor. Mat.* 2005, 81, 201–210.
- (19) Cundy, C. S.; Cox, P. A. The Hydrothermal Synthesis of Zeolites: Precursors, Intermediates and Reaction Mechanism. *Micropor. Mesopor. Mat.* 2005, 82, 1–78.
- (20) Ismail, M. N.; Fraiman, N. D.; Jr., D. M. C.; GURSOY, G.; Viveiros, E.; Ozkanat, O.; Ji, Z.; Willey, R. J.; Warzywoda, J.; Jr., A. S.; et al. First Unseeded Hydrothermal Synthesis of Microporous Vanadosilicate AM-6. *Micropor. Mesopor. Mat.* 2009, 120, 454–459.
- (21) Datta, S. J.; Yoon, K. B. Synthesis of Ideal AM-6 and Elucidation of  $V^{4+}$ -to- $O$  Charge Transfer in Vanadate Quantum Wires. *Angew. Chem. Int. Ed.* 2010, 49, 1–6.
- (22) Pohanish, R. P. *Sittig's Handbook of Toxic and Hazardous Chemicals and Carcinogens*; Edition, S., Ed.; Elsevier Inc. , 2012.
- (23) Xamena, F. X. L. I.; Calza, P.; Lamberti, C.; Prestipino, C.; Damin, A.; Bordiga, S.; Pelizzetti, E.; Zecchina, A. Enhancement of the ETS-10 Titanosilicate Activity in the Shape-Selective Photocatalytic Degradation of Large Aromatic Molecules by Controlled Defect Production. *J. Am. Chem. Soc.* 2003, 125, 2264–2271.
- (24) Bozhilov, K. N.; Valtchev, V. P. Transmission Electron Microscopy Characterization of a Large-Pore Titanium Silicate. *Mater. Res. Bull.* 1993, 28, 1209–1214.

# Chapter 4

## Comparative Adsorption Study of EVS-10 and ETS-10

### 4.1 Introduction

Molecular sieves have been used in many different areas such as separation<sup>1,2</sup>, drying<sup>3</sup>, adsorption<sup>4-6</sup>, purification<sup>7</sup> and catalysis<sup>8</sup>. Vanadium silicate similar to titanium silicate belongs to the category of mixed coordination molecular sieves. Due to its wide-pore size and thermal stability, Engelhard Titanium Silicate (ETS-10) is the-state-of-the-art in tetrahedral/octahedral framework microporous materials. It was first synthesized in 1990 by Kuznicki et al.<sup>9</sup>. ETS-10's structure has been solved by Anderson et al.<sup>10,11</sup>. The most fascinating aspect of ETS-10 structure is the infinite chains of titanium and oxygen atoms surrounded by a silicate ring structure. As a result a rod forms; it is the rod nature that imparts some of the fascinating properties of ETS-10<sup>12</sup>. Because of its unique structure among other octahedral/tetrahedral framework molecular sieves, ETS-10 has been the subject of extensive research. Scientists have attempted to synthesize comparable materials by heteroatom substitution in the framework atoms. Such substitutions can lead to the formation of new molecular sieves; i.e, titanium can be replaced by vanadium<sup>13</sup>, zirconium<sup>14,15</sup> or niobium<sup>16</sup> while silicon can be replaced by aluminum, copper or iron<sup>17</sup>. Kuznicki et al. was the first to demonstrate that ETS-10 structure allows the incorporation

of octahedral framework atoms such as cerium, zirconium, niobium and tetrahedral framework atoms such as aluminum, copper and iron into the framework dubbed as EXS<sup>17,18</sup>.

Vanadium silicate, EVS-10, is the analogue of titanium silicate, ETS-10 where titanium is entirely substituted by vanadium in the framework. Rocha et al.<sup>12,13</sup> was the first to report complete incorporation of vanadium into an ETS-10 structure through the use of ETS-10 seeds. Previously, we have demonstrated a simplified method to synthesize vanadium-substituted ETS-10 without the use of templates, reducing agents, or ETS-10 seeds. We dubbed our micro-porous vanadium silicate EVS-10<sup>19</sup>. Studies have been conducted on the adsorptive behaviour of ETS-10 for light hydrocarbons such as methane, ethane, ethylene, and carbon dioxide<sup>1,2,4,6,20-24</sup> as well as oxygen and nitrogen<sup>5,25,26</sup>. These gases are particularly important due to their individual commercial applications.

While the adsorption properties of ETS-10 have been established, the adsorptive properties of the vanadium analogue, EVS-10, have yet to be investigated. The purpose of this paper is to explore the adsorptive characteristics of this new sorbent, EVS-10. The adsorption isotherm data obtained for each of the above-mentioned gases are fitted to Toth, Langmuir, Redlich and Peterson by the unconstrained optimization technique. The Henry constants are calculated from a restricted range of the isotherm data using the Langmuir model of adsorption. The ideal selectivity is calculated in the Henry's law region to identify and exploit the adsorption characteristics of EVS-10 for different gas separation processes.

## 4.2 Theoretical Background

The experimental isotherms of methane, ethane, ethylene, carbon dioxide, nitrogen, and oxygen are fitted to some isotherm model:

Langmuir Model<sup>27</sup>:

$$q = q_s \frac{bp}{1 + bp} \quad (4.1)$$

Toth Model<sup>28</sup>

$$q = q_s \frac{p}{(b + p^t)^{1/t}} \quad (4.2)$$

Redlich Peterson Model<sup>29</sup>:

$$q = q_s \frac{bp}{1 + bp^\beta} \quad (4.3)$$

where  $q$  for a given adsorbent is the amount of gas adsorbed on the solid,  $p$  is the corresponding partial pressure in the gas phase,  $q_s$  represents the saturation or maximum adsorption capacity,  $b$  is the adsorption equilibrium constant. Parameters  $t$  and  $\beta$  are dimensionless and range between 0-1 and represent the heterogeneity of the adsorbent.

As reported by Al-Baghli et al<sup>20</sup> and Breck<sup>30</sup>, the theoretical value for the maximum loading can be calculated for microporous zeolites. This definition is used to cross-check with the saturation concentration predicted by the models:

$$q_s = \frac{\varepsilon}{v^*} \quad (4.4)$$

where  $\varepsilon$  (cc.g<sup>-1</sup>) and  $v^*$  (cc.mmol<sup>-1</sup>) are defined as the adsorbent pore volume and molar volume of the adsorbate at a given temperature, respectively. According to Dubinin<sup>31</sup> the molar volume is calculated from:

$$v^* = v_b + \frac{T - T_b}{T_c - T_b} (b - v_b) \quad (4.5)$$

where  $T_c$  and  $T_b$  (K) are the symbols of critical and boiling temperatures respectively.  $T$ (K) is the system's temperature.  $v_b$  ( $\text{cc.mol}^{-1}$ ) is the molar volume at boiling point temperature and  $b$  ( $\text{cc.mol}^{-1}$ ) is the van der Waal's volume. Above the critical temperature where no liquid can form by increasing the pressure,  $v^*$  is considered equal to the van der waal's volume. As stated by Al-Baghli et al.<sup>20</sup>, in the calculation of theoretical saturation concentration adsorbate molecules are presumed to be in a state similar to a highly compressed liquid.

The Henry constant for each model is calculated from

$$H = \lim_{p \rightarrow 0} \frac{q}{p} \quad (4.6)$$

The isosteric heat of adsorption ( $\Delta H^{\text{iso}}$ ) is defined as the standard enthalpy of adsorption at a fixed surface coverage. It is calculated from Van't Hoff equation. At low coverage, i.e. low pressure, where all models collapse to a common point, the equilibrium constant is equivalent to Henry's law constant.

$$\frac{d \ln K}{dT} = \frac{\Delta H^{\text{iso}}}{RT^2} \quad (4.7)$$

where  $K$  is the equilibrium constant,  $R$  is the gas constant and  $T$  is the temperature in Kelvin. An average value of isosteric heat of adsorption is obtained from the slope of a plot  $\ln K$  versus  $1/T$ .

The ideal selectivity in the Henry's law region is calculated from the high-resolution isotherm data in this region by using Langmuir equation.

$$\alpha_1^2 = \frac{K_2}{K_1} \quad (4.8)$$

### 4.3 Experimental

Hydrothermal synthesis of vanadium silicate, EVS-10, was carried out as previously described<sup>19</sup>. A mixture of 32 g sodium silicate (28.8% SiO<sub>2</sub>, 9.14% Na<sub>2</sub>O, Fisher), 12 g deionised water, 0.5 g sodium hydroxide, 2 g potassium chloride, 1 g sodium fluoride and 4.1 g sodium chloride was added to a mixture of 3.06 g vanadium sulfate and 12g of water. The resulting low viscosity gel was left aging for 3 days then transferred to a stainless steel autoclave and reacted for 7 days at 503 K. The final product was purple in color and was washed with deionised water and dried at 353 K.

Hydrothermal synthesis of ETS-10 was conducted as previously described<sup>18</sup>. In order to prepare the ETS-10 gel, 50 g sodium silicate (28.8% SiO<sub>2</sub>, 9.14% Na<sub>2</sub>O, Fisher), 3.8 g of KF (anhydrous, Fisher), 3.2 g of sodium hydroxide (97% NaOH, Fisher), 16.3 g of TiCl<sub>3</sub> solution (Fisher), and 4 g of HCl (1M, Fisher) was stirred for 1 h. The synthesis was carried out in a Teflon-lined autoclave for 64 h at 488 K. The final product with white color was washed with deionised water and dried at 373 K. No binder was added to the vanadium silicate or titanium silicate crystals for the adsorption studies.

A static volumetric adsorption instrument was used to generate high resolution, low-pressure equilibrium adsorption data. Ethane, methane, ethylene, carbon dioxide, nitrogen, and oxygen adsorption isotherms for EVS-10 and ETS-10 were obtained at 303, 323, 343 K and pressures up to 100 kPa on Micromeritics (ASAP 2020C). This instrument is equipped with low-pressure range transducers that permit measurements of the equilibrium data with high resolution at the Henry's law region. The samples were

run on the instrument configured in its chemisorption configuration and 200 mg samples were loaded into quartz U-tubes. Samples were activated under a N<sub>2</sub> flow of approximately 200 mL/min by heating the sample at 10 °C/min up to 523K. The sample was held isothermally and under flow for 15 min before the N<sub>2</sub> flow was shut off and the sample subjected to vacuum. The sample was evacuated at a pressure of <0.5 Pa for 60 min and cooled to the analysis temperature under vacuum. Once the temperature in the furnace was stable at the analysis temperature the isotherm data collection was started.

Surface area and pore volume measurements were carried out on the same instrument but configured for micropore analysis under cryogenic conditions. Samples were outgassed overnight under vacuum at 0.5 Pa and 523K. Argon was used as the probe gas and liquid argon was used as the cryogen bath. This choice was made to overcome the limitation associated with localized adsorption of N<sub>2</sub> on cationic sites within the zeolite framework. The helium that was introduced at the end of the out-gassing step was removed by mounting the sample on the analysis port and evacuating the sample, backfilling it with argon, and evacuating the sample again. This cycle was carried out 5 times before the analysis was started. Adsorption data was collected by introducing fixed doses into the sample and allowing the system to reach equilibrium. The dosing was continued until the fractional pressure reached 0.03 P/P<sub>0</sub>. The free-space of the sample was measured after the argon physisorption experiment was completed and the adsorption data was corrected with the measured freespace data. The surface area of the samples was calculated using the Langmuir model and all but the first 10 experimental points were used for the analysis of the surface area. The pore size distribution and pore volume were calculated using the Horvath-Kawazoe data reduction and the cylindrical Saito-Foley pore geometry

with interaction parameter  $3.49\text{e-}43 \text{ erg.cm}^4$ . The instrument allows the precise dosing of very low partial pressures of the adsorbent which results in isotherm data in the micropore region.

## **4.4 Result and Discussion**

### **4.4.1 Characterization**

The XRD patterns in Figure 4.1 for ETS-10 and EVS-10 are virtually identical in d-spacing and reflection intensity ratios even though the EVS-10 sample does not show the peaks characteristic of the ETS-4 impurity that tends to co-crystallize in small amounts with ETS-10. The XRD patterns suggest the crystalline morphologies of the two materials are indistinguishable. The images obtained from the field emission scanning electron microscope (FE-SEM) reveals similar morphology but different crystal size between EVS-10 and ETS-10. EVS-10 has a crystal size of about 100-200 nm whereas ETS-10 has a crystal size of about  $8\mu\text{m}$  (Figure 4.2). The difference in crystallite size is likely due to the different conditions under which ETS-10<sup>18</sup> and EVS-10 are synthesized. The EVS-10 gel is aged longer before being introduced into the autoclave and the synthesis temperature is 30 °C higher compared to ETS-10.

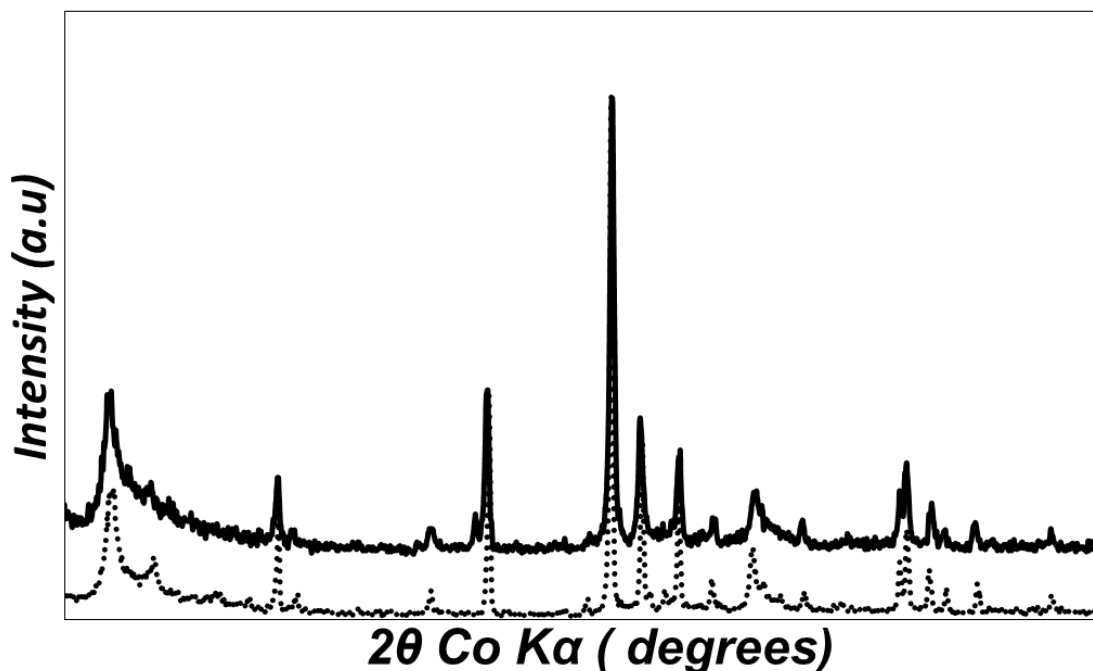


Figure 4.1: XRD patterns of EVS-10 synthesised at 503K (solid line) and ETS-10 synthesized at 488K (dashed line)<sup>19</sup>.

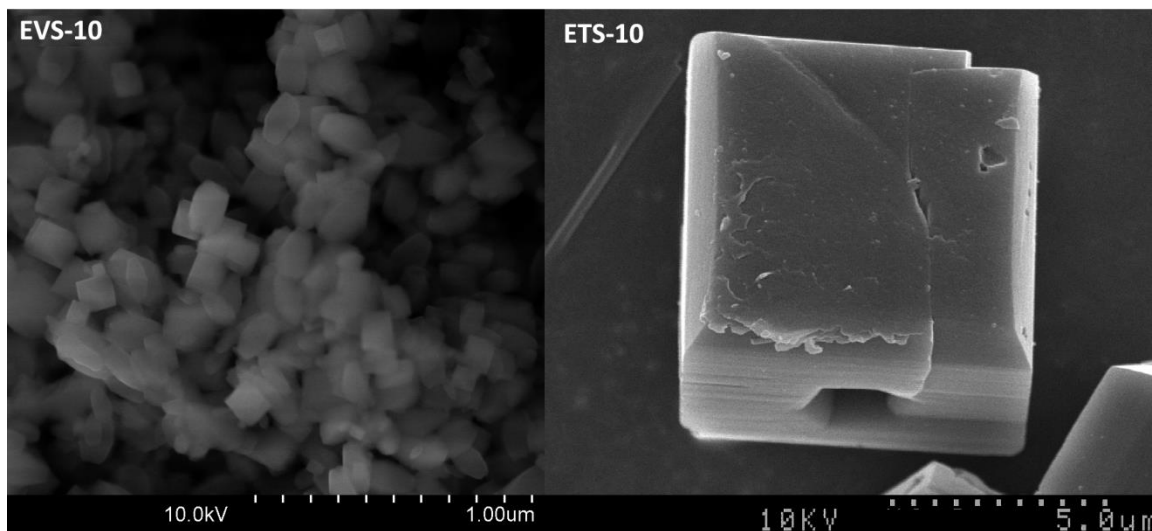
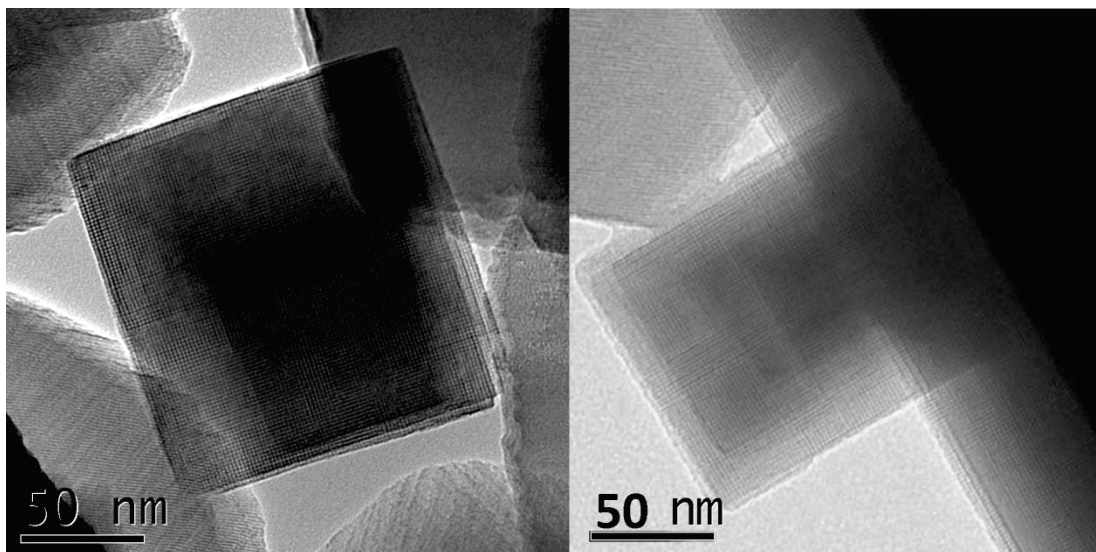


Figure 4.2: Right: SEM image of the seedless, template-free and reducing agent free vanadium silicate EVS-10. Left: SEM image of ETS-10.

To better image the EVS-10 crystallites, transmission electron microscopy (TEM) images were collected<sup>32,33</sup>. The crystalline habits seen in Figure 4.3 are similar to those seen for ETS-10 in the FE-SEM images and confirm a comparable morphology between EVS-10

and ETS-10.



**Figure 4.3:** Left: TEM image on the seedless, template-free, reducing agent-free vanadium silicate crystals. The microporous structure of the new material, EVS-10, is clearly shown. Right: TEM image of ETS-10 crystal adopted from<sup>34</sup>.

The surface area and porosity data calculated for ETS-10 and EVS-10 are summarized in Table 4.1. It can be seen that the EVS 10 sample has an incrementally higher specific surface area which could be due to differences in phase purity; the XRD suggests some measurable fraction of ETS-4 in the ETS-10 sample. The pore volumes calculated are similarly comparable to the surface area results and show only a 3% difference between samples. Again, the presence of a minor impurity phase in ETS-10 is expected to be the cause of this difference.

An interesting difference between the materials lies in their pore size distributions (Figure 4.4). The pore size distribution for EVS-10 is unimodal and relatively discreet compared to ETS 10. While the two materials share the same value for the peak pore size, the profile for ETS-10 is asymmetric and shows a shoulder to higher pore diameter that is not evident in EVS-10. While the two materials share the same value for the peak pore size,

the profile for ETS-10 is asymmetric and shows a shoulder to higher pore diameter that is not evident in EVS-10.

**Table 4.1: Micropore analysis under cryogenic conditions for EVS-10 and ETS-10. Samples were outgassed overnight under vacuum at 0.5 Pa and 523 K. Argon was used as the probe gas and liquid argon was used as the cryogen bath.**

Parameter	EVS-10	ETS-10
Pore size (Å)	8.27	8.65
Micropore volume (cm <sup>3</sup> /g)	0.123876	0.120257
Langmuir Surface area (m <sup>2</sup> /g)	367.96	361.57

This shoulder is the cause of the difference in calculated average pore size seen in Table 4.1, and could be related to the scale of the crystallites. The ETS-10 crystal structure is actually composed of a series of polymorphs which stack sequentially and create disorder within the crystal structure<sup>11</sup>. The ETS-10 crystals, being two orders of magnitude larger than the EVS-10 crystallites, could be expected to have more defects introduced into the crystals due to the commensurately larger number of polymorph combinations. EVS-10, by nature of its nanoscale particles, could be expected to suffer from fewer crystalline defects as a result of polymorph stacking faults.

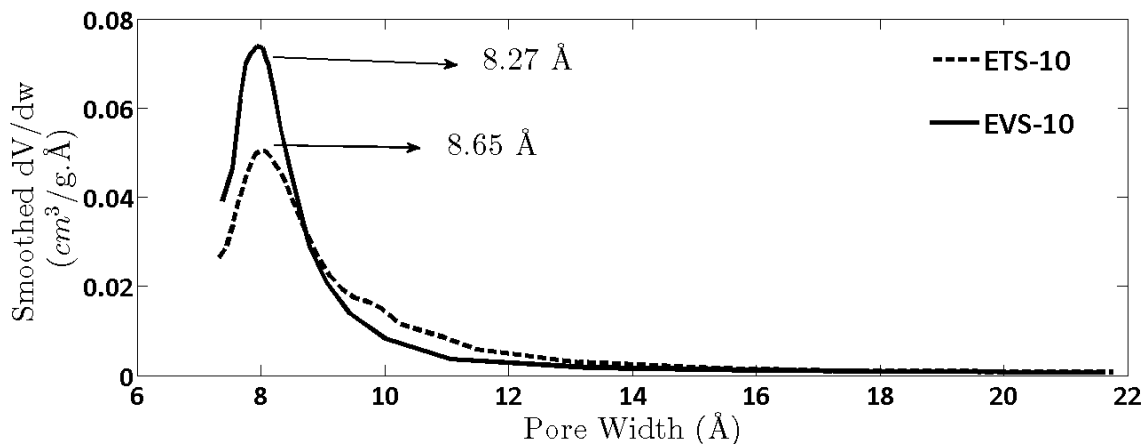


**Figure 4.4: Horvath-Kawazoe differential pore volume plot: solid line represents EVS-10 and dashed line - ETS-10.**

The composition of the molecular sieves was assessed using energy-dispersive X-ray spectroscopy (EDX). The results in

Table 4.2 indicate a strong similarity in the elemental composition of the two materials; particularly in cation (mol%) and cation equivalence ratios. The cation equivalents in both cases fall short of the expected value of 2 to fully balance the divalent charge on the titanium, though sodium is a light elements and the uncertainty in its measurement is thus relatively high. The Si/Ti ratio is somewhat different between the two materials though this difference may not be as significant as it appears from the EDX data as large changes in the Ti/Si ratio should have an effect on the crystal structure yet no significant differences are seen in the powder x-ray diffraction patterns. Within the limit of the accuracy of the method we consider the composition, and particularly the cation composition, to be equivalent.

**Table 4.2: Mol equivalents of each element in the molecular structure of EVS-10 and ETS-10 from EDX analysis.**

Adsorbent	Mol%						
	Na	K	V	Ti	Si	(Na+K)/V	(Na+K)/Ti
EVS-10	1.15	0.44	1		3.21	1.59	
ETS-10	1.08	0.46		1	3.96		1.54

#### 4.4.2 Single Component Adsorption Isotherm

A single isotherm model cannot be used to fit the full range of isotherm profiles for methane, ethane, ethylene, carbon dioxide, nitrogen and oxygen. Adsorption isotherms are fitted to Toth, Langmuir and Redlich Peterson model by the unconstrained optimization technique. A large number of isotherm models exist. Some are thermodynamically consistent while others are empirical. The best isotherm model was selected to be the one with both a good SSE and which predicts  $q_s$  which is consistent with values calculated from Eq. (4.4).

Different parameters need to be examined to choose the best isotherm model. One parameter is the sum of squares due to error (SSE) which measures the total response values deviation from the fit to the response values. A value close to zero is an indication of a good fit. The other factor is the predicted saturation concentration by the model, which should not vary significantly with isotherm temperatures and should be in good agreement with the theoretical saturation concentration calculated from Eq. (4.4). Toth model best fits to rectangular isotherms and Langmuir model best fits to linear isotherms.

Redlich Peterson model is an empirical equation which provides a good fit to both rectangular and linear isotherms. It provides the smallest SSE value when fit to the experimental isotherm data of all the above-mentioned gases compared to the other two models. However, it underestimates the saturation concentration compared to the theoretical values. We picked the isotherm model which has the closest saturation concentration prediction within the factor of 2 difference. In cases such as oxygen and nitrogen Redlich Peterson underestimates the saturation concentration by the order of 7 compared to the theoretical saturation concentration calculated from Eq. (4.4), which makes it unacceptable. The micropore volume for our as-synthesized ETS-10 (0.120257 cc.g<sup>-1</sup>) is higher than the one reported by Al-Baghli et al.<sup>20</sup> which is 0.1195 cc.g<sup>-1</sup>. Therefore, our reported values for the theoretical saturation limit are slightly higher than the ones reported by Al-Baghli et al.<sup>20</sup> on ETS-10. These values are summarized in Table 4.3. The theoretical saturation concentrations reported for EVS-10 are slightly higher than the values on ETS-10 for similar gases due to slightly higher micropore volume of EVS-10 compared to ETS-10 (see Table 4.3).

**Table 4.3: Theoretical saturation concentrations calculated from Eq. 4.4 at 303K and predicted saturation concentrations from the fit of the best models on the isotherm data at 303K.**

Theoretical Saturation Concentration (mmol.g <sup>-1</sup> )	CH <sub>4</sub>	C <sub>2</sub> H <sub>4</sub>	C <sub>2</sub> H <sub>6</sub>	CO <sub>2</sub>	N <sub>2</sub>	O <sub>2</sub>
EVS-10	2.87	2.13	1.88	2.90	3.20	3.88
ETS-10	2.79	2.07	1.83	2.81	3.11	3.77
Predicted Saturation concentration (mmol.g <sup>-1</sup> )						
EVS-10	2.09	2.14	1.96	3.09	1.64	1.9
ETS-10	2.12	2.31	2.05	3.21	1.80	1.99

As shown in Figure 4.5 and Figure 4.6, ethylene, ethane, and carbon dioxide best fit to Toth model and methane best fit to Langmuir model on both EVS-10 and ETS-10, respectively. These results are in agreement with the results reported by Al baghli et al.<sup>20</sup>. Similar to methane, nitrogen and oxygen best fit to Langmuir model on both EVS-10 and ETS-10 (Figure 4.7). The parameters for the best fitting models for each of the above mentioned gases on EVS-10 and ETS-10 are reported in Table 4.4 and Table 4.5.

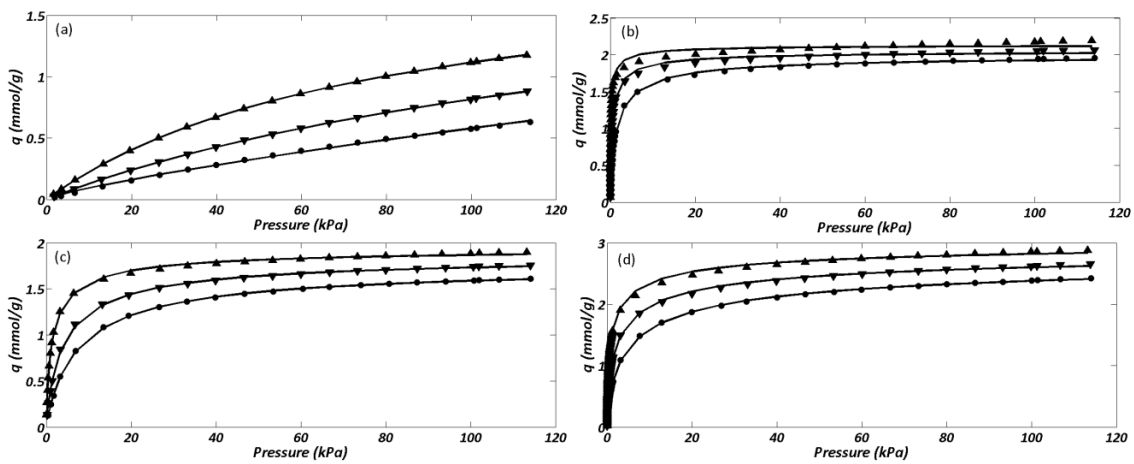


**Figure 4.5:** Fit of (a) Langmuir model to methane isotherm, (b) Toth model to ethylene isotherm, (c) Toth model to ethane isotherm and (d) Fit Toth model to CO<sub>2</sub> isotherm. All the adsorption data are on vanadosilicate EVS-10: ▲ - 303K, ▼ - 323K and ● - 343K.

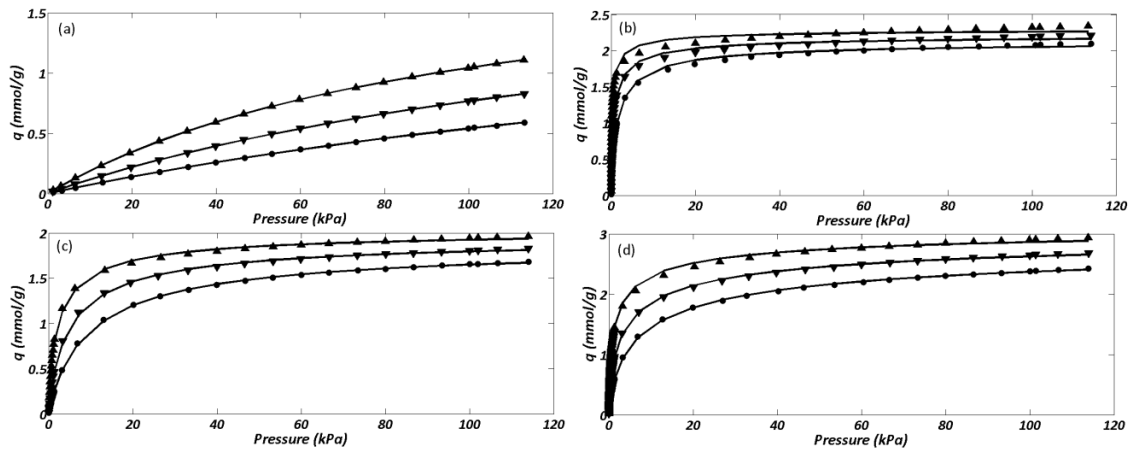


**Figure 4.6:** Fit of (a) Langmuir model to methane isotherm, (b) Toth model to ethylene isotherm, (c) Toth model to ethane isotherm and (d) Fit Toth model to CO<sub>2</sub> isotherm. All the adsorption data are on titanossilicate ETS-10 at: ▲ - 303K, ▼ - 323K and ● - 343K.

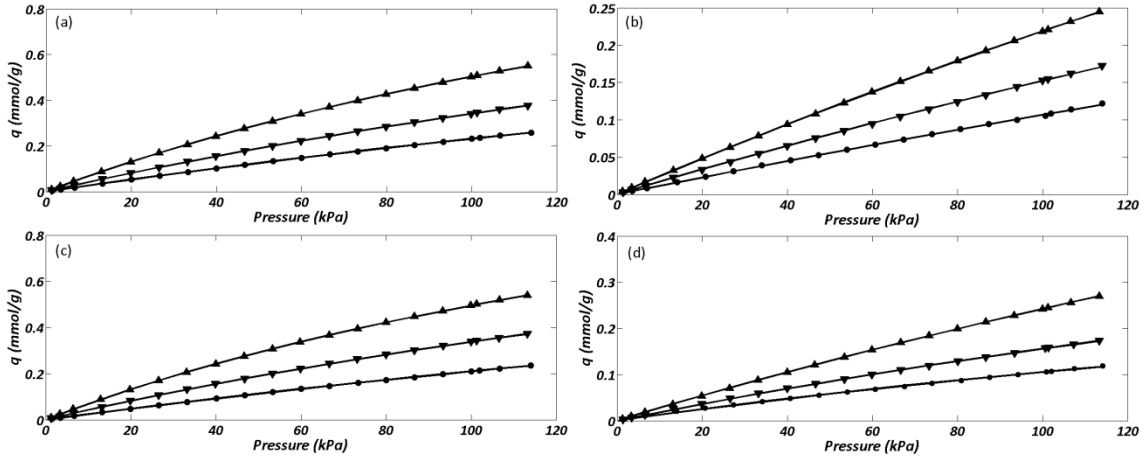


Figure 4.7: Fit of Langmuir model to the isotherms of (a)  $N_2$  and (b)  $O_2$  on ETS-10; (c)  $N_2$  and (d)  $O_2$  on EVS-10 at: ▲ - 303K, ▼ - 323K and ● - 343K.

Table 4.4: Unconstrained Optimization Parameter for the Best Model on ETS-10

$C_2H_6$				$CO_2$			
	Toth Model				Toth Model		
T/K	303	323	343	T/K	303	323	343
SSE	1.034e-02	1.710e-03	4.733e-04	SSE	5e-02	1.5e-02	2e-03
$q_s/mm\text{ol.g}^{-1}$	1.956	1.877	1.771	$q_s/mm\text{ol.g}^{-1}$	3.094	2.984	2.891
b/kPa	9.151e-01	2.319	4.651	b/kPa	4.560e-01	7.780e-01	1.292
t	7.172e-01	7.774e-01	8.412e-01	t	4.930e-01	5.130e-01	5.350e-01
$H/mm\text{ol.g}^{-1}.kpa^{-1}$	2.213572	6.361e-01	2.849e-01	$H/mm\text{ol.g}^{-1}.kpa^{-1}$	1.519e+01	4.866	1.791
$C_2H_4$				$CH_4$			
	Toth Model				Langmuir Model		
T/K	303	323	343	T/K	303	323	343
SSE	1.216e-01	3.220e-02	9.372e-03	SSE	7.940e-06	2.671e-05	2.379e-05
$q_s/mm\text{ol.g}^{-1}$	2.139	2.058	2.004	$q_s/mm\text{ol.g}^{-1}$	2.087	1.994	1.831
b/kPa	1.657e-01	3.901e-01	9.655e-01	b/kPa	1.267e-02	6.420e-03	4.587e-03
t	6.785e-01	7.230e-01	7.477e-01	$H/mm\text{ol.g}^{-1}.kpa^{-1}$	2.644e-02	1.280e-02	8.400e-03
$H/mm\text{ol.g}^{-1}.kpa^{-1}$	3.025e+01	8.788e-01	1.93386				
$N_2$				$O_2$			
	Langmuir Model				Langmuir Model		
T/K	303	323	343	T/K	303	323	343
SSE	5.286e-06	2.113e-06	3.748e-06	SSE	1.881e-06	7.71e-06	2.861e-05
$q_s/mm\text{ol.g}^{-1}$	1.643	1.574	1.483	$q_s/mm\text{ol.g}^{-1}$	1.895	0.9432	0.5686
b/kPa	4.310e-03	2.729e-03	1.644e-03	b/kPa	1.465e-03	1.978e-03	2.268e-03
$H/mm\text{ol.g}^{-1}.kpa^{-1}$	7.081e-03	4.295e-03	2.438e-03	$H/mm\text{ol.g}^{-1}.kpa^{-1}$	2.776e-03	1.866e-03	1.290e-03

**Table 4.5: Unconstrained Optimization Parameter for the Best Model on EVS-10**

<b>C<sub>2</sub>H<sub>6</sub></b>				<b>CO<sub>2</sub></b>			
<b>Toth Model</b>				<b>Toth Model</b>			
	<b>303</b>	<b>323</b>	<b>343</b>		<b>303</b>	<b>323</b>	<b>343</b>
T/K				T/K			
SSE	1.050e-02	3.314e-03	1.308e-03	SSE	5.499e-02	1.538e-02	3.752e-03
q <sub>s</sub> /mmol.g <sup>-1</sup>	2.047	1.968	1.888	q <sub>s</sub> /mmol.g <sup>-1</sup>	3.207	3.142	3.000
b/kPa	1.273	2.694	5.734	b/kPa	5.565e-01	9.806e-01	1.71
β	7.231e-01	7.801e-01	8.392e-01	β	4.931e-01	5.071e-01	5.471e-01
H/mmol.g <sup>-1</sup> .kpa <sup>-1</sup>	1.466	5.524e-01	2.356e-01	H/mmol.g <sup>-1</sup> .kpa <sup>-1</sup>	1.053e+01	3.266	1.125
<b>C<sub>2</sub>H<sub>4</sub></b>				<b>CH<sub>4</sub></b>			
<b>Toth Model</b>				<b>Langmuir Model</b>			
	<b>303</b>	<b>323</b>	<b>343</b>		<b>303</b>	<b>323</b>	<b>343</b>
T/K				T/K			
SSE	1.337e-01	4.308e-02	2.720e-02	SSE	1.389e-05	1.561e-05	2.320e-05
q <sub>s</sub> /mmol.g <sup>-1</sup>	2.305	2.226	2.138	q <sub>s</sub> /mmol.g <sup>-1</sup>	2.115	2.078	1.949
b/kPa	2.325e-01	4.599e-01	1.005	b/kPa	9.733e-03	5.835e-03	3.827e-03
β	6.348e-01	6.652e-01	7.502e-01	H/mmol.g <sup>-1</sup> .kpa <sup>-1</sup>	2.0585e-02	1.2125e-02	7.459e-03
H/mmol.g <sup>-1</sup> .kpa <sup>-1</sup>	2.294e+01	7.155	2.123				
<b>N<sub>2</sub></b>				<b>O<sub>2</sub></b>			
<b>Langmuir Model</b>				<b>Langmuir Model</b>			
	<b>303</b>	<b>323</b>	<b>343</b>		<b>303</b>	<b>323</b>	<b>343</b>
T/K				T/K			
SSE	4.653e-06	7.271e-07	4.029e-06	SSE	2.742e-06	6.082e-06	8.244e-06
q <sub>s</sub> /mmol.g <sup>-1</sup>	1.798	1.719	1.553	q <sub>s</sub> /mmol.g <sup>-1</sup>	1.994	1.466	1.355
b/kPa	3.889e-03	2.475e-03	1.749e-03	b/kPa	1.232e-03	1.158e-03	8.545e-04
H/mmol.g <sup>-1</sup> .kpa <sup>-1</sup>	6.992e-03	4.255e-03	2.716e-03	H/mmol.g <sup>-1</sup> .kpa <sup>-1</sup>	2.457e-03	1.698e-03	1.158e-03

#### 4.4.3 Henry Constant, Heat of Adsorption

The shape of the isotherm reveals the strength of the adsorption on the adsorbent surface. The more rectangular the isotherm is, the higher the heat of adsorption. The heat of adsorption provides a quantitative measurement for the strength of the bonding between sorbate and adsorbent surface. Ethylene, ethane and carbon dioxide on both ETS-10 and EVS-10 have rectangular isotherms while methane, nitrogen and oxygen have more linear isotherms. Likewise, the more rectangular the isotherm the higher the Henry constant. The Henry constants are calculated by fitting the Langmuir form of adsorption to a restricted range of the isotherm data. This choice was made to allow for the Henry's Law constant to be extracted directly from the Langmuir equation. By restricting the pressure range to provide a good fit to the Langmuir equation we were able to achieve the

best assessment of the Henry constant for all isotherms at all temperatures. The Henry constant and the heat of adsorption values are reported in Table 4.6. The Henry constant data can be used to calculate the isosteric heat of adsorption of a pure gas using the Van't Hoff equation.

<b>a. Henry Cte</b>	<b>EVS-10</b>	<b>ETS-10</b>
<b>C<sub>2</sub>H<sub>4</sub></b>	19.0	17.0
<b>C<sub>2</sub>H<sub>6</sub></b>	1.5	1.3
<b>CH<sub>4</sub></b>	2.5e-02	2.4e-02
<b>CO<sub>2</sub></b>	6.0	8.0
<b>N<sub>2</sub></b>	7e-03	8e-03
<b>O<sub>2</sub></b>	2.58e-03	2.85e-03
<b>b. ΔH</b>		
<b>C<sub>2</sub>H<sub>4</sub></b>	45.0	42.0
<b>C<sub>2</sub>H<sub>6</sub></b>	33.0	32.5
<b>CH<sub>4</sub></b>	22.0	22.0
<b>CO<sub>2</sub></b>	37.0	37.5
<b>N<sub>2</sub></b>	18.0	19.7
<b>O<sub>2</sub></b>	13.0	17.0

**Table 4.6: Comparison of Henry's constants (mol kg<sup>-1</sup> kPa<sup>-1</sup>) and heats of adsorption (kJ mol<sup>-1</sup>) from Langmuir isotherm at 298K.**

Heats of adsorption values for the various gases are comparable for EVS-10 and ETS-10, which suggests similar bonding strengths of all the above-mentioned gases to both EVS-10 and ETS-10. There are modest differences in the heat of adsorption for C<sub>2</sub>H<sub>4</sub>, N<sub>2</sub>, and O<sub>2</sub>, which could imply a subtle difference in how strongly these gases interact with the cations in the framework. The differences, however, are not consistent for a single material. The similarity of Van't Hoff plots (Figure 4.8) for all species (r-square varies between 0.9935-1.0) on both adsorbents indicate that the differences in the heats of adsorption could simply be due to experimental error; especially with weakly adsorbing gases, such as O<sub>2</sub>. The differences seen are more likely caused by the uncertainty in the

measurement of the sample temperature than by any fundamental difference in adsorption mechanism. The chemical and structural information for the two materials are so comparable that a difference in adsorption mechanism is unlikely.

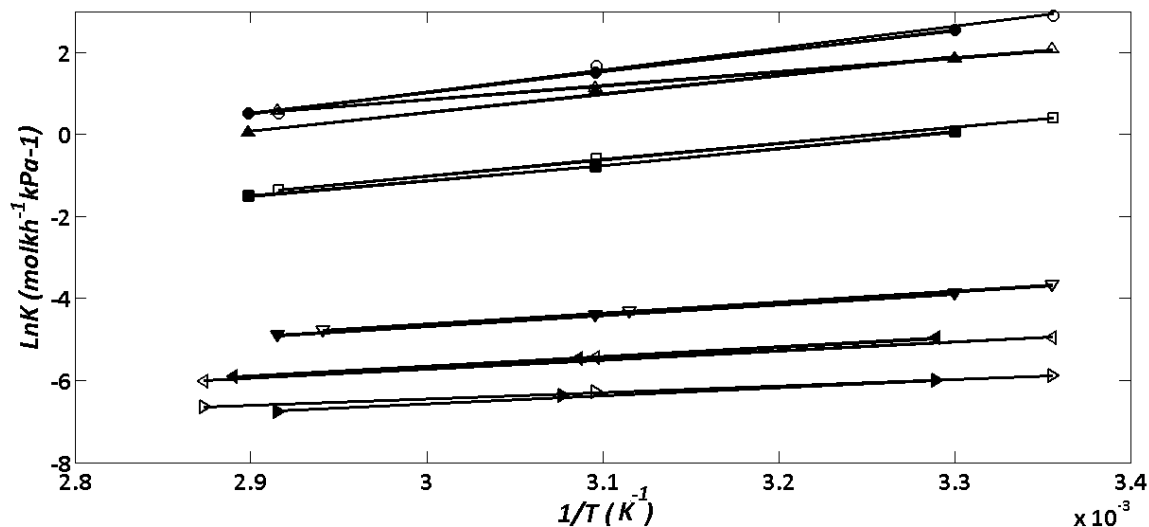


**Figure 4.8:** Van Hoff's plot of Henry's constant values from experimental data at 303, 323, and 343K:  $\circ$  -  $C_2H_4$ ,  $\square$  -  $C_2H_6$ ,  $\nabla$  -  $CH_4$ ,  $\Delta$  -  $CO_2$ ;  $\triangleleft$  -  $N_2$ ,  $\triangleright$  -  $O_2$ . Void symbols represent EVS-10 and solid symbols represent ETS-10. The solid lines represent the regression lines.

#### 4.4.4 Ideal/Henry Selectivity

The ideal selectivity for a selected series of separations was calculated for both adsorbents and the ratios are presented in Table 4.7. As expected from the calculation of the heats of adsorptions, both adsorbents display similar preferences for a range of gas pairs. Small differences between the two adsorbents manifest in certain cases, though the single-component selectivities for both materials are of the same order of magnitude for each gas pair. These results suggest that EVS-10 will have equivalent adsorptive properties compared to ETS-10, albeit with the framework consisting of vanadate chains instead of titanate chains.

**Table 4.7: Comparison of Ideal/Henry's selectivities ( $\alpha$ ) at 298 K.**

<b>Selectivity (<math>\alpha</math>)</b>	<b>EVS-10</b>	<b>ETS-10</b>
$\alpha$ (C <sub>2</sub> H <sub>4</sub> /C <sub>2</sub> H <sub>6</sub> )	13	13
$\alpha$ (C <sub>2</sub> H <sub>6</sub> /CH <sub>4</sub> )	60	55
$\alpha$ (CO <sub>2</sub> /CH <sub>4</sub> )	364	357
$\alpha$ (CH <sub>4</sub> / N <sub>2</sub> )	3.50	3.0
$\alpha$ ( C <sub>2</sub> H <sub>4</sub> / CH <sub>4</sub> )	755	703
$\alpha$ (CO <sub>2</sub> /N <sub>2</sub> )	1271	1047
$\alpha$ (CO <sub>2</sub> /O <sub>2</sub> )	3303	2987

## 4.5 Conclusion

As-synthesized EVS-10 has a composition and structure almost indistinguishable from as-synthesized ETS-10, except for its crystallite size. Similar heats of adsorption on both EVS-10 and ETS-10 confirm comparable bonding strength for all the measured gases. The similarities in the structure and composition of EVS-10 and ETS-10 suggest that the two materials should have comparable adsorption properties. The structural data combined with the adsorption data suggest that, for ETS-10 structure types, analogous materials formed through isomorphic heteroatom substitution of titanium will have similar adsorption properties.

## References

- (1) Shi, M.; Lin, C. C. H.; Kuznicki, T. M.; Hashisho, Z.; Kuznicki, S. M. Separation of a Binary Mixture of Ethylene and Ethane by Adsorption on Na-ETS-10. *Chem. Eng. Sci.* 2010, *65*, 3494–3498.
- (2) Anson, a.; Lin, C. C. H.; Kuznicki, T. M.; Kuznicki, S. M. Separation of Ethylene/ethane Mixtures by Adsorption on Small-Pored Titanosilicate Molecular Sieves. *Chem. Eng. Sci.* 2010, *65*, 807–811.
- (3) Kapoor, A.; Yang, R. T. Kinetic Separation of Methane-carbon Dioxide Mixture by Adsorption on Molecular Sieve Carbon. *Chem. Eng. Sci.* 1989, *44*, 1723–1733.
- (4) Anson, A.; Wang, Y.; Lin, C. C. H.; Kuznicki, T. M.; Kuznicki, S. M. Adsorption of Ethane and Ethylene on Modified ETS-10. *Chem. Eng. Sci.* 2008, *63*, 4171–4175.
- (5) Anson, A.; Kuznicki, S. M.; Kuznicki, T.; Haastrup, T.; Wang, Y.; Lin, C. C. H.; Sawada, J. A.; Eyring, E. M.; Hunter, D. Adsorption of Argon, Oxygen, and Nitrogen on Silver Exchanged ETS-10 Molecular Sieve. *Micropor. Mesopor. Mat.* 2008, *109*, 577–580.
- (6) Anson, A.; Lin, C. C. H.; Kuznicki, S. M.; Sawada, J. a. Adsorption of Carbon Dioxide, Ethane, and Methane on Titanosilicate Type Molecular Sieves. *Chem. Eng. Sci.* 2009, *64*, 3683–3687.
- (7) Ackley, M. W.; Rege, S. U.; Saxena, H. Application of Natural Zeolites in the Purification and Separation of Gases (A Review). *Micropor. Mesopor. Mat.* 2003, *61*, 25–42.
- (8) Corma, A. From Microporous to Mesoporous Molecular Sieve Materials and Their Use in Catalysis. *Chem. Rev.* 1997, *97*, 2373–2419.
- (9) Kuznicki, S.; Madon, R. J.; Koermer, G. S.; Thrush, K. A. Large-Pored Molecular Sieves and Their Use as Catalysts and Ion Exchangers. 0405978B1, 1991.
- (10) Anderson, M. W.; Terasaki, O.; Ohsuna, T.; Philippou, A.; MacKay, S. P.; Ferreira, A.; Rocha, J.; Lidin, S. Structure of the Microporous Titanosilicate ETS-10. *Stud. Surf. Sci. Catal.* 1995, *98*, 258–259.
- (11) Anderson, M. W.; Terasaki, O.; Ohsuna, T.; Philippou, A.; MacKay, S. P.; Ferreira, A.; Rocha, J.; Lidin, S. Structure of the Microporous Titanosilicate ETS-10. *Nature* 1994, *367*, 347–351.
- (12) Rocha, J.; Anderson, M. W. Microporous Titanosilicates and Other Novel Mixed Octahedral-Tetrahedral Framework Oxides. *Inorg. Chem.* 2000, 801–818.

- (13) Rocha, J.; Brandão, P.; Lin, Z.; Anderson, M. W.; Alfredsson, V.; Terasaki, O. The First Large-Pore Vanadosilicate Framework Containing Hexacoordinated Vanadium. *Angew. Chem. Int. Ed. Engl.* 1997, *36*, 100–102.
- (14) Rocha, J.; Ferreira, A.; Lin, Z.; Anderson, M. W. Synthesis of Microporous Titanosilicate ETS-10 from TiCl<sub>3</sub> and TiO<sub>2</sub>: A Comprehensive Study. *Micropor. Mesopor. Mat.* 1998, *23*, 253–263.
- (15) Lin, Z.; Rocha, J.; Ferreira, P.; Thursfield, A.; Agger, J. R.; Anderson, M. W. Synthesis and Structural Characterization of Microporous Framework Zirconium Silicate. *J. Phys. Chem. B* 1999, *103*, 957–963.
- (16) Rocha, J.; Brandão, P.; Phillippou, A.; Anderson, M. W. Synthesis and Characterisation of a Novel Microporous Niobium Silicate Catalyst. *Chem. Commun.* 1998, 2687–2688.
- (17) Kuznicki, S. M.; Thrush, K. A. Large-Pored Molecular Sieves Containing at Least One Octahedral Site and Tetrahedral Sites of at Least One Type, 2002.
- (18) Kuznicki, S. M. Large-Pored Crystalline Titanium Molecular Sieve Zeolites. 5011591, 1991.
- (19) Mani, F.; Wu, L.; Kuznicki, S. M. A Simplified Method to Synthesize Pure Vanadium, Silicate Analogue of ETS-10. *Micropor. Mesopor. Mat.* 2013, *177*, 91–96.
- (20) Al-baghli, N. A.; Loughlin, K. F. Adsorption of Methane, Ethane, and Ethylene on Titanosilicate ETS-10 Zeolite. *J. Chem. Eng. Data* 2005, *50*, 843–848.
- (21) Al-Baghli, N. A.; Loughlin, K. F. Binary and Ternary Adsorption of Methane, Ethane, and Ethylene on Titanosilicate ETS-10 Zeolite. *J. Chem. Eng. Data* 2006, *51*, 248–254.
- (22) Kuznicki, S. M.; Anson, A.; Segin, T.; Lin, C. C. H. Modified ETS-10 Zeolites for Olefin Separation, 2011.
- (23) Magnowski, N. B. K.; Avila, A. M.; Lin, C. C. H.; Shi, M.; Kuznicki, S. M. Extraction of Ethane from Natural Gas by Adsorption on Modified ETS-10. *Chem. Eng. Sci.* 2011, *66*, 1697–1701.
- (24) Shi, M.; Avila, A. M.; Yang, F.; Kuznicki, T. M.; Kuznicki, S. M. High Pressure Adsorptive Separation of Ethylene and Ethane on Na-ETS-10. *Chem. Eng. Sci.* 2011, *66*, 2817–2822.

- (25) Anson, A.; Kuznicki, S. M.; Kuznicki, T.; Dunn, B. C.; Eyring, E. M.; Hunter, D. B. Separation of Argon and Oxygen by Adsorption on a Titanosilicate Molecular Sieve. *Separ. Sci. Technol.* 2009, *44*, 1604–1620.
- (26) Shi, M.; Kim, J.; Sawada, J. A.; Lam, J.; Sarabadan, S.; Kuznicki, T. M.; Kuznicki, S. M. Production of Argon Free Oxygen by Adsorptive Air Separation on Ag-ETS-10. *AIChE J.* 2013, *59*, 982–987.
- (27) Ruthven, D. M. *Principles of Adsorption and Adsorption Processes*; John Wiley & Sons, Inc., 1984.
- (28) Toth, J. State Equations of the Solid-Gas Interface Layers. *Acta. Chim. Acad. Sci. Hung* 1971, *69*, 311–328.
- (29) Wu, F.-C.; Liu, B.-L.; Wu, K.-T.; Tseng, R.-L. A New Linear Form Analysis of Redlich-Peterson Isotherm Equation for the Adsorptions of Dyes. *Chem. Eng. J.* 2010, *162*, 21–27.
- (30) Breck, D. W. *Zeolite Molecular Sieves: Structure, Chemistry, and Use*; John Wiley & Sons, Inc., 1974.
- (31) Dubinin, M. M. Adsorption Properties and Secondary Pore Structure of Adsorbents That Exhibit Molecular-Sieve Action. II. Comparison of Calculated and Experimental Limiting Values for Adsorption and Adsorption Volumes for Type A Synthetic Zeolites. *Izv. Akad. Nauk. Ser. Khim.* 1961, 1183–1191.
- (32) Xamena, F. X. L. I.; Calza, P.; Lamberti, C.; Prestipino, C.; Damin, A.; Bordiga, S.; Pelizzetti, E.; Zecchina, A. Enhancement of the ETS-10 Titanosilicate Activity in the Shape-Selective Photocatalytic Degradation of Large Aromatic Molecules by Controlled Defect Production. *J. Am. Chem. Soc.* 2003, *125*, 2264–2271.
- (33) Bozhilov, K. N.; Valtchev, V. P. Transmission Electron Microscopy Characterization of a Large-Pore Titanium Silicate. *Mater. Res. Bull.* 1993, *28*, 1209–1214.
- (34) Casado, C.; Amghouz, Z.; García, J. R.; Boulahya, K.; González-Calbet, J. M.; Téllez, C.; Coronas, J. Synthesis and Characterization of Microporous Titanosilicate ETS-10 Obtained with Different Ti Sources. *Mater. Res. Bull.* 2009, *44*, 1225–1231.

# Chapter 5

## A Proposed Adsorption Mechanism for Na-ETS-10

### 5.1 Introduction

The structure of ETS-10 is unique in that pore walls are composed entirely of silica while the chains of titania octahedra impart a negative charge that must be offset with mobile cations<sup>1-3</sup>. ETS-10 has been reported to have unique adsorption properties for light hydrocarbons such as methane, ethane, ethylene, carbon dioxide and water<sup>4-12</sup> and the cause of these differences likely lies in the structural differences of ETS-10 compared to conventional aluminosilicate and siliceous molecular sieves. The driving force behind these differences has been suggested to be due to the diffuse charge of the cations exerted through the wall. While the majority of cations undoubtedly reside behind the walls and in close proximity to the titania chains, for monovalent ions, molecular modelling and MQMAS NMR experiments have identified that a fraction of the ions likely reside within the pore system<sup>1,13</sup>. In this way ETS-10 has both the ionic character of aluminosilicate zeolites and the non-polar character of the crystalline silicate molecular sieves.

This study was carried out in order to understand how the structure of ETS-10 affects its adsorption properties toward gases having a range of polarizability and quadrupole moments. To benchmark its adsorptive behaviour, gas adsorption isotherms were

collected for Na-ETS-10, 13X, and highly siliceous ZSM-5 using a series of gases and a range of temperatures. 13X was selected because its pore size is comparable to ETS-10 and is similarly charge-balanced by sodium ions<sup>14</sup>. Highly siliceous H-ZSM-5<sup>3</sup> (Si/Al=800) was selected because it has a comparable pore size<sup>15</sup> and, lacking cations, its adsorption characteristics for the gases selected are driven entirely by van der Waals interactions with the (virtually) pure silica framework. All three adsorbents have pore sizes well in excess of the gases being studied which will prevent steric influences from influencing the analysis. These reference adsorbents have been studied in detail previously. Researchers have reported the use of zeolite 13X<sup>14,16-21</sup> and silicalite<sup>22-26</sup> which has close adsorptive characteristic to high siliceous ZSM-5, for the adsorption of methane, ethane, ethylene and carbon dioxide. Choudhary et al. and Graham et al. also studied the pure component entropy changes for the adsorption of methane, ethane, ethylene and carbon dioxide on silicalite<sup>22,23</sup>. They have concluded that ethane at low surface coverage, and methane, ethylene and carbon dioxide at all the adsorbate loadings, are weakly adsorbed on the silicalite surface so they can freely move on the adsorbent surface. They reported a rise in the adsorbed methane mobility and a decrease on ethane, ethylene and carbon dioxide mobility as the loading increases.

In this study, the thermodynamics of adsorption were calculated to examine each sieve's preferences towards gases having a range of polarizability and quadrupole moments. The isosteric heat of adsorption with respect to loading was calculated to provide insight as to the energetic heterogeneity for each adsorbent and the interaction between the adsorbates

---

<sup>3</sup> The highly siliceous ZSM-5 selected will function in all appreciable aspects as silicalite for the purpose of this study.

and the adsorbent. Ethane, ethylene, methane, and carbon dioxide were chosen as probe gases because their range of molecular weight, molar volume, polarizability, and quadrupole moment—when combined—allow for a broad basis of comparison. Adsorption data was collected with high resolution up to 1.1 bar and at 3 temperatures 303, 323 and 343 K. The resulting isotherms ranged from linear to highly rectangular in nature and a single adsorption model could not fit all data sets accurately. This created an obstacle since an accurate representation of the data across the entire pressure range is critical in order to precisely calculate the change of the isosteric heat of adsorption with loading.

The Langmuir description of adsorption is a useful equation to calculate the limiting heat of adsorption because the equation directly calculates the Henry's Law constant, that is, the slope of the isotherm at low loading. To apply the Langmuir form of adsorption to non-linear isotherms it was necessary to restrict the pressure range to allow the equation to fit the data precisely. This was particularly the case for CO<sub>2</sub> and ethylene adsorption on 13X and Na-ETS-10. Knowing the Henry constants, the limiting heat of adsorption can be calculated from the Van't Hoff equation (Eq. 5.1) where R is the gas constant and T (K) is the temperature. The limiting heat of adsorption, however, only provides information about the enthalpy of the process at low loadings. To fully understand the adsorption mechanism of ETS-10 it was necessary to calculate the isosteric heat of adsorption across all loadings.

$$\frac{d \ln K}{dT} = \frac{\Delta H^{iso}}{RT^2} \quad (5.1)$$

To calculate the isosteric heat of adsorption, the entire pressure range needs to be fit and accurately described by an equation that can be manipulated to solve for pressure or loading. As mentioned previously, the Langmuir description of adsorption only fits a restricted number of the isotherms collected in this study. As a result, several adsorption models were tried to determine which models best described each gas-solid pair. The importance of having an accurate representation of the data cannot be overstated as differences between the fit and data can have a significant influence on the calculated isosteric heat of adsorption. The Langmuir model provided the most accurate fit to the linear isotherms for methane and ethane while the Redlich-Peterson model provided the most precise fit to the rectangular isotherms except for CO<sub>2</sub> and C<sub>2</sub>H<sub>4</sub> on 13X where the Toth model provided the best fit.

To determine the isosteric heat of adsorption for all gases on all adsorbents a Matlab solver was developed to facilitate the calculations. The isosteric heat of adsorption for a single gas is calculated by determining the pressure necessary, at each temperature, to achieve the same specified loading on the solid. Ideally, the isotherm expression can be inverted and expressed as pressure versus loading. Unfortunately, while the Langmuir equation can be inverted, the Toth and Redlich Peterson equations do not have an analytical solution. To overcome this limitation, a solver function was developed in Matlab where the resulting pressure for a specified input loading could be solved for all of the isotherm equations. By carrying out this calculation for the isotherms at each temperature the resulting isosteric pressures could be applied to the Van't Hoff equation and the isosteric heat of adsorption can be calculated at any specified loading.

While the enthalpy of adsorption provides information about the energetic heterogeneity of the surface of the adsorbent and drives the free energy of the process, the *entropy* of adsorption represents the mobility of the adsorbate on the surface of the molecular sieve and thus provides a better description of the interaction between a solid and gas. To calculate the entropy of adsorption the Gibbs free energy must first be known. The Gibbs free energy as a function of pressure at a given temperature can be calculated directly from the isotherms using the equilibrium pressure and by adopting a reference pressure; here taken as 101.32 kPa. The free energy change is simply equal to the work required in order to bring an adsorbate from the gas to the adsorbed state. Once  $\Delta G$  and  $\Delta H$  are known for an adsorbent-adsorbate pair then the entropy,  $\Delta S$  can be calculated directly from the Gibbs free energy equation. By examining the adsorption characteristics of ionic and non-ionic adsorbents with gases having a range of properties it is possible to contrast the adsorption behaviour of NaX and ZSM-5 against ETS-10 to determine which mechanism dominates ETS-10.

## 5.2 Theoretical Background

### 5.2.1 Isotherm models

The experimental isotherms of methane, ethane, ethylene, carbon dioxide are fitted to the following isotherms:

Langmuir adsorption isotherm <sup>27</sup>:

$$q = q_s \frac{bp}{1 + bp} \quad (5.2)$$

Toth model <sup>28</sup> :

$$q = q_s \frac{p}{(b + p^t)^{1/t}} \quad (5.3)$$

Redlich Peterson <sup>29</sup> :

$$q = q_s \frac{bp}{1 + bp^\beta} \quad (5.4)$$

where  $q$  for a given adsorbent represents the amount of gas adsorbed on the surface of the adsorbent,  $p$  denotes the corresponding partial pressure in the gas phase,  $q_s$  stands for the saturation adsorption capacity, and  $b$  represents the adsorption equilibrium constant. Parameters  $t$  and  $\beta$  symbolize the heterogeneity of the adsorbent, are dimensionless, and range between 0-1.

### 5.2.2 Gibbs Energy and Entropy of Adsorption

The values of free energy and entropy changes due to adsorption are assessed from the adsorption data using the following equations <sup>22</sup>:

$$\Delta G = -RT \ln \frac{P_0}{P} \quad (5.5)$$

$$\Delta G = \Delta H - T\Delta S \quad (5.6)$$

$$S_a = S_g + \Delta S \quad (5.7)$$

where  $\Delta G$ ,  $\Delta H$ , and  $\Delta S$  is denoted for change in standard Gibbs free energy, heat of adsorption, and entropy in the adsorption process.  $P_0$  is the reference pressure, which is chosen to be 101.32 kPa.  $S_a$  is the entropy of the adsorbed phase and  $S_g$  is the entropy of the adsorbate gases which is taken from the handbook of the chemical thermodynamics of the organic compounds<sup>30</sup>.

The entropy change of the system,  $\Delta S$ , needs to be corrected for the contribution of entropy change in the adsorbed phase and in the gas phase using the relation from Gregg S. J.<sup>31</sup>; the corrected entropy change is denoted as  $\Delta S_m$ .

$$\Delta S_m = \Delta S + R \ln\left(\frac{A^+}{A}\right) \quad (5.8)$$

$$A^+ = 4.08 \times 10^{-16} T \quad (5.9)$$

$$A = 4 \times 0.866 \left( \frac{M}{4A_1 D_s \sqrt{2}} \right)^{\frac{2}{3}} \quad (5.10)$$

$$D_s = \frac{PM}{RT} \quad (5.11)$$

where  $A^+$  is the standard molecular area in  $\text{cm}^2$  and  $A$  is the molecular area of the adsorbate in the same units.  $M$  is the molecular weight of the gas,  $A_1$  is Avogadro's number,  $D_s$  is the density of the gas at the equilibrium pressure and temperature and  $R$  is the universal gas constant<sup>32</sup>.

During adsorption there are three sources of entropy associated with adsorbed molecules relative to the surface of the solid: translational motion (normal to the adsorbing surface), rotational motion (stationary, in plane), and vibrational motion (mobile, in plane)<sup>33</sup>.  $\Delta S_t$  ( $\text{J} \cdot \text{mol}^{-1} \cdot \text{K}^{-1}$ ) is the theoretical entropy change where all movement perpendicular to the surface of the solid in two and three dimensions is denied to the adsorbate and is defined as follows:<sup>31,33</sup>.

$$\Delta S_t = S_{t3D} - S_{t2D} \quad (5.12)$$

$$S_{t3D} = R \ln(M^{1.5} T^{2.5}) - 9.61 \quad (5.13)$$

$$S_{t2D} = 0.667 S_{t3D} + 2.76 \ln T - 12.71 \quad (5.14)$$

$S_{3D}$  and  $S_{2D}$  ( $J.mol^{-1}.K^{-1}$ ) are three-dimensional and two-dimensional translation entropies, respectively. It is noted that the units of all the constants in the equations are in ( $J.mol^{-1}.K^{-1}$ ) so the gas constant  $R$  is equal to  $8.314$  ( $J.mol^{-1}.K^{-1}$ ):

The change of entropy due to adsorption therefore provides information about the mobility of the adsorbate on the surface of the solid. The gas-solid interaction can fall into either a supermobile, mobile, or immobile/localized adsorption depending on the amount of enthalpy lost between the gas phase and adsorbed phase<sup>33</sup>. When strongly adsorbed, the vibrational entropy of the adsorbed molecule associated with translational motion (perpendicular to the surface) dominates because the molecule cannot escape from the potential well created by the adsorption site to occupy lateral sites<sup>33</sup>. In weak adsorption; the entropy of the gas is dominated by vibrational motion (parallel to the surface) because there is little barrier to movement across the surface of the solid<sup>33</sup>. Supermobile adsorption occurs when the corrected entropy loss of the system ( $\Delta S_m$ ) is less than if all movement perpendicular to the surface were denied to the adsorbate; i.e  $\Delta S_m < \Delta S_t$ <sup>33</sup>. In such cases, the gases are only loosely associated with the surface and are in dynamic exchange with the gas phase. In general, immobile-localized adsorption occurs when the corrected entropy loss of the system is larger than the theoretical entropy; i.e.  $\Delta S_m > \Delta S_t$  while situations where  $\Delta S_m = \Delta S_t$  produces mobile adsorption<sup>33</sup>. These bounds make intuitive sense since stronger adsorption sites, marked by high isosteric heats, should provide for more immobile-localized adsorption than weaker sites. It is expected that ion-dipole adsorption, being a stronger adsorption force compared to

van der Waals, should result in more localized adsorption. Cationic molecular sieves should favour localized adsorption for polar (or quadrupolar) molecules.

## **5.3 Experimental**

### **5.3.1 Materials**

ETS-10 was synthesized by mixing 50 g of sodium silicate (28.8% SiO<sub>2</sub>, 9.14% Na<sub>2</sub>O, Fisher) with 3.2 g of sodium hydroxide (97+% NaOH, Fisher), 3.8 g of KF (anhydrous, Fisher), 4 g of HCl (1M), and 16.3 g of TiCl<sub>3</sub> solution (Fisher). The mixture was stirred for 1 hour then transferred to Teflon lined autoclave and heated at 488 K for 64 h under autogenous pressure. The final product is washed with de-ionized water and dried in an oven at 373 K<sup>34</sup>. Zeolite 13X powder was received from Sigma – Aldrich and CZP 800, a high siliceous ZSM-5 powder with a Si/Al>800, was received from Clariant.

### **5.3.2 Isotherm Measurements**

In this study, a manometric adsorption apparatus Micromeritics (ASAP 2020C) is used to generate high-resolution equilibrium adsorption data for ethane, methane, ethylene, and carbon dioxide at 303, 323, 343K and pressures up to 110 kPa. This instrument is equipped with low-pressure range transducers that permit direct measurement of the adsorption capacity in the Henry's law region. 200 mg samples were loaded into quartz U-tubes and run using the instrument's chemisorption configuration. ETS-10 was outgassed at 10 °C/min to 523K, under 200 mL/min N<sub>2</sub> flow, then it was held isothermally for 15 min under N<sub>2</sub> flow. The sample was then evacuated to a pressure of <0.5 Pa for 60 min and cooled to the analysis temperature under vacuum. The isotherm data collection was started when the temperature in the furnace was stable at the analysis temperature. The same sequence was applied to 13X and ZSM-5 but these samples were

activated to 623 K. The activation temperatures were determined by choosing the lowest temperature in the thermal gravimetric profiles (not shown) at which the sieve showed no additional weight loss. The ZSM-5 sample was activated to a higher temperature than necessary due to its high thermal stability. For each adsorbent, the same sample was used for all isotherm measurements and the sample was re-activated (using the same activation sequence) between CO<sub>2</sub> and C<sub>2</sub>H<sub>4</sub> isotherms to ensure all adsorbed gas was completely desorbed. For methane ethane an extended evacuation step (180 min) was adequate to remove all of the adsorbed gas prior to the next isotherm measurement. The free space for each sample the sample was measured by helium expansion after each isotherm at each analysis temperature.

## **5.4 Results and Discussion**

### **5.4.1 Single-Component Adsorption Isotherms**

To allow the experimental adsorption data to be manipulated in Matlab, the data must be fit to an equation that provides both an accurate and precise fit otherwise the calculation of the isosteric heats will be corrupted. For several gas-solid pairs, the isotherms were too rectangular to fit to a simple equation such as the Langmuir equation without creating significant differences between the data and the fit. As a result, several other adsorption models were tried to determine the best fit for each gas-solid pair. The Langmuir, Toth, and Redlich-Peterson equations were all fit to each of the isotherms using an unconstrained optimization technique and the best equation was determined by selecting the simplest model that had the best SSE value (Figure 5.1). For the purpose of calculating the isosteric heat of adsorption and the adsorption entropy the priority is placed on an accurate fit to the experimental data regardless of the form of the isotherm

equation. As such, the Redlich-Peterson model was used extensively because, while it is an empirical equation, it frequently provided the best fit to the experimental data. The details of the isotherm selected and the fit parameters for each gas and temperature are provided in the Appendix A and the details of the isotherm raw data for each gases at three temperature can be found in Appendix C.

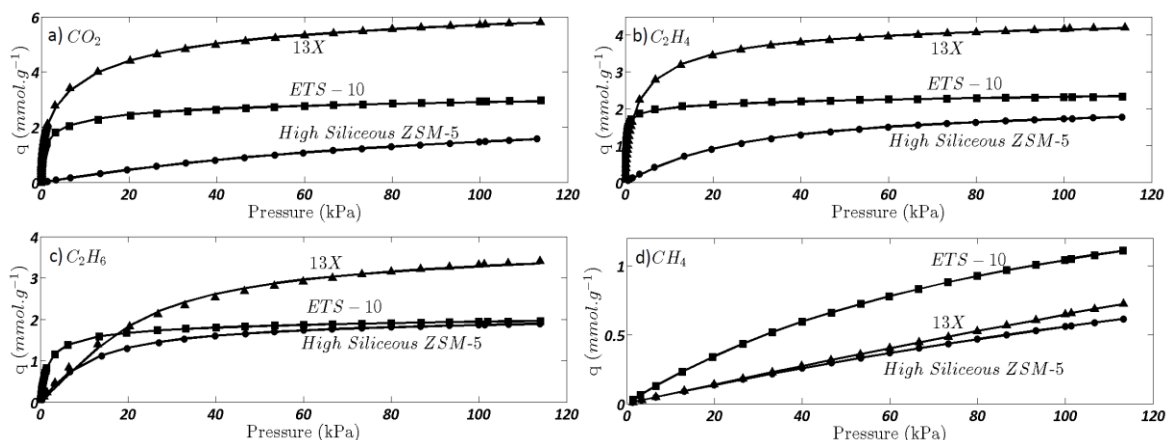


**Figure 5.1: Fit of the models with the most precise fit to the isotherm: (a) CO<sub>2</sub> and (b) C<sub>2</sub>H<sub>4</sub> both fit to langmuir on ZSM-5, to Redlich Peterson on ETS-10 and to Toth on 13X (c) C<sub>2</sub>H<sub>6</sub> fits to Langmuir on 13X and ZSM-5 and to Redlich Peterson on ETS-10 (d) CH<sub>4</sub> fits to Langmuir in all the three adsorbents. All the adsorption data are at 303K.**

#### 5.4.2 Limiting Heat of Adsorption and Polarizability

The shape of an isotherm provides a qualitative measurement for the strength of the interaction between the adsorbate and adsorbent surface. Rectangular isotherms are the result of the stronger bonding between the adsorbate and adsorbent surface, which leads to the higher heat of adsorption. On both ETS-10 and 13X, C<sub>2</sub>H<sub>4</sub> and CO<sub>2</sub> have rectangular isotherms while these gases have linear isotherms on high siliceous ZSM-5 which suggests, qualitatively, that ETS-10 has at least some ionic component to its adsorption mechanism.

The limiting heats of adsorption, i.e. heat of adsorption at low loading, of the pure gases

were calculated from the Henry constant data using the Van't Hoff equation. The Henry constant is the slope of the isotherm at low pressure and this constant can be determined directly from the Langmuir equation. The entire pressure range could be used for gas-solid pairs that produced linear isotherms while for gas-solid pairs that produced rectangular isotherms the Henry constants were calculated by fitting a restricted pressure range of the isotherm data. By restricting the pressure range a consistently good fit to the Langmuir equation was obtained and an accurate and consistent assessment of the Henry constant for all isotherms could be derived. The Van't Hoff equation was applied to the Henry constants determined through the fits to obtain the limiting heat of adsorption whose values are reported in Table 5.1. The reported values on highly siliceous ZSM-5, 13X and ETS-10 are consistent with previously measured heat of adsorption on silicalite, 13X, and ETS-10 in the literature<sup>8,14,16,21,22,26,35-48</sup>

The nature of the adsorption sites on ETS-10 is suggested by the limiting heat of adsorption for ethylene, which is much greater for ETS-10 than it is for ZSM-5 and even exceeds that of 13X. For CO<sub>2</sub>, however, ETS-10 displays an intermediate heat of adsorption; greater than ZSM-5 but not as great as 13X. This trend suggests an ionic component to the adsorption mechanism of ETS-10 which can be stronger, in some cases, but is not identical to 13X. The trend in the limiting heats of adsorption for methane and ethane suggests that ETS-10 also has a significantly *apolar* character as the heats for these gases are comparable to ZSM-5 and greater than those for the polar 13X surface. Na-ETS-10 appears to show characteristics of both types of sieves simultaneously, which suggests that ETS-10 has either some type of hybrid adsorption mechanism or has multiple sites for adsorption which can demonstrate selectivity for their preferred

adsorbates.

**Table 5.1: A comparison of the Heat of Adsorption ( $\text{kJ}\cdot\text{mol}^{-1}$ ) on silicalite, 13X and ETS-10 between the reported value in the literature and values calculated from the Langmuir isotherm at 298K. High siliceous ZSM-5 is comparable to silicalite in the literature.**

Adsorbents	CH <sub>4</sub>		C <sub>2</sub> H <sub>6</sub>		C <sub>2</sub> H <sub>4</sub>		CO <sub>2</sub>	
	By Us	By Literature	By Us	By Literature	By Us	By Literature	By Us	By Literature
13X	17	19.25 <sup>21</sup> , 19.0 <sup>36</sup> , 16.12 <sup>40,42</sup> , 15.4 <sup>43</sup> , 17.8 <sup>46</sup> , 15.675 <sup>41</sup>	25	23 <sup>21</sup> , 27.2 <sup>21</sup> , 25.94 <sup>37</sup> , 31.38 <sup>39</sup> , 26.4 <sup>43</sup> , 27.75 <sup>44</sup> , 26.4 <sup>5</sup> , 26.2 <sup>46</sup> , 29.22 <sup>16</sup> , 27 <sup>35</sup> , 32 <sup>16</sup>	40	32.6 <sup>38</sup> , 40 <sup>16</sup> , 38.4 <sup>14</sup> , 27.91 <sup>16</sup>	44	48.95 <sup>21</sup> , 34.44 <sup>16</sup> , 54.729 <sup>41</sup>
Silicalite	21	21 <sup>47</sup> , 38.5 <sup>48</sup> , 21.49 <sup>49</sup> , 27.5 <sup>22</sup> , 20 <sup>26</sup>	32	30 <sup>48</sup> , 30 <sup>41</sup> , 29 <sup>22</sup>	30	26 <sup>22</sup>	26	20 <sup>22</sup> , 28 <sup>48</sup> , 24.6 <sup>26</sup>
ETS-10	22	20.784 <sup>8</sup>	33	33.846 <sup>8</sup> , 33 <sup>35</sup>	42	42.795 <sup>8</sup> , 34 <sup>35</sup>	37	

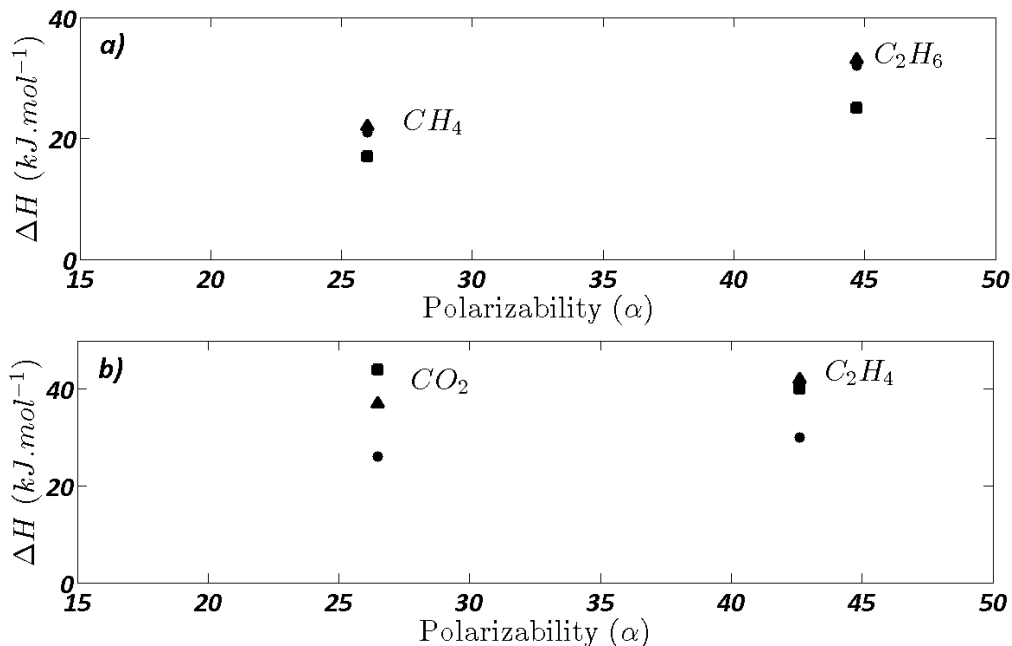
The gas molecules' polarizability ( $\alpha$ ) and quadrupole moment affects the strength of the interaction between the adsorbate and the adsorbent surface and the gases included in this study were selected to have a range of properties. C<sub>2</sub>H<sub>4</sub> and CO<sub>2</sub> are both have relatively strong quadrupoles though ethylene is the more polarizable of the two. The polarizability of the alkanes simply follows their molecular weight and while ethane has a small quadrupole moment it is only about half as strong as ethylene.

Table 5.2 summarizes the properties of the gases used in this study. Since the adsorbate characteristics are constant, differences in the measured heat of adsorption must be derived from the properties of the molecular sieve and how the gas interacts with its surface. The trend in heat of adsorption with respect to polarizability can provide insights into the nature of the gas-solid interactions.

**Table 5.2: Properties of adsorbate gas<sup>21</sup>**

Gas	Mol. Wt (g.mol <sup>-1</sup> )	Kinetic Diameter (Å)	Polarizability (x10 <sup>-25</sup> cm <sup>3</sup> )	Quadropole moment (x10 <sup>26</sup> esu.cm <sup>2</sup> )
CH <sub>4</sub>	16.043	3.758	26.00	0.0
C <sub>2</sub> H <sub>6</sub>	30.070	4.443	44.70	0.65
C <sub>2</sub> H <sub>4</sub>	28.054	4.163	42.60	1.5
CO <sub>2</sub>	44.010	3.3-3.94	26.5	4.3

Figure 5.2a shows a plot of the limiting heat of adsorption versus the polarizability for methane and ethane on each of the adsorbents while Figure 5.2b is the same plot for CO<sub>2</sub> and ethylene. As expected, for both sets of molecules,  $\Delta H$  increases as  $\alpha$  increases for all adsorbents. For CO<sub>2</sub> and ethylene, ETS-10 follows roughly the same trend as 13X which suggests a comparable, though not identical, interaction between the gases and the solids for these two adsorbents. 13X has been established to adsorb polar and quadrupolar molecules through an ion-dipole mechanism<sup>20,41,50</sup> and the observation that Na-ETS-10 behaves comparably to 13X suggests that Na-ETS-10 has a similar adsorption mechanism for quadrupolar molecules. For the alkanes, ETS-10 is comparable to ZSM-5 which suggests that ETS-10 is capable of adsorbing saturated hydrocarbons through an induced-dipole mechanism as occurs with ZSM-5<sup>51</sup>. These results indicate that a diffuse charge adsorption mechanism - where the alkali cations behind the pore wall act at a distance on the adsorbed molecules - is not likely since the adsorption enthalpy vs. polarizability trends for Na-ETS-10 should be unique compared to 13X and ZSM-5.



**Figure 5.2: Isosteric heat of adsorption as a function of adsorbate polarizability: ● represents high siliceous ZSM-5, ■ represents 13X, ▲ represents ETS-10.**

### 5.4.3 Variation of Adsorbate Heat of Adsorption with Loading

The variation of the heat of adsorption ( $\Delta H$ ) with loading ( $q$ ) provides information about the energetic homogeneity of the surface of the adsorbent and is a necessary step in calculating the entropy of adsorption. A Matlab code was developed to solve for the pressure required to achieve a specified loading at each experimental temperature using the Langmuir, Toth, or Redlich-Peterson equations fit to the experimental data. The code allowed for accurate interpolation so the isosteric heats could be calculated with high resolution for any of the isotherm equations used. The isosteric heat for each specified loading was calculated by applying the Van't Hoff equation to the pressure-temperature data. The quality of the data and the fits generated a linear trend in the Van't Hoff plots with  $r^2$  values above 0.98 for all the specified loading.

The isosteric heat of adsorption for each gas on each adsorbent is shown in Figure 5.3a-d. An energetically heterogeneous surface (toward a specific probe molecule) has a distribution of adsorption sites that ranges from strong to weak and these sites are progressively filled by the adsorbate in this order. Such adsorbents exhibit this characteristic due to their composition and structure and, for zeolites in particular, their crystal structure, and the manner in which the cations are distributed through the structure. Energetically homogeneous surfaces, on the other hand, have a narrow range or singular type of adsorption site which provides for little difference in adsorption enthalpy as the loading on the molecular sieve increases. A lack of polarity across the surface of the adsorbent is typical for such adsorbents as the presence of isolated cations or acid sites can selectively attract polarizable molecules and create a gradient in adsorption enthalpy.

Figure 5.3a-c demonstrates that 13X has an energetically heterogeneous surface toward most molecules as evidenced by the steady decrease in the heat of adsorption versus loading for carbon dioxide, ethylene, and ethane. The energetic heterogeneity that 13X demonstrates toward the gases having a stronger quadrupole is related to its structure. In 13X the sodium ions are distributed across several discrete crystallographic sites<sup>52</sup> some of which are accessible to the incoming gas molecules and some of which are shielded within the sodalite cages and unavailable to species that cannot diffuse through the 6-membered rings. The location of the cations within the crystal structure creates the distribution of adsorption sites and results in the steady, decreasing trend in the isosteric heat versus loading plots. The trend for methane on 13X is distinct as the data shows an incremental increase in adsorption enthalpy as a function of loading. The absolute heat of

adsorption for methane is so low that it does not distinguish between the cation and framework oxygen sites and the upward trend suggests that intermolecular interactions between adsorbed molecules have a more significant effect on the adsorption enthalpy than the polarity of the surface of the sieve.

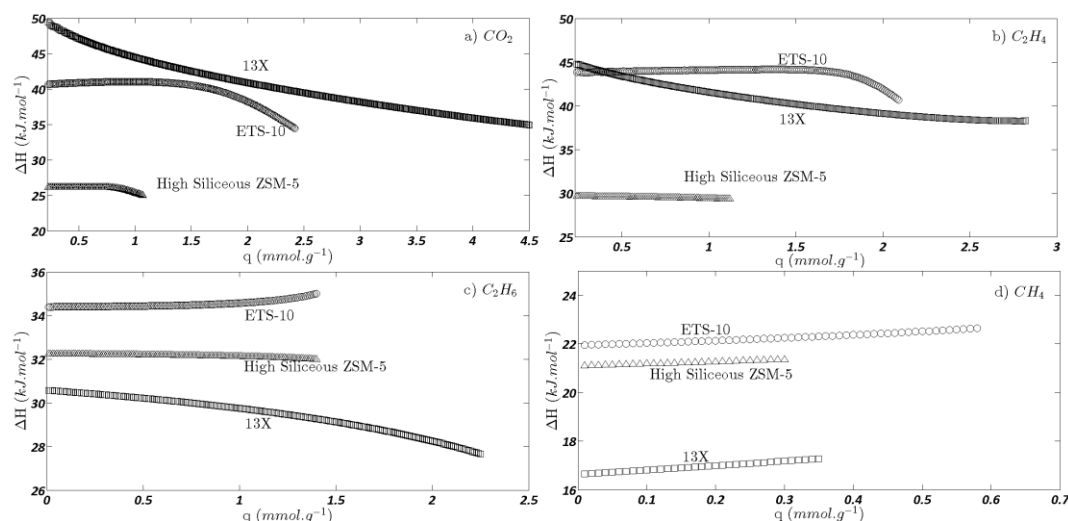


**Figure 5.3: Comparison of the variation of isosteric heat of adsorption ( $-\Delta H$ ) at different adsorbate loading in the adsorption of  $\text{CO}_2$ ,  $\text{C}_2\text{H}_4$ ,  $\text{C}_2\text{H}_6$ ,  $\text{CH}_4$  on 13X, ETS-10 and high siliceous ZSM-5.**

In contrast, the trends for methane, ethane and ethylene on ZSM-5 show effectively no slope across the entire range of loadings studied.  $\text{CO}_2$ , similarly, shows a uniform adsorption enthalpy until the highest loadings where the adsorption enthalpy tapers off slightly which suggests that  $\text{CO}_2$  differentiates between surface sites to a greater extent than do the hydrocarbons. The isosteres for ZSM-5 are characteristic of an energetically homogeneous surface derived from a highly crystalline structure having virtually no cations or aluminium present to disrupt the homogeneity of the purely siliceous framework. The equivalent behaviour of ethane and ethylene on ZSM-5 suggests that the

adsorption field for hydrocarbons on this molecular sieve is substantially uniform and that, as expected, ZSM-5 acts predominately through an induced dipole mechanism.

While the limiting heats of adsorption presented in Table 5.1 for Na-ETS-10 clearly indicate an ion-dipole adsorption mechanism comparable to 13X, this molecular sieve displays an adsorption surface significantly more homogeneous than 13X. For ETS-10, the ethane, ethylene, and CO<sub>2</sub> isosteric heats are constant as a function of loading until a loading is reached where the enthalpy rapidly falls. The ethylene trend on ETS-10 is comparable to the CO<sub>2</sub> trend and is significantly different from the ethane trend. These results clearly demonstrate that there is an ionic component to the adsorption of polar molecules on Na-ETS-10, yet the expected progressive decrease in enthalpy as a function of loading is not comparable to conventional cationic molecular sieves. The unexpected energetic homogeneity of ETS-10 must lie in a combination of how the gas molecules interact with the surface and the nature of the surface that ETS-10 presents to the gas stream.

#### **5.4.4 Change of Adsorption Entropy with Loading**

The adsorption entropy provides direct insight into the nature of the interaction of the gas on the surface of the solid. In order to calculate the adsorption entropy, the Gibbs free energy change must first be calculated through Eq.5.5. Exemplary details of these calculations are provided for carbon dioxide in Appendix B Table1-3. As expected the Gibbs free energy is negative for the spontaneous adsorption process and the results reveal that  $-\Delta G$  decreases with increasing adsorbate coverage on the surface which is in good agreement with what Choudhary et al <sup>22</sup> have reported. The entropy change of the

system ( $-\Delta S$ ), and the adsorbed phase entropy ( $S_a$ ) are calculated from Eq. 5.6-5.7, respectively. The results, tabulated in Appendix B in Table 1-3, indicate a rise in the loss of entropy for the system ( $-\Delta S$ ) as the adsorbate loading increases which indicates that molecules are getting more ordered.

The entropy of the adsorbed phase is equal to the sum of the entropy loss due to adsorption and the entropy of the adsorbate at standard pressure (which is assumed to be constant at all loading (see Eq. 5.7)). Therefore an *increase* in entropy *loss* will lead to a decrease in entropy of the adsorbed phase ( $S_a$ ). This means that the adsorbed species' freedom reduces along the surface of the solid. This reduction may come about at low loadings due to strong adsorption interactions or at high loadings due to steric interactions exerted on incoming molecules by molecules already present on the surface. The change in the adsorbed phase entropy indicates that unlike the alkanes, gases with strong quadrupoles go through more adsorbed phase entropy change ( $\Delta S_a$ ) versus loading on a more heterogeneous surface like ETS-10 and 13X than a homogenous surface like ZSM-5. Similarly, alkanes undergo more adsorbed phase entropy change on a homogeneous surface.

The purpose of the entropy calculations was to gain insight about the mobility of the adsorbed phase on the surface of the solid in the equilibrium state. This goal is best achieved by comparing the corrected entropy change of the adsorption system ( $\Delta S_m$ ) versus adsorbate loading with the theoretical entropy of the adsorption system. Both of these two terms are defined theoretically in Eq. 5.8 and 5.12, respectively. As stated in Eq. 5.12, the theoretical entropy of the system with respect to the surface is defined as the difference between the three and two-dimensional translation entropies. This difference

between the two and three dimensional translation entropies provides a baseline for the degree of freedom of the adsorbed gas on the surface of the adsorbent.

Figure 5.4a-d depicted a comparison between the corrected entropy change ( $\Delta S_m$ ) and theoretical entropy change ( $\Delta S_t$ ) at the same adsorbate loadings used in the isosteric heat calculations. For methane, where there is a relatively low affinity for the surface,  $-\Delta S_m$  trends upward suggesting that the molecules adsorbed on the surface get more constrained as the loading rises. The upward drift in the plot is likely driven by intermolecular interactions in the adsorbed phase as evidenced by the rise in the heat of adsorption as a function of loading in Figure 5.3. The same argument can be applied to Figure 5.4c where ETS-10 is the only adsorbent to show a rising heat of adsorption as a function of loading for ethane. The pore size for all adsorbents is comparable and so steric effects are unlikely; therefore differences between adsorbents are likely due to channel geometry and how the adsorbate interacts with the channel walls.

In Figure 5.4a and b, the entropy trends for  $\text{CO}_2$  and ethylene confirm that these more quadrupolar gases are relatively immobile on the surface of 13X and Na-ETS-10 since the plots are positioned well above the  $\Delta S_t$  demarcation. Such immobility infers strong, localized adsorption which, given the structure and composition of the two sieves, is almost certainly due to ion-dipole interactions. The behaviour toward  $\text{CO}_2$  is different for ETS-10 compared to 13X and suggests that the gas is more mobile on the surface of the titanosilicate until higher loadings are reached. For ethylene, however, ETS-10 shows an ability to localize ethylene, which continues to rise as a function of loading, while 13X displays very similar behaviour for ethylene than it does for  $\text{CO}_2$ .

The consistent behaviour of 13X toward both CO<sub>2</sub> and ethylene provides a reference for ion-quadrupole interactions. The observations that Na-ETS-10 displays different behaviours for CO<sub>2</sub> and ethylene coupled with its unique adsorption thermodynamics for ethane provides the first evidence that the titanosilicate has multiple characteristics which act in tandem to increase the adsorptive selectivity for unsaturated hydrocarbons.

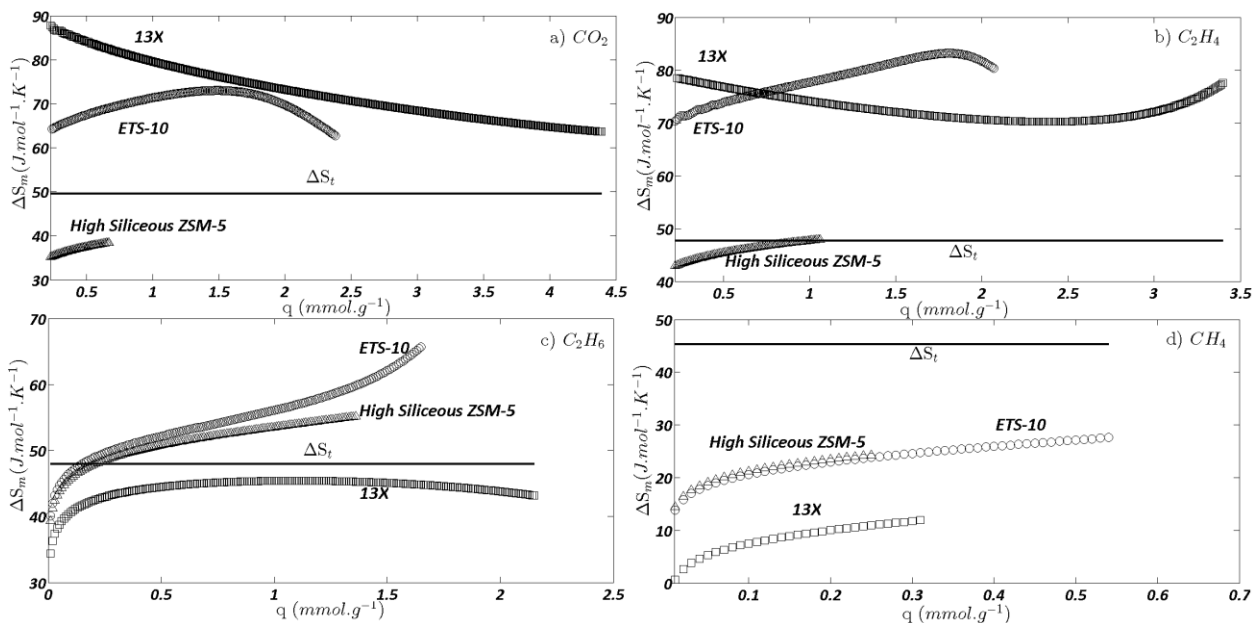


**Figure 5.4:** Comparison of the corrected entropy change ( $-\Delta S_m$ ) at different adsorbate loading with the theoretical entropy change ( $\Delta S_t$ ) in the adsorption of CO<sub>2</sub>, C<sub>2</sub>H<sub>4</sub>, C<sub>2</sub>H<sub>6</sub>, CH<sub>4</sub> on 13X, ETS-10 and high siliceous ZSM-5. All the entropy change data are at 343 K.

#### 5.4.5 ETS-10 Crystal Structure

The adsorptive behaviour of ETS-10 can be rationalized by examining its crystal structure. The structure of ETS-10 is composed of two polymorphs which stack in such a way that the 12-ring pore system is continuous. The stacking creates disorder in the structure and, as such, ETS-10 does not have a solution that fits into a single crystal system.

Anderson<sup>3</sup> has solved the structure of the monoclinic, so-called, beta polymorph of ETS-10 using a combination of techniques including, x-ray diffraction, HRTEM, and molecular simulation to yield the periodic positions of the framework atoms. The structure solution, however, did not locate the extra framework cations within the lattice. Grillo<sup>53</sup> subsequently used molecular modelling to place the sodium and potassium cations within the lattice of the structure of the beta polymorph and determined each sites' affinity toward sodium and potassium ions. The refinement of the beta polymorph structure unit cell dimensions differed somewhat from the structure solution proposed by Anderson but the deviation was small and the ion positions from the energy minimization calculations can be considered representative of their position within the structure proposed by Anderson.

A structure that combines both the framework and non-framework ions was assembled using the atomic coordinates and unit cell dimensions provided by Anderson<sup>3</sup> with the atomic positions for the Na and K cations provided by Grillo. Sites I-III were populated with sodium ions while Site IV was populated with potassium ions at the position specified for that ion. While most of the sites have a calculated preference for potassium, this cation allocation was chosen to maintain the observed 3:1 Na:K mole ratio of the cations in the sieve<sup>54</sup> and because Site IV showed a 4X stronger affinity for potassium compared to the remaining sites.

The combined data was visualized in Mercury and an image of the structure is shown in Figure 5.5, which represents the 12-ring pore structure viewed down the 110 plane. It is evident from the figure that the pore structure of as-synthesized ETS-10 (which contains both Na<sup>+</sup> and K<sup>+</sup> ions) is energetically heterogeneous and that this heterogeneity is

brought about by the asymmetric distribution of cations in the structure. Unlike aluminosilicate molecular sieves where the aluminum is isomorphically substituted for silicon and randomly distributed throughout the framework, the orthogonal chains of titania create discrete bands of cations in the structure.

Assigning only Site IV to potassium (to maintain the experimental Na/K mole ratio) results in a structure where the potassium ions are entirely obscured by the framework and do not intrude into the pore system. There exists the possibility that each of the cation sites is fractionally populated by both sodium and potassium ions and that the channels see a mixture of ions; the mild potassium selectivity that modelling calculates for Site II and III suggests this could be the case. A mixture of cation types across Sites II and III would similarly require that Site IV be fractionally occupied by sodium ions, which the molecular modelling suggests is highly unfavourable. The importance of having potassium in the synthesis mixture coupled with the observed Na/K stoichiometry in the sieve and the molecular simulation results, which establish a strong energy minimization for potassium in Site IV, suggests that potassium has a promoting effect on templating the structure of ETS-10. If this is indeed the case, then the adsorption behaviour of Na/K-ETS-10 should be driven by the affinity of the sodium ion toward the adsorbate. The heats of adsorption calculated for ETS-10 are somewhat lower than those for 13X but this difference could be due to partial shielding of the  $\text{Na}^+$  ions by the framework which would reduce their charge density. The difference might also be caused by the partial substitution of potassium for sodium at Site III. Potassium ions have a lower charge density and will adsorb gases less strongly than sodium<sup>52</sup>. A broader study of a range of

ion-exchanged forms of ETS-10 would be required to conclude which effect predominates.

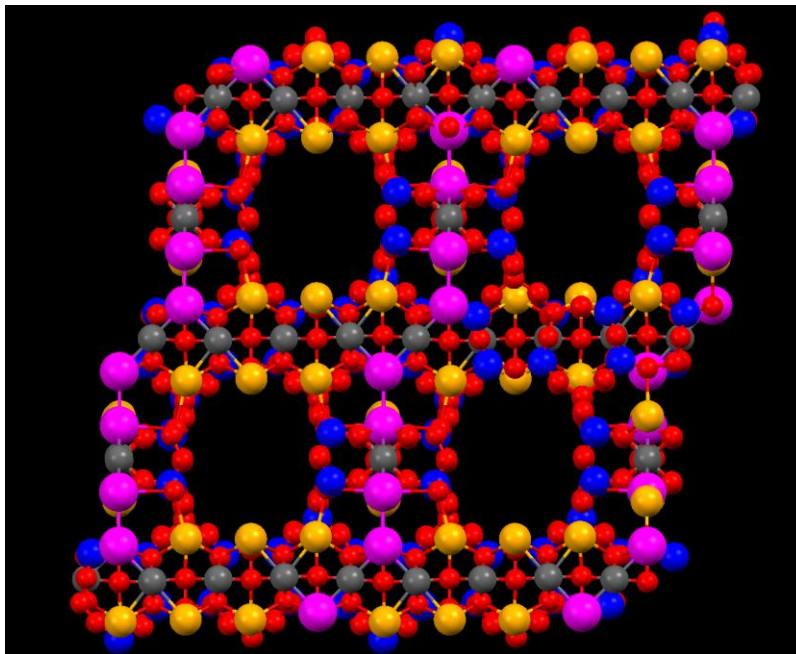


**Figure 5.5: ETS structure visualized in Mercury combines both the framework and non-framework ions using the atomic coordinates and unit cell dimensions provided by Anderson<sup>3</sup> with the atomic positions for the Na and K cations provided by Grillo<sup>53</sup>. Representation of 12-ring pore structure viewed down the 110 plane. Titanium atoms are grey, silicon is blue, oxygen is red, potassium is violet, and sodium is orange.**

The titania chains that run in-plane with the image stagger their charge-balancing cations across the breadth of the 5-membered rings and as the titania chain propagates across the unit cell one of these cations clearly intrudes into the channel. Cations having their charge exposed to the pore and channel system is a necessary feature for ion-dipole interactions and is a common feature in aluminosilicate molecular sieves such as 13X. The difference between aluminosilicate molecular sieves and ETS-10 is that the latter

presents only a single, crystallographically distinct cation into the channel. That the incoming gases only see Site III cations is likely the cause of the energetic homogeneity seen for adsorption of polar molecules on ETS-10.

The titania chains that run *normal* to the plane of the image are a component of the 7-membered rings that link the titania chains that run orthogonally. The ions associated with titania chains running normal to the surface of the image are completely encapsulated and do not intrude through the pore wall. As a result, the pore walls peripheral to the 7-membered rings mimic the pore walls of ZSM-5 which are energetically homogeneous because they are purely siliceous.

Within a single adsorption channel, the short arcs of the pore oval will present a highly polarizing aspect to a gas stream while the long arcs will display a non-polar character. The mixed octahedral-tetrahedral framework of ETS-10 thus allows this molecular sieve to simultaneously present two different adsorption surfaces to an incoming gas stream. This unique structural characteristic suggests that ETS-10 may demonstrate a strong affinity for both quadrupolar and non-quadrupolar gases and why unsaturated hydrocarbons are so preferentially adsorbed. Unsaturated organics such as ethylene could take advantage of both the van der Waals interaction with the silicate walls and the ion-quadrupole interaction with the cations which, in combination, could increase its adsorption enthalpy and drive the high selectivity measured for this adsorbent.

## **5.5 Conclusion**

The unique adsorption characteristics of ETS-10 could be derived from the mixed octahedral-tetrahedral structure of the molecular sieve that provides a pore system having, simultaneously, both polar and non-polar surfaces. The bi-functional pore system

has a high degree of energetic homogeneity yet, also appears to promote strong, localized adsorption around the alkali cations. The particularly favourable interaction of unsaturated hydrocarbons with the surface of Na-ETS-10 could be due to these molecules being able to take advantage of both characteristics of the pore system to minimize their energy. We propose that a synergistic interaction between these two aspects helps explain the uniquely high selectivities measured on Na-ETS-10 for alkenes over alkanes.

## References

- (1) Anderson, M. W.; Agger, J. R.; Luigi, D.-P.; Baggaley, A. K.; Rocha, J. Cation Sites in ETS-10:  $^{23}\text{Na}$   $3\text{Q}$  MAS NMR and Lattice Energy Minimisation Calculations. *Phys.Chem.Chem.Phys.* 1999, *1*, 2287–2292.
- (2) Rocha, J.; Anderson, M. W. Microporous Titanosilicates and Other Novel Mixed Octahedral-Tetrahedral Framework Oxides. *Inorg. Chem.* 2000, 801–818.
- (3) Anderson, M. W.; Terasaki, O.; Ohsuna, T.; Philippou, A.; MacKay, S. P.; Ferreira, A.; Rocha, J.; Lidin, S. Structure of the Microporous Titanosilicate ETS-10. *Nature* 1994, *367*, 347–351.
- (4) Anson, A.; Wang, Y.; Lin, C. C. H.; Kuznicki, T. M.; Kuznicki, S. M. Adsorption of Ethane and Ethylene on Modified ETS-10. *Chem. Eng. Sci.* 2008, *63*, 4171–4175.
- (5) Shi, M.; Lin, C. C. H.; Kuznicki, T. M.; Hashisho, Z.; Kuznicki, S. M. Separation of a Binary Mixture of Ethylene and Ethane by Adsorption on Na-ETS-10. *Chem. Eng. Sci.* 2010, *65*, 3494–3498.
- (6) Anson, a.; Lin, C. C. H.; Kuznicki, T. M.; Kuznicki, S. M. Separation of Ethylene/ethane Mixtures by Adsorption on Small-Pored Titanosilicate Molecular Sieves. *Chem. Eng. Sci.* 2010, *65*, 807–811.
- (7) Anson, A.; Lin, C. C. H.; Kuznicki, S. M.; Sawada, J. a. Adsorption of Carbon Dioxide, Ethane, and Methane on Titanosilicate Type Molecular Sieves. *Chem. Eng. Sci.* 2009, *64*, 3683–3687.
- (8) Al-baghli, N. A.; Loughlin, K. F. Adsorption of Methane, Ethane, and Ethylene on Titanosilicate ETS-10 Zeolite. *J. Chem. Eng. Data* 2005, *50*, 843–848.
- (9) Al-Baghli, N. A.; Loughlin, K. F. Binary and Ternary Adsorption of Methane, Ethane, and Ethylene on Titanosilicate ETS-10 Zeolite. *J. Chem. Eng. Data* 2006, *51*, 248–254.
- (10) Nalaparaju, A.; Zhao, X. S.; Jiang, J. Molecular Interplay of Cations and Nonpolar/Polar Sorbates in Titanosilicate ETS-10. *J. Phys. Chem. C* 2008, *112*, 12861–12868.
- (11) Kuznicki, S. M.; Thrush, K. A. Large Pored Molecular Sieves with Charged Octahedral Titanium and Charged Tetrahedral Aluminum Sites. US5244650, October 1993.
- (12) Steven M. Kuznicki, Alejandro ANson, Tetyana Segin, C. C. H. L. Modified ETS-10 Zeolites for Olefin Separation. 8017825 B2, 2011.

- (13) Pillai, R. S.; Gomes, J. R. B.; Jorge, M. Molecular Simulation of the Adsorption of Methane in Engelhard Titanosilicate Frameworks. *Langmuir* 2014, 30, 7435–7446.
- (14) Triebe, R. W.; Tezel, F. H.; Khulbe, K. C. Adsorption of Methane, Ethane and Ethylene on Molecular Sieve Zeolites. *Gas Sep. Purif.* 1996, 10, 81–84.
- (15) Kuznicki, S.; Madon, R. J.; Koermer, G. S.; Thrush, K. A. Large-Pored Molecular Sieves and Their Use as Catalysts and Ion Exchangers. 0405978B1, 1991.
- (16) Hyun, S. H.; Danner, R. P. Equilibrium Adsorption of Ethane, Ethylene, Isobutane, Carbon Dioxide, and Their Binary Mixtures on 13X Molecular Sieves. *J. Chem. Eng. Data* 1982, 27, 196–200.
- (17) Yang, J.; Lee, C.-H.; Chang, J.-W. Separation of Hydrogen Mixtures by a Two-Bed Pressure Swing Adsorption Process Using Zeolite 5A. *Ind. Eng. Chem. Res.* 1997, 36, 2789–2798.
- (18) Habgood, H. W. Adsorptive and Gas Chromatographic Properties of Various Cationic Forms of Zeolite X. *Can. J. Chem.* 1964, 42, 2340–2350.
- (19) Silva, F. A. Da; Rodrigues, A. E. Adsorption Equilibria and Kinetics for Propylene and Propane over 13X and 4A Zeolite Pellets. *Ind. Eng. Chem. Res.* 1999, 38, 2051–2057.
- (20) Mulgundmath, V. P.; Tezel, F. H.; Saatcioglu, T.; Golden, T. C. Adsorption and Separation of CO<sub>2</sub>/N<sub>2</sub> and CO<sub>2</sub>/CH<sub>4</sub> by 13X Zeolite. *Can. J. Chem. Eng.* 2012, 90, 730–738.
- (21) Sircar, S.; Myers, A. L. *Handbook of Zeolite Science and Technology (Gas Separation by Zeolites)*; Marcel Dekker Inc., New York, 2003.
- (22) Choudhary, V. R.; Mayadevi, S. Adsorption of Methane, Ethane, Ethylene, and Carbon Dioxide on Silicalite-L. *Zeolites* 1996, 17, 501.
- (23) Graham, P.; Hughes, A. D.; Rees, L. V. C. Sorption of Binary Gas Mixtures in Zeolites: I. Sorption of Nitrogen and Carbon Dioxide Mixtures in Silicalite. *Gas Sep. Purif.* 1989, 3, 56.
- (24) Hampson, J. A.; Rees, L. V. C. Adsorption of Ethane and Propane in Silicalite-1 and Zeolite NaY: Determination of Single Components, Mixture and Partial Adsorption Data Using an Isosteric System. *J. Chem. Soc. Faraday Trans.* 1993, 89, 3169–3176.
- (25) Golden, T. C.; Sircar, S. Gas Adsorption on Silicalite. *J. Colloid Interface Sci.* 1994, 162, 182–188.

- (26) Rees, L. V. C.; Bruckner, P.; Hampson, J. Sorption of N<sub>2</sub>, CH<sub>4</sub> and CO<sub>2</sub> in Silicalite-1. *Gas Sep. Purif.* 1991, 5, 67.
- (27) Yang, R. T. *Adsorbents, Fundamentals and Applications*; John Wiley & Sons, Inc.: Hoboken, New Jersey, 2003; p. 410.
- (28) Toth, J. State Equations of the Solid-Gas Interface Layers. *Acta. Chim. Acad. Sci. Hung* 1971, 69, 311–328.
- (29) Wu, F.-C.; Liu, B.-L.; Wu, K.-T.; Tseng, R.-L. A New Linear Form Analysis of RedlichPeterson Isotherm Equation for the Adsorptions of Dyes. *Chem. Eng. J.* 2010, 162, 21–27.
- (30) Daniel Richard Stull, Edgar F. Westrum, G. C. S. *The Chemical Thermodynamics of Organic Compounds*; John Wiley & Sons, Inc.: United States of America, 1969; p. 865.
- (31) Gregg, S. J. *The Surface Chemistry of Solids*; Barnes & Noble: Reinhold Publishing Corporation: New York, 1961; p. 393.
- (32) Emmett, P. H.; Brunauer, S. The Use of Low Temperature van Der Waals Adsorption Isotherms in Determining the Surface Area of Iron Synthetic Ammonia Catalysts. *J.Am.Chem.Soc.* 1937, 59, 1553–1564.
- (33) Kemball, C. Entropy of Adsorption. In; Frankenburg, W. G.; Komarewsky, I. V.; Keightley, E. S., Eds.; *Advances in Catalysis and Related Subjects*; Academic Press Inc., 1950; Vol. 2, pp. 233–250.
- (34) Kuznicki, S. M. Large-Pored Crystalline Titanium Molecular Sieve Zeolites. 5011591, 1991.
- (35) Shi, M.; Avila, A. M.; Yang, F.; Kuznicki, T. M.; Kuznicki, S. M. High Pressure Adsorptive Separation of Ethylene and Ethane on Na-ETS-10. *Chem. Eng. Sci.* 2011, 66, 2817–2822.
- (36) Ding, T.-F.; Ozawa, S.; Yanazaki, T.; Watamuki, I.; Ogina, Y. A Generalized Treatment of Adsorption of Methane onto Various Zeolites. *Langmuir* 1988, 4, 392–396.
- (37) Avgul, N. N.; Bezus, G. A.; Dzhigit, M. O. Heats of Adsorption on X-Type Zeolites Containing Different Alkali Metal Cations; Molecular Sieve Zeolites-II. In *Molecular Sieve Zeolites-II*; M., F. E.; S; B., L., Eds.; American Chemical Society: Washington, DC., 1971; pp. 184–192.
- (38) Reyes, D. R. S. Adsorptive Separation of Light Olefins from Paraffins. *Micropor. Mesopor. Mat.* 2007, 104, 59–66.

- (39) Barrer, R. M.; Bultitude, F. W.; Sutherland, J. W. Structure of Faujasite and Properties of Its Inclusion Complexes with Hydrocarbons. *Trans.Faraday Soc.* 1957, 53, 1111–1123.
- (40) Rolniak, P.; Kobayashi, R. Analysis of Methane and Several Mixtures of Methane and Carbon Dioxide at Elevated Pressures at near Ambient Temperatures on 5A and 13X Molecular Sieves by Tracer Perturbation Chromatography. *AICHE J.* 1980, 26, 616–624.
- (41) Caventi, S.; Grande, C. A.; Rodrigues, A. E. Adsorption Equilibrium of Methane, Carbon Dioxide, and Nitrogen on Zeolite 13X at High Pressures. *J. Chem. Eng. Data* 2004, 49, 1095–1101.
- (42) Park, Y.-J.; Lee, S.-J.; Moon, J.-H.; Choi, D.-K.; Lee, C.-H. Adsorption Equilibria of O<sub>2</sub>, N<sub>2</sub>, and Ar on Carbon Molecular Sieve and Zeolites 10X, 13X, and LiX. *J. Chem. Eng. Data* 2006, 51, 1001–1008.
- (43) Stach, H.; Thamm, H.; Fiedler, K.; Schirmer, W. Contribution to the Thermodynamics of Adsorption of N-Paraffins on NaX Type Zeolite. In *Academy of Sciences*; 1979; pp. 85–93.
- (44) Cochran, T. W.; Kabel, R. L.; Danner, R. P. Vacancy Solution Theory of Adsorption Using Flory-Huggins Activity Coefficient Equations. *AICHE J.* 1985, 31, 268–277.
- (45) Fiedler, K.; Stach, H.; Schirmer, W. Adsorption Thermodynamics of N-Paraffins in Zeolite NaCaA. In *Academy of Sciences*; 1979; pp. 75–84.
- (46) Schirmer, W. Results and Perspectives of the Investigation of Hydrocarbon Adsorption in the Central Institute of Physical Chemistry of the Academy of Sciences of the GDR. In *Academy of Sciences*; 1979; pp. 1–14.
- (47) Vigne-Maeder, F.; Auroux, A. Potential Maps of Methane, Water, and Methanol in Silicalite. *J. Phys. Chem.* 1990, 94, 316–322.
- (48) Kiselev, A. V; Lopatkin, A. A.; Shulga, A. A. Molecular Statistical Calculation of Gas Adsorption by Silicalite. *Zeolites* 1985, 5, 261–267.
- (49) Chiang, A. S.; Dixon, A. G.; Ma, Y. H. The Determination of Zeolite Crystal Diffusivity by Gas chromatography—I. Theoretical. *Chem. Eng. Sci.* 1984, 39, 1451–1459.
- (50) Silva, J. A. C.; Schumann, K.; Rodrigues, A. E. Sorption and Kinetics of CO<sub>2</sub> and CH<sub>4</sub> in Binderless Beads of 13X Zeolite. *Micropor. Mesopor. Mat.* 2012, 158, 219–228.

- (51) Choudhary, V. R.; Mayadevi, S. Adsorption of Methane, Ethane, Ethylene, and Carbon Dioxide on High Silica Pentasil Zeolites and Zeolite-like Materials Using Gas Chromatography Pulse Technique. *Sep. Sci. Technol.* 1993, 28, 2197–2209.
- (52) Breck, D. W. *Zeolite Molecular Sieves: Structure, Chemistry, and Use*; John Wiley & Sons, Inc., 1974.
- (53) Grillo, M. E.; Carrazza, J. Computational Modeling of the Nonframework Cation Location and Distribution in Microporous Titanosilicate ETS-10. *J. Phys. Chem.* 1996, 100, 12261–12264.
- (54) Tanchuk, B.; Sawada, J. A.; Rezaei, S.; Kuznicki, S. M. Adsorptive Drying of CO<sub>2</sub> Using Low Grade Heat and Humid, Ambient Air. *Sep. Purif. Technol.* 2013, 120, 354–361.

# Chapter 6

## Spontaneous Formation of Silver Nanoparticles on the Vanadium Silicate EVS-10

### 6.1 Introduction

EVS-10 is a fully vanadium-substituted form of the titanosilicate ETS-10. The ETS-10 structure type is characterized by having a framework composed of orthogonal chains of highly symmetric, corner-sharing titania octahedra which link together via silicate tetrahedra to form a 3D network containing pores and channels of molecular dimensions. The oxidation state of the transition metal creates a net negative charge on the framework which is offset by mobile and exchangeable metal cations<sup>1-4</sup>. The ETS-10 structure-type is compelling, in part, due to the structure having the best example of 1D metal oxide quantum wires<sup>1,5-9</sup>. Such continuous wires are difficult to fabricate by conventional methods and are of interest as model compounds to study the quantum behaviour of nanoscale semiconductors<sup>1,6-8,10-14</sup>. The isomorphic substitution of vanadium for titanium was first accomplished by Rocha et al.<sup>15</sup> and refined by Ismail et al.<sup>16</sup> and Datta et al.<sup>9</sup>. As the vanadium content in the framework increases the structure becomes more conductive because the band gap of the MO<sub>6</sub> semiconductor chains is reduced<sup>8</sup>. We have previously reported on the synthesis of a seed-free, pure vanadium analogue of ETS-10

which was coined EVS-10<sup>17</sup>. EVS-10 has been shown to have comparable structural and adsorptive characteristics compared to its titanosilicate counterpart and differentiates itself principally in its vibrant violet colour, nano-scale crystallites, and a reduced occurrence of pore twinning<sup>17,18</sup>.

The exchange of the alkali cations present in the as-synthesized sieve is a facile process because most molecular sieves display a strong preference toward silver ions<sup>19-21</sup>. For ETS-10, the exchange of silver for sodium and potassium yields a material with photochromic properties<sup>8,19,22</sup> and uniquely powerful adsorption characteristics toward noble gases<sup>23-28</sup>. However, when the same ion exchange techniques are applied to EVS-10 the material displays none of the hallmark properties of its titanate cousin. The cause behind this unexpected behaviour was explored using a range of crystallographic and spectroscopic tools to understand the interaction of silver with the EVS-10 framework. Through powder X-ray diffraction (XRD), X-ray photoelectron microscopy (XPS) and Raman spectroscopy the spontaneous formation of silver metals through a redox pairing with vanadium is demonstrated.

## **6.2 Experimental**

### **6.2.1 Synthesis**

Vanadium silicate, EVS-10, was hydrothermally synthesized as previously discussed in<sup>17</sup>. The first gel is a mixture of 32 g of sodium silicate (28.8% SiO<sub>2</sub>, 9.14% Na<sub>2</sub>O, Fisher), 12 g of deionised water, 0.5 g of sodium hydroxide, 2 g of potassium chloride, 1 g of sodium fluoride and 4.1 g of sodium chloride. The second gel is a mixture of 3.06 g of vanadium sulfate and 12 g of water. These two gel mixtures are added and stirred together. The resulting low viscosity gel was left aging for 3 days then transferred to a

stainless steel autoclave. After aging, the autoclaves remained in the furnace for 7 days at 503 K. The final product was purple in color and was washed with deionised water and dried at 353 K.

### **6.2.2 Ion exchange**

We assumed that the cation exchange capacity (CEC) of EVS-10 is equal to 5 meq/g adsorbent. With the above assumption a series of samples ranging from 1 to 100% cation exchange of EVS-10 are prepared. We have chosen to prepare 1%, 5%, 10%, 25%, and 50% silver exchange vanadosilicate EVS-10. It should be noted that 1% Ag-EVS-10 means silver occupied 1% of the total CEC of the as-synthesized EVS-10. Correspondingly, 50% Ag-EVS-10 means silver has occupied half of the total CEC of the as-synthesized material. Therefore, to make the above mentioned series, pure AgNO<sub>3</sub> solutions ranging from 5 to 250 mM were prepared in 1 L polyethylene screw-capped bottles. 10 g of as-synthesized EVS-10 was added to the solution. The bottles were wrapped in aluminum foil and the suspension was stirred at room temperature on a magnetic stir plate for 48 h. The resulting ion-exchanged solutions were washed with deionised water and dried at room temperature overnight.

### **6.2.3 EDX**

Energy dispersive X-ray spectroscopy (EDX) measurements were acquired on a Zeiss EVO MA 15 LaB<sub>6</sub> filament scanning electron microscope that is equipped with an EDX system. EDX acquired with a peltier-cooled 10 mm<sup>2</sup> Bruker Quantax 200 Silicon drift detector with 123 eV resolution. The backscattered images were taken using a Si diode detector. Secondary electron images were obtained using a Everhart-Thornley detector.

The samples were not coated and they were run under variable pressure (VP) mode.

#### 6.2.4 XRD

XRD patterns were obtained by a Rigaku Ultima IV unit equipped with a D/Tex detector, with *Fe* filter. The results were acquired with Co K wavelength with the average wavelength of  $1.790260 \text{ \AA}$  (Cobalt tube  $38 \text{ kV}$ ,  $38 \text{ mA}$ ). Samples were run from  $5$  to  $90^\circ$  on a continuous scan using a top-pack mount at a speed of  $2^\circ 2\text{-}\theta$  per min with a step size of  $0.02^\circ$ . JADE 9.1 equipped with 2011 ICDD database was used for data analysis.

#### 6.2.5 TEM

The transmission electron microscopy (TEM) was conducted on JEM2200FS at accelerating voltage of  $200 \text{ kV}$ . High angle annular dark field (HAADF) was used in scanning transmission electron microscopy (STEM) mode to collect images for all the samples.

#### 6.2.6 XPS

XPS measurements were performed on AXIS 165 spectrometer (Kratos Analytical) at the Alberta Centre for Surface Engineering and Science (ACES), University of Alberta. The base pressure in the analytical chamber was lower than  $3 \times 10^{-8} \text{ Pa}$ . Monochromatic Al  $K\alpha$  source ( $h\nu = 1486.6 \text{ eV}$ ) was used at a power of  $168 \text{ W}$ . The analysis spot was  $400 \times 700 \text{ \mu m}$ . The resolution of the instrument is  $0.55 \text{ eV}$  for  $\text{Ag}^{3d}$  and  $0.70 \text{ eV}$  for  $\text{Au}^{4f}$  peaks.

The survey scans were collected for binding energy spanning from  $1100 \text{ eV}$  to  $0$  with analyzer pass energy of  $160 \text{ eV}$  and a step of  $0.4 \text{ eV}$ . For the high-resolution spectra the pass-energy was  $20 \text{ eV}$  with a step of  $0.1 \text{ eV}$ . Electron flood gun was used to compensate

the sample charging. Vision-2 instrument software was applied to process the data. The spectra were calibrated for C<sup>1s</sup> binding energy position at 284.8 eV.

### 6.2.7 Raman Spectroscopy

Raman analysis of the samples was performed with a Nicolet Almega XR Dispersive Raman System utilizing a 24 mW 532 nm wavelength laser, at 25% power level, integration time of 2 s, and two exposures. High resolution grating with x10 objective was used, resulting in an approximately 2 μm diameter sampling cross section.

## 6.3 Results and discussion

### 6.3.1 EDX

The EDX results shown in Table 6.1 confirm that the exchange conditions produced a series of adsorbents having a linearly increasing silver content. The total cation content should reflect the stoichiometry of the framework and, in the case of EVS-10, each vanadium is expected to be offset with two monovalent cations. The results in Table 6.1 show that the total cation equivalents in the samples rise with increasing silver. This trend could be due to having the silver selectively replace protons in the framework at higher silver exchange concentration or the trend could simply be due to the inherent uncertainty of quantifying the lighter, alkali metals using this spectroscopic technique.

**Table 6.1: EDX results on the silver exchanged EVS-10 series expressed as mole ratios to vanadium.**

Ag-EVS-10	Si:V	Na:V	K:V	Ag:V	Cation Equivalents
1%	3.84	1.17	0.47	0.02	1.67
5%	3.67	1.12	0.46	0.14	1.72
10%	3.82	1.05	0.46	0.19	1.71
25%	3.69	0.94	0.43	0.45	1.82
50%	3.74	0.59	0.42	0.92	1.93

The observation that silver displaces the alkali cations almost quantitatively under the experimental conditions indicates that EVS-10 has a strong affinity for silver. It is apparent that the sieve has a stronger affinity toward potassium as more sodium is exchanged compared to potassium through the ion exchange process. The progressive replacement of the alkali by silver also indicates that the adsorbent is stable toward the exchange conditions. If the framework of the molecular sieve was damaged during the ion-exchange process one would expect to see a discrepancy in the trend between the amount of silver in solution and the amount of silver that exchanges into the sieve and/or a change in the overall cation equivalents measured per mole of vanadium.

### **6.3.2 XRD**

Powder XRD was used to track the crystallinity of the molecular sieve framework across the range of silver exchanges. Figure 6.1 shows the diffraction patterns for the as-synthesized and silver-exchanged samples. The peak widths are uniform across all samples which indicate the framework has not undergone any measurable distortion. However, while not evident in the figure, the relative intensities of a number of the reflections do change from sample to sample. As the silver content in the sieve increases, the powder patterns undergo subtle changes where some reflections increase in relative intensity and others are reduced in relative intensity.

The changes in the relative intensity of the peaks in the powder patterns can be justified by simulating the powder patterns for Na/K-EVS-10 and 50%Ag-EVS-10. It has been established that as-synthesized EVS-10 is structurally equivalent to as-synthesized ETS-10<sup>17,18</sup> and the ion-exchange properties of the titanium sieve should be comparable for the vanadium analogue. The powder pattern for Na/K-EVS-10 was simulated by

merging the crystallographic data for the beta polymorph reported by Anderson et al.<sup>29</sup> with the coordinate information for the cations published by Grillo and Carrazza<sup>30</sup> and by substituting the Ti(IV) for V(IV). For the Na/K form of EVS-10, only Site IV was populated with potassium ions while the remaining sites were populated with sodium ions.

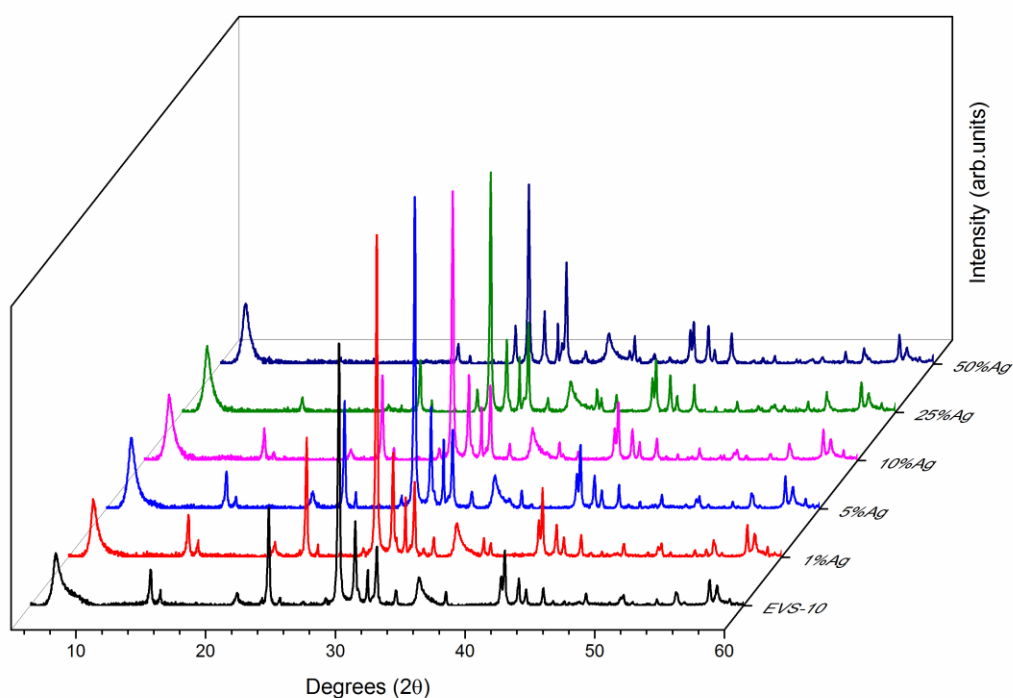


**Figure 6.1: Powder XRD profiles for the as-synthesized EVS-10 and silver exchanged EVS-10 samples.**

This selection was done to preserve the observed Na/K mole ratio<sup>31</sup> and because a much greater affinity for potassium was calculated for Site IV compared to the remaining sites<sup>30</sup>. The powder pattern for the 50%Ag sample was calculated using the same vanadium-substituted beta polymorph data and by substituting silver at sites 1, 2, and 3 using an

occupancy factor of 0.6 as suggested by the EDX data. Site 4 was fully occupied by potassium because the EDX results suggest that the 1-in-4 ratio for potassium is maintained even at 50%Ag exchange. The powder patterns were simulated using cobalt radiation and the simulated patterns were normalized to their most intense reflection. It should be noted that, due to the polymorphic nature of the ETS-10 structure-type, the reflections in the simulated patterns of the beta polymorph will always differ slightly from the experimental patterns. The representation of the EVS-10 structure is shown in Figure 6.2 where oxygen is red, silicon is blue, vanadium is violet, the silver cation positions are grey, and the potassium cation positions are orange.

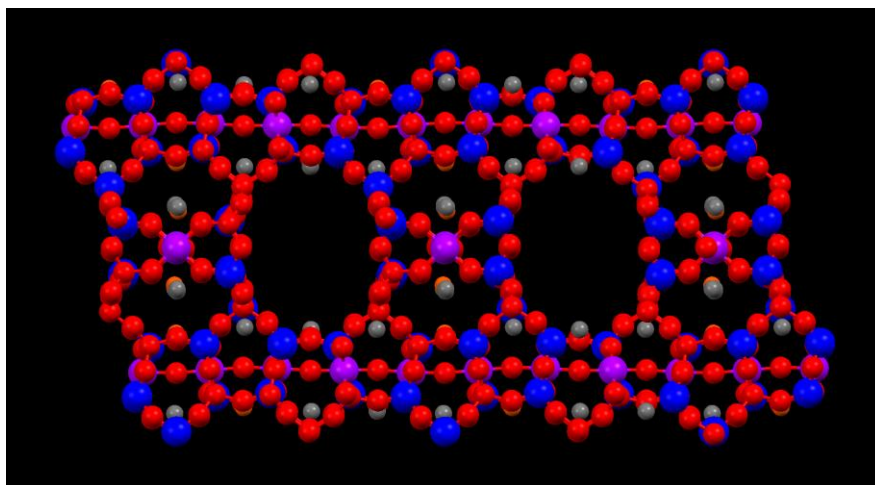


**Figure 6.2: Framework representation of the EVS-10 structure adopted from the crystallographic data reported by Anderson <sup>29</sup> and the coordinate information for the cations published by Grillo <sup>30</sup>. Red, blue, and violet represent oxygen, silicon and vanadium respectively. The cation positions are grey and orange.**

Figure 6.3 shows the calculated and experimental differences in relative intensity between the 50%Ag and EVS-10 patterns. The powder patterns were normalized to their most intense reflection before the signal for the 50%Ag pattern was subtracted from the

EVS-10 pattern. The changes in relative intensities for the simulated powder patterns largely follow what is observed in the experimental patterns in that the lower angle peak intensity is suppressed while the higher angle peaks are predominately enhanced in their intensity. The predicted and experimental results, while not identical, suggest that the changes in relative intensity seen in the powder patterns of Ag-EVS-10 as a function of silver exchange can be explained by silver replacing sodium in the unit cell. The result further suggests that the silver maintains roughly the same crystallographic positions in the unit cell as the sodium ions. If the silver leaves the framework a proton is normally left behind to charge-balance the framework. The substitution of sodium by protons was modelled and the simulated patterns predict that intensity of all of the lower-angle reflections would be enhanced; an effect which is not observed in the experimental patterns.

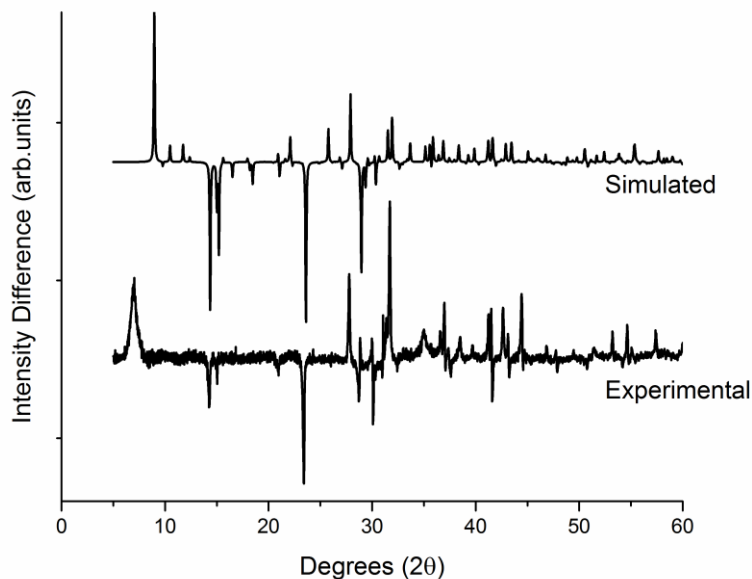


**Figure 6.3: The simulated and experimental differences in relative, normalized intensity for the 50%Ag and EVS-10 powder patterns.**

A number of reflections in the powder patterns undergo small shifts in position as the silver loading on the sieve increases. Figure 6.4 shows an example of the changes for the powder patterns for a pair of higher angle reflections. The shift to smaller angle as the silver content is increased indicates the crystal planes associated with the reflections move away from each other as a result of silver ion-exchange but the shift apparent in Figure 6.4 does not occur for all of the reflections in the powder patterns. The lower angle reflections, however, do not change position as a function of silver loading which suggests that the framework is not undergoing widespread changes as silver is progressively substituted for sodium. The cause of the apparent expansion evident in the higher angle reflections is unclear.

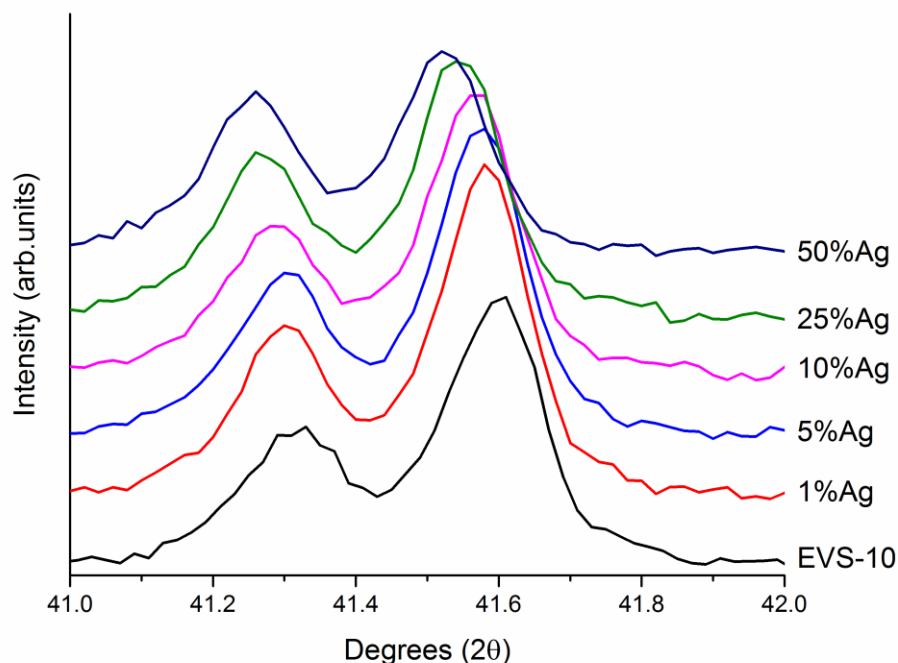


**Figure 6.4: The angular shift in the experimental powder XRD patterns as a function of silver exchange.**

### 6.3.3 TEM

It was noted that samples exchanged to greater than 5% lost the characteristic violet colour of the parent sieve and turned progressively darker shades of gray. This behaviour is not typical for silver-exchanged ETS-10 though a colour change for Ag-ETS-10 does appear after thermal treatment. The change in colouration for Ag-EVS-10 was suspected to be the result of the formation of silver metal on the surface of the crystallites although reflections associated with silver metal are completely absent from all of the XRD patterns. This absence of silver metal is unambiguous because the characteristic for silver metal at  $44.97^\circ$  and  $51.94^\circ$  (2 $\theta$ ) do not overlap with any of the reflections from the EVS-10 pattern. TEM images were collected for the silver-exchanged samples to determine the state and distribution of silver in the framework of EVS-10.

A series of representative images is given in Figure 6.5. The images for the 1% and 5%Ag samples show no dark spots characteristic of metallic clusters<sup>32-35</sup>. At 10% and 25%Ag mottling is seen in parts of the image, which suggests that the silver concentration is increasing in specific areas of the crystals though it may or may not indicate aggregation or agglomeration. This mottling increases in the 50%Ag sample where the bright spots—as a result of collecting the image in dark-field—are larger but still evenly distributed. The large bright spot in the image for the 50%Ag sample is not metallic silver as the EDX map for this sample (not shown) indicates that these charged areas contain all the elements characteristic of Ag-EVS-10. The series of images indicate that silver nanoparticles on the order of 2-4 nm form spontaneously on the surface of EVS-10 and that the silver particles remain uniformly distributed throughout the framework as the degree of silver exchange is increased. An electron diffraction pattern

(not shown) on one of the metal regions was collected and the analysis confirmed that the small particulates in the 50%Ag sample were due to metallic silver.

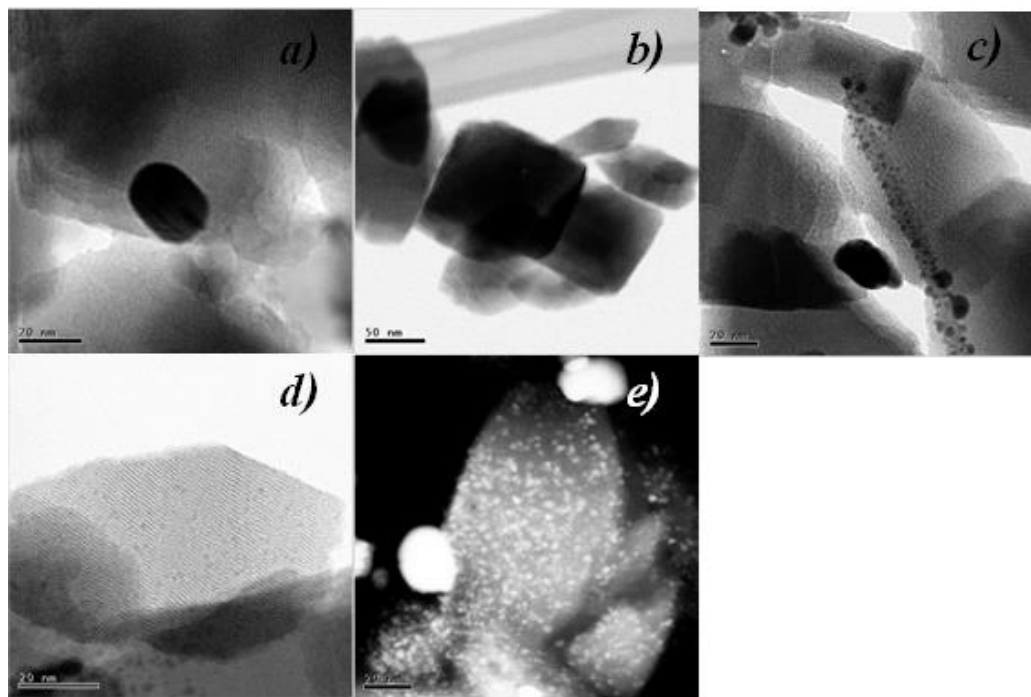


**Figure 6.5: TEM images of for the silver-exchanged EVS-10 samples. a) 1%Ag b)5%Ag c)10%Ag d)25%Ag e)50%Ag**

### 6.3.4 XPS

XPS spectroscopy was used to confirm that the oxidation state of the silver was changing as a result of the silver ion exchange and the normalized Ag 3d<sub>3/2</sub> spectra for the 1% to 50% samples are shown in Figure 6.6. The spectra show an obvious shift in binding energy between the 1%Ag and 50% Ag samples. The breadth of the Ag 3d<sub>3/2</sub> band for the 10% Ag sample clearly indicates the presence of more than one silver site. The Ag 3d<sub>3/2</sub> band for all of the samples was deconvoluted in the CASAXPS software using a Shirley background and allowing the software to fit the band to three Gaussian-Lorentzian peaks

constrained to having a FWHM no greater than unity for the ionic silver components and no greater than 0.7 for the metallic component. The mean peak positions for the deconvoluted spectra are shown in Table 6.2.

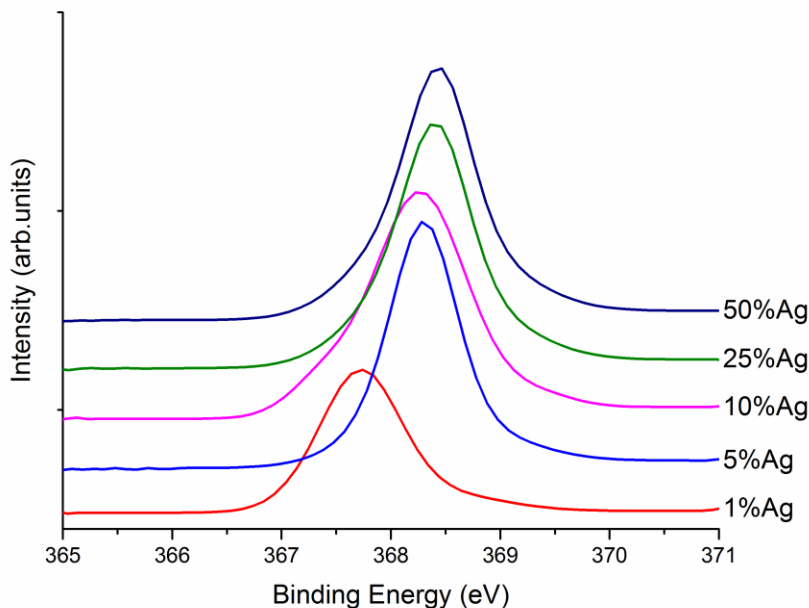


**Figure 6.6: Silver 3d<sub>3/2</sub> XPS results for silver-exchanged EVS-10**

**Table 6.2: Mean peak positions of the bands deconvoluted from and Ag 3d<sub>3/2</sub> XPS spectra.**

Silver exchange	Peak 1(ev)	Peak 2(ev)	Peak 3 (ev)
1%	367.72		368.75
5%	367.84	368.3	369.02
10%	367.59	368.3	369.29
25%	367.92	368.41	369.03
50%	367.93	368.44	369.05

The deconvolution of the Ag 3d<sub>3/2</sub> band indicates that, with the exception of the 1%Ag sample, three distinct binding energies can be found for silver which have an average binding energies of 367.7, 368.4 and 369.1 eV. These binding energies correspond to Ag<sup>+</sup> (referenced as Ag<sub>2</sub>O), Ag(0), and silver bound to a charged molecular sieve framework

respectively <sup>36</sup>. The proportion of each type of silver in each sample is shown in Figure 6.7. The results in this figure indicate that the 1%Ag sample preserves silver as an ion. The agreement of the dominant peak with the binding energy for Ag<sub>2</sub>O is reasonable since the silver ions in a molecular sieve framework will share electron density with the framework oxygen bound to the vanadium metal centers and will thus exist in a state comparable to the pure oxide. The second, minor peak for the 1%Ag sample has a binding energy of 368.7 eV which places it midway between Ag<sub>2</sub>O and silver-exchanged zeolite and references metallic silver alloys and silver phosphite glasses <sup>36</sup>. This peak is assigned to ionic silver bound to the molecular sieve framework rather than to metallic silver because only the 1%Ag sample lacked discolouration after exchange which strongly suggests that the silver remained in its ionic form. The remaining 5%-50%Ag samples clearly show the presence of metallic silver which is in agreement with the change in colouration observed for these samples and what was observed in the TEM images. The 5-50%Ag samples also show contributions from two minor peaks assigned to different forms of ionic silver having a higher binding energy. It cannot be stated unambiguously that silver actually exists in three distinct states in the molecular sieve since these minor contributions could be merely an artefact of the data and the fitting process. It is clear, however, that beyond 1%Ag exchange, the incoming silver ions are reduced to metal in the framework of EVS-10.

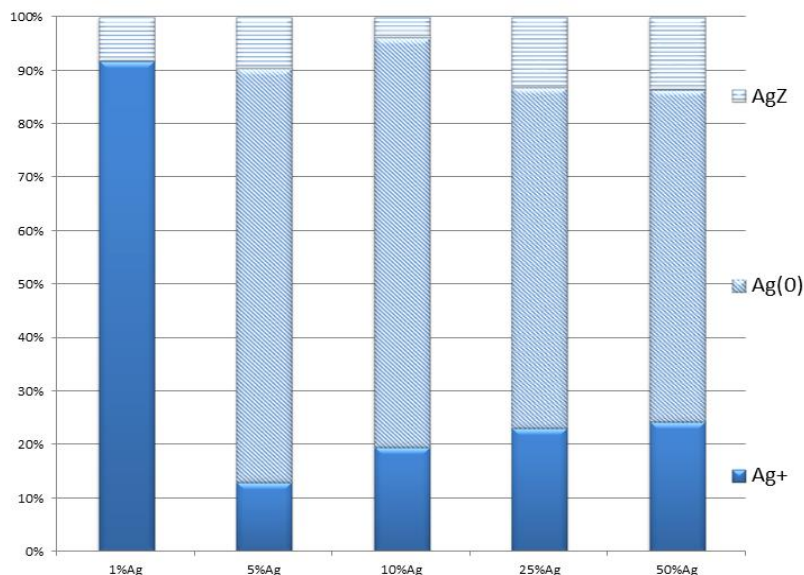


**Figure 6.7: The proportion of each silver band deconvoluted from the Ag 3d<sub>3/2</sub> spectra for the silver-exchanged samples. Binding energies characteristic of Ag<sub>2</sub>O are labelled as Ag<sup>+</sup> while those for silver metal and zeolite-bound silver ions are labelled Ag<sup>(0)</sup> and AgZ respectively.**

The existence of silver metal in the EVS-10 crystals requires that another component in the framework has to be oxidized. Of the various species that make up the framework of EVS-10, vanadium is the only species likely to change its oxidation state under the ion exchange conditions. The V 2p<sub>3/2</sub> band for the as-synthesized and silver exchanged samples is shown in Figure 6.8 and shows a gradual shift in the binding energy as well as peak broadening as the silver exchange is increased.

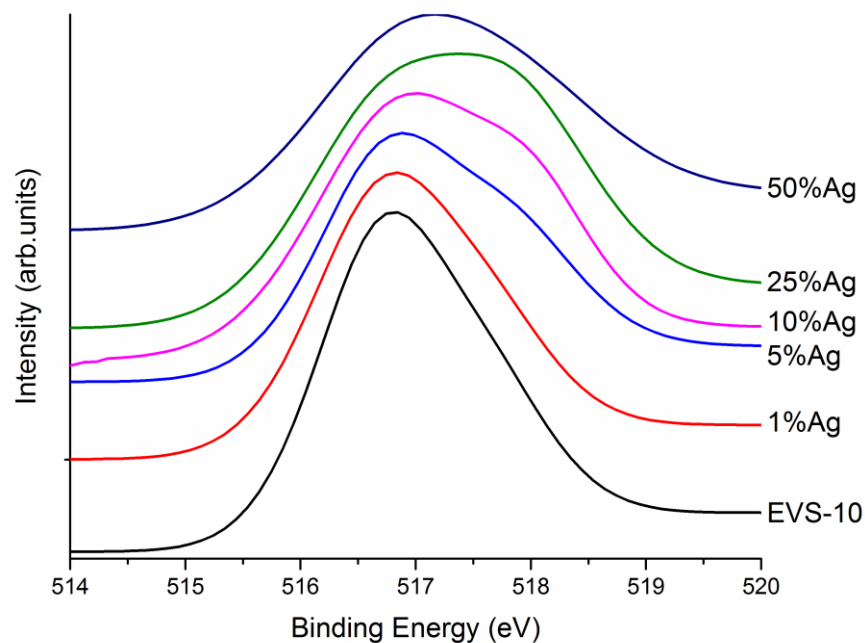


**Figure 6.8: Vanadium  $2p_{3/2}$  XPS spectra for EVS-10 and the silver-exchanged forms of EVS-10**

The V  $2p_{3/2}$  band was fit in the same manner as the silver XPS spectra though it was not possible to maintain a consistent FWHM peak width constraint for all samples. As a result the spectra were fit by constraining the FWHM for the two contributing peaks to be equal to each other within  $\pm 0.2$  eV. The mean peak positions from the deconvolution are presented in Table 6.3.

**Table 6.3: Mean peak positions of the bands deconvoluted from and V 2p<sub>3/2</sub> XPS spectra.**

Silver exchange	Peak 1(ev)	Peak 2(ev)
1%	516.7	517.69
1%	516.71	517.68
5%	516.74	517.86
10%	516.6	517.8
25%	516.69	517.88
50%	516.92	518.12
100%	516.93	518.46

The V 2p<sub>3/2</sub> band was deconvoluted into two peaks having average binding energies of 516.8 and 517.9 eV. The reported binding energies for V<sup>5+</sup> and V<sup>4+</sup> oxides have a great deal of overlap though the average binding energy for V<sup>4+</sup> and V<sup>5+</sup> oxides is different by about 1 eV which suggests the lower binding energy is associated with V<sup>4+</sup> and the higher binding energy with V<sup>5+</sup><sup>36</sup>. The proportion of vanadium in each oxidation state is shown in Figure 6.9. The deconvolution of the V 2p<sub>3/2</sub> XPS spectrum for the as-synthesized material (indicated as 0% Ag) suggests the framework contains vanadium in both the 4+ and 5+ oxidation states which is in agreement with other preparations of vanadium-substituted ETS-10<sup>9,15,37</sup>. The vanadium XPS results for the 1% sample are identical to the as-synthesized sample which is in agreement with the XRD results which indicated that these two samples are virtually indistinguishable. Since V<sup>5+</sup> requires only one charge equivalent to balance its charge—compared to the two required for V<sup>4+</sup>—the presence of the vanadium in the higher oxidation state should reduce the total number of cations in the framework. The atomic composition of the 1% Ag sample (Table 6.1) indicates that there are 1.7 cation equivalents for each vanadium atom.

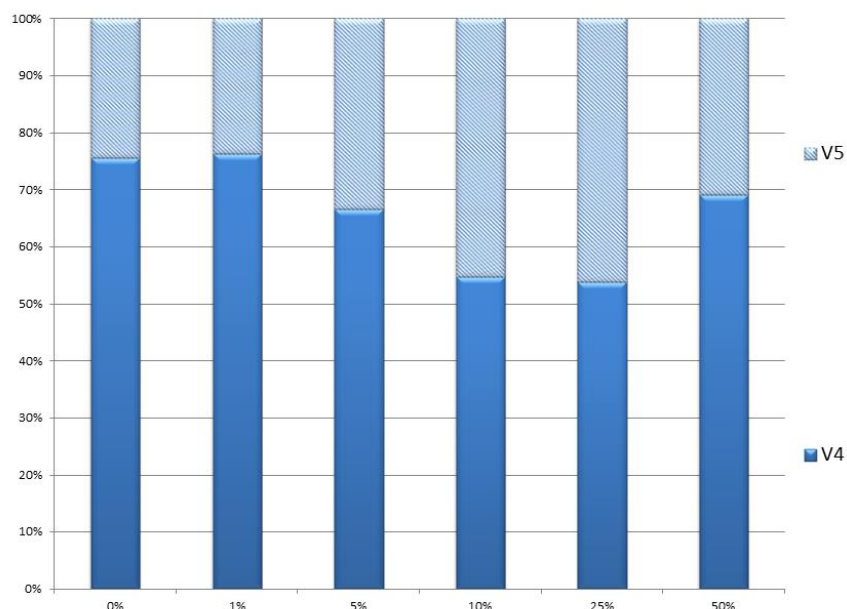


**Figure 6.9: The proportion of each vanadium band deconvoluted from the V 2p<sub>3/2</sub> spectra for EVS-10 and the silver-exchanged EVS-10 samples. The 0% sample represents as-synthesized EVS-10 while the remaining labels specify the silver loading. The solid bars are binding energies characteristic of V<sup>4+</sup> while the shaded bars are binding energies characteristic of V<sup>5+</sup>.**

If the entire framework was composed of V<sup>4+</sup> octahedral this figure is expected to approach 2. The observation that only 80% of the cation equivalents are present in the 1%Ag sample largely agrees with the vanadium XPS results and suggests that the difference between the expected and measured cation balance is likely due to the presence of a significant amount of V<sup>5+</sup>.

At 5%Ag exchange there is an obvious increase in the amount of V<sup>5+</sup> present in the sample which increases again for the 10%Ag sample. The proportion of V<sup>5+</sup> seems to plateau after 10%Ag and then reverses at 50%Ag exchange where a decrease in the

proportion of  $V^{5+}$  is noted. A lack of a correlation between the degree of silver exchange and the  $V 2p_{3/2}$  peak deconvolution could be due to the inherent uncertainty in the deconvolution process. While efforts have been made to provide a consistent set of deconvolution conditions for all the samples, the calculated proportions of  $V^{4+}$  and  $V^{5+}$  are easily influenced by changing the baseline conditions or by changing constraints on the peak widths and positions.

### 6.3.5 Raman Spectroscopy

Vanadium oxide octahedra have Raman-active bands and the V-O-V stretch has been reported to lie between about  $800\text{-}900\text{ cm}^{-1}$  <sup>8,9,15</sup>. The Raman shift is highly sensitive to bond length <sup>38-41</sup> so Raman spectroscopy was used to confirm the trend in the oxidation state of vanadium seen in the XPS results. The spectra for the various samples are shown in Figure 6.10.

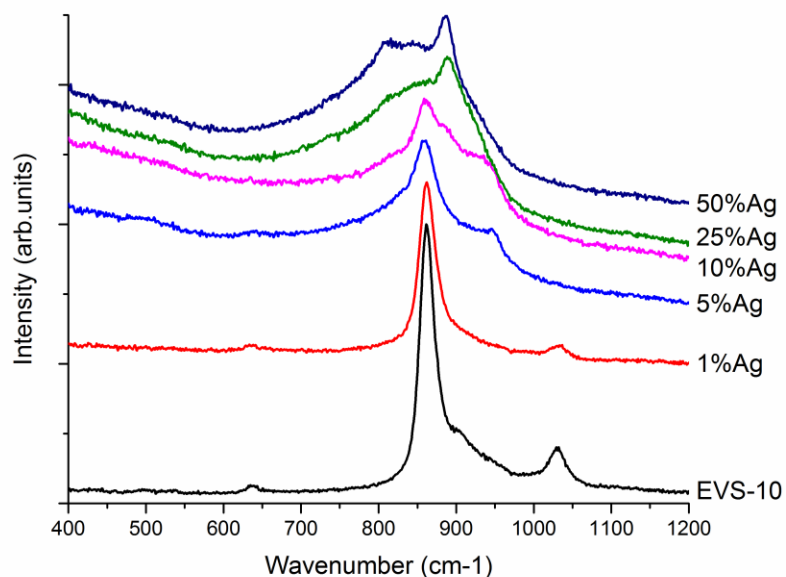


**Figure 6.10: Raman spectra for EVS-10 and the silver-exchanged EVS-10 samples.**

The intense peak in the EVS-10 spectrum at  $860\text{ cm}^{-1}$  has been assigned to a V-O-V stretch<sup>8</sup> and because the XPS results indicate that this sample is predominately composed of  $\text{V}^{4+}$  the band at  $860\text{ cm}^{-1}$  is assigned to the vibration of  $\text{V}^{4+}$ -O bonds. A smaller peak at  $1030\text{ cm}^{-1}$  is observed which could be assigned to terminal V=O bonds<sup>15</sup> though the subsequent disappearance of this band in the remaining silver-exchanged samples suggests that the band at  $1030\text{ cm}^{-1}$  is more likely a vibration mode associated with the highly symmetric vanadia octahedral. The silver exchange process is not expected to reduce the number of terminal V=O bonds on the surface of the crystals. A small, unassigned peak is seen in the spectrum of EVS-10 at  $640\text{ cm}^{-1}$  which is also seen in other reported structures of vanadium-substituted ETS-10<sup>8,9,15</sup>. The simultaneous disappearance of this peak with the one at  $1030\text{ cm}^{-1}$  indicates that the band at  $640\text{ cm}^{-1}$  is also likely associated with a vibration mode of the vanadia octahedra.

The Raman spectrum for 1%Ag sample is comparable to that of the as-synthesized sieve which is in agreement with both the XRD and XPS and confirms that this degree of silver exchange did not have a significant effect on the structure. The baseline for the 1%Ag sample, however, was found to be more pronounced. While the two samples appear to be structurally identical the difference seen in the Raman spectra suggests that either the Raman spectrum is highly sensitive to cation content or that the silver is interacting with the incoming laser light. Ag-ETS-10 has been shown to display photochromism<sup>19</sup> which is driven one way by temperature and reversed by exposing the material to laser light at 532 nm. This is the same wavelength used as the Raman excitation source so the influence of silver on the Raman baseline seems likely as the effect gets greater as the silver content of the sieve is increased.

For the 5%Ag and 10%Ag samples the band at  $860\text{ cm}^{-1}$  shows a decrease in intensity and broad shoulders appear at both high and low frequency. The attenuation of the  $\text{V}^{4+}\text{-O}$  band is in agreement with the vanadium XPS results which indicate a progressive conversion of  $\text{V}^{4+}$  to  $\text{V}^{5+}$ . The loss of the peaks at  $640$  and  $1030\text{ cm}^{-1}$  is likely due to a disruption in the symmetry of the vanadate octahedra brought about by bond-length differences between  $\text{V}^{4+}\text{-O}$  and  $\text{V}^{5+}\text{-O}$ . The XRD results, though, confirm the crystal structure of the 10%Ag sample is virtually unchanged compared to the as-synthesized material and so the distortion of the vanadia octahedra does not appear to create widespread changes in the unit cell. Small, progressive changes could, however, be masked in the XRD patterns due to the intrinsic disorder associated with the polymorphic structure of EVS-10. The inherent disorder in the crystal system could be averaging out effects that could otherwise be seen in a structure with a higher degree of periodicity.

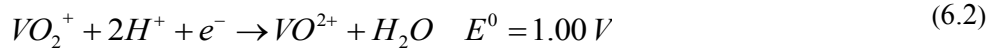
The spectrum for the 25%Ag sample shows a prominent band at  $880\text{ cm}^{-1}$  and the previously sharp band at  $860\text{ cm}^{-1}$  has collapsed to a broad shoulder centered on about  $840\text{ cm}^{-1}$ . The band at  $880\text{ cm}^{-1}$  is assigned to  $\text{V}^{5+}\text{-O}$  and is just visible in the shoulder of the 10%Ag sample. The increase in the intensity of this band is expected to be due to the progressive conversion of  $\text{V}^{4+}$  to  $\text{V}^{5+}$  seen in the vanadium XPS results. The position of the band at  $880\text{ cm}^{-1}$  suggests that the bond length for  $\text{V}^{5+}\text{-O}$  is shorter than that for  $\text{V}^{4+}\text{-O}$ <sup>38</sup>. Unlike the vanadium XPS deconvolution results, the Raman spectra suggest that the  $\text{V}^{4+}/\text{V}^{5+}$  ratio is distinct for the 25%Ag sample compared to the 10%Ag sample. Given the uncertainty associated with deconvoluting the XPS spectra, the  $\text{V}^{4+}/\text{V}^{5+}$  ratio calculated from the XPS results is likely lower for the 25% sample than the XPS peak-fitting results imply.

In the spectrum for the 50%Ag sample the prominent shoulder centered at  $840\text{ cm}^{-1}$  seen in the 25%Ag sample sharpens and can almost be resolved as a second band. This new band lies to low frequency of the original V-O-V stretch for EVS-10 by about  $20\text{ cm}^{-1}$ . The vanadium XPS results suggest that the sharpening of this band should be associated with an increase in the amount of  $\text{V}^{4+}$  for the 50%Ag sample. The red-shift in this new band suggests that the electronic environment of  $\text{V}^{4+}$  in the highly silver-exchanged sieves is different compared to the other samples and the differences can be tentatively assigned to the substitution of the majority of sodium for silver in the framework. The XPS and Raman data both suggest an increase in the amount of  $\text{V}^{4+}$  associated with the 50%Ag sample which indicates that the change in the vanadium oxidation state is reversible. Again, the higher-angle reflections in the XRD patterns for the highly silver exchanged samples (Figure 6.1) manifest an increase in  $d$ -spacing compared to as-synthesized EVS-10 but there are no substantive changes to the position of the lower angle reflections nor to the intensity of the first reflection. The framework of EVS-10 appears to be capable of accommodating changes in the oxidation state of the vanadium without suffering any measurable framework degradation.

The Raman spectroscopy results agree with the vanadium XPS results and confirm that the vanadium in the framework of Ag-EVS-10 changes oxidation state as the function of silver exchange. The observation that the change in oxidation state of the vanadium relates to the degree of silver exchange infers a stoichiometric relationship between the two. These observations, coupled with the spontaneity of the process, can be explained using a galvanic mechanism.

### 6.3.6 Silver-Vanadium Redox Chemistry

The standard half-cell potential for silver reduction is given by Eq. 6.1 and the standard half-cell potential for vanadium reduction is given in Eq. 6.2:



The half-cell potential of  $V^{5+}$  suggests that vanadium is the stronger oxidizer, however, the half-cell potential for vanadium reduction is greatly affected by pH. Figure 6.11 shows the theoretical vanadium speciation for water having an ionic strength of zero and shows that the half-cell potential for  $VO_2^+$  falls quickly away as the pH is increased. At a pH of about 4 which is typical of the starting pH of the silver nitrate solutions used in this study the half cell potential for  $V^{5+}$  reduction is less than 0.5 V. Under these conditions silver ions become the stronger oxidizer and the  $V^{4+}$  in the framework can be reduced.

The moles of silver dissolved in solution were calculated assuming the framework was composed entirely of  $V^{4+}$  octahedra. The XPS results, however, indicate that about a quarter of the vanadium in the framework is  $V^{5+}$  which only requires one cation equivalent to achieve neutrality. The amount of silver introduced into the exchange solution was therefore in excess of that needed to achieve the desired stoichiometry. For example, at a silver exchange ratio of 25% the framework is exposed to enough silver to exchange almost 60%, rather than 50%, of the framework vanadium.

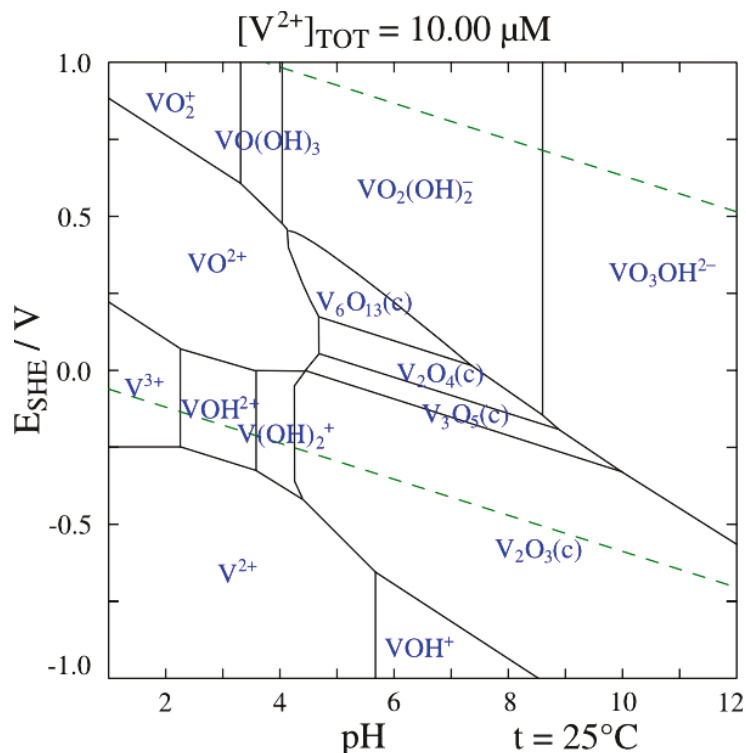


**Figure 6.11: Pourbaix diagram for vanadium speciation in water having an ionic strength of zero<sup>42</sup>**

The reduction of silver appears to dominate the ion exchange process at lower silver loadings because the silver XPS results in Figure 6.7 indicate the fraction of metallic silver to ionic silver is greater at 5 and 10% than it is at higher exchange levels. At 25 and 50% exchange about a quarter of the silver is retained as  $\text{Ag}^+$  (in the same state as for the 1%Ag sample) which suggests either that the  $\text{V}^{5+}$  in the framework has exchanged an alkali cation ion for  $\text{Ag}^+$  or that a newly formed  $\text{V}^{5+}$  has exchanged its remaining sodium ion in favour of a silver ion.

The presence (Figure 6.7) of roughly 10% of “zeolite”-bound silver in all of the samples except the 10%Ag sample is difficult to justify because its proportion does not seem to be affected by the exchange conditions. In order for a the silver to remain ionic it must either

be associated with an ion that cannot be oxidized, such as  $V^{5+}$ , or it must be in a framework location that is isolated from the vanadia chains. There is precedence for such a isolated cation site in the ETS-10 crystal lattice as Anderson et al.<sup>29</sup> has identified a fraction of sodium ions located within the silica pores and residing away from the titania chains. Anderson et al.<sup>29</sup> assigned this fifth type of site an occupancy of 0.5 which agrees reasonably well with the silver XPS results which suggest about a tenth of the silver could be located in this unique framework site. There is no precedence for any other ion occupying this position and it is not known whether this site can be successfully exchanged for other ions. The identification of this third type of silver could also simply be an artefact of the deconvolution which required a third peak to achieve the best fit to the experimental spectra using the fitting parameters specified.

The vanadium XPS and Raman results both indicate the amount of  $V^{4+}$  increases for the 50%Ag sample. This reversal was unexpected but can be rationalized using the same electrochemistry. As the concentration of silver increases in the exchanging solution there is a resultant drop in pH because the nitrate salt is a weak acid. The decrease in pH raises the half-cell potential for vanadium making  $V^{5+}$  a stronger oxidizer. At the same time a relatively small amount of free silver ion in solution and a relatively large amount of silver metal in the framework will decrease, through the Nernst relationship, the half-cell potential of the silver. The ion-exchange conditions for the 50%Ag sample appear to be such to allow the galvanic reaction to reverse and toggle the newly formed  $V^{5+}$  back to  $V^{4+}$  and the  $Ag^0$  back to  $Ag^+$ . The silver XPS results do not show the expected increase in the ratio of silver ion to silver metal to support this hypothesis but the silver XPS deconvolution is not definitive because the small difference (roughly 0.3 eV) in binding

energy for the Ag 3d<sub>3/2</sub> band between ionic and metallic silver makes it difficult to unambiguously assign the oxidation state of the silver.

Rather than a reduction of V<sup>5+</sup> to V<sup>4+</sup> the results for the 50%Ag sample might also be explained by a form of V<sup>5+</sup> which has a higher electron density surrounding the metal center. To explain the XPS and Raman results the V<sup>5+</sup> would need to gain electron density from its surrounding oxygen atoms or from silver nanoparticles situated close enough to the vanadium metal center to create an alloy. Vanadium, however, has the lowest electronegativity of the three species which makes it somewhat unlikely that the shift seen in the XPS and Raman spectra is the result of vanadium pulling electron density away from either of these two species.

## 6.4 Conclusions

The data collected establishes that a galvanic reaction occurs between silver and vanadium during the ion exchange of silver into EVS-10. The introduction of silver into the framework causes the V<sup>4+</sup> in the framework to be oxidized to V<sup>5+</sup> and results in the formation of silver metal nanoparticles which appear to remain adjacent to the vanadium metal centers. The powder XRD patterns demonstrate the framework of EVS-10 is completely stable toward the changes to the oxidation state of vanadium and the complete lack of reflections assigned to metallic silver support the TEM images that the reduced silver species do not aggregate and are too small to be detected by the diffractometer. The data for the 50%Ag sample suggests, but is not conclusive, that the redox reaction is reversible by means of changing the ion exchange conditions to bias the half-cell potentials of the two reactions.

## References:

- (1) Rocha, J.; Anderson, M. W. Microporous Titanosilicates and Other Novel Mixed Octahedral-Tetrahedral Framework Oxides. *Inorg. Chem.* 2000, 39, 801–818.
- (2) Kuznicki, S.; Madon, R. J.; Koermer, G. S.; Thrush, K. A. Large-Pored Molecular Sieves and Their Use as Catalysts and Ion Exchangers. 0405978B1, 1991.
- (3) Anderson, M. W.; Terasaki, O.; Ohsuna, T.; Philippou, A.; MacKay, S. P.; Ferreira, A.; Rocha, J.; Lidin, S. Structure of the Microporous Titanosilicate ETS-10. *Stud. Surf. Sci. Catal.* 1995, 98, 258–259.
- (4) Rocha, J.; Ferreira, A.; Lin, Z.; Anderson, M. W. Synthesis of Microporous Titanosilicate ETS-10 from  $TiCl_3$  and  $TiO_2$ : A Comprehensive Study. *Micropor. Mesopor. Mat.* 1998, 23, 253–263.
- (5) Rocha, J.; Lin, Z. Microporous Mixed Octahedral-Pentahedral-Tetrahedral Framework Silicates. *Rev. Miner. Geochem.* 2005, 57, 173–201.
- (6) Lamberti, C. Electron-Hole Reduced Effective Mass in Monoatomic ...-O-Ti-O-Ti-O-... Quantum Wires Embedded in the Siliceous Crystalline Matrix of ETS-10. *Micropor. Mesopor. Mat.* 1999, 30, 155–163.
- (7) Xiong, C.; Aliev, A. E.; Gnade, B.; Balkus, K. J. Fabrication of Silver Vanadium Oxide and  $V_2O_5$  Nanowires for Electrochromics. *ACS Nano* 2008, 2, 293–301.
- (8) Nash, M. J.; Rykov, S.; Lobo, R. F.; Doren, D. J.; Wachs, I. Photocatalytic Activity of Vanadium-Substituted ETS-10. *J. Phys. Chem. C* 2007, 111, 7029–7037.
- (9) Datta, S. J.; Yoon, K. B. Synthesis of Ideal AM-6 and Elucidation of  $V^{4+}$ -to-O Charge Transfer in Vanadate Quantum Wires. *Angew. Chem. Int. Ed.* 2010, 49, 1–6.
- (10) Quyang, M., Huang, J.-L., Lieber, C. M. Fundamental Electronic Properties and Applications of Single Walled Carbon Nanotubes. *Acc. Chem. Res.* 2002, 35, 1018–1025.
- (11) Golden, J. H.; DiSalvo, F. J.; Frechet, J. M. J.; Silcox, J.; Thomas, M.; Elman, J. Subnanometer-Diameter Wires Isolated in a Polymer Matrix by Fast Polymerization. *Sci. New Ser.* 1996, 273, 782–784.
- (12) Golden, J.H., Deng, H., DiSalvo, F.J., Fréchet, J.M.J., Thompson, P. . Monodisperse Metal Clusters 10 Angstroms in Diameter in a Polymeric Hoost: The “Monomer as Solvent” Approach. *Science (80-. )*. 1995, 268, 1463–1466.

- (13) Venkataraman, L.; Lieber, C. M. Molybdenum Selenide Molecular Wires as One-Dimensional Conductors. *Phys. Rev. Lett.* 1999, *83*, 5334–5337.
- (14) Krisnandi, Y. K.; Southon, P. D.; Adesina, A. A.; Howe, R. F. ETS-10 as a Photocatalyst. *Int.J.Photoenergy* 2003, *5*, 131–140.
- (15) Rocha, J.; Brandão, P.; Lin, Z.; Anderson, M. W.; Alfredsson, V.; Terasaki, O. The First Large-Pore Vanadosilicate Framework Containing Hexacoordinated Vanadium. *Angew. Chem. Int. Ed. Engl.* 1997, *36*, 100–102.
- (16) Ismail, M. N.; Fraiman, N. D.; Callahan, D. M.; Gursoy, G.; Viveiros, E.; Ozkanat, O.; Ji, Z.; Willey, R. J.; Warzywoda, J.; Sacco, A. First Unseeded Hydrothermal Synthesis of Microporous Vanadosilicate AM-6. *Microporous Mesoporous Mater.* 2009, *120*, 454–459.
- (17) Mani, F.; Wu, L.; Kuznicki, S. M. A Simplified Method to Synthesize Pure Vanadium, Silicate Analogue of ETS-10. *Micropor. Mesopor. Mat.* 2013, *177*, 91–96.
- (18) Mani, F.; Sawada, J. A.; Kuznicki, S. M. Comparative Adsorption Study of EVS-10 and ETS-10. *Micropor. Mesopor. Mat.* 2015, *204*, 43–49.
- (19) Galioglu, S.; Isler, M.; Demircioglu, Z.; Koc, M.; Vocanson, F.; Destouches, N.; Turan, R.; Akata, B. Photochromic Behavior of Silver Nanoparticle Incorporated Titanosilicate ETS-10 Films. *Microporous Mesoporous Mater.* 2014, *196*, 136–144.
- (20) Breck, D. W. *Zeolite Molecular Sieves: Structure, Chemistry, and Use*; John Wiley & Sons, Inc., 1974.
- (21) Antonio, F. M.; Neves, C. I. Study of Silver Species Stabilized in Different Microporous Zeolites. *Micropor. Mesopor. Mat.* 2013, *181*, 83–87.
- (22) Stathatos, E.; Lianos, P. Photocatalytically Deposited Silver Nanoparticles on Mesoporous TiO<sub>2</sub> Films. *Langmuir* 2000, *16*, 2398–2400.
- (23) Kuznicki, S. M.; Anson, A.; Koenig, A.; Kuznicki, T. M.; Haastrup, T.; Eyring, E. M.; Hunter, D. Xenon Adsorption on Modified ETS-10. *J. Phys. Chem. C* 2007, *111*, 1560–1562.
- (24) Anson, A.; Kuznicki, S. M.; Kuznicki, T.; Haastrup, T.; Wang, Y.; Lin, C. C. H.; Sawada, J. A.; Eyring, E. M.; Hunter, D. Adsorption of Argon, Oxygen, and Nitrogen on Silver Exchanged ETS-10 Molecular Sieve. *Micropor. Mesopor. Mat.* 2008, *109*, 577–580.

- (25) Naoi, K.; Sakamoto, T.; Matsuura, H.; Akatsuka, H. Experimental Study on the Effect of Different Noble Gas Admixtures on the Gas Temperature of Oxygen Plasma. *J. Adv. Oxid. Technol.* 2005, 8, 25–32.
- (26) Sebastian, J.; Jasra, R. V. Sorption of Nitrogen, Oxygen, and Argon in Silver-Exchanged Zeolites. *Ind. Eng. Chem. Res.* 2005, 44, 8014–8024.
- (27) Shi, M.; Kim, J.; Sawada, J. A.; Lam, J.; Sarabadan, S.; Kuznicki, T. M.; Kuznicki, S. M. Production of Argon Free Oxygen by Adsorptive Air Separation on Ag-ETS-10. *AIChE J.* 2013, 59, 982–987.
- (28) Anson, A.; Kuznicki, S. M.; Kuznicki, T.; Dunn, B. C.; Eyring, E. M.; Hunter, D. B. Separation of Argon and Oxygen by Adsorption on a Titanosilicate Molecular Sieve. *Separ. Sci. Technol.* 2009, 44, 1604–1620.
- (29) Anderson, M. W.; Agger, J. R.; Luigi, D.-P.; Baggaley, A. K.; Rocha, J. Cation Sites in ETS-10:  $^{23}\text{Na}$  3Q MAS NMR and Lattice Energy Minimisation Calculations. *Phys.Chem.Chem.Phys.* 1999, 1, 2287–2292.
- (30) Grillo, M. E.; Carrazza, J. Computational Modeling of the Nonframework Cation Location and Distribution in Microporous Titanosilicate ETS-10. *J. Phys. Chem.* 1996, 100, 12261–12264.
- (31) Tanchuk, B.; Sawada, J. A.; Rezaei, S.; Kuznicki, S. M. Adsorptive Drying of CO<sub>2</sub> Using Low Grade Heat and Humid, Ambient Air. *Sep. Purif. Technol.* 2013, 120, 354–361.
- (32) Morones, J. R.; Elechiguerra, J. L.; Camacho, A.; Holt, K.; Kouri, J. B.; Ramírez, J. T.; Yacaman, M. J. The Bactericidal Effect of Silver Nanoparticles. *Nanotechnology* 2005, 16, 2346.
- (33) Sondi, I.; Salopek-Sondi, B. Silver Nanoparticles as Antimicrobial Agent: A Case Study on E. Coli as a Model for Gram-Negative Bacteria. *J. Colloid Interface Sci.* 2004, 275, 177–182.
- (34) Sun, Y.; Xia, Y. Shape-Controlled Synthesis of Gold and Silver Nanoparticles. *Science* 2002, 298, 2176–2179.
- (35) Bois, L.; Chassagneux, F.; Battiez, Y.; Bessueille, F.; Mollet, L.; Parola, S.; Destouches, N.; Toulhoat, N.; Moncoffre, N. Chemical Growth and Photochromism of Silver Nanoparticles into a Mesoporous Titania Template. *Langmuir* 2010, 26, 1199–1206.
- (36) <http://srdata.nist.gov/xps/NIST>.

- (37) Ismail, M. N.; Fraiman, N. D.; Jr., D. M. C.; Gursoy, G.; Viveiros, E.; Ozkanat, O.; Ji, Z.; Willey, R. J.; Warzywoda, J.; Jr., A. S.; et al. First Unseeded Hydrothermal Synthesis of Microporous Vanadosilicate AM-6. *Micropor. Mesopor. Mat.* 2009, *120*, 454–459.
- (38) Hardcastle, F. D.; Wachs, I. E. Determination of Vanadium-Oxygen Bond Distances and Bond Orders by Raman Spectroscopy. *J. Phys. Chem.* 1991, *95*, 5031–5041.
- (39) Went, G. T.; Oyama, S. T.; Bell, A. T. Laser Raman Spectroscopy of Supported Vanadium Oxide Catalysts. *J. Phys. Chem.* 1990, *94*, 4240–4246.
- (40) Jones, W. J. High-Resolution Raman Spectroscopy of Gases and the Determination of Molecular Bond Lengths. *Can. J. Phys.* 2000, *78*, 327–390.
- (41) Chan, S. S.; Wachs, I. E.; Murrell, L. L.; Wang, L.; Hall, W. K. In Situ Laser Raman Spectroscopy of Supported Metal Oxides. *J. Phys. Chem.* 1984, *88*, 5831–5835.
- (42) Al-Kharafi, F. M.; Badawy, W. A. Electrochemical Behaviour of Vanadium in Aqueous Solutions of Different pH. *Electrochim. Acta* 1997, *42*, 579–586.

# Chapter 7

## Separation Studies of Ethane/Methane Binary Mixture by Adsorption on EVS-10

### 7.1 Introduction

Natural gas is a hydrocarbon gas mixtures consisting primarily of methane, but it also contains various amount of other hydrocarbons such as ethane, propane that takes up few volume percentage. It also contains butane and propane which takes up to less than one volume percent<sup>1</sup>. Ethane is the second largest component of natural gas; it ranges from 3 to 8 % by volume<sup>1</sup> and is separated from the natural gas because it is the main feedstock source to produce ethylene which is one of the largest petrochemical products used in plastic, rubber and film industry<sup>2,3</sup>. Ethane goes under steam cracking and thermal decomposition to produce ethylene with over 90 million tonnes produced annually, worldwide. Prior to use natural gas as a fuel, it must go under certain process in order to remove the higher value hydrocarbons such as ethane to fulfill the specification of marketable natural gas..

Natural gas purification is traditionally done by cryogenic distillation or absorptive separation<sup>4</sup>. The former involves high pressure conditions and

cryogenic temperatures below 123K and the latter involves contacting natural gas with lean absorption oil. Adsorption methods may offer a benefit over expensive and energy-intensive separation processes such as cryogenic distillation, and absorption. The cost-efficient and energy-efficient characteristics of separation by adsorption on molecular sieves are due to the versatility of molecular sieves<sup>2,5,6</sup>.

Many studies have been conducted on adsorption of methane and ethane by conventional zeolites such as H-mordenite, 13X, CaX<sup>7-10</sup>. Different types of Zeolite A such as 4A, 5A and LiA have been investigated for ethane adsorption by Loughlin et al.<sup>11</sup>. Based on the literature, zeolite 4A has been preferably used more for methane, ethane adsorption<sup>10-12</sup> due to its less costly synthesis compared to 5A and LiA.

ETS-10 has shown particularly strong selectivity toward small olefins<sup>2,3,13-16</sup> which is the reason we have chosen to look into the adsorption properties of vanadium substituted ETS-10 towards small olefins such as ethane and methane.

## **7.2 Experimental**

### **7.2.1 Sample Preparation**

EVS-10—vanadium silicate analogue of ETS-10—were synthesized by hydrothermal synthesis using vanadyl sulfate as vanadium source<sup>17</sup>. The gel was obtained in two steps. In the first step 32 g of sodium silicate solution (28.8wt% SiO<sub>2</sub>, 9.14wt% Na<sub>2</sub>O, Fisher Scientific) was mixed with 12 g distilled water and stirred to homogenize the gel. 0.5 g sodium hydroxide (99wt%, Fisher Scientific), 2.0 g potassium chloride (99wt%, Fisher Scientific), 1 g sodium fluoride (99wt%,

Fisher Scientific), and 4.1 g sodium chloride (99wt%, Fisher Scientific) were added to the mixture. In the second step, a solution containing 3.06g vanadyl (IV) sulfate hydrate obtained from Acros. Organics and 12 g distilled water were mixed and stirred together for 2 hours to homogenize and obtain a dark green gel. The initial pH of the mixture was between 10.2-10.4 as measured using a Fisher scientific pH meter model 720A (accuracy 0.02 pH units). Following this step, the gel was left to age under static condition at room temperature for 3 days. Syntheses were carried out in 700 ml Teflon-lined stainless steel autoclaves under autogenous pressure at 230 °C for 7 days. Then the autoclave was removed from the oven and quenched at room temperature with cold water and the product with the purple color was washed with distilled water several times and dried at 80 °C overnight. Characterization

### **7.2.2 Low Pressure Isotherms**

A static volumetric adsorption instrument was used to generate high resolution, low-pressure equilibrium adsorption data. Ethane and methane adsorption isotherms for EVS were obtained at 303, 323, 343 K and pressures up to 100 kPa on a Micromeritics ASAP 2020C. This instrument is equipped with low-pressure range transducers that permit measurements of the equilibrium data with high resolution at the Henry's law region. The samples were run on the instrument configured in its chemisorption configuration and 200 mg samples were loaded into quartz U-tubes. Samples were activated under a N<sub>2</sub> flow of approximately 200 mL/min by heating the sample at 10 °C/min up to 523K. The sample was held isothermally and under flow for 15 min before the N<sub>2</sub> flow was shut off and

the sample subjected to vacuum. The sample was evacuated at a pressure of  $<0.5$  Pa for 60 min and cooled to the analysis temperature under vacuum. Once the temperature in the furnace was stable at the analysis temperature the isotherm data collection was started.

### **7.2.3 Inverse Gas Chromatography**

Inverse gas chromatography (IGC) analysis was performed on a Varian 3800 gas chromatograph instrument which is equipped with a thermal conductivity detector (TCD). Test adsorbents were packed in to 10 inch length copper columns with a 1/4 inch OD. The columns were filled with approximately 3.5 g pelletized adsorbent (20–50mesh) and were activated at 250 °C for 3 hrs under a helium flow of 30 ml/min. Pure methane, pure ethane and a binary mixture of 80% methane and 20% ethane was introduced into the column by 1mL pulse injections.

### **7.2.4 Bench-scale multicomponent Adsorption**

Bench-scale demonstration is illustrated in Figure 7.1 and Figure 7.2. Breakthrough experiments were conducted on a fixed bed filled with 30 g pelletized, granular (20-50mesh) tested adsorbent. The bed was a cylindrical stainless steel chamber with a volume of about 45 cc, the inner diameter of 1.6cm and a length of 23cm. After filling up the bed with the tested adsorbent, it was activated at 523 K for 2 hours under 30 ml/min of helium flow. The feed composition was a binary mixture of 80% methane and 20% ethane. The gas mixture was prepared and certified by Praxair. The analysis of methane and

ethane breakthrough profiles was conducted using a mass spectrometer (MS). The MS plots were collected using a Pfeiffer Omnistar QMA 200 residual gas analyzer configured with a stainless steel capillary heated to 200 °C and connected to the outlet of the bed by means of a stainless steel adapter and a ¼” branch T-fitting. The capillary was positioned at the center of the tee to sample the evolved gases. Experiments were run in MID mode with fragments at  $m/z = 15, 16, 18, 28, 30, 32$ . These fragments were selected to differentiate between methane and ethane, and to identify any potential influence from the components in air ( $N_2, O_2, \text{water}$ ). A septum was positioned in the tee in the outlet line before enters to MS in order to take sample to quantify the gas composition by injecting into the gas chromatography. Before introducing the feed to the bed, the rotameter was calibrated by a Coriolis mass flow meter in order to send the feed at 170 ml/min. Prior to exposing the adsorbent to the feed, the entire system has been swept with helium in order to minimize the amount of air in the dead volume of the system and to desorb the small amount of air that might be adsorbed by the adsorbent after reconnecting the activated bed to the system. After the signal for oxygen, nitrogen, water and methane and ethane were down to undetectable levels, the feed was sent to bed to begin the adsorption step. The feed mixture was introduced into the fixed-bed column at a flow rate of 170 mL/min at room temperature and atmospheric pressure. A continuous flow of gas was run through the bed until the concentration of the outlet gas was equal to the inlet gas at which point the bed was saturated. The outlet gas composition was analyzed quantitatively by injecting 1 ml of the gas into the Varian 3800 gas

chromatograph (GC) equipped with a thermal conductivity detector and a HayeSep D column. Desorption step was performed by injecting water into the column and the desorbed gas composition was analyzed by gas chromatography equipped with HayeSep D column.

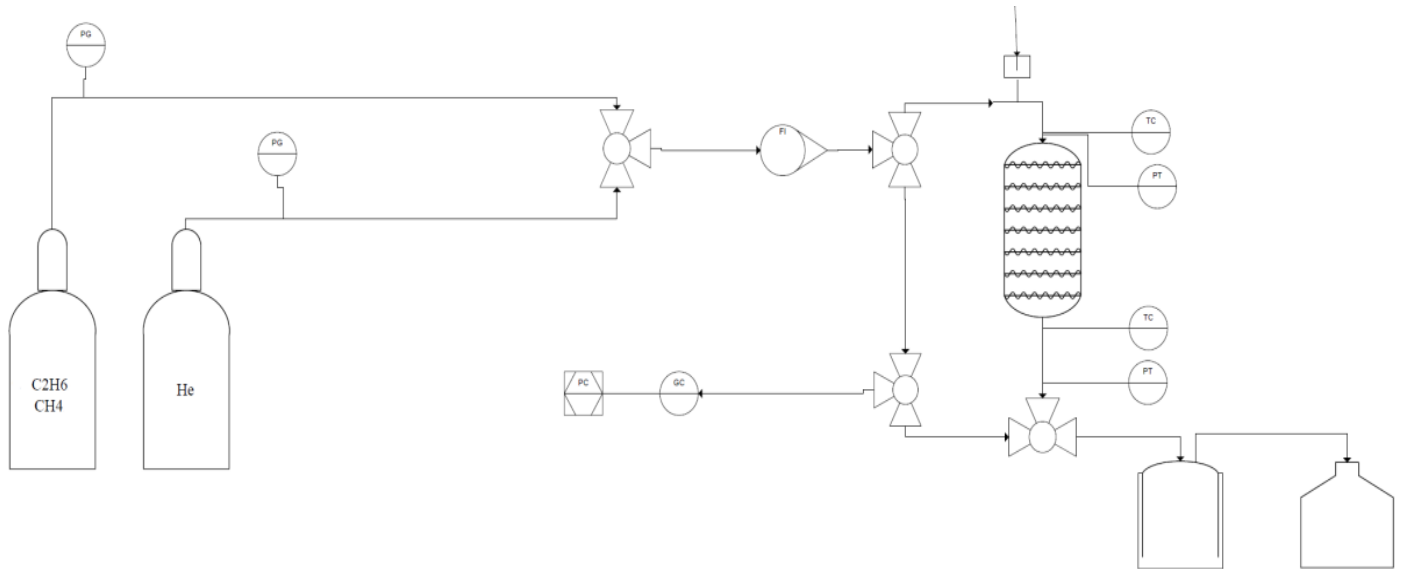


**Figure 7.1: Multicomponent Adsorption/Desorption Schematic**



**Figure 7.2: Multicomponent Adsorption/Desorption test stand. Left picture shows front of the set-up and right one displays the rear of the set-up.**

#### 7.2.4.1 Mass flow meter calibration

We have used a rotameter in the set up. In order to calibrate the rotameter, it has been connected it to a Coriolis mass flow meter. By calibrating the rotameter we determine the equivalent set point to 170 ml/min feed gas flow at experimental condition. In order to calibrate the rotameter we have connected Coriolis flow meter to the bed inlet just before the rotameter. We set the rotameter at different numbers then read the Coriolis reading. The Coriolis reading is in terms of percentage flow. Based on the manufacture chart, at full capacity (100%) the reading flow with Coriolis is equivalent to 200 gr/hr. After converting the Coriolis readings to standard cubic centimeter per minute (SCCM), we should calculate the flow at the experiment condition. The standard condition is defined as 100 kPa and zero degree centigrade. Our experiment condition is 100 kPa and 298 K. Table 7.1 summarizes these reading values. It is noted that the molecular weight of the feed gas composed of 80% methane and 20% ethane is equal to 18.8 g/mol.

**Table 7.1: Summarizing values for rotameter calibration with Coriolis mass flow meter.**

Rotameter set point	Coriolis Reading (% value)	gr/hr	mol/hr	SCCM	ml/min
140	10.82	21.64	1.148	428.7	467.94
110	8.25	16.5	0.875	326.2	356.79
80	6.15	12.3	0.652	243.6	265.97
50	3.57	7.14	0.378	141.4	154.39
30	2.18	4.36	0.231	86.37	94.27
10	1.05	2.1	0.111	41.6	45.41

Figure 7.3 shows the calibration curve for the rotameter based on the Coriolis reading. From this plot it is determined that in order to have a flow of 170 ml/min, the rotameter should be set at 52.

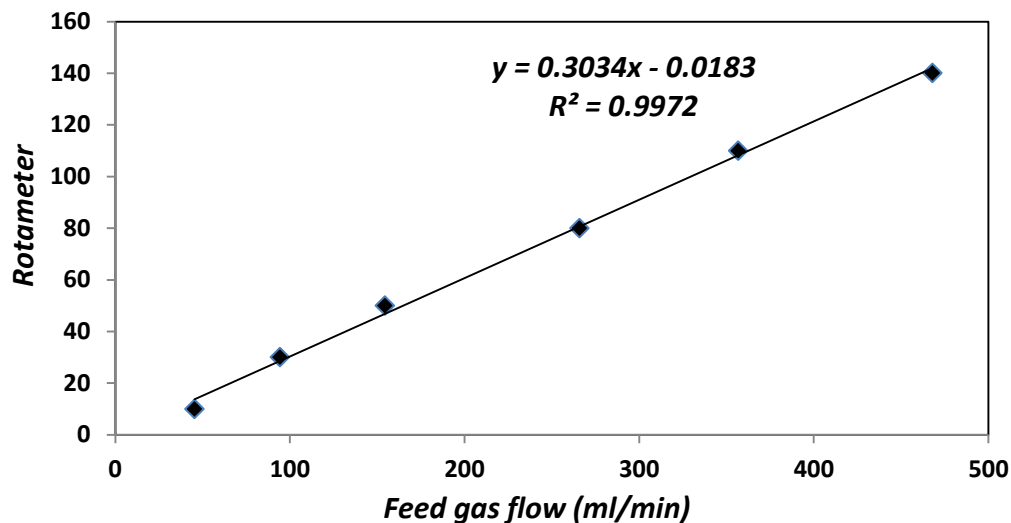


Figure 7.3: Calibration curve for rotameter.

#### 7.2.4.2 Dead volume measurement

In order to calculate the capacity of the adsorbent, i.e. the number of moles of the adsorbed gas, we need to discount for the moles of the gas that are held in the dead space of the system. There are two sources of dead volume in the system: piping in the system and void inside the adsorbent. The latter is a combination of interparticle void, intraparticle void and intracrystalline void. The intercrystalline water inside the adsorbent can be measured by the difference between the dead volume before and after activating the adsorbent. The gas expansion pycnometer technique was used in order to measure the dead volume. A gas pycnometer is an instrument with a known volume that is used for measuring the volume of solids whether the solids are porous or non-porous, powdered or granular by a method of gas expansion. The underlying logic is based on the Boyle's law which describes how the pressure of a gas tends to

reduce as the volume of a gas increases. Boyle's law states that for a closed system when the temperature and amount of gas stays unchanged then the absolute pressure introduced to a given mass of an ideal gas is proportional to inverse of the volume it occupies ( $P \propto \frac{1}{V}$ ). For two gases the law can be expressed as  $P_1V_1 = P_2V_2$ .

The gas pycnometer consisted of two chambers. One with a removable gas-tight lid to hold the sample and a second chamber of fixed internal volume. The device consists of a pressure gauge—connected to the first chamber—and a valve to connect to a gas under pressure. The two chambers are connected through a valved pathway. The system has a vent to release the pressure. The standard volume of the manifold denoted as  $V_1$ —the first chamber—is 56.54 cc. the pycnometer is connected to a helium cylinder and attached to the test stand by a valve. While the valve to the second chamber is closed, A pulse of helium ( $P_1$ ) was introduced to the first chamber. Next the valve is opened and the gas filled up the entire system ( $V_2$ ) and the pressures is recorded as  $P_2$ . Then the pressure was released (Figure 7.4). The volume of the entire system  $V_2$  can be calculated through Boyle's law. The difference between  $V_2$  and  $V_1$  is the dead volume of the system. This experiment was repeated number of times for different pressures. The standard deviation of the analysis was about 0.37 indicated that the data points tend to be very close to the expected value. The same experiment was repeated before and after bed activation in order to calculate the intracrystalline volume. This is due to the fact that sieves lose water during activation so the volume occupied with intracrystalline water before activation will contribute to

the system dead volume. In our system the intercrystalline water added about 7% to the total dead volume of the system. The dead volume from the piping, the fittings and the void between the adsorbent grains which is 5.57 cc is calculated from the difference between the total dead volume of the system after activation (50.57cc) and the total volume of the bed (45cc). As a result the total percentage of the bed dead volume is about 12%.

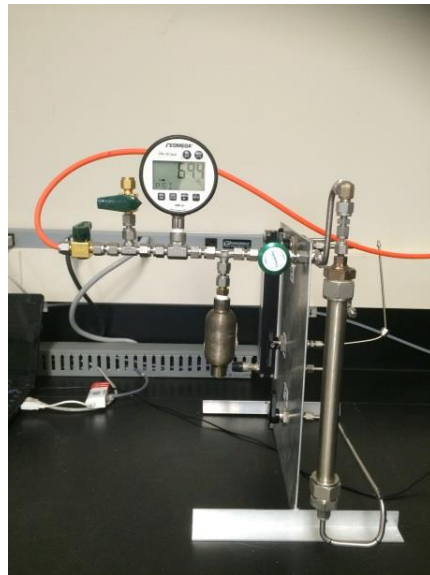


**Figure 7.4: Gas Pycnometer**

## **7.3 Theoretical Background**

### **7.3.1 Pure gas isotherms**

Pure methane and ethane isotherms were fitted to both Langmuir Dual site isotherm (equ. 7.1) and Langmuir (equ. 7.2).

$$q = \frac{m_1 bP}{1 + bP} + \frac{m_2 dP}{1 + dP} \quad (7.1)$$

where  $q$  is the amount adsorbed on the solid, the pressure in the gas phase denoted as  $P$ ,  $m_1$  and  $m_2$  are the saturation capacities<sup>4</sup> on two different set of sites.  $b$  and  $d$  are the affinity parameters on the first and second set of sites, respectively. It is assumed that  $b$  is conventionally larger than  $d$  since the sites with stronger affinity with the gas molecule get occupied before the weaker site.

$$q = \frac{q_s b P}{1 + b P} \quad (7.2)$$

where  $q_s$  represents the saturation concentration and  $b$  denotes the adsorption equilibrium constant,  $P$  corresponds to the partial pressure in the gas phase and  $q$  stands for the amount of gas adsorbed on the surface of the adsorbent.

### 7.3.2 Mixed-gas Adsorption Model

An important method for the estimation of mixed-gas adsorption is IAST or ideal adsorbed solution theory in which the adsorbed phase is assumed to be ideal. IAST predictions are made by solving the equations (1-3). The IAST theory equation is similar to Raoult's law for vapor-liquid equilibrium:

$$P y_i = P_i^0(\pi) x_i \rightarrow P_i = P_i^0(\pi) x_i \quad (7.3)$$

where  $P$  is total pressure of the system and  $y_i$  is the mole fraction of species  $i$  in the gas phase, saturated partial vapor pressure of component  $i$  in its pure state at the same temperature and spreading pressure of the adsorbed phase is denoted as  $P_i^0(\pi)$  and the mole fraction of species  $i$  in the adsorbed phase is represented by  $x_i$ .

---

<sup>4</sup> The number of moles of gas adsorbed per unit mass of adsorbent at infinite pressure.

$x_i$  is calculated from equation below:

$$\sum_i x_i = \sum_i Py_i / P_i^0 = 1 \quad (7.4)$$

The above equation shows the relation between gas phase and the adsorbed phase in equilibrium. The spreading pressure of each component is equal to the spreading pressure of the mixture. The spreading pressure is defined by Gibbs adsorption isotherm as follows<sup>18</sup>:

$$\frac{\pi A}{RT} = \int_0^{P_i^0} \frac{q_i^0(p)}{p} dP = \int_0^{P_j^0} \frac{q_j^0(p)}{p} dP \quad (7.5)$$

$i$  and  $j$  refers to two components in the mixture.

Binary mixture of ethane-methane isotherms were determined from the pure gas isotherms using dual site Langmuir adsorption<sup>19</sup>. In the case of the Langmuir dual site the IAST equations (Eq.1 to 3) are solved for each of the two sites. Dual site is an effective model since it provides a flexible mathematical form to correlate the pure-gas isotherms, and since an analytical solution for the integral of equation 5 is easily available. Then the spreading pressure of the dual site Langmuir model in equation 5 is defined as<sup>19</sup>:

$$\frac{\pi A}{RT} = m^1 \ln(1 + bP) + m^2 \ln(1 + dP) \quad (7.6)$$

The IAST equations can be solved for each of the two sites. Then the IAST will reduce to the remarkably simple form<sup>19</sup>:

$$n_i = \frac{m_1 b_i P y_i}{1 + \sum_j b_j P y_j} + \frac{m_2 d_i P y_i}{1 + \sum_j d_j P y_j} \quad (7.7)$$

where  $m_1$  and  $m_2$  are the saturation capacities on the two sites and  $b_i$  and  $d_i$  are the affinity parameters for gas  $i$  on the two sites, and  $y_i$  is the vapor phase mole fraction of gas  $i$ . We assume Arrhenius temperature dependencies for the affinity parameters<sup>19</sup>:

$$b_i = b_i^0 e^{\frac{Q_i^b}{R(\frac{1}{T} - \frac{1}{T^0})}} \quad (7.8)$$

$$d_i = d_i^0 e^{\frac{Q_i^d}{R(\frac{1}{T} - \frac{1}{T^0})}} \quad (7.9)$$

Where  $b_i^0$  and  $d_i^0$  define the two affinity parameters of gas I at the reference temperature of  $T^0$  and  $Q_i^{(b)}$  and  $Q_i^{(d)}$  are the heats of adsorption of gas I on the two sites.

### 7.3.3 Henry's constant, Limiting Selectivity and Isothermic Heats of Adsorption

Henry's law constant ( $K$ ) is calculated from ratio of  $q$  over  $P$  when  $P$  approaches zero.

For Langmuir dual site it is calculated as:

$$K = \lim_{p \rightarrow 0} \frac{q}{p} = m_1 b + m_2 d \quad (7.10)$$

For Langmuir isotherm model, it is estimated as:

$$K = \lim_{p \rightarrow 0} \frac{q}{p} = q_s b \quad (7.11)$$

The limiting selectivity of ethane/methane was estimated from the ratio of their respective Henry's law constants:

$$\alpha = \frac{K_{C_2H_6}}{K_{CH_4}} \quad (7.12)$$

The equilibrium selectivity (bed selectivity) was calculated from the ratio of the component in the gas phase and in the adsorbed phase.

$$\alpha_j^i = \frac{x_i/y_i}{x_j/y_j} \quad (7.13)$$

where  $x_i$  and  $y_i$  are the equilibrium mole fractions in the adsorbed phase and gas phase of component  $i$ , respectively.

In order to determine the isosteric heat of adsorption at different loadings a Matlab code was developed to simplify the calculations. The isosteric heat of adsorption for a single gas is calculated by determining the pressure necessary, at each temperature, to achieve the same loading on the solid. Ideally, the isotherm expression can be inverted and expressed as pressure versus loading. Unfortunately, the Langmuir dual site equation cannot be inverted. To overcome this limitation, a solver function was developed in Matlab where the resulting pressure for a specified input loading could be solved. By carrying out this calculation for the isotherms at each temperature the resulting isosteric pressures could be applied to the Van't Hoff equation and the isosteric heat of adsorption can be calculated at any specified loading from

$$Q_{st,i} = -\Delta H = -R \left[ \frac{\partial \ln k}{\partial (1/T)} \right]_q \quad (7.14)$$

In this study the working capacity of a given adsorbent is defined as the adsorption capacity between pressures of 1-100 kPa.

## 7.4 Results and Discussion

### 7.4.1 Single component adsorption

Methane and ethane single component isotherms at 303, 323 and 343 K are shown in Figure 7.5 and Figure 7.6. The solid line is from fitting the experimental isotherm to dual site Langmuir and Langmuir isotherm in Figure 7.5 and Figure 7.6, respectively. As it is shown in the Figure 7.5b and Figure 7.6b, the ethane isotherm is rectangular, which is the result of the strong bonding between ethane and the surface of EVS-10. Therefore Langmuir isotherm could not provide an accurate fit for the entire range of ethane loadings on EVS-10 whereas Langmuir dual site model as shown in Figure 7.5b fits precisely to the experimental data. While due to the weaker interaction between methane and the surface of EVS-10, methane shows a linear isotherm. As a result of the linearity of methane isotherm in the entire range of loading, it fits to both Langmuir and dual site Langmuir model as shown in Figure 7.5a and Figure 7.6a. The experimental data have been fitted to the models through minimizing the summation of the squared difference therefore determining the model constraints. Table 7.2, Table 7.3, and Table 7.4 summarizes the fitting parameters of both models.

**Table 7.2: Fitting Parameters of ethane, methane after fitting the isotherm to Dual Site Langmuir model and Langmuir model at 298K.**

298K	Dual Site Langmuir				$r^2$
	$m_1$ (mol.kg <sup>-1</sup> )	$m_2$ (mol.kg <sup>-1</sup> )	$b$ kPa <sup>-1</sup>	$d$ kPa <sup>-1</sup>	
CH <sub>4</sub>	1.082	0.944	0.010	0.016	1.0
C <sub>2</sub> H <sub>6</sub>	1.630	4.00e-01	9.580e-01	2.140e-02	1.0
	Langmuir		b		$r^2$
	q <sub>s</sub>				
CH <sub>4</sub>	1.994		1.267e-02		0.9832
C <sub>2</sub> H <sub>6</sub>	1.864		7.198e-01		0.973

**Table 7.3: Fitting Parameters of ethane, methane after fitting the isotherm to Dual Site Langmuir model and Langmuir model at 323K.**

323K	Dual Site Langmuir				$r^2$
	$m_1$ (mol.kg <sup>-1</sup> )	$m_2$ (mol.kg <sup>-1</sup> )	$b$ kPa <sup>-1</sup>	$d$ kPa <sup>-1</sup>	
CH <sub>4</sub>	1.645	5.69e-01	4.76e-03	1.01e-02	1.0
C <sub>2</sub> H <sub>6</sub>	1.53	3.81e-01	3.37e-01	1.87e-02	1.0
	Langmuir		b		$r^2$
	q <sub>s</sub>				
CH <sub>4</sub>	2.087		6.420e-03		0.987
C <sub>2</sub> H <sub>6</sub>	1.78		2.513e-01		0.981

**Table 7.4: Fitting Parameters of ethane, methane after fitting the isotherm to Dual Site Langmuir model and Langmuir model at 343K.**

343K	Dual Site Langmuir				$r^2$
	$m_1$ (mol.kg <sup>-1</sup> )	$m_2$ (mol.kg <sup>-1</sup> )	$b$ kPa <sup>-1</sup>	$d$ kPa <sup>-1</sup>	
CH <sub>4</sub>	1.060	9.0e-01	5.630e-03	2.750e-03	1.0
C <sub>2</sub> H <sub>6</sub>	1.490	3.260e-01	1.680e-01	1.320e-02	1.0
	Langmuir		b		$r^2$
	q <sub>s</sub>				
CH <sub>4</sub>	1.831		4.587e-03		0.984
C <sub>2</sub> H <sub>6</sub>	1.693		1.349e-01		0.985

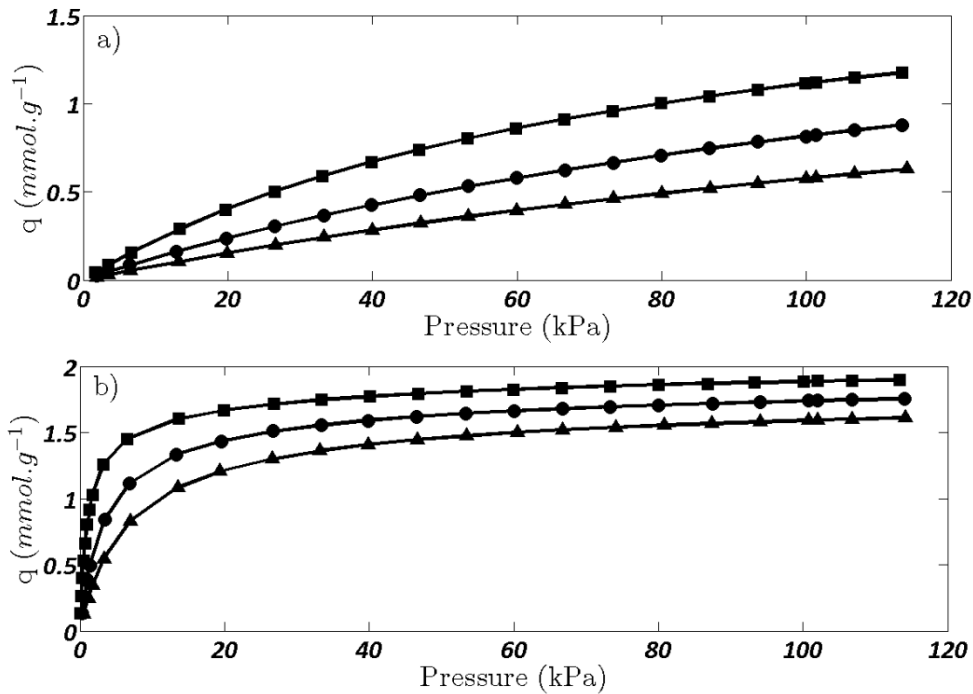


Figure 7.5: a) methane and b) ethane low pressure isotherms on EVS-10. ‘■’, ‘●’ and ‘▲’ represent experimental data at 298, 323, 343 K, respectively. Solid line is from the dual site adsorption model.

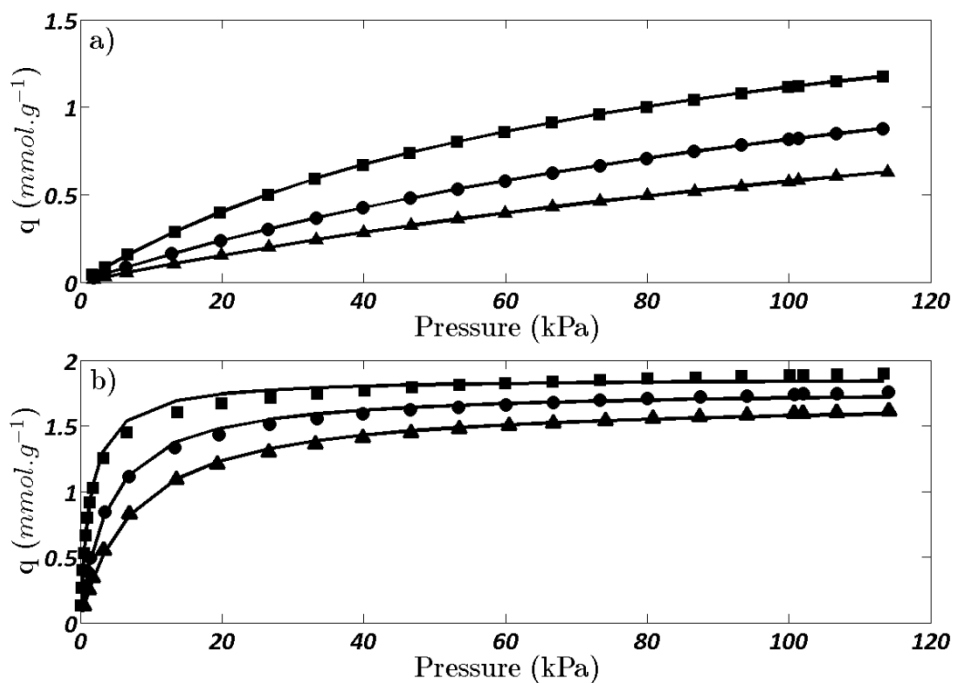


Figure 7.6: a) methane and b) ethane low pressure isotherms on EVS-10. ‘■’, ‘●’ and ‘▲’ represent experimental data at 303, 323, 343 K, respectively. Solid line is from the Langmuir adsorption model.

## 7.4.2 Heat of Adsorption

The heat of adsorption at low loading (so called as limiting heat of adsorption) for both ethane and methane were calculated from the Henry's constant. The Henry constant is the slope of the isotherm at low pressure and can be determined directly from the Langmuir dual site equation using Equ. 7.6. Due to the more accurate fit with dual site Langmuir model, the rest of the calculation is preceded by this model. The entire pressure range could be used for both methane and ethane isotherm on EVS-10 in order to accurately estimate the Henry's constant. Next, the limiting heat of adsorption at low loading can be estimated using Van't Hoff equation (eq. 7.10). Following that we can estimate limiting selectivity from eq 7.8. Table 7.5 summarizes limiting heat of adsorption and selectivity on EVS-10 using Dual site Langmuir adsorption.

**Table 7.5: Adsorption Parameters for methane and ethane on EVS-10 at 298K fit to Dual site Langmuir adsorption model.**

Adsorbate	Henry's Constant (kPa <sup>-1</sup> )	-ΔH (kJ.mol <sup>-1</sup> )	Limiting Selectivity α (C <sub>2</sub> H <sub>6</sub> /CH <sub>4</sub> )
CH <sub>4</sub>	2.547e-02	34.60	N/A
C <sub>2</sub> H <sub>6</sub>	1.570	22.31	53

The values of Henry's constants can be plotted as a function of 1/T as shown in Figure 7.7 to calculate the adsorption heats at low loading.

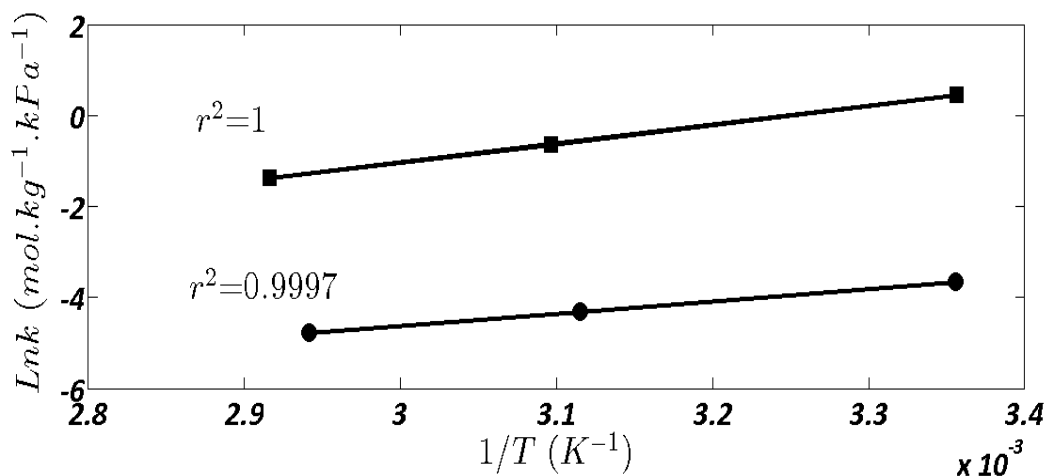


**Figure 7.7: Van't Hoff plot of Henry constants values fit to Langmuir dual site at 298, 323, 343 K: '■' and '●' represents methane and ethane on EVS-10, respectively.**

The variation of heat of adsorption with loading provides information regarding the energetic homogeneity of the surface of the adsorbent. As mentioned earlier in chapter 4, A Matlab code was developed to solve for the pressure required to achieve a specified loading at each experimental temperature using the Langmuir Dual site equation fit to the experimental data. The code allowed for accurate interpolation so the isosteric heats could be calculated with high resolution. The isosteric heat for each specified loading was calculated by applying the Van't Hoff equation to the pressure-temperature data. The quality of the data and the fits generated a linear trend in the Van't Hoff plots with  $r^2$  values above 0.99 for all the specified loading. The isosteric heat of adsorption for methane and ethane is shown in Figure 7.8. As mentioned in chapter 4, due to the structure of EVS-10, the vanadium analogue of ETS-10, it shows more heterogeneity toward the more polarizable gas—here ethane more than methane. The upward trend in ethane suggests that the intermolecular interactions between the adsorbed molecules of

ethane have more significant effect on the adsorption enthalpy than the interaction between ethane and EVS-10 surface. As it is shown in Figure 7.8, the methane isosteric heats is constant as a function of loading; this means the surface of EVS-10 appears to be energetically more homogenous with regards to methane due to less polarizability of methane compared to ethane.

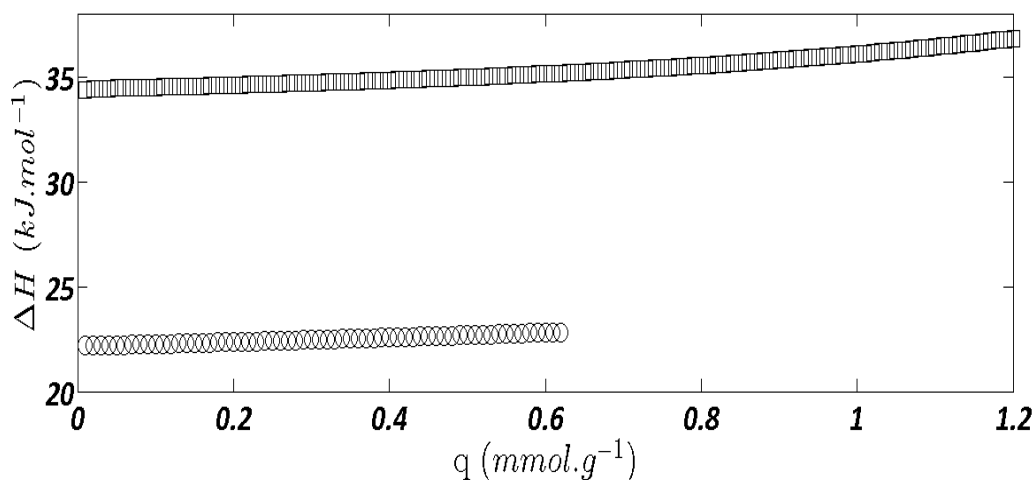


**Figure 7.8: Variation of isosteric heat of adsorption at different adsorbate loading on EVS-10. The experimental isotherm data were fitted to Dual site Langmuir adsorption. Symbol '□' represents Ethane and, '○' represents methane.**

### 7.4.3 Equilibrium Binary Selectivity

The equilibrium selectivities for C<sub>2</sub>H<sub>6</sub>/CH<sub>4</sub> (80/20) mixtures adsorbed on EVS-10 is estimated according to the IAST calculation and using the dual site adsorption model to represent the pure gas isotherms. The equilibrium selectivity at zero pressure must approach the Henry's selectivity at room temperature. As it is shown in Figure 7.9 the binary selectivity agrees with Henry's selectivity which is

53 at room temperature and zero pressure on EVS-10. IAST predicts a drop in selectivity with increasing pressure.

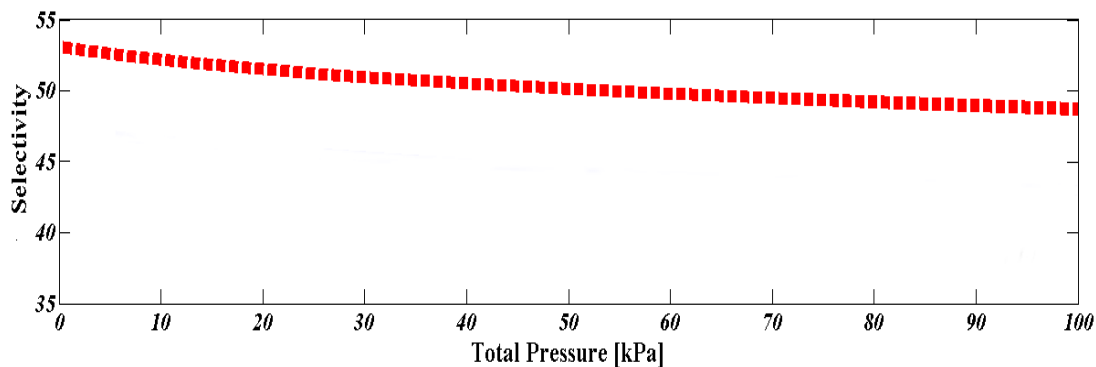


**Figure 7.9: C<sub>2</sub>H<sub>6</sub>/CH<sub>4</sub> (80/20) equilibrium selectivity (binary selectivity) at ambient temperature and pressure predicted by IAST using dual site Langmuir for pure-gas isotherm.**

The drop in selectivity with pressure depends on the relative amount of the two sets of sites. If the first set of sites are highly selective compared to the second set of sites, increased pressure will not affect selectivity<sup>19</sup>. On the other hand, if there are a significant number of the less selective sites (as in the present case), selectivity will drop sharply with increased pressure.

#### 7.4.4 Inverse Gas Chromatography

Inverse gas chromatography experiments were used to determine the relative affinity of EVS-10 toward ethane and methane. A typical set of IGC elution profile shows signal intensity versus time. The signal intensity corresponds to the relative concentration of the gas eluted from the column and time corresponds to the retention time it takes for the component to elute from the column. The gas with shorter retention time elutes earlier because it has a weaker interaction with

the adsorbents and the adsorbate with longer retention time which elutes later has stronger interaction with the adsorbents. As it is shown in Figure 7.10 methane comes earlier than ethane which indicates weaker interaction compared to ethane with the surface of adsorbent. Figure 7.10 and Figure 7.11 shows inverse gas chromatography (IGC) analysis of the separation of Pure stream of CH<sub>4</sub> and C<sub>2</sub>H<sub>6</sub> and a mixture of 80:20 (CH<sub>4</sub>:C<sub>2</sub>H<sub>6</sub>) on EVS-10 at 150°C, respectively.

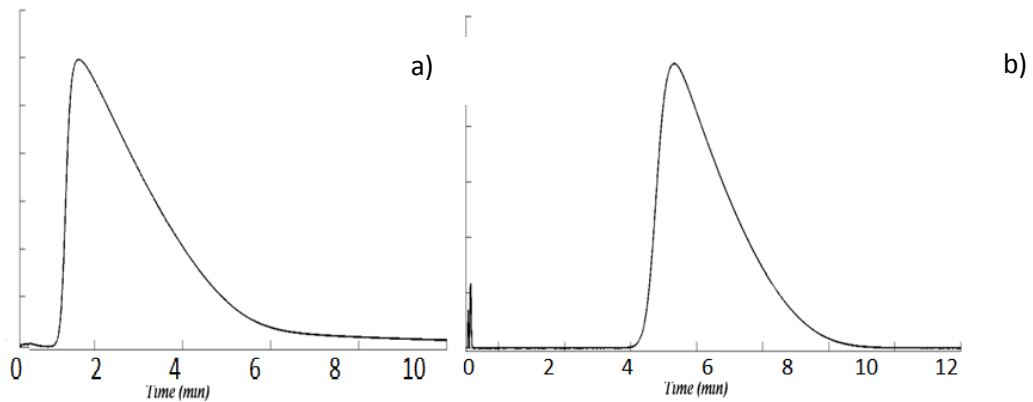


**Figure 7.10: Inverse Gas Chromatography from Pure stream of a) methane and b) ethane at 150°C on EVS-10**

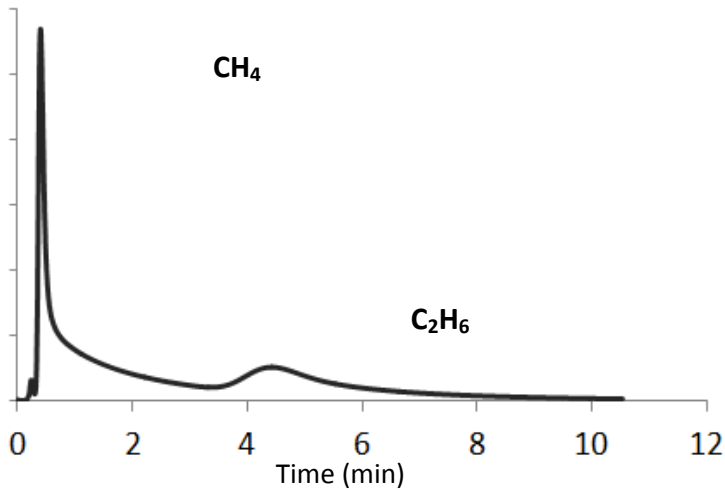


**Figure 7.11: Inverse Gas Chromatography of a feed with composition of 80% methane and 20% ethane on EVS-10.**

#### 7.4.5 Bench Scale Multicomponent Adsorption

The signal at  $m/z = 32$  was found not to change over the course of the experiment which established the absence of  $O_2$  in the system and confirmed the system was adequately leak-tight. The signals at  $m/z = 28$  and  $30$  were compared and the trends in the signals found to be identical. This comparison confirms the absence of  $N_2$  in the system because otherwise the signal at  $m/z = 28$  would be different compared to the signal at  $m/z = 30$ . The tightness of the seals on the system is further confirmed by the trend in the signal at  $m/z = 18$  (assigned to water) which did not change over the course of the experiment. The signals at  $m/z = 16$  and  $15$  were compared and the trends found to be indistinguishable which demonstrated that ethane does not contribute to the signal associated with the methane. These comparisons allowed us to select the fragments at  $m/z = 16$  and  $28$  and assign them to methane and ethane respectively.

Breakthrough curves for ethane and methane on EVS-10 at 298K and 100 kPa is shown in Figure 7.12. The feed gas was composed of 80% methane and 20% ethane which was introduced to bed at the flow rate of 170 ml/min. The breakthrough concentration profiles are plotted as a function of signal intensity versus time. As it is shown in the plot, methane breakthrough happens after 4.7 min and and ethane breakthrough occurs after 28.5 minutes of introducing the feed gas to the column.

The breakthrough time can be also predicted from the isotherm data of the pure gas plotted in Figure 7.5 knowing the feed composition, flow rate and the amount of the adsorbent in the bed as described below. Methane and ethane capacity is

obtained from the pure isotherms at 100kPa and 298K as 1.12 and 1.88 mmol/g, respectively. According to Avogadro's law, one mmole of ideal gas at STP condition (101kPa and 273K) occupies 22.4 ml. Based on the Avogadro's law, the capacity of ethane and methane on 30 g EVS-10 using a gas mixture of 80% methane and 20% ethane is calculated as 5787 and 862 scc. Knowing the gas flow rate (170 ml/min), the predicted breakthrough curve for ethane and methane is estimated to be 34 and 5 minute from the isotherms at experiment condition (101 kPa and 298 K).

**Table 7.6: A comparison between the predicted and the experimental breakthrough time.**

Adsorbate	Isotherm Capacity (mmol/g)	Predicted Breakthrough Time (min)	Experimental Breakthrough Time (min)
CH <sub>4</sub>	1.120	5	4.70
C <sub>2</sub> H <sub>6</sub>	1.885	34	28.5

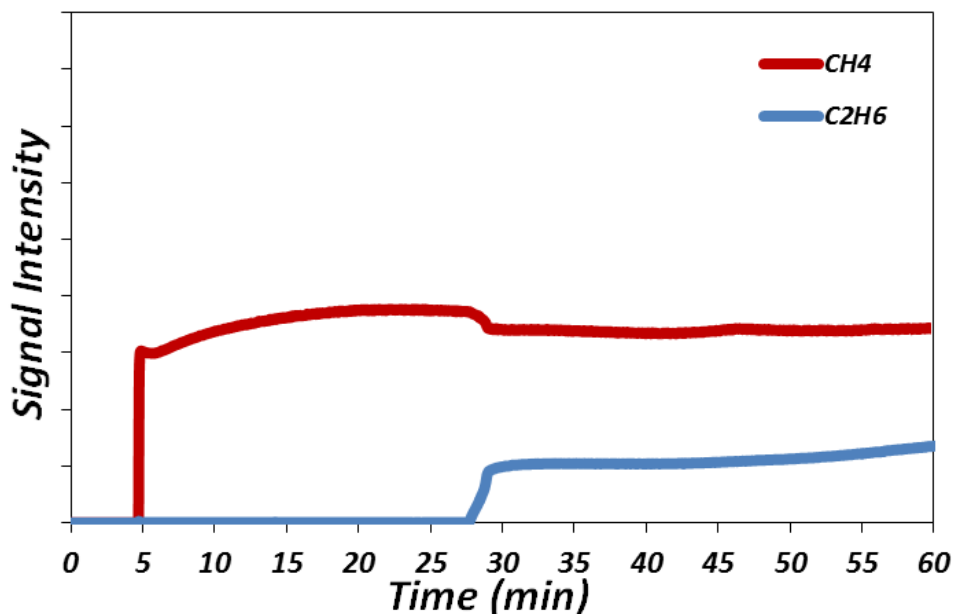


**Figure 7.12: C<sub>2</sub>H<sub>6</sub>/CH<sub>4</sub> Breakthrough curve on EVS-10 at room temperature. Feed gas: 80% CH<sub>4</sub> and 20% C<sub>2</sub>H<sub>6</sub> at 170 ml/min flow rate.**

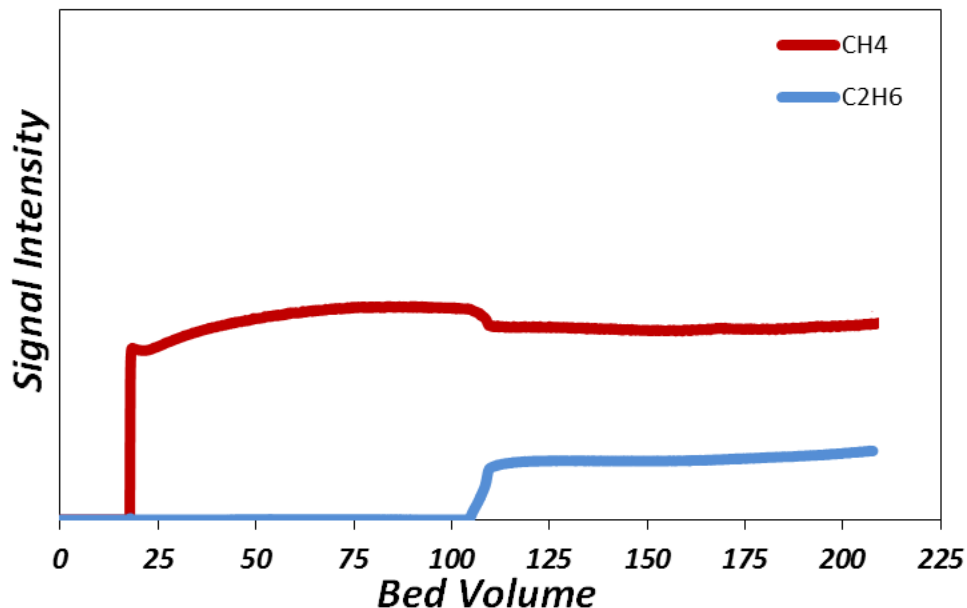


**Figure 7.13: C<sub>2</sub>H<sub>6</sub>/CH<sub>4</sub> Breakthrough curve on EVS-10 at room temperature in terms of equivalent bed volume. With 170 ml/min feed flow rate and a bed volume of 45ml, CH<sub>4</sub> breakthrough occurs at approximately 18 BV and C<sub>2</sub>H<sub>6</sub> breakthrough occurs at approximately 104 BV.**

Methane experimental breakthrough happens 4.7 min after introducing the feed to bed which is the equivalent of 18 bed volumes. Ethane breakthrough occurs 28.5 min after sending the gas mixture to bed; this is equivalent to about 104 bed volumes. The small difference between the experimental and the predicted breakthrough curve can be explained by the experimental conditions as follows. Since the bed is not isothermal, there is always be a thermal gradient along the bed which effects on the breakthrough profile; therefore, the predicted breakthrough time is slightly longer than the experimental breakthrough time. The other reason is due to the competition between methane and ethane adsorption. In the experiment a mixture of ethane and methane has been introduced to the bed but the isotherms were obtained on pure streams so there

was no competition for adsorption. In the competition between 20% ethane and 80% methane, the former is more favorably adsorbed than the latter. Therefore it releases more heat during adsorption which also affects the mass transfer front. Since the temperature profile does not move at the same rate as the mass transfer front, the ethane breakthrough profile is affected and is not coming out as sharp as methane profile (see Figure 7.12)

#### **7.4.6 Desorption**

After the bed outlet concentration reached to the inlet feed concentration, the bed has reached to its saturation capacity. To start the desorption step, water was injected to the saturated bed. After flooding the saturated bed with water all the adsorbed ethane and methane molecules will be thoroughly desorbed. The set-up is connected to a gas tank which is filled with water to collect the desorbed gases as shown in Figure 7.14. As the gas is desorbed from the bed it is going to replace the water inside the gas tank. The replaced water is collected inside a graduated cylinder. The amount of the replaced water is equal to the amount of the gas desorbed. The total moles of gas desorbed is approximately about 1252 ml which is equivalent to 1159 scc and 51.7 mmolgas. 1 ml of the collected gas is injected into a gas chromatography equipped with a standard HayeSep D column. The result of the desorbed gas analysis is shown in Figure 7.15a. The desorbed gas is enriched with up to 90% ethane. Knowing the composition of the desorbed gas, we have calculated the contribution from each methane and ethane. It is calculated that about 46.5 and 5.2 mmol of the total desorbed gas belong to ethane and methane, respectively. It should be noted that the total moles of the desorbed

gas contains the desorbed gas from the dead volume and the desorbed gas from the adsorbent solid volume. As it is mentioned earlier the total dead volume of the system is approximately 50 cc. Using the ideal gas law, we have calculated the total moles in the dead volume which is about 2 mmol gas. Considering the feed composition 80% CH<sub>4</sub> and 20% C<sub>2</sub>H<sub>6</sub>, approximately 1.6 mmol of the total desorbed gas in the dead volume is methane and 0.4 mmol is ethane. Therefore the net moles of the desorbed methane after deducting the moles in the dead volume is about 46.1 mmol ethane and 3.49 mmol of methane. The ethane/methane binary bed selectivity at room temperature and 100 kPa on EVS-10 is about 36 using equation 7.13.

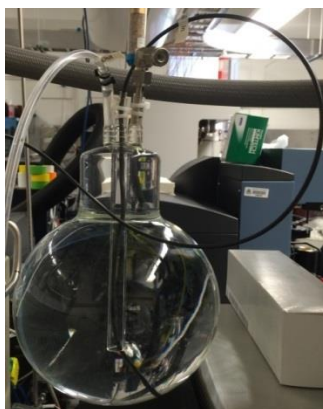


**Figure 7.14: The gas tank connected to set up filled with water in order to collect the desorbed gas.**

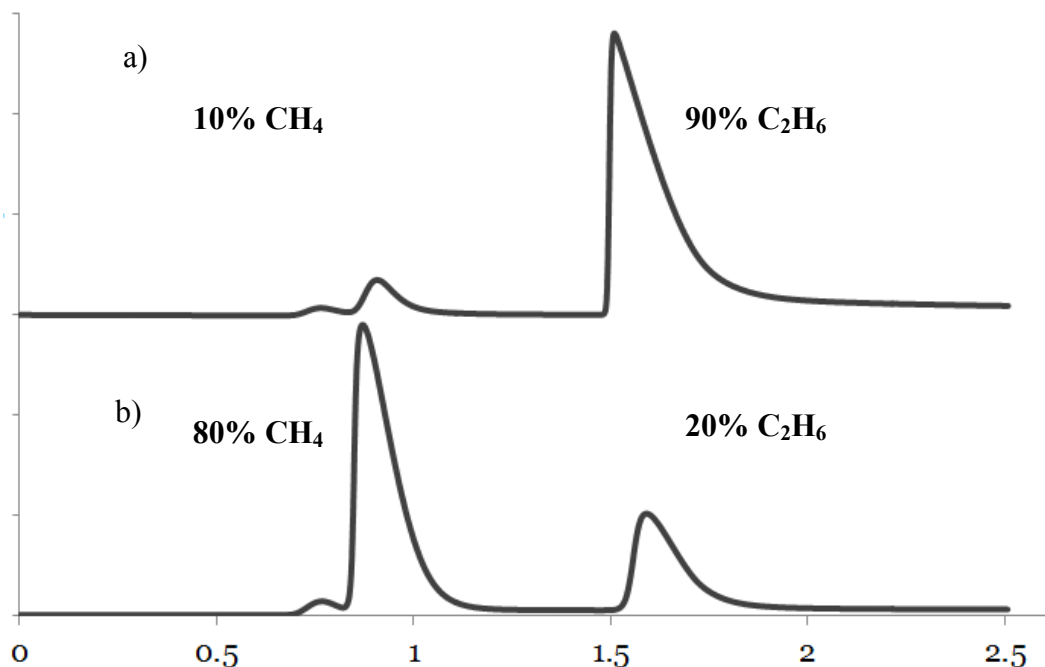


**Figure 7.15: Gas Chromatography results on a) desorbed gas: 10% methane and 90% ethane, b) feed gas: 80% methane and 20% ethane.**

## 7.5 Conclusion

In this work, ethane is separated from methane in a gas mixture contained 80% methane and 20% ethane by adsorption on vanadosilicate EVS-10 at ambient temperature and pressure. It shows bed selectivity equal to 36 on EVS-10 for 80% methane and 20% ethane. EVS-10 demonstrates ethane capacity equal to 104 bed volume. This study establishes that vanadosilicate EVS-10 is an effective adsorptive material to separate ethane from methane in a binary mixture. Further research is needed to investigate if adsorption on EVS-10 could be used to separate methane and ethane at higher pressures, such as natural gas pipeline pressures which can range from 200 psia (~1400 kPa) to about 1500 psia (~10300 kPa).

## References

- (1) Mokhatab, S.; Poe, A. W.; Speight, G. J. *Handbook of Natural Gas Transmission and Processing*; Gulf Professional Publishing: United States of America, 2006.
- (2) Shi, M.; Avila, A. M.; Yang, F.; Kuznicki, T. M.; Kuznicki, S. M. High Pressure Adsorptive Separation of Ethylene and Ethane on Na-ETS-10. *Chem. Eng. Sci.* 2011, *66*, 2817–2822.
- (3) Shi, M.; Lin, C. C. H.; Kuznicki, T. M.; Hashisho, Z.; Kuznicki, S. M. Separation of a Binary Mixture of Ethylene and Ethane by Adsorption on Na-ETS-10. *Chem. Eng. Sci.* 2010, *65*, 3494–3498.
- (4) Sircar, S.; A., M. L. Chapter 22: Gas Separation by Zeolites. In *Hand book of Zeolite Science and Technology*; Auerbach, M. S.; Carrado, A. K.; Dutta, K. P., Eds.; Marcel Dekker, Inc., 2003; Vol. 10.
- (5) Yang, R. T. *Gas Separation by Adsorption Process*; Butterworth, Boston, 1987.
- (6) Masel, R. I. *Principles of Adsorption and Reaction on Solid Surfaces*; A Wiley-Interscience Publication, 1996; p. 998.
- (7) Caventi, S.; Grande, C. A.; Rodrigues, A. E. Adsorption Equilibrium of Methane, Carbon Dioxide, and Nitrogen on Zeolite 13X at High Pressures. *J. Chem. Eng. Data* 2004, *49*, 1095–1101.
- (8) Mulgundmath, V. P.; Tezel, F. H.; Saatcioglu, T.; Golden, T. C. Adsorption and Separation of CO<sub>2</sub>/N<sub>2</sub> and CO<sub>2</sub>/CH<sub>4</sub> by 13X Zeolite. *Can. J. Chem. Eng.* 2012, *90*, 730–738.
- (9) Breck, D. W. *Zeolite Molecular Sieves: Structure, Chemistry, and Use*; John Wiley & Sons, Inc., 1974.
- (10) Dexin, Z.; Youfan, G. Prediction of Breakthrough Curves in the System of CH<sub>4</sub>, C<sub>2</sub>H<sub>6</sub> and CO<sub>2</sub> Coadsorption on 4A Molecular Sieve. *Gas Sep. Purif.* 1988, *2*, 28–33.
- (11) Loughlin, K. F.; Ruthven, D. M. The Sorption and Diffusion of Ethane in Type A Zeolites. *Chem. Eng. Sci.* 1972, *27*, 1401–1408.
- (12) Triebe, R. W.; Tezel, F. H.; Khulbe, K. C. Adsorption of Methane, Ethane and Ethylene on Molecular Sieve Zeolites. *Gas Sep. Purif.* 1996, *10*, 81–84.

- (13) Al-Baghli, N. A.; Loughlin, K. F. Binary and Ternary Adsorption of Methane, Ethane, and Ethylene on Titanosilicate ETS-10 Zeolite. *J. Chem. Eng. Data* 2006, *51*, 248–254.
- (14) Al-baghli, N. A.; Loughlin, K. F. Adsorption of Methane, Ethane, and Ethylene on Titanosilicate ETS-10 Zeolite. *J. Chem. Eng. Data* 2005, *50*, 843–848.
- (15) Anson, A.; Lin, C. C. H.; Kuznicki, S. M.; Sawada, J. a. Adsorption of Carbon Dioxide, Ethane, and Methane on Titanosilicate Type Molecular Sieves. *Chem. Eng. Sci.* 2009, *64*, 3683–3687.
- (16) Magnowski, N. B. K.; Avila, a. M.; Lin, C. C. H.; Shi, M.; Kuznicki, S. M. Extraction of Ethane from Natural Gas by Adsorption on Modified ETS-10. *Chem. Eng. Sci.* 2011, *66*, 1697–1701.
- (17) Mani, F.; Wu, L.; Kuznicki, S. M. A Simplified Method to Synthesize Pure Vanadiu, Silicate Analogue of ETS-10. *Micropor. Mesopor. Mat.* 2013, *177*, 91–96.
- (18) Ruthven, D. M. *Principles of Adsorption and Adsorption Processes*; John Wiley & Sons, Inc. , 1984.
- (19) Mathias, P. M.; Kumar, R.; Moyer, J. D.; Schork, J. M.; Srinivasan, S. R.; Auvil, S. R.; Talu, O. Correlation of Multicomponent Gas Adsorption by the Dual-Site Langmuir Model. Application to Nitrogen/Oxygen Adsorption on 5A-Zeolite. *Ind. & Eng. Chem. Res.* 1996, *35*, 2477–2483.

# Chapter 8

## Summary, Conclusion and Future Suggestions

### 8.1 Summary and Conclusion

Adsorption processes have gained a lot of attention due to their more energy efficient, separation technique compared to conventional cryogenic distillation method. Adsorptive separation and purification of gas mixtures by selective adsorption of one or more component on a microporous solid adsorbent is a key unit operation in medical, electronic, environmental, chemical and petrochemical gas industries<sup>1</sup>. This is attributed to the commercial availability of a range of porous adsorbents such as zeolites which offer various choices of core adsorptive characteristics such as equilibria, kinetics and heats for a known gas separation or purification application. Besides, adsorption processes have a lot of flexibility in the design and operation of adsorptive separation and purification due to the possibility of tailoring the adsorbent for a specific application<sup>1</sup>. A successful adsorptive process requires a combination of an optimized adsorbent with an energy efficient process design. Indeed, zeolites have played an important role in the expansion of adsorption technology. They could be used to remove a trace or dilute impurities from a gas such as gas drying, desulfurization and removal of toxic, heavier, and corrosive compounds from a contaminated gas stream. Furthermore, zeolites are

largely used for bulk separation of gas mixtures to increase the product recovery and purity while reducing the overall energy requirement. Zeolites are also used for gas analysis. The prime example of this would be in the gas chromatography , which is largely used as an analytical tool<sup>1</sup>.

Changing the adsorbent properties can improve or enable different separations; therefore, study into molecular sieves is always evolving to find ways to improve separation selectivities. EVS-10 is one of those attempts to find improvements by changing the structure and composition of a sieve to determine the promising application.

Concluding remarks about the materials discussed in the thesis are summarized as follows:

- **Chapter 1**

This chapter provided an introduction to different class of molecular sieves. It breaks down the differences and the similarities between each class of the sieves. The research objectives of the Thesis were explained in this chapter. Background information with respect to gas separation processes especially adsorption process was also provided.

- **Chapter 2**

The fundamental principles behind adsorption processes as well as different adsorption models for pure and mixed-gas isotherms were discussed in this chapter.

- **Chapter 3**

This chapter discussed the detailed synthesis of the first highly pure microporous vanadosilicate (EVS-10/AM-6). It has been hydrothermally synthesized by a simple template-free, reducing agent-free method in the absence of titanosilicate ETS-10 seeds.

Direct comparison between EVS-10 and ETS-10 showed successful isomorphous substitution of titanium with vanadium in the framework. The existence of vanadium is confirmed by energy dispersive X-ray spectroscopy and inductively coupled plasma mass spectrometry. The scan electron microscopy and the X-ray diffractometry show similar crystal morphology and similar molecular structure between the as-synthesized material and the ETS-10. Preliminary results indicate a potentially bigger pore size ( $\sim 9.8\text{\AA}$  vs.  $\sim 8.4\text{\AA}$ ), with a similar internal surface area to ETS-10. Nitrogen was used as a probe gas in these analyses. Similar to ETS-10, EVS-10 may be useful for semiconductor and other electronic applications. This new simplified synthesis method may allow the economical production of EVS-10 / AM-6 for quantum wire and other applications.

#### **Chapter 4**

A detailed comparative study between EVS-10 and ETS-10 was conducted after successfully incorporated vanadium into ETS-10 structure. This study compared the structural and adsorptive characteristics of EVS-10 with ETS-10. The structures were characterized by powder XRD, EDX, argon physisorption, and SEM/TEM. The Henry Law constants and heats of adsorption were calculated for both adsorbents from low pressure adsorption data using  $\text{CH}_4$ ,  $\text{C}_2\text{H}_6$ ,  $\text{C}_2\text{H}_4$ ,  $\text{N}_2$ ,  $\text{O}_2$ , and  $\text{CO}_2$  for pressures up to 100 kPa and temperatures of 303, 323, and 343 K. The adsorption data were fit using Langmuir, Toth, and Redlich-Peterson isotherms. The best model was selected based on the quality of fit to the data and how closely the model predicted the saturation concentration compared to the value calculated from the measured pore volume data. The structural properties for EVS-10 were almost indistinguishable from ETS-10. The adsorption data reflected this similarity in that both adsorbents had similar heats of

adsorption and selectivities for a wide range of gases. These results suggested that heteroatom substitution in ETS-10 did not necessarily affect its adsorption properties if the framework dimensions and composition remained similar.

## **Chapter 5**

In this chapter an adsorption mechanism for ETS-10 was proposed by contrasting the adsorption properties of as-synthesized ETS-10 with 13X and high siliceous ZSM-5. ETS-10 is a unique structure type in that the walls of the channels where adsorption takes place are made entirely of silica, while the octahedral titania chains in the structure impart a negative charge that is offset by exchangeable cations; a portion of which reside in the channels. To determine whether adsorption on Na-ETS-10 is driven predominately by cationic or van der Waals effects, the adsorption affinity for several gases was measured on all three adsorbents. The adsorption mechanism was probed by using the isotherms to calculate both the enthalpy and entropy of adsorption as a function of loading and by contrasting the behaviour of ETS-10 against both 13X and ZSM-5. The results of the analysis indicate that the sieve has, simultaneously, a high affinity for both non-polar and polar gases, which is believed to result from a sparse number of highly deshielded cations that exist in the otherwise non-polar channels. This bi-functional characteristic is borne out of the crystal structure of ETS-10 where the cations are located in discrete bands within the unit cell rather than being uniformly distributed throughout the structure.

## **Chapter 6**

This chapter looked into the ion-exchange behaviour of the as synthesized EVS-10 and ETS-10 with silver. The as-synthesized form of EVS-10 shares virtually identical

adsorptive characteristics of the same form of ETS-10. However, when silver is exchanged into EVS-10 the adsorptive characteristics of Ag-EVS-10 display none of the hallmark properties of Ag-ETS-10. In fact, a sample of fully silver exchanged EVS-10 failed to show any adsorptive properties although the framework remains intact after activation.

In this chapter, the phenomenon associated with the ion-exchange of silver ions into the microporous vanadosilicate EVS-10 is explored. EVS-10 is composed of orthogonal chains of vanadia octahedra which connect through silicate bridges to form pores and channels of molecular dimensions. The divalent charge on the vanadium is offset by mobile and exchangeable cationic counter-ions. It was found that silver replaces sodium quantitatively and that, unexpectedly, the silver ions are spontaneously reduced to silver metal which appear as nano-scale metal clusters in the TEM images. The reduction of the silver ions is accompanied by an oxidation of the framework vanadium and this redox pair is established through XPS and Raman spectroscopy. The mechanism for this unique behaviour is believed to be explained by a galvanic reaction between the incoming  $\text{Ag}^+$  and the framework  $\text{V}^{4+}$ .

Silver nanoparticles have attracted attention due to their unique optical, electrical and thermal properties which make them attractive solutions for conductive inks, pastes and fillers.

Silver-impregnated molecular sieves have demonstrated the ability to form nano-scale silver aggregates on their surfaces (CHA/ETS-2, ETS-10, others). The inclusion of silver in molecular sieves has been shown to modify their properties toward alkene<sup>2,3</sup> and noble

gas separation<sup>4</sup> and can impart antimicrobial or photochromic properties<sup>5</sup> depending on the silver content and the molecular sieve framework type.

## **Chapter 7**

In this chapter separation of ethane from methane from a binary gas mixture was conducted by adsorption on EVS-10. In this study a feed consisted of 80% methane and 20% ethane was used. The bed selectivity resulted from adsorptive separation on EVS-10 was 36 at room temperature and atmospheric pressure. This study suggested that EVS-10 could be an effective candidate for separation of ethane from the gas streams which are highly enriched in methane. In other words, EVS-10 could be potentially used in cases such as natural gas purification. The majority of natural gas is methane, but it also contains other hydrocarbons such as ethane, propane, butane, etc. Ethane increases the natural gas heating value; however to meet the standard heating value of a marketable natural gas a portion of ethane needs to be removed. On the other hand, it is a feed to produce ethylene, which is one of the largest petrochemical products used in plastic, rubber and film industry, through steam cracking process. Natural gas purification traditionally is done by energy-intensive cryogenic distillation. This study introduces EVS-10 as a potential adsorbent for the energy efficient adsorptive separation methods to replace the energy intensive separation processes such as cryogenic distillation, and absorption. EVS-10 is the vanadium analogue of ETS-10 that has demonstrated the highest ethane over methane selectivity compared to the classical zeolites such as 13X and 5A. The Henry's selectivity on EVS-10 is 60 whereas it is reported 52 for ETS-10<sup>6</sup>. The new sorbent, EVS-10, may potentially increase the recovery of ethane from natural

gas and may lead to cost reduction of natural gas liquids removal from natural gas feedstocks.

## 8.2 Future Work

- EVS-10 has no or few charges in the silica rings in the structure but if aluminum is incorporated into the EVS-10 structure more charge will be localized in the pore mouth (inside 12-rings where adsorption happens). This could dramatically change the adsorption characteristic because incorporating aluminum into the structure may introduce cations inside the pores besides the ion-exchange capacity will increase.
- Silver exchanging of as-synthesized ETS-10 automatically reduced silver to silver nanoparticles. Recent work shows acid washing of as-synthesized EVS-10 would oxidize vanadium to  $V^{5+}$ . Then silver exchanging the acid-washed EVS-10 (H-EVS-10) would stabilize it against silver reduction and silver would remain as silver ions and then  $Ag^+$ -H-EVS-10 is a compelling material and be worth as a cathode for primary batteries.
- EVS-10 has been shown to be effective to separate a binary mixture of ethane and methane with a composition of 80% methane and 20% ethane at ambient pressure and temperature. In future, EVS-10 could be investigated to separate a gas stream enriched with methane at higher pressures such as as natural gas pipeline pressures which can range from 200 psia (~1400 kPa) to about 1500 psia (~10300 kPa).
- Adsorption of Carbondioxide on EVS-10 have been studied and the low pressure isotherms and henry's selectivity has been reported in Chapter 3.

The study of carbondioxide on EVS-10 could be extended into using EVS-10 as an adsorbent to dry carbondioxide wet streams using low grade heat and ambient air as a regeneration gas. This idea is raised by the similar studies on ETS-10 for CO<sub>2</sub> drying using a low grade heat and humid, ambient air<sup>7</sup>. This study has reported ETS-10 is a promising desiccant for drying CO<sub>2</sub> to trace levels of moisture. It suggested that the calcium form of ETS-10 had the highest breakthrough capacity of the Na form or the Ca/H- forms of ETS-10, or compared to the commercial silica or zeolite 4A<sup>7</sup>. Due to the similarities between ETS-10 and its vanadium analogue, the study of CO<sub>2</sub> drying can be extended to test EVS-10 as an adsorbent.

- Adsorption of carbondioxide, nitrogen and oxygen on EVS-10 has been studied in Chapter 3. EVS-10 shows a high selectivity for separation of carbondioxide from nitrogen and oxygen. Carbondioxide has been identified as an indoor air contaminant. Air filtering is an effective approach to improve and maintain the indoor air quality. Adsorption filters are one of the most common types of air purifiers. The preliminary study on adsorption of carbondioxide, air and nitrogen on EVS-10 can be extended to the use of EVS-10 in the air filters to adsorb carbondioxide from indoor air. Further research is required to investigate the adsorptive behaviour of EVS-10 towards other common contaminants besides carbondioxide found indoor such as carbon monoxide, ozone, lead, particulates, nitrogen dioxide and volatile organic compounds (VOCs).

## References

- (1) Sircar, S.; A., M. L. Chapter 22: Gas Separation by Zeolites. In *Hand book of Zeolite Science and Technology*; Auerbach, M. S.; Carrado, A. K.; Dutta, K. P., Eds.; Marcel Dekker, Inc., 2003; Vol. 10.
- (2) Bülow, M.; Guo, C. J.; Shen, D.; Fitch, F. R.; Shirley, A. I.; Malik, V. A. Separation of Alkenes and Alkanes. US6200366B1, 2001.
- (3) Tiscornia, I.; Irusta, S.; Prádanos, P.; Tellez, C.; Coronas, J.; Santamaría, J. Preparation and Characterization of Titanosilicate Ag-ETS-10 for Propylene and Propane Adsorption. *J. Phys. Chem. C* 2007, *111*, 4702–4709.
- (4) Kuznicki, S. M.; Anson, A.; Koenig, A.; Kuznicki, T. M.; Haastrup, T.; Eyring, E. M.; Hunter, D. Xenon Adsorption on Modified ETS-10. *J. Phys. Chem. C* 2007, *111*, 1560–1562.
- (5) Galioglu, S.; Isler, M.; Demircioglu, Z.; Koc, M.; Vocanson, F.; Destouches, N.; Turan, R.; Akata, B. Photochromic Behavior of Silver Nanoparticle Incorporated Titanosilicate ETS-10 Films. *Microporous Mesoporous Mater.* 2014, *196*, 136–144.
- (6) Magnowski, N. B. K.; Avila, a. M.; Lin, C. C. H.; Shi, M.; Kuznicki, S. M. Extraction of Ethane from Natural Gas by Adsorption on Modified ETS-10. *Chem. Eng. Sci.* 2011, *66*, 1697–1701.
- (7) Tanchuk, B.; Sawada, J. A.; Rezaei, S.; Kuznicki, S. M. Adsorptive Drying of CO<sub>2</sub> Using Low Grade Heat and Humid, Ambient Air. *Sep. Purif. Technol.* 2013, *120*, 354–361.

# Bibliography

Ackley, M. W.; Rege, S. U.; Saxena, H. Application of Natural Zeolites in the Purification and Separation of Gases (A Review). *Micropor. Mesopor. Mat.* 2003, *61*, 25–42.

Al-Baghli, N. A.; Loughlin, K. F. Adsorption of Methane, Ethane, and Ethylene on Titanosilicate ETS-10 Zeolite. *J. Chem. Eng. Data* 2005, *50*, 843–848.

Al-Baghli, N. A.; Loughlin, K. F. Binary and Ternary Adsorption of Methane, Ethane, and Ethylene on Titanosilicate ETS-10 Zeolite. *J. Chem. Eng. Data* 2006, *51*, 248–254.

Al-Kharafi, F. M.; Badawy, W. A. Electrochemical Behaviour of Vanadium in Aqueous Solutions of Different pH. *Electrochim. Acta* 1997, *42*, 579–586.

Anderson, M. W.; Agger, J. R.; Luigi, D.-P.; Baggaley, A. K.; Rocha, J. Cation Sites in ETS-10:  $^{23}\text{Na}$   $3\text{Q}$  MAS NMR and Lattice Energy Minimisation Calculations. *Phys.Chem.Chem.Phys.* 1999, *1*, 2287–2292.

Anderson, M. W.; Terasaki, O.; Ohsuna, T.; Philippou, A.; MacKay, S. P.; Ferreira, A.; Rocha, J.; Lidin, S. Structure of the Microporous Titanosilicate ETS-10. *Nature* 1994, *367*, 347–351.

Anderson, M. W.; Terasaki, O.; Ohsuna, T.; Philippou, A.; MacKay, S. P.; Ferreira, A.; Rocha, J.; Lidin, S. Structure of the Microporous Titanosilicate ETS-10. *Stud. Surf. Sci. Catal.* 1995, *98*, 258–259.

Anson, A.; Kuznicki, S. M.; Kuznicki, T.; Dunn, B. C.; Eyring, E. M.; Hunter, D. B. Separation of Argon and Oxygen by Adsorption on a Titanosilicate Molecular Sieve. *Separ. Sci. Technol.* 2009, *44*, 1604–1620.

Anson, A.; Kuznicki, S. M.; Kuznicki, T.; Haastrup, T.; Wang, Y.; Lin, C. C. H.; Sawada, J. A.; Eyring, E. M.; Hunter, D. Adsorption of Argon, Oxygen, and Nitrogen on Silver Exchanged ETS-10 Molecular Sieve. *Micropor. Mesopor. Mat.* 2008, *109*, 577–580.

Anson, A.; Lin, C. C. H.; Kuznicki, S. M.; Sawada, J. a. Adsorption of Carbon Dioxide, Ethane, and Methane on Titanosilicate Type Molecular Sieves. *Chem. Eng. Sci.* 2009, *64*, 3683–3687.

Anson, A.; Lin, C. C. H.; Kuznicki, T. M.; Kuznicki, S. M. Separation of Ethylene/ethane Mixtures by Adsorption on Small-Pored Titanosilicate Molecular Sieves. *Chem. Eng. Sci.* 2010, *65*, 807–811.

Anson, A.; Wang, Y.; Lin, C. C. H.; Kuznicki, T. M.; Kuznicki, S. M. Adsorption of Ethane and Ethylene on Modified ETS-10. *Chem. Eng. Sci.* 2008, *63*, 4171–4175.

Antonio, F. M.; Neves, C. I. Study of Silver Species Stabilized in Different Microporous Zeolites. *Micropor. Mesopor. Mat.* 2013, *181*, 83–87.

Avgul, N. N.; Bezus, G. A.; Dzhigit, M. O. Heats of Adsorption on X-Type Zeolites Containing Different Alkali Metal Cations; Molecular Sieve Zeolites-II. In *Molecular Sieve Zeolites-II*; M., F. E.; S; B., L., Eds.; American Chemical Society: Washington, DC., 1971; pp. 184–192.

Bois, L.; Chassagneux, F.; Battiez, Y.; Bessueille, F.; Mollet, L.; Parola, S.; Destouches, N.; Toulhoat, N.; Moncoffre, N. Chemical Growth and Photochromism of Silver Nanoparticles into a Mesoporous Titania Template. *Langmuir* 2010, *26*, 1199–1206.

Barrer, R. M.; Bultitude, F. W.; Sutherland, J. W. Structure of Faujasite and Properties of Its Inclusion Complexes with Hydrocarbons. *Trans.Faraday Soc.* 1957, *53*, 1111–1123.

Baussy, G.; Caruba, R.; Baumer, A.; Turco, G. Mineralogie Experimentale Dans Le System ZrO<sub>2</sub>-SiO<sub>2</sub>-Na<sub>2</sub>O-H<sub>2</sub>O. Correlations Petrogenetiques. *Bull. Soc. Miner. Crystallogr.* 1974, *97*, 433–444.

Bozhilov, K. N.; Valtchev, V. P. Transmission Electron Microscopy Characterization of a Large-Pore Titanium Silicate. *Mater. Res. Bull.* 1993, *28*, 1209–1214.

Brandao, P.; Valente, A.; ad Artur Ferreira and<p>Michael W. Anderson, A. P.; Rocha, J. Hydrothermal Synthesis and Characterisation of Two Novel Large-Pore Framework Vanadium Silicates. *Eur. J. Inorg. Chem.* 2003, 1175–1180.

Breck, D. W. *Zeolite Molecular Sieves: Structure, Chemistry, and Use*; John Wiley & Sons, Inc., 1974.

Brunauer, S.; Deming, L. S.; Deming, W. E.; Teller, E. On a Theory of the van Der Waals Adsorption of Gases. *J. Am. Chem. Soc.* 1940, *62*, 1723–1732.

Bulow, M.; Guo, C. J.; Shen, D.; Fitch, F. R.; Shirley, A. I.; Malik, V. A. Separation of Alkenes and Alkanes. US6200366B1, 2001.

Casado, C.; Amghouz, Z.; García, J. R.; Boulahya, K.; González-Calbet, J. M.; Téllez, C.; Coronas, J. Synthesis and Characterization of Microporous Titanosilicate ETS-10 Obtained with Different Ti Sources. *Mater. Res. Bull.* 2009, *44*, 1225–1231.

Caventi, S.; Grande, C. A.; Rodrigues, A. E. Adsorption Equilibrium of Methane, Carbon Dioxide, and Nitrogen on Zeolite 13X at High Pressures. *J. Chem. Eng. Data* 2004, *49*, 1095–1101.

Chan, S. S.; Wachs, I. E.; Murrell, L. L.; Wang, L.; Hall, W. K. In Situ Laser Raman Spectroscopy of Supported Metal Oxides. *J. Phys. Chem.* 1984, *88*, 5831–5835.

Choudhary, V. R.; Mayadevi, S. Adsorption of Methane, Ethane, Ethylene, and Carbon Dioxide on Silicalite-L. *Zeolites* 1996, *17*, 501.

Choudhary, V. R.; Mayadevi, S. Adsorption of Methane, Ethane, Ethylene, and Carbon Dioxide on High Silica Pentasil Zeolites and Zeolite-like Materials Using Gas Chromatography Pulse Technique. *Sep. Sci. Technol.* 1993, *28*, 2197–2209.

Chiang, A. S.; Dixon, A. G.; Ma, Y. H. The Determination of Zeolite Crystal Diffusivity by Gas chromatography—I. Theoretical. *Chem. Eng. Sci.* 1984, *39*, 1451–1459.

Ching, W. Y.; Xu, Y. N.; Gu, Z. Q. Structure and Properties of Microporous Titanosilicate Determined by First-Principles Calculations. *Phys. Rev. B - Condens. Matter Mater. Phys.* 1996, *54*.

Chue, K. T.; Kim, J. N.; Yoo, Y. J.; Cho, S. H.; Yang, R. T. Comparison of Activated Carbon and Zeolite 13X for CO<sub>2</sub> Recovery from Flue Gas by Pressure Swing Adsorption. *Ind. Eng. Chem. Res.* 1995, *34*, 591–598.

Cochran, T. W.; Kabel, R. L.; Danner, R. P. Vacancy Solution Theory of Adsorption Using Flory-Huggins Activity Coefficient Equations. *AIChE J.* 1985, *31*, 268–277.

Corcoran, E.; Vaughan, D. Hydrothermal Synthesis of Mixed Octahedral-Tetrahedral Oxides: Synthesis and Characterization of Sodium Stannosilicates. *Solid State Ionics* 1989, *32-33*, 423–429.

Corcoran, E. W.; Newsam, J. M.; King, H. E.; Vaughan, D. E. W. Phase Identification of Hydrothermal Crystallization Products from M<sub>2</sub>O-SiO<sub>2</sub>-SnO<sub>2</sub>-H<sub>2</sub>O Gels or Solutions. In *Zeolite Synthesis*; pp. 603–616.

Corma, A. From Microporous to Mesoporous Molecular Sieve Materials and Their Use in Catalysis. *Chem. Rev.* 1997, *97*, 2373–2419.

Cundy, C. S.; Cox, P. A. The Hydrothermal Synthesis of Zeolites: Precursors, Intermediates and Reaction Mechanism. *Micropor. Mesopor. Mat.* 2005, *82*, 1–78.

Daniel Richard Stull, Edgar F. Westrum, G. C. S. *The Chemical Thermodynamics of Organic Compounds*; John Wiley & Sons, Inc.: United States of America, 1969; p. 865.

Datta, S. J.; Yoon, K. B. Synthesis of Ideal AM-6 and Elucidation of V<sup>4+</sup>-to-O Charge Transfer in Vanadate Quantum Wires. *Angew. Chem. Int. Ed.* 2010, *49*, 1–6.

Dexin, Z.; Youfan, G. Prediction of Breakthrough Curves in the System of CH<sub>4</sub>, C<sub>2</sub>H<sub>6</sub> and CO<sub>2</sub> Coadsorption on 4A Molecular Sieve. *Gas Sep. Purif.* 1988, *2*, 28–33.

Ding, T.-F.; Ozawa, S.; Yanazaki, T.; Watamuki, I.; Ogina, Y. A Generalized Treatment of Adsorption of Methane onto Various Zeolites. *Langmuir* 1988, 4, 392–396.

Do, D. D. *Adsorption Analysis: Equilibria and Kinetics*; Imperial College Press, 1998; p. 892.

Dubinin, M. M. Adsorption Properties and Secondary Pore Structure of Adsorbents That Exhibit Molecular-Sieve Action. II. Comparison of Calculated and Experimental Limiting Values for Adsorption and Adsorption Volumes for Type A Synthetic Zeolites. *Izv. Akad. Nauk. Ser. Khim.* 1961, 1183–1191.

Emmett, P. H.; Brunauer, S. The Use of Low Temperature van Der Waals Adsorption Isotherms in Determining the Surface Area of Iron Synthetic Ammonia Catalysts. *J. Am. Chem. Soc.* 1937, 59, 1553–1564.

Ferdov, S. Temperature- and Vacuum-Induced Framework Contraction of Na-ETS-4. *Langmuir* 2010, 26, 2684–2687.

Ferreira, A.; Lin, Z.; Rocha, J.; Morais, C. M.; Lopes, M.; Fernandez, C. Ab Initio Structure Determination of a Small-Pore Framework Sodium Stannosilicate. *J. Inorg. Chem.* 2001, 14, 3330–3335.

Fiedler, K.; Stach, H.; Schirmer, W. Adsorption Thermodynamics of N-Paraffins in Zeolite NaCaA. In *Academy of Sciences*; 1979; pp. 75–84.

Flor R. Siperstein, A. L. M. Mixed-Gas Adsorption. *AIChE J.* 2001, 47, 1141–1159.

Galioglu, S.; Isler, M.; Demircioglu, Z.; Koc, M.; Vocanson, F.; Destouches, N.; Turan, R.; Akata, B. Photochromic Behavior of Silver Nanoparticle Incorporated Titanosilicate ETS-10 Films. *Microporous Mesoporous Mater.* 2014, 196, 136–144.

Golden, J. H.; DiSalvo, F. J.; Frechet, J. M. J.; Silcox, J.; Thomas, M.; Elman, J. Subnanometer-Diameter Wires Isolated in a Polymer Matrix by Fast Polymerization. *Sci. New Ser.* 1996, 273, 782–784.

Golden, J.H., Deng, H., DiSalvo, F.J., Fréchet, J.M.J., Thompson, P. . Monodisperse Metal Clusters 10 Angstroms in Diameter in a Polymeric Host: The “Monomer as Solvent” Approach. *Science (80- )*. 1995, 268, 1463–1466.

Golden, T. C.; Sircar, S. Gas Adsorption on Silicalite. *J. Colloid Interface Sci.* 1994, 162, 182–188.

Graham, P.; Hughes, A. D.; Rees, L. V. C. Sorption of Binary Gas Mixtures in Zeolites: I. Sorption of Nitrogen and Carbon Dioxide Mixtures in Silicalite. *Gas Sep. Purif.* 1989, 3, 56.

Gregg, S. J. *The Surface Chemistry of Solids*; Barnes & Noble: Reinhold Publishing Corporation: New York, 1961; p. 393.

Grillo, M. E.; Carrazza, J. Computational Modeling of the Nonframework Cation Location and Distribution in Microporous Titanosilicate ETS-10. *J. Phys. Chem.* 1996, *100*, 12261–12264.

Habgood, H. W. Adsorptive and Gas Chromatographic Properties of Various Cationic Forms of Zeolite X. *Can. J. Chem.* 1964, *42*, 2340–2350.

Hampson, J. A.; Rees, L. V. C. Adsorption of Ethane and Propane in Silicalite-1 and Zeolite NaY: Determination of Single Components, Mixture and Partial Adsorption Data Using an Isothermic System. *J. Chem. Soc. Faraday Trans.* 1993, *89*, 3169–3176.

Hardcastle, F. D.; Wachs, I. E. Determination of Vanadium-Oxygen Bond Distances and Bond Orders by Raman Spectroscopy. *J. Phys. Chem.* 1991, *95*, 5031–5041.

[Http://srdata.nist.gov/xps/NIST](http://srdata.nist.gov/xps/NIST).

Hyun, S. H.; Danner, R. P. Equilibrium Adsorption of Ethane, Ethylene, Isobutane, Carbon Dioxide, and Their Binary Mixtures on 13X Molecular Sieves. *J. Chem. Eng. Data* 1982, *27*, 196–200.

Ismail, M. N.; Fraiman, N. D.; Jr., D. M. C.; Gursoy, G.; Viveiros, E.; Ozkanat, O.; Ji, Z.; Willey, R. J.; Warzywoda, J.; Jr., A. S.; et al. First Unseeded Hydrothermal Synthesis of Microporous Vanadosilicate AM-6. *Micropor. Mesopor. Mat.* 2009, *120*, 454–459.

Jale, S. R.; Ojo, A.; Fitch, F. R. Synthesis of Microporous Zirconosilicates Containing ZrO<sub>6</sub> Octahedra and SiO<sub>4</sub> Tetrahedra. *Chem Commun.* 1999, 411–412.

Jeong, N. C.; Lee, M. H.; Yoon, K. B. No Title. *Angew.Chem.Int.Edit.* 2007, *46*, 5868–5872.

Ji, Z.; Warzywoda, J.; Jr., A. S. Competitive Nucleation and Growth in Seeded Batch Crystallization of Titanosilicate ETS-10 Using Ti(SO<sub>4</sub>)<sub>2</sub>. *Micropor. Mesopor. Mat.* 2005, *81*, 201–210.

Jones, W. J. High-Resolution Raman Spectroscopy of Gases and the Determination of Molecular Bond Lengths. *Can. J. Phys.* 2000, *78*, 327–390.

Kapoor, A.; Yang, R. T. Kinetic Separation of Methane-carbon Dioxide Mixture by Adsorption on Molecular Sieve Carbon. *Chem. Eng. Sci.* 1989, *44*, 1723–1733.

Kemball, C. Entropy of Adsorption. In; Frankenburg, W. G.; Komarewsky, I. V; Keightley, E. S., Eds.; *Advances in Catalysis and Related Subjects*; Academic Press Inc., 1950; Vol. 2, pp. 233–250.

Kiselev, A. V.; Lopatkin, A. A.; Shulga, A. A. Molecular Statistical Calculation of Gas Adsorption by Silicalite. *Zeolites* 1985, 5, 261–267.

Knaebel, K. S.; Farooq, S.; Ruthven, D. M. *Pressure Swing Adsorption*; Wiley-VCH, New York, 1994.

Krisnandi, Y. K.; Southon, P. D.; Adesina, A. A.; Howe, R. F. ETS-10 as a Photocatalyst. *Int.J.Photoenergy* 2003, 5, 131–140.

Kuznicki, S. M.; Anson, A.; Koenig, A.; Kuznicki, T. M.; Haastrup, T.; Eyring, E. M.; Hunter, D. Xenon Adsorption on Modified ETS-10. *J. Phys. Chem. C* 2007, 111, 1560–1562.

Kuznicki, S. M., Anson, A., Segin, T., Lin, C. C. H. Modified ETS-10 Zeolites for Olefin Separation. 8017825 B2, 2011.

Kuznicki, S. M. Large-Pored Crystalline Titanium Molecular Sieve Zeolites. 5011591, 1991.

Kuznicki, S. M.; Madon, R. J.; Koermer, G. S.; Thrush, K. A. Large-Pored Molecular Sieves and Their Use as Catalysts and Ion Exchangers. 0405978B1, 1991.

Kuznicki, S. M. Small-Pored Crystalline Titanium Molecular Sieve Zeolites and Their Use in Gas Separation Processes, May 2000.

Kuznicki, S. M.; Thrush, K. A. Large Pored Molecular Sieves with Charged Octahedral Titanium and Charged Tetrahedral Aluminum Sites. US5244650, October 1993.

Kuznicki, S. M.; Thrush, K. A. Large-Pored Molecular Sieves Containing at Least One Octahedral Site and Tetrahedral Sites of at Least One Type, 2002.

Kuznicki, S. M.; Thrush, K. A. Removal of Heavy Metals, Especially Lead, from Aqueous Systems Containing Competing Ions Utilizing Wide-Pored Molecular Sieves of the ETS-10 Type, 1991.

Ismail, M. N.; Fraiman, N. D.; Callahan, D. M.; Gursoy, G.; Viveiros, E.; Ozkanat, O.; Ji, Z.; Willey, R. J.; Warzywoda, J.; Sacco, A. First Unseeded Hydrothermal Synthesis of Microporous Vanadosilicate AM-6. *Microporous Mesoporous Mater.* 2009, 120, 454–459.

Lamberti, C. Electron-Hole Reduced Effective Mass in Monoatomic ...-O-Ti-O-Ti-O-... Quantum Wires Embedded in the Siliceous Crystalline Matrix of ETS-10. *Micropor. Mesopor. Mat.* 1999, 30, 155–163.

Lin, C. C. H.; Sawada, J. A.; Wu, L.; Haastrup, T.; Kuznicki, S. M. Anion-Controlled Pore Size of Titanium Silicate Molecular Sieves. *J. Am. Chem. Soc.* 2009, 131, 609–614.

Lin, Z.; Rocha, J.; Ferreira, P.; Thursfield, A.; Agger, J. R.; Anderson, M. W. Synthesis and Structural Characterization of Microporous Framework Zirconium Silicate. *J. Phys. Chem. B* 1999, *103*, 957–963.

Loughlin, K. F.; Ruthven, D. M. The Sorption and Diffusion of Ethane in Type A Zeolites. *Chem. Eng. Sci.* 1972, *27*, 1401–1408.

Magnowski, N. B. K.; Avila, a. M.; Lin, C. C. H.; Shi, M.; Kuznicki, S. M. Extraction of Ethane from Natural Gas by Adsorption on Modified ETS-10. *Chem. Eng. Sci.* 2011, *66*, 1697–1701.

Mani, F.; Sawada, J. A.; Kuznicki, S. M. Comparative Adsorption Study of EVS-10 and ETS-10. *Micropor. Mesopor. Mat.* 2015, *204*, 43–49.

Mani, F.; Wu, L.; Kuznicki, S. M. A Simplified Method to Synthesize Pure Vanadium Silicate Analogue of ETS-10. *Micropor. Mesopor. Mat.* 2013, *177*, 91–96.

Masel, R. I. *Principles of Adsorption and Reaction on Solid Surfaces*; A Wiley-Interscience Publication, 1996; p. 998.

Mathias, P. M.; Kumar, R.; Moyer, J. D.; Schork, J. M.; Srinivasan, S. R.; Auvil, S. R.; Talu, O. Correlation of Multicomponent Gas Adsorption by the Dual-Site Langmuir Model. Application to Nitrogen/Oxygen Adsorption on 5A-Zeolite. *Ind. & Eng. Chem. Res.* 1996, *35*, 2477–2483.

Milton, R. M. Molecular Sieve Adsorbents. 2,882,244, April 1959.

Mokhatab, S.; Poe, A. W.; Speight, G. J. *Handbook of Natural Gas Transmission and Processing*; Gulf Professional Publishing: United States of America, 2006.

Morones, J. R.; Elechiguerra, J. L.; Camacho, A.; Holt, K.; Kouri, J. B.; Ramirez, J. T.; Yacaman, M. J. The Bactericidal Effect of Silver Nanoparticles. *Nanotechnology* 2005, *16*, 2346.

Mulgundmath, V. P.; Tezel, F. H.; Saatcioglu, T.; Golden, T. C. Adsorption and Separation of CO<sub>2</sub>/N<sub>2</sub> and CO<sub>2</sub>/CH<sub>4</sub> by 13X Zeolite. *Can. J. Chem. Eng.* 2012, *90*, 730–738.

Nalaparaju, A.; Zhao, X. S.; Jiang, J. Molecular Interplay of Cations and Nonpolar/Polar Sorbates in Titanosilicate ETS-10. *J. Phys. Chem. C* 2008, *112*, 12861–12868.

Naoui, K.; Sakamoto, T.; Matsuura, H.; Akatsuka, H. Experimental Study on the Effect of Different Noble Gas Admixtures on the Gas Temperature of Oxygen Plasma. *J. Adv. Oxid. Technol.* 2005, *8*, 25–32.

Nash, M. J.; Rykov, S.; Lobo, R. F.; Doren, D. J.; Wachs, I. Photocatalytic Activity of Vanadium-Substituted ETS-10. *J. Phys. Chem. C* 2007, *111*, 7029–7037.

Notaro, F.; Ackley, M. W.; Smolarek, J. Recover Industrial Gas via Adsorption. *Chem. Eng.* 1999, *106*, 104–108.

Park, Y.-J.; Lee, S.-J.; Moon, J.-H.; Choi, D.-K.; Lee, C.-H. Adsorption Equilibria of O<sub>2</sub>, N<sub>2</sub>, and Ar on Carbon Molecular Sieve and Zeolites 10X, 13X, and LiX. *J. Chem. Eng. Data* 2006, *51*, 1001–1008.

Perego, C.; Carati, A.; Ingallina, P.; Mantegazza, M. A.; Bellussi, G. Production of Titanium Containing Molecular Sieves and Their Application in Catalysis. *Appl. Catal. A-Gen.* 2001, *221*, 63–72.

Pillai, R. S.; Gomes, J. R. B.; Jorge, M. Molecular Simulation of the Adsorption of Methane in Engelhard Titanosilicate Frameworks. *Langmuir* 2014, *30*, 7435–7446.

Pohanish, R. P. *Sittig's Handbook of Toxic and Hazardous Chemicals and Carcinogens*; Edition, S., Ed.; Elsevier Inc., 2012.

Quyng, M., Huang, J.-L., Lieber, C. M. Fundamental Electronic Properties and Applications of Single Walled Carbon Nanotubes. *Acc. Chem. Res.* 2002, *35*, 1018–1025.

Rao, P. R. H.; Belhekar, A. A.; Hedge, S. G.; Ramaswamy, A. V; Ratnasamy, P. Studies on Crystalline Microporous Vanadium Silicates. II. FTIR, NMR, and ESR Spectroscopy and Catalytic Oxidation of Alkylaromatics over VS-2. *J. Catal.* 1993, *141*, 595–603.

Rees, L. V. C.; Bruckner, P.; Hampson, J. Sorption of N<sub>2</sub>, CH<sub>4</sub> and CO<sub>2</sub> in Silicalite-1. *Gas Sep. Purif.* 1991, *5*, 67.

Reyes, D. R. S. Adsorptive Separation of Light Olefins from Paraffins. *Micropor. Mesopor. Mat.* 2007, *104*, 59–66.

Rocha, J.; Anderson, M. W. Microporous Titanosilicates and Other Novel Mixed Octahedral-Tetrahedral Framework Oxides. *Inorg. Chem.* 2000, 801–818.

Rocha, J.; Brandao, P.; Lin, Z.; Anderson, M. W.; Alfredsson, V.; Terasaki, O. The First Large-Pore Vanadosilicate Framework Containing Hexacoordinated Vanadium. *Angew. Chem. Int. Ed. Engl.* 1997, *36*, 100–102.

Rocha, J.; Brandao, P.; Phillippou, A.; Anderson, M. W. Synthesis and Characterisation of a Novel Microporous Niobium Silicate Catalyst. *Chem. Commun.* 1998, 2687–2688.

Rocha, J.; Ferreira, A.; Lin, Z.; Anderson, M. W. Synthesis of Microporous Titanosilicate ETS-10 from TiCl<sub>3</sub> and TiO<sub>2</sub>: A Comprehensive Study. *Micropor. Mesopor. Mat.* 1998, *23*, 253–263.

Rocha, J.; Ferreira, P.; Lin, Z.; R. Agger, J.; W. Anderson, M.; J., R. A.; M., W. A. Synthesis and Characterisation of a Microporous Zirconium Silicate with the Structure of Petarasite. *Chem. Commun.* 1998, 1269–1270.

Rocha, J.; Lin, Z. Microporous Mixed Octahedral-Pentahedral-Tetrahedral Framework Silicates. *Rev. Miner. Geochem.* 2005, 57, 173–201.

Rolniak, P.; Kobayashi, R. Analysis of Methane and Several Mixtures of Methane and Carbon Dioxide at Elevated Pressures at near Ambient Temperatures on 5A and 13X Molecular Sieves by Tracer Perturbation Chromatography. *AICHE J.* 1980, 26, 616–624.

Ruthven, D. M. *Principles of Adsorption and Adsorption Processes*; John Wiley & Sons, Inc. , 1984.

Sankar, G.; Bell, R. G.; Thomas, J. M.; Anderson, M. W.; Wright, P. A.; Rocha, J. Determination of the Structure of Distorted TiO<sub>6</sub> Units in the Titanosilicate ETS-10 by a Combination of X-Ray Absorption Spectroscopy and Computer Modeling. *J. Phys. Chem.* 1996, 100, 449–452.

Schirmer, W. Results and Perspectives of the Investigation of Hydrocarbon Adsorption in the Central Institute of Physical Chemistry of the Academy of Sciences of the GDR. In *Academy of Sciences*; 1979; pp. 1–14.

Sebastian, J.; Jasra, R. V. Sorption of Nitrogen, Oxygen, and Argon in Silver-Exchanged Zeolites. *Ind. Eng. Chem. Res.* 2005, 44 , 8014–8024.

Sherman, J. D. Synthetic Zeolites and Other Microporous Oxide Molecular Sieves. 1999, 96, 3471–3478.

Shi, M.; Avila, A. M.; Yang, F.; Kuznicki, T. M.; Kuznicki, S. M. High Pressure Adsorptive Separation of Ethylene and Ethane on Na-ETS-10 . *Chem. Eng. Sci.* 2011, 66, 2817–2822.

Shi, M.; Kim, J.; Sawada, J. A.; Lam, J.; Sarabadan, S.; Kuznicki, T. M.; Kuznicki, S. M. Production of Argon Free Oxygen by Adsorptive Air Separation on Ag-ETS-10. *AICHE J.* 2013, 59, 982–987.

Shi, M.; Lin, C. C. H.; Kuznicki, T. M.; Hashisho, Z.; Kuznicki, S. M. Separation of a Binary Mixture of Ethylene and Ethane by Adsorption on Na-ETS-10. *Chem. Eng. Sci.* 2010, 65, 3494–3498.

Silva, F. A. Da; Rodrigues, A. E. Adsorption Equilibria and Kinetics for Propylene and Propane over 13X and 4A Zeolite Pellets. *Ind. Eng. Chem. Res.* 1999, 38, 2051–2057.

Silva, J. A. C.; Schumann, K.; Rodrigues, A. E. Sorption and Kinetics of CO<sub>2</sub> and CH<sub>4</sub> in Binderless Beads of 13X Zeolite. *Micropor. Mesopor. Mat.* 2012, 158, 219–228.

Sircar, S.; Myers, A. L. Chapter 22: Gas Separation by Zeolites. In *Hand book of Zeolite Science and Technology*; Auerbach, M. S.; Carrado, A. K.; Dutta, K. P., Eds.; Marcel Dekker, Inc., 2003; Vol. 10.

Sircar, S.; Myers, A. L. *Handbook of Zeolite Science and Technology (Gas Separation by Zeolites)*; Marcel Dekker Inc., New York, 2003.

Song, C.; Yan, Z. *Characterization and Cracking of the Modified USY Zeolites with Mixed Organic Acid*; Dongying, China.

Sondi, I.; Salopek-Sondi, B. Silver Nanoparticles as Antimicrobial Agent: A Case Study on E. Coli as a Model for Gram-Negative Bacteria. *J. Colloid Interface Sci.* 2004, 275, 177–182.

Stach, H.; Thamm, H.; Fiedler, K.; Schirmer, W. Contribution to the Thermodynamics of Adsorption of N-Paraffins on NaX Type Zeolite. In *Academy of Sciences*; 1979; pp. 85–93.

Stathatos, E.; Lianos, P. Photocatalytically Deposited Silver Nanoparticles on Mesoporous TiO<sub>2</sub> Films. *Langmuir* 2000, 16, 2398–2400.

Sun, Y.; Xia, Y. Shape-Controlled Synthesis of Gold and Silver Nanoparticles. *Science* 2002, 298, 2176–2179.

Tanchuk, B.; Sawada, J. A.; Rezaei, S.; Kuznicki, S. M. Adsorptive Drying of CO<sub>2</sub> Using Low Grade Heat and Humid, Ambient Air. *Sep. Purif. Technol.* 2013, 120, 354–361.

Thomos, W. J.; Crittenden, B. *Adsorption Technology and Design*; Elsevier Science Technology Books, 1998.

Tiscornia, I.; Irusta, S.; Prádanos, P.; Tellez, C.; Coronas, J.; Santamaría, J. Preparation and Characterization of Titanosilicate Ag-ETS-10 for Propylene and Propane Adsorption. *J. Phys. Chem. C* 2007, 111, 4702–4709.

Toth, J. State Equations of the Solid-Gas Interface Layers. *Acta. Chim. Acad. Sci. Hung* 1971, 69, 311–328.

T.P. Das, A.J. Chandwadkar, A.P. Budhkar, S. S. Studies on the Synthesis of ETS-10 II. Use of Organic Templates. *Microporous Mater.* 1996, 5, 401–410.

Triebe, R. W.; Tezel, F. H.; Khulbe, K. C. Adsorption of Methane, Ethane and Ethylene on Molecular Sieve Zeolites. *Gas Sep. Purif.* 1996, 10, 81–84.

Valtchev, V.; Mintova, S. Synthesis of Titanium Silicate ETS-10: The Effect of Tetramethylammonium on the Crystallization Kinetics. *Zeolites* 1994, 14, 697–700.

- Valtchev, V. P. Influence of Different Organic Bases on the Crystallization of Titanium Silicate ETS-10. *J. Chem. Soc. Chem. Commun.* 1994, 261.
- Venkataraman, L.; Lieber, C. M. Molybdenum Selenide Molecular Wires as One-Dimensional Conductors. *Phys. Rev. Lett.* 1999, 83, 5334–5337.
- Vigne-Maeder, F.; Auroux, A. Potential Maps of Methane, Water, and Methanol in Silicalite. *J. Phys. Chem.* 1990, 94, 316–322.
- Went, G. T.; Oyama, S. T.; Bell, A. T. Laser Raman Spectroscopy of Supported Vanadium Oxide Catalysts. *J. Phys. Chem.* 1990, 94, 4240–4246.
- Wu, F.-C.; Liu, B.-L.; Wu, K.-T.; Tseng, R.-L. A New Linear Form Analysis of Redlich-Peterson Isotherm Equation for the Adsorptions of Dyes. *Chem. Eng. J.* 2010, 162, 21–27.
- Xamena, F. X. L. I.; Calza, P.; Lamberti, C.; Prestipino, C.; Damin, A.; Bordiga, S.; Pelizzetti, E.; Zecchina, A. Enhancement of the ETS-10 Titanosilicate Activity in the Shape-Selective Photocatalytic Degradation of Large Aromatic Molecules by Controlled Defect Production. *J. Am. Chem. Soc.* 2003, 125, 2264–2271.
- Xiong, C.; Aliev, A. E.; Gnade, B.; Balkus, K. J. Fabrication of Silver Vanadium Oxide and V<sub>2</sub>O<sub>5</sub> Nanowires for Electrochromics. *ACS Nano* 2008, 2, 293–301.
- Xu, J.; Malek, A.; Farooq, S. Production of Argon from an Oxygen-Argon Mixture by Pressure Swing Adsorption. *Ind. Eng. Chem. Res.* 2006, 45, 5775–5787.
- Yang, J.; Lee, C.-H.; Chang, J.-W. Separation of Hydrogen Mixtures by a Two-Bed Pressure Swing Adsorption Process Using Zeolite 5A. *Ind. Eng. Chem. Res.* 1997, 36, 2789–2798.
- Yang, R. T. *Adsorbents, Fundamentals and Applications*; John Wiley & Sons, Inc.: Hoboken, New Jersey, 2003; p. 410.
- Yang, R. T. *Gas Separation by Adsorption Process*; Butterworth, Boston, 1987.
- Yilmaz, B.; Deng, J.; Jr., A. S. Electrical Transport Through Monoatomic Titania Chains. *Appl. Phys. Lett.* 2007, 90, 152101–152103.

# Appendix

## Appendix A: Unconstrained Optimization Parameter for the most accurate fit on ETS-10, 13X and high silicalite ZSM-5

Table 1: Unconstrained Optimization Parameter for the most accurate fit on ETS-10

<b>C<sub>2</sub>H<sub>6</sub></b>				<b>CO<sub>2</sub></b>			
	<b>Redlich Peterson Model</b>				<b>Redlich Peterson Model</b>		
	<b>303</b>	<b>323</b>	<b>343</b>	<b>T/K</b>	<b>303</b>	<b>323</b>	<b>343</b>
<b>T/K</b>				<b>SSE</b>	2.287e-02	9.687e-03	3.943e-03
<b>SSE</b>	9.021e-04	4.394e-04	2.758e-04	<b>q<sub>s</sub>/mmol.g<sup>-1</sup></b>	1.763	1.540	1.358
<b>q<sub>s</sub>/mmol.g<sup>-1</sup></b>	1.533	1.458	1.401	<b>b/kPa</b>	3.064	1.21	5.664e-01
<b>b/kPa</b>	7.684e-01	3.355e-01	1.597e-01	<b>β</b>	8.887e-01	8.783e-01	8.710e-01
<b>β</b>	9.453e-01	9.459e-01	9.476e-01	<b>H/mmol.g<sup>-1</sup>.kpa<sup>-1</sup></b>	5.402	1.863	7.691e-01
<b>H/mmol.g<sup>-1</sup>.kpa<sup>-1</sup></b>	1.178	4.891e-01	2.237e-01				
<b>C<sub>2</sub>H<sub>4</sub></b>				<b>CH<sub>4</sub></b>			
	<b>Redlich Peterson Model</b>				<b>Langmuir Model</b>		
	<b>303</b>	<b>323</b>	<b>343</b>	<b>T/K</b>	<b>303</b>	<b>323</b>	<b>343</b>
<b>T/K</b>				<b>SSE</b>	1.389e-05	1.561e-05	2.320e-05
<b>SSE</b>	1.963e-02	2.105e-03	1.932e-03	<b>q<sub>s</sub>/mmol.g<sup>-1</sup></b>	2.115	2.078	1.949
<b>q<sub>s</sub>/mmol.g<sup>-1</sup></b>	1.839	1.719	1.638	<b>b/kPa</b>	9.733e-03	5.835e-03	3.827e-03
<b>b/kPa</b>	8.129	2.920	1.099	<b>H/mmol.g<sup>-1</sup>.kpa<sup>-1</sup></b>	2.0585e-02	1.2125e-02	7.459e-03
<b>β</b>	9.501e-01	9.466e-01	9.460e-01				
<b>H/mmol.g<sup>-1</sup>.kpa<sup>-1</sup></b>	1.495e+01	5.019	1.800				

**Table 2: Unconstrained Optimization Parameter for the Best Models on 13X**

<b>C<sub>2</sub>H<sub>4</sub></b>				<b>CO<sub>2</sub></b>			
<b>Toth Model</b>				<b>Toth Model</b>			
	<b>303</b>	<b>323</b>	<b>343</b>		<b>303</b>	<b>323</b>	<b>343</b>
<b>T/K</b>				<b>T/K</b>			
<b>SSE</b>	1.305e-02	3.506e-03	2.090e-02	<b>SSE</b>	1.171e-01	3.800e-02	1.179e-02
<b>q<sub>s</sub>/mmol.g<sup>-1</sup></b>	4.72	4.506	4.280	<b>q<sub>s</sub>/mmol.g<sup>-1</sup></b>	8.987	8.732	8.392
<b>b/kPa</b>	1.051	2.125	4.362	<b>b/kPa</b>	6.265e-01	9.632e-01	1.541
<b>t</b>	5.699e-01	6.333e-01	6.992e-01	<b>t</b>	3.096e-01	3.376e-01	3.741e-01
<b>H/mmol.g<sup>-1</sup>.kpa<sup>-1</sup></b>	4.325	1.370	5.206e-01	<b>H/mmol.g<sup>-1</sup>.kpa<sup>-1</sup></b>	4.069e+01	9.757	2.641
<b>C<sub>2</sub>H<sub>6</sub></b>				<b>CH<sub>4</sub></b>			
<b>Langmuir Model</b>				<b>Langmuir Model</b>			
	<b>303</b>	<b>323</b>	<b>343</b>		<b>303</b>	<b>323</b>	<b>343</b>
<b>T/K</b>				<b>T/K</b>			
<b>SSE</b>	1.028e-01	4.375e-02	1.102e-02	<b>SSE</b>	9.516e-06	1.692e-05	8.284e-06
<b>q<sub>s</sub>/mmol.g<sup>-1</sup></b>	4.184	4.384	4.781	<b>q<sub>s</sub>/mmol.g<sup>-1</sup></b>	7.395	6.187	4.691
<b>b/kPa</b>	3.827e-02	1.743e-02	8.140e-03	<b>b/kPa</b>	9.581e-04	7.705e-04	7.154e-04
<b>H/mmol.g<sup>-1</sup>.kpa<sup>-1</sup></b>	1.601e-01	7.641e-02	3.892e-02	<b>H/mmol.g<sup>-1</sup>.kpa<sup>-1</sup></b>	7.085e-03	4.767e-03	3.356e-03

**Table 3: Unconstrained Optimization Parameter for the Best Models on high siliceous ZSM-5**

<b>CH<sub>4</sub></b>				<b>CO<sub>2</sub></b>			
<b>Langmuir Model</b>				<b>Langmuir Model</b>			
	<b>303</b>	<b>323</b>	<b>343</b>		<b>303</b>	<b>323</b>	<b>343</b>
<b>T/K</b>				<b>T/K</b>			
<b>SSE</b>	4.204e-06	3.031e-05	7.558e-06	<b>SSE</b>	9.942e-04	3.654e-04	3.485e-04
<b>q<sub>s</sub>/mmol.g<sup>-1</sup></b>	2.525	2.314	2.33	<b>q<sub>s</sub>/mmol.g<sup>-1</sup></b>	3.296	3.393	3.323
<b>b/kPa</b>	2.839e-03	1.971e-03	1.209e-03	<b>b/kPa</b>	8.040e-03	4.124e-03	2.511e-03
<b>H/mmole.g<sup>-1</sup>.kpa<sup>-1</sup></b>	7.168e-03	4.561e-03	2.817e-03	<b>H/mmole.g<sup>-1</sup>.kpa<sup>-1</sup></b>	2.650e-02	1.399e-02	8.344e-03
<b>C<sub>2</sub>H<sub>4</sub></b>				<b>C<sub>2</sub>H<sub>6</sub></b>			
<b>Langmuir Model</b>				<b>Langmuir Model</b>			
	<b>303</b>	<b>323</b>	<b>343</b>		<b>303</b>	<b>323</b>	<b>343</b>
<b>T/K</b>				<b>T/K</b>			
<b>SSE</b>	1.784e-03	1.531e-03	1.113e-03	<b>SSE</b>	4.119e-03	3.024e-03	2.612e-03
<b>q<sub>s</sub>/mmol.g<sup>-1</sup></b>	2.23	2.246	2.267	<b>q<sub>s</sub>/mmol.g<sup>-1</sup></b>	2.093	2.075	2.105
<b>b/kPa</b>	3.428e-02	1.697e-02	8.721e-03	<b>b/kPa</b>	8.065e-02	3.793e-02	1.806e-02
<b>H/mmole.g<sup>-1</sup>.kpa<sup>-1</sup></b>	7.644e-02	3.811e-02	1.977e-02	<b>H/mmole.g<sup>-1</sup>.kpa<sup>-1</sup></b>	1.688e-01	7.870e-02	3.801e-02

## Appendix B: Values of Entropy, Gibbs Free Energy and Adsorbate Entropy on high silicalite ZSM-5, ETS-10 and 13X at 343K at different loadings

Table 1: Thermodynamic data for the adsorption of carbon dioxide on high siliceous ZSM-5. All data sets are at 343 K.

q (mmol/g)	$\Delta G$ (KJ/mol)	$\Delta S$ (J/mol.K)	$S_a$ (J/mol.K)
0.01	-12.57685416	-39.84741563	178.7343835
0.02	-10.60238478	-45.63334376	172.9484554
0.03	-9.44374306	-49.0275742	169.554225
0.04	-8.619158955	-51.44288743	167.1389117
0.05	-7.977590807	-53.32173294	165.2600662
0.06	-7.451763595	-54.86101833	163.7207808
0.07	-7.00585805	-56.16632552	162.4154736
0.08	-6.618371197	-57.30009908	161.2817001
0.09	-6.275543925	-58.30325685	160.2785423
0.1	-5.967930675	-59.20289997	159.3788992
0.11	-5.688774667	-60.01912746	158.5626717
0.12	-5.433146432	-60.76668201	157.8151172
0.13	-5.197247147	-61.45611272	157.1256864
0.14	-4.978158315	-62.09626758	156.4855316
0.15	-4.773550393	-62.6939751	155.8878241
0.16	-4.581545819	-63.25473892	155.3270602
0.17	-4.400609176	-63.78335285	154.7984463
0.18	-4.229481258	-64.28292171	154.2988775
0.19	-4.067094976	-64.75686655	153.8249326
0.2	-3.912536709	-65.20786543	153.3739337
0.21	-3.765059162	-65.63781574	152.9439834
0.22	-3.623988218	-66.04927974	152.5325194
0.23	-3.488750037	-66.44364638	152.1381528
0.24	-3.358853362	-66.82235567	151.7594435
0.25	-3.233858032	-67.18669784	151.3951013
0.26	-3.11336745	-67.53754228	151.0442569
0.27	-2.997046575	-67.87645735	150.7053418
0.28	-2.884596636	-68.20402569	150.3777735
0.29	-2.775727731	-68.52080395	150.0609952
0.3	-2.670201763	-68.82807632	149.7537228
0.31	-2.567803808	-69.12588654	149.4559126
0.32	-2.468325831	-69.41513753	149.1666616
0.33	-2.37158584	-69.6966559	148.8851433
0.34	-2.277418204	-69.97034089	148.6114583
0.35	-2.185677814	-70.236911	148.3448882

0.36	-2.096219913	-70.49679052	148.0850086
0.37	-2.008917628	-70.7506445	147.8311547
0.38	-1.923659802	-70.99821251	147.5835867
0.39	-1.840327708	-71.2401357	147.3416635
0.4	-1.758832912	-71.47667328	147.1051259
0.41	-1.679077998	-71.70811081	146.8736884
0.42	-1.600972827	-71.93441938	146.6473798
0.43	-1.524448211	-72.15638807	146.4254111
0.44	-1.449420758	-72.37396817	146.207831
0.45	-1.375826706	-72.58734661	145.9944526
0.46	-1.303597501	-72.79643118	145.785368
0.47	-1.232673522	-73.00198293	145.5798162
0.48	-1.163003153	-73.2035669	145.3782323
0.49	-1.094525501	-73.40194782	145.1798513
0.5	-1.027191709	-73.59668266	144.9851165
0.51	-0.960963695	-73.78846931	144.7933299
0.52	-0.895786163	-73.97688359	144.6049156
0.53	-0.831622386	-74.16232629	144.4194729
0.54	-0.768430248	-74.34492086	144.2368783
0.55	-0.706177269	-74.52476251	144.0570367
0.56	-0.644825591	-74.70196221	143.879837
0.57	-0.584339497	-74.87662466	143.7051745
0.58	-0.524688619	-75.04883887	143.5329603
0.59	-0.465844155	-75.21868927	143.3631099
0.6	-0.407775533	-75.38626547	143.1955337
0.61	-0.350460141	-75.55134064	143.0304585
0.62	-0.293863958	-75.71460074	142.8671984
0.63	-0.237970111	-75.87550898	142.7062902
0.64	-0.1827504	-76.03473428	142.5470649
0.65	-0.128183979	-76.19175149	142.3900477
0.66	-0.074250959	-76.34720516	142.234594
0.67	-0.020926714	-76.50058123	142.0812179

---

**Table 2: Thermodynamic data for the adsorption of carbon dioxide on ETS-10. All data sets are at 343 K.**

q (mmol/g)	$\Delta G$ (KJ/mol)	$\Delta S$ (J/mol.K)	$S_a$ (J/mol.K)
0.01	-25.67072674	-40.4973874	178.5362946
0.02	-23.66003017	-46.93052245	172.1031596
0.03	-22.46078062	-50.98832212	168.0453599
0.04	-21.60698281	-54.06900534	164.9646767
0.05	-20.94144644	-56.56483721	162.4688448
0.06	-20.39119881	-57.98522727	161.0484547
0.07	-19.92380245	-59.26784746	159.7658345
0.08	-19.51433744	-60.54139523	158.4922868
0.09	-19.14934195	-61.78432	157.249362
0.1	-18.82157757	-62.92951595	156.1041661
0.11	-18.52203645	-63.67916428	155.3545177
0.12	-18.24755476	-64.47470734	154.5589747
0.13	-17.99255676	-65.29318625	153.7404958
0.14	-17.75424499	-66.1308272	152.9028548
0.15	-17.53039058	-66.76172511	152.2719569
0.16	-17.32037274	-67.34789877	151.6857832
0.17	-17.12136616	-67.96996622	151.0637158
0.18	-16.93216522	-68.62272862	150.4109534
0.19	-16.7517553	-69.15643836	149.8772436
0.2	-16.57927436	-69.64023074	149.3934513
0.21	-16.41398368	-70.15881884	148.8748632
0.22	-16.25606251	-70.7035709	148.3301111
0.23	-16.10327932	-71.13956448	147.8941175
0.24	-15.95601176	-71.56566199	147.46802
0.25	-15.81383201	-72.02424452	147.0094375
0.26	-15.67569369	-72.49632424	146.5373578
0.27	-15.54198849	-72.85850068	146.1751813
0.28	-15.41240884	-73.25421168	145.7794703
0.29	-15.28667903	-73.67875118	145.3549308
0.3	-15.16399227	-74.04435095	144.9893311
0.31	-15.04472848	-74.3942388	144.6394432
0.32	-14.92816541	-74.7745461	144.2591359
0.33	-14.81417425	-75.13697159	143.8967104
0.34	-14.70263559	-75.45781374	143.5758683
0.35	-14.59389643	-75.80647131	143.2272107
0.36	-14.48736218	-76.15337626	142.8803057
0.37	-14.38293939	-76.45244275	142.5812393
0.38	-14.28095125	-76.7783536	142.2553284
0.39	-14.18048058	-77.1033447	141.9303373

0.4	-14.08149295	-77.38927147	141.6444105
0.41	-13.9846951	-77.70275214	141.3309299
0.42	-13.8892644	-78.00039287	141.0332891
0.43	-13.79551819	-78.27953589	140.7541461
0.44	-13.7033945	-78.584979	140.448703
0.45	-13.61250952	-78.85351434	140.1801677
0.46	-13.52283795	-79.13099246	139.9026895
0.47	-13.43466052	-79.42007673	139.6136053
0.48	-13.34733191	-79.67425202	139.35943
0.49	-13.26143101	-79.95384322	139.0798388
0.5	-13.17662931	-80.20880976	138.8248723
0.51	-13.09263301	-80.46955525	138.5641268
0.52	-13.00997063	-80.73338945	138.3002926
0.53	-12.92808485	-80.9775899	138.0560921
0.54	-12.84697584	-81.24648461	137.7871974
0.55	-12.76688485	-81.47795206	137.5557299
0.56	-12.68755426	-81.73532011	137.2983619
0.57	-12.60921107	-81.96780799	137.065874
0.58	-12.53161046	-82.21523841	136.8184436
0.59	-12.45453178	-82.44782913	136.5858529
0.6	-12.37819961	-82.68839748	136.3452845
0.61	-12.30260862	-82.91812655	136.1155555
0.62	-12.22775292	-83.15296851	135.8807135
0.63	-12.15343049	-83.37844273	135.6552393
0.64	-12.07964944	-83.61133002	135.422352
0.65	-12.0066024	-83.83050152	135.2031805
0.66	-11.93391847	-84.0628177	134.9708643
0.67	-11.86196946	-84.27533113	134.7583509
0.68	-11.79040087	-84.50325693	134.5304251
0.69	-11.71922817	-84.71468008	134.3190019
0.7	-11.64862924	-84.93342245	134.1002596
0.71	-11.57844433	-85.1489372	133.8847448
0.72	-11.50868461	-85.35887407	133.6748079
0.73	-11.43935995	-85.57769099	133.455991
0.74	-11.37033003	-85.7820367	133.2516453
0.75	-11.30175827	-85.99113931	133.0425427
0.76	-11.23350876	-86.20394392	132.8297381
0.77	-11.16559657	-86.40418205	132.6295
0.78	-11.09817073	-86.60909536	132.4245866
0.79	-11.03083716	-86.81837705	132.215305
0.8	-10.96388386	-87.0149678	132.0187142
0.81	-10.89732033	-87.21506495	131.8186171
0.82	-10.83090815	-87.4179106	131.6157714

0.83	-10.76479213	-87.61671121	131.4169708
0.84	-10.69898638	-87.81113609	131.2225459
0.85	-10.63327334	-88.00703075	131.0266513
0.86	-10.56790533	-88.20366413	130.8300179
0.87	-10.50278227	-88.40074671	130.6329353
0.88	-10.43781287	-88.59129982	130.4423822
0.89	-10.37301922	-88.78163344	130.2520486
0.9	-10.30842175	-88.97168839	130.0619936
0.91	-10.24403931	-89.16169982	129.8719822
0.92	-10.17979087	-89.35103325	129.6826488
0.93	-10.1156989	-89.53962365	129.4940584
0.94	-10.0516901	-89.7273936	129.3062884
0.95	-9.987881885	-89.91371321	129.1199688
0.96	-9.92420186	-90.09908197	128.9346
0.97	-9.860672102	-90.28314616	128.7505358
0.98	-9.797227005	-90.46609589	128.5675861
0.99	-9.733891139	-90.64757022	128.3861118
1	-9.670604998	-90.82832103	128.205361
1.01	-9.607475747	-91.00803782	128.0256442
1.02	-9.544365296	-91.18683095	127.8468511
1.03	-9.481379085	-91.3649744	127.6687076
1.04	-9.418387699	-91.54255339	127.4911286
1.05	-9.355494633	-91.71984751	127.3138345
1.06	-9.292650671	-91.89699936	127.1366826
1.07	-9.22988186	-92.07132592	126.9623561
1.08	-9.167143384	-92.24440567	126.7892763
1.09	-9.10439473	-92.41780463	126.6158774
1.1	-9.041731732	-92.59153489	126.4421471
1.11	-8.979048432	-92.76126776	126.2724142
1.12	-8.916375066	-92.93184104	126.101841
1.13	-8.853739938	-93.10230353	125.9313785
1.14	-8.791048268	-93.26974281	125.7639392
1.15	-8.728391912	-93.43910789	125.5945741
1.16	-8.665739512	-93.6044053	125.4292767
1.17	-8.603006177	-93.7719653	125.2617167
1.18	-8.540281603	-93.93544371	125.0982383
1.19	-8.477539896	-94.10013068	124.9335513
1.2	-8.414758002	-94.26290598	124.770776
1.21	-8.351915541	-94.42469784	124.6089842
1.22	-8.289096419	-94.58613235	124.4475497
1.23	-8.226178925	-94.74698269	124.2866993
1.24	-8.163198591	-94.90540753	124.1282745
1.25	-8.100141129	-95.06318665	123.9704954

1.26	-8.037040924	-95.22022041	123.8134616
1.27	-7.97388463	-95.37625777	123.6574242
1.28	-7.910660828	-95.5313318	123.5023502
1.29	-7.847359902	-95.68518064	123.3485014
1.3	-7.783931239	-95.83795092	123.1957311
1.31	-7.720454756	-95.98970084	123.0439812
1.32	-7.656881917	-96.14086073	122.8928213
1.33	-7.593209169	-96.28970254	122.7439795
1.34	-7.529434215	-96.43768154	122.5960005
1.35	-7.465555923	-96.58509076	122.4485912
1.36	-7.401536879	-96.73058995	122.3030921
1.37	-7.337453538	-96.87511651	122.1585655
1.38	-7.273233817	-97.01829982	122.0153822
1.39	-7.20888275	-97.16070477	121.8729772
1.4	-7.144440173	-97.30076728	121.7329147
1.41	-7.079843302	-97.44011791	121.5935641
1.42	-7.015133859	-97.5777666	121.4559154
1.43	-6.950287188	-97.71436422	121.3193178
1.44	-6.885281892	-97.84939333	121.1842887
1.45	-6.820160638	-97.9827303	121.0509517
1.46	-6.754874027	-98.11480798	120.918874
1.47	-6.689465629	-98.24550013	120.7881819
1.48	-6.62389088	-98.37435642	120.6593256
1.49	-6.558166053	-98.50161943	120.5320626
1.5	-6.492307219	-98.62753232	120.4061497
1.51	-6.426277043	-98.75133408	120.2823479
1.52	-6.360068764	-98.87362375	120.1600583
1.53	-6.293702951	-98.99434173	120.0393403
1.54	-6.227174837	-99.11321212	119.9204699
1.55	-6.160505627	-99.23017347	119.8035085
1.56	-6.093644856	-99.345372	119.68831
1.57	-6.026594245	-99.45880271	119.5748793
1.58	-5.959401991	-99.57003624	119.4636458
1.59	-5.892024983	-99.67977696	119.3539051
1.6	-5.82444697	-99.78720275	119.2464793
1.61	-5.756717839	-99.89274855	119.1409335
1.62	-5.688802087	-99.99622748	119.0374545
1.63	-5.620688976	-100.0976706	118.9360114
1.64	-5.552409497	-100.1969883	118.8366937
1.65	-5.483954974	-100.2939158	118.7397662
1.66	-5.415300308	-100.3888156	118.6448664
1.67	-5.346460771	-100.4816434	118.5520386
1.68	-5.277433966	-100.5721166	118.4615654

1.69	-5.20821928	-100.6602368	118.3734452
1.7	-5.138817735	-100.7460011	118.287681
1.71	-5.069215275	-100.8294502	118.2042318
1.72	-4.999449317	-100.9104757	118.1232063
1.73	-4.929476425	-100.9892035	118.0444785
1.74	-4.859320507	-101.0655642	117.9681178
1.75	-4.788974816	-101.1392878	117.8943942
1.76	-4.718434903	-101.2106768	117.8230052
1.77	-4.647712739	-101.2794068	117.7542752
1.78	-4.576792925	-101.3455225	117.6881596
1.79	-4.50569048	-101.4092699	117.6244121
1.8	-4.434407422	-101.470064	117.563618
1.81	-4.362934327	-101.5285113	117.5051707
1.82	-4.291277049	-101.5843052	117.4493768
1.83	-4.219430309	-101.6371713	117.3965107
1.84	-4.147403125	-101.687663	117.346019
1.85	-4.075205414	-101.7354616	117.2982204
1.86	-4.002813595	-101.780346	117.2533361
1.87	-3.930252752	-101.8228227	117.2108593
1.88	-3.857514726	-101.862336	117.171346
1.89	-3.784604533	-101.8991611	117.1345209
1.9	-3.711518174	-101.9330199	117.1006621
1.91	-3.638253861	-101.964497	117.069185
1.92	-3.564831441	-101.9932451	117.0404369
1.93	-3.491241929	-102.0190006	117.0146814
1.94	-3.417488357	-102.0420445	116.9916376
1.95	-3.34357529	-102.0626531	116.9710289
1.96	-3.269508669	-102.0802298	116.9534522
1.97	-3.195278414	-102.0950937	116.9385883
1.98	-3.120902509	-102.1074822	116.9261998
1.99	-3.046374406	-102.1171247	116.9165573
2	-2.971706001	-102.1239867	116.9096953
2.01	-2.896894273	-102.1283666	116.9053154
2.02	-2.821938327	-102.1299773	116.9037047
2.03	-2.746853956	-102.1290629	116.9046192
2.04	-2.671628427	-102.1253703	116.9083117
2.05	-2.596280127	-102.119426	116.914256
2.06	-2.520813759	-102.1106367	116.9230454
2.07	-2.445215413	-102.0996222	116.9340599
2.08	-2.369506753	-102.08603	116.947652
2.09	-2.293683841	-102.0701613	116.9635207
2.1	-2.217751057	-102.0520033	116.9816787
2.11	-2.141720098	-102.0312325	117.0024495

2.12	-2.065579952	-102.0081705	117.0255115
2.13	-1.989350834	-101.9830484	117.0506336
2.14	-1.91302506	-101.9555988	117.0780832
2.15	-1.836613587	-101.9260797	117.1076023
2.16	-1.760117528	-101.8941981	117.1394839
2.17	-1.6835396	-101.8605256	117.1731564
2.18	-1.606893878	-101.8247316	117.2089504
2.19	-1.530175362	-101.7871205	117.2465615
2.2	-1.453390648	-101.7473833	117.2862987
2.21	-1.376542752	-101.7060908	117.3275912
2.22	-1.299640499	-101.662638	117.371044
2.23	-1.222684767	-101.6176017	117.4160803
2.24	-1.145686417	-101.5709506	117.4627315
2.25	-1.068640347	-101.5226993	117.5109827
2.26	-0.99155559	-101.4728217	117.5608603
2.27	-0.914441832	-101.4212898	117.6123922
2.28	-0.837294142	-101.3684075	117.6652745
2.29	-0.760124418	-101.3141405	117.7195415
2.3	-0.682934077	-101.2584845	117.7751975
2.31	-0.6057259	-101.2014316	117.8322505
2.32	-0.528507287	-101.1432499	117.8904321
2.33	-0.451283037	-101.0839257	117.9497563
2.34	-0.374055682	-101.0234516	118.0102304
2.35	-0.296832079	-100.9618077	118.0718743
2.36	-0.219613676	-100.8992795	118.1344025
2.37	-0.142403181	-100.8358592	118.1978228
2.38	-0.065210214	-100.7712293	118.2624527
2.39	0.011963696	-100.7059646	118.3277174
2.4	0.089113084	-100.6400495	118.3936325

---

**Table 3: Thermodynamic data for the adsorption of carbon dioxide on 13X. All data sets are at 343 K.**

q (mmol/g)	$\Delta G$ (KJ/mol)	$\Delta S$ (J/mol.K)	$S_a$ (J/mol.K)
0.01	-28.39962652	-41.48246697	177.551215
0.02	-26.41058725	-47.41159714	171.6220849
0.03	-25.08305338	-54.84585432	164.1878277
0.04	-24.15316774	-59.8410322	159.1926498
0.05	-23.41214286	-64.11200097	154.921681
0.06	-22.79167398	-68.0530958	150.9805862
0.07	-22.26848822	-71.46055854	147.5731235
0.08	-21.80911078	-74.49743364	144.5362484
0.09	-21.3935708	-77.34819411	141.6854879
0.1	-21.02204592	-79.99436211	139.0393199
0.11	-20.68166929	-82.46104797	136.572634
0.12	-20.37055428	-84.75661515	134.2770669
0.13	-20.08368361	-86.91501198	132.11867
0.14	-19.81159416	-88.99668503	130.036997
0.15	-19.55791381	-89.10759435	129.9260877
0.16	-19.32009063	-88.81764268	130.2160393
0.17	-19.09387874	-88.784648	130.249034
0.18	-18.8801218	-88.92678024	130.1069018
0.19	-18.67548679	-89.21110593	129.8225761
0.2	-18.48092689	-89.61110564	129.4225764
0.21	-18.29373286	-90.09638459	128.9372974
0.22	-18.11488012	-90.64934053	128.3843415
0.23	-17.94357909	-91.25690545	127.7767766
0.24	-17.77776058	-91.21639699	127.817285
0.25	-17.61837369	-91.15493645	127.8787456
0.26	-17.46363857	-91.20197429	127.8317077
0.27	-17.3144573	-91.34533593	127.6883461
0.28	-17.1704009	-91.56134752	127.4723345
0.29	-17.03001912	-91.84146278	127.1922192
0.3	-16.89312275	-92.18043532	126.8532467
0.31	-16.76148599	-92.24051575	126.7931663
0.32	-16.63189475	-92.22078879	126.8128932
0.33	-16.50701175	-92.27115239	126.7625296
0.34	-16.38477216	-92.39063549	126.6430465
0.35	-16.26506703	-92.56303916	126.4706428
0.36	-16.14858115	-92.78956642	126.2441156
0.37	-16.03512605	-92.87374749	126.1599345
0.38	-15.92380189	-92.86947157	126.1642104
0.39	-15.81453267	-92.92124389	126.1124381
0.4	-15.70792138	-93.02586881	126.0078132

0.41	-15.60317582	-93.17521129	125.8584707
0.42	-15.50086277	-93.33488984	125.6987922
0.43	-15.40085878	-93.31925602	125.714426
0.44	-15.30187748	-93.35454881	125.6791332
0.45	-15.20563	-93.43407214	125.5996099
0.46	-15.11031238	-93.5555197	125.4781623
0.47	-15.01699773	-93.66623866	125.3674434
0.48	-14.92507985	-93.66715965	125.3665224
0.49	-14.83501873	-93.70963717	125.3240448
0.5	-14.74624921	-93.79038329	125.2432987
0.51	-14.65920638	-93.90495036	125.1287316
0.52	-14.57290722	-93.93450031	125.0991817
0.53	-14.48824486	-93.95959769	125.0740843
0.54	-14.40472239	-94.02108535	125.0125967
0.55	-14.3227289	-94.114649	124.919033
0.56	-14.2417978	-94.157619	124.876063
0.57	-14.16190464	-94.17990833	124.8537737
0.58	-14.08302564	-94.23489601	124.798786
0.59	-14.00513774	-94.32033104	124.713351
0.6	-13.9285817	-94.34859713	124.6850849
0.61	-13.85259995	-94.37722744	124.6564546
0.62	-13.77788898	-94.43462559	124.5990564
0.63	-13.70406614	-94.51031106	124.5233709
0.64	-13.63111248	-94.52002759	124.5136544
0.65	-13.55900957	-94.55828025	124.4754018
0.66	-13.48773949	-94.62396208	124.4097199
0.67	-13.41728479	-94.65541129	124.3782707
0.68	-13.34762853	-94.68222939	124.3514526
0.69	-13.2787542	-94.73488571	124.2987963
0.7	-13.21064576	-94.77923871	124.2544433
0.71	-13.14328761	-94.79968823	124.2339938
0.72	-13.07666456	-94.84524248	124.1884395
0.73	-13.01049808	-94.89208148	124.1416005
0.74	-12.94530724	-94.91030786	124.1233742
0.75	-12.88055611	-94.95275645	124.0809256
0.76	-12.81649427	-94.99465662	124.0390254
0.77	-12.75334908	-95.01361994	124.0200621
0.78	-12.69038376	-95.05697883	123.9767032
0.79	-12.62830868	-95.08877683	123.9449052
0.8	-12.56664408	-95.11272177	123.9209602
0.81	-12.50561311	-95.15829897	123.875383
0.82	-12.44520334	-95.1783186	123.8553634
0.83	-12.38519057	-95.2084874	123.8251946

0.84	-12.32578387	-95.24877916	123.7849028
0.85	-12.26676788	-95.26591951	123.7677625
0.86	-12.20834285	-95.30336708	123.7303149
0.87	-12.15049726	-95.32696722	123.7067148
0.88	-12.09302834	-95.35382199	123.67986
0.89	-12.03593649	-95.38914534	123.6445367
0.9	-11.97940592	-95.40748682	123.6261952
0.91	-11.92342574	-95.44451473	123.5891673
0.92	-11.86780823	-95.46136976	123.5723123
0.93	-11.8125532	-95.49195076	123.5417312
0.94	-11.7576602	-95.51568825	123.5179938
0.95	-11.70329582	-95.54079149	123.4928905
0.96	-11.64928567	-95.5677657	123.4659163
0.97	-11.59562892	-95.58937008	123.4443119
0.98	-11.54248265	-95.61847705	123.415205
0.99	-11.48968175	-95.6370223	123.3966597
1	-11.43722508	-95.6670286	123.3666534
1.01	-11.38511131	-95.68416251	123.3495195
1.02	-11.33333899	-95.71334494	123.3203371
1.03	-11.28190654	-95.73053297	123.303149
1.04	-11.23081225	-95.75833043	123.2753516
1.05	-11.1800543	-95.77559234	123.2580897
1.06	-11.12976773	-95.80104961	123.2326324
1.07	-11.07967426	-95.81957336	123.2141087
1.08	-11.02991117	-95.84264473	123.1910373
1.09	-10.9803463	-95.86369317	123.1699888
1.1	-10.93123963	-95.88399354	123.1496885
1.11	-10.88245659	-95.90683299	123.126849
1.12	-10.83387132	-95.9244638	123.1092182
1.13	-10.78560906	-95.95014036	123.0835417
1.14	-10.73754777	-95.9650941	123.0685879
1.15	-10.68992572	-95.98688766	123.0467943
1.16	-10.64250325	-96.0060749	123.0276071
1.17	-10.59528332	-96.02438556	123.0092964
1.18	-10.5483805	-96.04815153	122.9855305
1.19	-10.50179183	-96.06260515	122.9710769
1.2	-10.4554061	-96.08226539	122.9514166
1.21	-10.40922553	-96.10277985	122.9309022
1.22	-10.36335698	-96.11862385	122.9150582
1.23	-10.31769408	-96.13850767	122.8951743
1.24	-10.27234011	-96.15691697	122.876765
1.25	-10.22709185	-96.17328162	122.8604004
1.26	-10.18215226	-96.19251844	122.8411636

1.27	-10.13751794	-96.2108708	122.8228112
1.28	-10.09299468	-96.22658356	122.8070984
1.29	-10.04868186	-96.24458392	122.7890981
1.3	-10.0046728	-96.26431176	122.7693703
1.31	-9.960781699	-96.27906215	122.7546199
1.32	-9.917192806	-96.2952548	122.7384272
1.33	-9.87372568	-96.31341249	122.7202695
1.34	-9.830558818	-96.33098995	122.7026921
1.35	-9.787516947	-96.34588745	122.6877946
1.36	-9.744688549	-96.36190483	122.6717772
1.37	-9.70199034	-96.37899365	122.6546884
1.38	-9.659589965	-96.39666822	122.6370138
1.39	-9.61732187	-96.41164169	122.6220403
1.4	-9.575268977	-96.42657112	122.6071109
1.41	-9.53335235	-96.4425544	122.5911276
1.42	-9.491652276	-96.45877944	122.5749026
1.43	-9.450091865	-96.4751793	122.5585027
1.44	-9.408748887	-96.49094919	122.5427328
1.45	-9.367548435	-96.50572668	122.5279553
1.46	-9.326565868	-96.52045236	122.5132296
1.47	-9.285728205	-96.53533766	122.4983443
1.48	-9.245037489	-96.55037668	122.4833053
1.49	-9.204495608	-96.56585366	122.4678283
1.5	-9.164173344	-96.58098408	122.4526979
1.51	-9.123933276	-96.59616608	122.4375159
1.52	-9.083914025	-96.61128777	122.4223942
1.53	-9.043981758	-96.62644717	122.4072348
1.54	-9.004271074	-96.64067485	122.3930072
1.55	-8.964651612	-96.6552177	122.3784643
1.56	-8.925190588	-96.66959123	122.3640908
1.57	-8.885888908	-96.68379282	122.3498892
1.58	-8.84674738	-96.69782014	122.3358619
1.59	-8.807705748	-96.71213748	122.3215445
1.6	-8.768827246	-96.72656165	122.3071204
1.61	-8.730053028	-96.74068368	122.2929983
1.62	-8.691444436	-96.7549053	122.2787767
1.63	-8.652944	-96.76881356	122.2648684
1.64	-8.614611246	-96.78252572	122.2511563
1.65	-8.576390044	-96.79591469	122.2377673
1.66	-8.538338179	-96.8093925	122.2242895
1.67	-8.500346047	-96.8232767	122.2104053
1.68	-8.462525972	-96.8366624	122.1970196
1.69	-8.424771014	-96.8504389	122.1832431

1.7	-8.387190378	-96.86428979	122.1693922
1.71	-8.349731692	-96.87836682	122.1553152
1.72	-8.312345228	-96.89165514	122.1420269
1.73	-8.275135724	-96.90472049	122.1289615
1.74	-8.238002581	-96.91785432	122.1158277
1.75	-8.200998339	-96.93119415	122.1024879
1.76	-8.164075422	-96.94516754	122.0885145
1.77	-8.127284848	-96.95817804	122.075504
1.78	-8.090627554	-96.97080239	122.0628796
1.79	-8.05405751	-96.98404314	122.0496389
1.8	-8.017577271	-96.99789288	122.0357891
1.81	-7.981234973	-97.01047378	122.0232082
1.82	-7.944986054	-97.0233636	122.0103184
1.83	-7.908788143	-97.03697481	121.9967072
1.84	-7.872777048	-97.04946531	121.9842167
1.85	-7.836821021	-97.06237572	121.9713063
1.86	-7.8009665	-97.07586122	121.9578208
1.87	-7.765172847	-97.08830118	121.9453808
1.88	-7.729527038	-97.10147171	121.9322103
1.89	-7.693946348	-97.11445358	121.9192284
1.9	-7.658474618	-97.12683002	121.906852
1.91	-7.623113202	-97.14004577	121.8936362
1.92	-7.587823512	-97.15247425	121.8812078
1.93	-7.552608188	-97.16584619	121.8678358
1.94	-7.517508642	-97.17801349	121.8556685
1.95	-7.482487438	-97.19111274	121.8425693
1.96	-7.447546882	-97.20339887	121.8302831
1.97	-7.412726663	-97.21649525	121.8171868
1.98	-7.377953423	-97.22887607	121.8048059
1.99	-7.3432671	-97.24158453	121.7920975
2	-7.308669575	-97.25432544	121.7793566
2.01	-7.274162633	-97.2668039	121.7668781
2.02	-7.239712662	-97.27969676	121.7539852
2.03	-7.205357406	-97.29202548	121.7416565
2.04	-7.17109836	-97.3046549	121.7290271
2.05	-7.136902876	-97.3173899	121.7162921
2.06	-7.10277349	-97.32993339	121.7037486
2.07	-7.06874589	-97.34247171	121.6912103
2.08	-7.03475548	-97.35490228	121.6787797
2.09	-7.000870612	-97.36789624	121.6657858
2.1	-6.967060152	-97.3803849	121.6532971
2.11	-6.9332944	-97.39274402	121.640938
2.12	-6.899607756	-97.40516368	121.6285183

2.13	-6.866002043	-97.41792831	121.6157537
2.14	-6.832478996	-97.43045344	121.6032286
2.15	-6.799009988	-97.44311172	121.5905703
2.16	-6.765597634	-97.4558956	121.5777864
2.17	-6.732274021	-97.46842236	121.5652596
2.18	-6.698982048	-97.48085746	121.5528245
2.19	-6.665782842	-97.49331351	121.5403685
2.2	-6.632649035	-97.50586981	121.5278122
2.21	-6.599582741	-97.51852023	121.5151618
2.22	-6.566558062	-97.53133982	121.5023422
2.23	-6.533605485	-97.5439505	121.4897315
2.24	-6.500726842	-97.55634698	121.477335
2.25	-6.467896898	-97.56889208	121.4647899
2.26	-6.435144906	-97.58150107	121.4521809
2.27	-6.402419699	-97.59403245	121.4396496
2.28	-6.3697767	-97.60690511	121.4267769
2.29	-6.337191527	-97.61961024	121.4140718
2.3	-6.304640889	-97.6322153	121.4014667
2.31	-6.272178145	-97.64485544	121.3888266
2.32	-6.239754616	-97.65767169	121.3760103
2.33	-6.2073977	-97.67029494	121.3633871
2.34	-6.175084867	-97.68308021	121.3506018
2.35	-6.142818681	-97.69573032	121.3379517
2.36	-6.110601605	-97.7088176	121.3248644
2.37	-6.078459561	-97.72139777	121.3122842
2.38	-6.046347451	-97.73418093	121.2995011
2.39	-6.014314306	-97.74702504	121.286657
2.4	-5.982315897	-97.75976852	121.2739135
2.41	-5.950354992	-97.77298278	121.2606992
2.42	-5.918456536	-97.78572639	121.2479556
2.43	-5.886600325	-97.79863733	121.2350447
2.44	-5.854788838	-97.81170842	121.2219736
2.45	-5.823046004	-97.82458061	121.2091014
2.46	-5.79133078	-97.83766252	121.1960195
2.47	-5.759667153	-97.85059495	121.1830871
2.48	-5.72803639	-97.86372189	121.1699601
2.49	-5.696482437	-97.87691601	121.156766
2.5	-5.664945376	-97.8900612	121.1436208
2.51	-5.633448577	-97.90308974	121.1305923
2.52	-5.602014417	-97.91622652	121.1174555
2.53	-5.570605115	-97.92958101	121.104101
2.54	-5.539262609	-97.94274197	121.09094
2.55	-5.507930502	-97.95616253	121.0775195

2.56	-5.476669426	-97.9693773	121.0643047
2.57	-5.445424074	-97.98283623	121.0508458
2.58	-5.414234958	-97.99613224	121.0375498
2.59	-5.383085414	-98.00960332	121.0240787
2.6	-5.351959499	-98.02300594	121.0106761
2.61	-5.32087815	-98.03656917	120.9971128
2.62	-5.289843528	-98.04999702	120.983685
2.63	-5.258840011	-98.06362448	120.9700575
2.64	-5.22787017	-98.07715437	120.9565276
2.65	-5.19693648	-98.09086925	120.9428128
2.66	-5.166041327	-98.10447247	120.9292095
2.67	-5.135187012	-98.1182471	120.9154349
2.68	-5.104358973	-98.13194561	120.9017364
2.69	-5.073559879	-98.14584998	120.887832
2.7	-5.042808722	-98.15990519	120.8737768
2.71	-5.012091217	-98.17357318	120.8601088
2.72	-4.981393694	-98.187473	120.846209
2.73	-4.950734878	-98.2015504	120.8321316
2.74	-4.920101262	-98.2155548	120.8181272
2.75	-4.889511052	-98.22972316	120.8039589
2.76	-4.858950903	-98.24380443	120.7898776
2.77	-4.828408044	-98.25812533	120.7755567
2.78	-4.797900413	-98.27234416	120.7613378
2.79	-4.767430298	-98.2864543	120.7472277
2.8	-4.736985145	-98.30078185	120.7329002
2.81	-4.706567546	-98.31531929	120.7183627
2.82	-4.676180001	-98.32976966	120.7039123
2.83	-4.645810629	-98.34416738	120.6895146
2.84	-4.615476355	-98.35875314	120.6749289
2.85	-4.58517942	-98.37323071	120.6604513
2.86	-4.554894284	-98.38796383	120.6457182
2.87	-4.524637603	-98.40261451	120.6310675
2.88	-4.494411803	-98.41746544	120.6162166
2.89	-4.464205804	-98.43225901	120.601423
2.9	-4.434022286	-98.44727717	120.5864048
2.91	-4.403876978	-98.46218462	120.5714974
2.92	-4.373745961	-98.47705067	120.5566313
2.93	-4.343632064	-98.49215685	120.5415252
2.94	-4.313550754	-98.50716861	120.5265134
2.95	-4.283479074	-98.5224422	120.5112398
2.96	-4.253444917	-98.53760708	120.4960749
2.97	-4.223425681	-98.55301845	120.4806636
2.98	-4.19342414	-98.56837856	120.4653034

2.99	-4.16345506	-98.58393435	120.4497477
3	-4.133496739	-98.59945896	120.434223
3.01	-4.103563896	-98.61490976	120.4187722
3.02	-4.07364724	-98.63060339	120.4030786
3.03	-4.043749473	-98.64624229	120.3874397
3.04	-4.013873209	-98.66181889	120.3718631
3.05	-3.984020976	-98.67790533	120.3557767
3.06	-3.954183981	-98.69365789	120.3400241
3.07	-3.924364931	-98.70964818	120.3240338
3.08	-3.894555443	-98.72561077	120.3080712
3.09	-3.86476928	-98.74179551	120.2918865
3.1	-3.83499811	-98.75793681	120.2757452
3.11	-3.805244627	-98.7743166	120.2593654
3.12	-3.775511439	-98.79063758	120.2430444
3.13	-3.745790621	-98.80692273	120.2267593
3.14	-3.716084933	-98.82345377	120.2102282
3.15	-3.686386813	-98.83996288	120.1937191
3.16	-3.65670929	-98.85670204	120.17698
3.17	-3.62705486	-98.8733743	120.1603077
3.18	-3.597406094	-98.89003015	120.1436519
3.19	-3.567765936	-98.90695079	120.1267312
3.2	-3.538146954	-98.9240998	120.1095822
3.21	-3.508541993	-98.94091846	120.0927635
3.22	-3.478944206	-98.95800607	120.0756759
3.23	-3.449356476	-98.97535426	120.0583277
3.24	-3.419781595	-98.99266523	120.0410168
3.25	-3.390222263	-99.00993115	120.0237509
3.26	-3.360671961	-99.02746064	120.0062214
3.27	-3.3311335	-99.04495582	119.9887262
3.28	-3.301609601	-99.0624088	119.9712732
3.29	-3.272085184	-99.08015302	119.953529
3.3	-3.242580876	-99.09812871	119.9355533
3.31	-3.213081782	-99.11579956	119.9178825
3.32	-3.183590815	-99.13402632	119.8996557
3.33	-3.154102293	-99.15195627	119.8817257
3.34	-3.124636037	-99.17011144	119.8635706
3.35	-3.095169445	-99.18826758	119.8454144
3.36	-3.065705589	-99.20670552	119.8269765
3.37	-3.036255602	-99.22510328	119.8085787
3.38	-3.006814043	-99.24376635	119.7899157
3.39	-2.977375715	-99.26213033	119.7715517
3.4	-2.947943571	-99.28105586	119.7526262
3.41	-2.918520472	-99.29966544	119.7340166

3.42	-2.889101439	-99.31855298	119.715129
3.43	-2.859689395	-99.33771	119.695972
3.44	-2.830279576	-99.35686056	119.6768214
3.45	-2.800874957	-99.37599607	119.6576859
3.46	-2.771478421	-99.39539788	119.6382841
3.47	-2.742085397	-99.41478952	119.6188925
3.48	-2.712691528	-99.43418361	119.5994984
3.49	-2.683307089	-99.4538401	119.5798419
3.5	-2.653920548	-99.47350269	119.5601793
3.51	-2.624535003	-99.49345211	119.5402299
3.52	-2.595160456	-99.51336968	119.5203123
3.53	-2.565778828	-99.53330776	119.5003743
3.54	-2.536407077	-99.55350695	119.4801751
3.55	-2.507034365	-99.57370892	119.4599731
3.56	-2.477657035	-99.59421401	119.439468
3.57	-2.448284906	-99.61470402	119.418978
3.58	-2.418914273	-99.63518971	119.3984923
3.59	-2.389548119	-99.65595214	119.3777299
3.6	-2.360176446	-99.67673056	119.3569514
3.61	-2.330802449	-99.69751572	119.3361663
3.62	-2.301429231	-99.71858835	119.3150937
3.63	-2.272059799	-99.73993974	119.2937423
3.64	-2.242684692	-99.76101784	119.2726642
3.65	-2.213307113	-99.78268257	119.2509994
3.66	-2.183930169	-99.80405572	119.2296263
3.67	-2.154550872	-99.82572542	119.2079566
3.68	-2.125166386	-99.84741015	119.1862719
3.69	-2.095779903	-99.8693904	119.1642916
3.7	-2.066394518	-99.89136747	119.1423145
3.71	-2.037001712	-99.91365577	119.1200262
3.72	-2.007604748	-99.93566638	119.0980156
3.73	-1.978206788	-99.95825934	119.0754227
3.74	-1.94879973	-99.98058893	119.0530931
3.75	-1.91939242	-100.003209	119.030473
3.76	-1.889976962	-100.0261424	119.0075396
3.77	-1.860562063	-100.0490741	118.9846079
3.78	-1.831134667	-100.0720421	118.9616399
3.79	-1.801703505	-100.0953107	118.9383713
3.8	-1.772266489	-100.1185963	118.9150857
3.81	-1.742821648	-100.1419045	118.8917775
3.82	-1.713372271	-100.1655157	118.8681664
3.83	-1.683916458	-100.1891454	118.8445366
3.84	-1.654452419	-100.2130887	118.8205933

3.85	-1.624978473	-100.2370608	118.7966212
3.86	-1.595497983	-100.2613415	118.7723405
3.87	-1.566009323	-100.2856459	118.7480361
3.88	-1.536510969	-100.3099784	118.7237036
3.89	-1.507001497	-100.3346328	118.6990492
3.9	-1.477489058	-100.3592958	118.6743862
3.91	-1.447962742	-100.383999	118.649683
3.92	-1.418426049	-100.409022	118.62466
3.93	-1.38887778	-100.4340786	118.5996034
3.94	-1.359321374	-100.4594484	118.5742336
3.95	-1.329755663	-100.4848452	118.5488368
3.96	-1.300179565	-100.5105619	118.5231201
3.97	-1.270587672	-100.5363243	118.4973577
3.98	-1.240987926	-100.5623992	118.4712828
3.99	-1.21137071	-100.5882349	118.4454471
4	-1.181748213	-100.6146655	118.4190165
4.01	-1.152106778	-100.6408611	118.3928209
4.02	-1.122458475	-100.6673664	118.3663156
4.03	-1.092790048	-100.6942198	118.3394622
4.04	-1.063113439	-100.7210968	118.3125852
4.05	-1.033419845	-100.748023	118.285659
4.06	-1.003712913	-100.7752777	118.2584043
4.07	-0.973992211	-100.8028619	118.2308201
4.08	-0.944257363	-100.8301974	118.2034846
4.09	-0.914504154	-100.8578758	118.1758062
4.1	-0.884740152	-100.8858753	118.1478067
4.11	-0.854957394	-100.913929	118.119753
4.12	-0.825155838	-100.9420373	118.0916447
4.13	-0.795342962	-100.970468	118.063214
4.14	-0.765511188	-100.9992433	118.0344387
4.15	-0.73566061	-101.0277833	118.0058988
4.16	-0.705794985	-101.0569463	117.9767357
4.17	-0.675910793	-101.0858734	117.9478086
4.18	-0.646008249	-101.1151434	117.9185386
4.19	-0.616091113	-101.1447454	117.8889366
4.2	-0.586152615	-101.1744093	117.8592727
4.21	-0.556193183	-101.2041339	117.8295481
4.22	-0.526216677	-101.2341977	117.7994843
4.23	-0.496220111	-101.2646093	117.7690727
4.24	-0.466203999	-101.2950775	117.7386045
4.25	-0.436165584	-101.3256104	117.7080716
4.26	-0.406108795	-101.3564862	117.6771958
4.27	-0.376030991	-101.3874229	117.6462591

4.28	-0.345932878	-101.4187082	117.6149738
4.29	-0.315812022	-101.4500593	117.5836227
4.3	-0.285669267	-101.4817637	117.5519183
4.31	-0.255502374	-101.513538	117.5201441
4.32	-0.225315374	-101.5453705	117.4883115
4.33	-0.195106117	-101.577847	117.455835
4.34	-0.164872592	-101.610104	117.423578
4.35	-0.134615888	-101.642718	117.390964
4.36	-0.104334164	-101.6756941	117.3579879
4.37	-0.07403152	-101.7087309	117.3249511
4.38	-0.04370043	-101.7418501	117.2918319
4.39	-0.013347964	-101.7756107	117.2580713

---

## Appendix C: Isotherm Raw Data

### Appendix C.I: Isotherm Raw Data of CH<sub>4</sub>, C<sub>2</sub>H<sub>6</sub>, C<sub>2</sub>H<sub>4</sub>, and CO<sub>2</sub> on ETS-10 at 303-323-343K

Table 1: Isotherm Raw data for CH<sub>4</sub> on ETS-10 at 303-323-343 K

303K		323K		343K	
P(kPa)	q (mmol/g)	P(kPa)	q (mmol/g)	P(kPa)	q (mmol/g)
1.393345	0.028768	1.27542773	0.015816964	1.34991577	0.010401786
3.174979	0.063545	3.30927914	0.039477679	3.43412792	0.025553571
6.657495	0.12867	6.47174166	0.075638393	6.5858198	0.048241071
12.69609	0.232107	12.87407401	0.145013393	13.07249106	0.092830357
19.5488	0.337598	19.79351705	0.214625	19.80562069	0.136732143
26.50455	0.433911	26.52023495	0.277950893	26.63779222	0.179790179
33.22291	0.517625	33.24505999	0.337241071	33.41572398	0.221183036
39.98493	0.592857	39.98220195	0.393165179	39.964673	0.259066964
46.62353	0.660848	46.62231484	0.445620536	46.78676705	0.294522321
53.32381	0.722116	53.301338	0.494151786	53.32569191	0.328875
59.88545	0.778438	60.00074273	0.539232143	60.01031367	0.364910714
66.54864	0.830813	66.60938349	0.580991071	66.72156877	0.397209821
73.22905	0.87917	73.27479672	0.620691964	73.32563734	0.4278125
79.89137	0.924228	79.89072899	0.659464286	79.9917304	0.457245536
86.57586	0.966853	86.58872074	0.697339286	86.63997459	0.485665179
93.2675	1.005013	93.25605349	0.732674107	93.31823794	0.513754464
99.92115	1.041205	99.9487399	0.765915179	99.98209156	0.541325893
101.3217	1.052393	101.3128788	0.774133929	101.3648258	0.546308036
106.6975	1.077969	106.6753378	0.797133929	106.675991	0.562361607
113.1208	1.108259	113.228899	0.825236607	113.2377102	0.588040179

**Table 2: High resolution Isotherm Raw data for C<sub>2</sub>H<sub>6</sub> on ETS-10 at 303-323-343 K**

303K		323K		343K	
P(kPa)	q (mmol/g)	P(kPa)	q (mmol/g)	P(kPa)	q (mmol/g)
0.058599	0.059732	0.12824793	0.057205357	0.06670332	0.014125
0.120197	0.11946	0.26248103	0.113866071	0.13318003	0.028053571
0.183367	0.17821	0.41133714	0.17090625	0.20052319	0.041991071
0.252537	0.237299	0.56657832	0.227714286	0.26897274	0.055852679
0.327345	0.296263	0.74442718	0.286017857	0.33800881	0.069723214
0.405832	0.35442	0.95665411	0.349875	0.40845786	0.083616071
0.49413	0.413455	1.18137125	0.413129464	0.48045319	0.097370536
0.589533	0.472388	1.39302499	0.464705357	0.55600763	0.1114375
0.69384	0.531116	3.3347661	0.805946429	0.62969587	0.124982143
0.826527	0.589491	7.18475003	1.120803571	0.73878859	0.145892857
0.955734	0.647964	13.29839457	1.33621875	0.83944342	0.162674107
1.098685	0.705214	19.4899263	1.450696429	0.93543275	0.179723214
1.267323	0.770996	26.06634845	1.525870536	1.03088888	0.196861607
1.449997	0.824438	33.12630302	1.587223214	1.13098385	0.2135
3.326395	1.16529	40.05802299	1.627401786	1.23610423	0.229696429
6.342867	1.386661	46.65919895	1.661191964	1.33747888	0.24628125
13.40826	1.586241	53.38186453	1.688276786	3.19730714	0.4815625
19.71424	1.668857	59.98531992	1.710964286	6.8258931	0.777696429
26.66944	1.727196	66.68557777	1.731575893	13.01579857	1.041691964
33.18334	1.767188	73.35733608	1.749714286	20.11495667	1.2035625
40.10396	1.799384	80.13425476	1.7656875	26.52352746	1.29915625
46.69688	1.824567	86.77382112	1.7783125	33.26410856	1.370495536
53.42603	1.846701	93.42227859	1.792450893	39.98378822	1.424098214
60.08699	1.865571	100.0568995	1.803883929	46.73921894	1.469482143
66.59455	1.880924	102.0441626	1.808977679	53.33307673	1.5066875
73.3357	1.895737	106.7207931	1.816017857	60.04335874	1.535892857
80.00701	1.90867	114.0430688	1.825209821	66.65451887	1.561236607
86.79431	1.921076			73.46512246	1.583995536
93.34095	1.931897			80.025322	1.603669643
100.0021	1.941862			86.68766933	1.622357143
102.0627	1.946254			93.47166624	1.639915179
106.6501	1.952344			100.0429697	1.654227679
113.9983	1.961214			102.025234	1.659089286
				106.701318	1.668276786
				114.0628372	1.68009375

**Table 3: High resolution Isotherm Raw data for C<sub>2</sub>H<sub>4</sub> on ETS-10 at 303-323-343 K**

303K		323K		343K	
P(kPa)	q (mmol/g)	P(kPa)	q (mmol/g)	P(kPa)	q (mmol/g)
0.006145	0.06025	0.01420978	0.059575893	0.00937099	0.015450893
0.012237	0.120513	0.02911272	0.120508929	0.01882196	0.030839286
0.018142	0.180781	0.0447888	0.181477679	0.02848621	0.046209821
0.024047	0.241049	0.0614513	0.2425	0.03811047	0.061589286
0.030072	0.301299	0.07935349	0.303540179	0.04770807	0.076950893
0.036164	0.36158	0.09918853	0.364513393	0.05793218	0.092267857
0.042763	0.421786	0.12158293	0.425388393	0.06858285	0.108129464
0.049041	0.48346	0.14488377	0.486267857	0.07886028	0.123678571
0.056373	0.54504	0.17061067	0.547325893	0.08885778	0.138575893
0.065184	0.606522	0.20024326	0.607883929	0.09938848	0.153861607
0.075608	0.66796	0.22955593	0.668566964	0.11034574	0.169107143
0.086645	0.729388	0.26586685	0.728870536	0.12271598	0.184236607
0.099309	0.790768	0.30311087	0.789214286	0.13260684	0.199553571
0.113292	0.852174	0.34630007	0.849227679	0.14413729	0.214741071
0.129448	0.913487	0.39668747	0.908794643	0.15568107	0.229910714
0.148056	0.974723	0.45505954	0.967709821	0.16717153	0.24509375
0.169424	1.03579	0.52118967	1.0276875	0.17946179	0.260517857
0.194605	1.096826	0.60152958	1.086919643	0.19305839	0.27540625
0.226383	1.157612	0.69455965	1.146227679	0.2046155	0.290428571
0.264427	1.218121	0.82068811	1.205352679	0.21810546	0.305441964
0.309403	1.278223	0.96222605	1.262991071	0.23130216	0.320482143
0.364562	1.337826	1.12613173	1.329401786	0.24411229	0.335558036
0.435504	1.396455	1.33803874	1.380799107	0.25818877	0.35053125
0.525375	1.455888	3.23563089	1.636160714	0.27162541	0.365549107
0.642399	1.514152	6.62583646	1.789366071	0.28574188	0.380508929
0.798494	1.566754	12.70926189	1.904008929	0.29920518	0.395526786
1.025117	1.630683	20.01066275	1.974111607	0.31530782	0.410316964
1.348143	1.690598	26.9202016	2.01653125	0.33183702	0.425084821
3.192002	1.851612	33.21442765	2.046272321	0.34599348	0.440049107
6.696166	1.96304	39.96796551	2.071620536	0.36169622	0.454879464
12.98934	2.050969	46.78231483	2.092200893	0.3771057	0.469754464
20.07017	2.104594	53.43670415	2.109642857	0.39452801	0.484464286
27.09762	2.143634	60.06943222	2.125517857	0.41047069	0.499267857
33.39172	2.170871	66.69844122	2.139008929	0.4282929	0.515620536
40.08471	2.194504	73.39996542	2.151392857	0.44742145	0.531611607
46.78136	2.21533	80.02450887	2.162924107	0.4673498	0.54759375
53.48628	2.233205	86.7805661	2.173285714	0.48662498	0.563674107
60.06518	2.249094	93.40301674	2.182875	0.50775303	0.579638393
66.62889	2.263379	100.0494747	2.191665179	0.52964089	0.595544643
73.27964	2.276786	101.9374159	2.19478125	0.55044902	0.611513393

80.14465	2.289013	106.7091427	2.200669643	0.57047068	0.627736607
86.76574	2.299906	114.0655698	2.207651786	0.59538445	0.643602679
93.42077	2.310879			0.61743227	0.65971875
100.0367	2.320022			0.64310585	0.675379464
101.8937	2.323446			0.70117133	0.701870536
106.7113	2.330085			0.72876443	0.7249375
113.3566	2.338308			0.76548858	0.74709375
				0.80469211	0.768991071
				0.85289339	0.790125
				0.89180366	0.812147321
				0.9376322	0.833598214
				0.98310083	0.855165179
				1.03072892	0.876209821
				1.07819705	0.897401786
				1.13322329	0.917892857
				1.18298418	0.938915179
				1.24543523	0.958852679
				1.2931433	0.979950893
				1.35536774	0.999754464
				3.32932746	1.35196875
				6.44350872	1.559223214
				13.50668915	1.738723214
				19.86433934	1.815303571
				26.98955759	1.872151786
				33.26849413	1.91109375
				39.99994418	1.94184375
				46.82831666	1.966616071
				53.46033824	1.986683036
				60.05366283	2.004491071
				66.67548696	2.01946875
				74.05757431	2.037366071
				80.04912938	2.049651786
				87.40728938	2.060799107
				94.0907381	2.068919643
				100.7919291	2.079799107
				102.0132503	2.082883929
				106.7211664	2.090174107
				114.0800462	2.097785714

**Table 4: High resolution Isotherm Raw data for CO<sub>2</sub> on ETS-10 at 303-323-343 K**

303K		323K		343K	
P(kPa)	q (mmol/g)	P(kPa)	P(kPa)	q (mmol/g)	P(kPa)
0.001453	0.016545	0.00290594	0.016361607	0.00638507	0.016084821
0.004106	0.032513	0.01045072	0.031897321	0.02419395	0.030776786
0.007052	0.048446	0.01896859	0.047361607	0.04461551	0.046669643
0.010091	0.064375	0.02789969	0.062794643	0.06623677	0.06253125
0.01321	0.080299	0.03704407	0.078196429	0.08985753	0.078258929
0.016436	0.096214	0.04637507	0.09359375	0.11298508	0.0940625
0.019808	0.112112	0.05634591	0.108928571	0.13867199	0.109700893
0.023274	0.128004	0.06566358	0.124308036	0.16297258	0.125473214
0.026767	0.143893	0.07616762	0.139598214	0.18917936	0.141169643
0.030446	0.159768	0.08657835	0.154892857	0.21829208	0.156625
0.034258	0.175629	0.0974423	0.170142857	0.24615178	0.172276786
0.038057	0.191491	0.10777305	0.1854375	0.27522451	0.187785714
0.042069	0.207335	0.12000999	0.2005625	0.30456384	0.203316964
0.046255	0.223161	0.12971423	0.215901786	0.33387651	0.21890625
0.050507	0.238987	0.14284428	0.230955357	0.36209612	0.234700893
0.054906	0.25479	0.15532116	0.246058036	0.3948346	0.250196429
0.059332	0.270589	0.16753144	0.261169643	0.42486709	0.265933036
0.063757	0.286397	0.17958176	0.276303571	0.46279094	0.281107143
0.06805	0.302205	0.19319169	0.291308036	0.49532947	0.296589286
0.073315	0.317929	0.20653502	0.306334821	0.52722816	0.312517857
0.078314	0.333692	0.22129133	0.321241071	0.56397897	0.327982143
0.083339	0.349429	0.23438139	0.336290179	0.60111635	0.3433125
0.088884	0.365138	0.25049736	0.35109375	0.6407731	0.358464286
0.094256	0.380857	0.26437389	0.366075893	0.69405311	0.380669643
0.099828	0.396549	0.27831707	0.381040179	0.75414475	0.40090625
0.106413	0.412152	0.29427308	0.395861607	0.81282341	0.421116071
0.110479	0.427978	0.31134881	0.410584821	0.86932928	0.441660714
0.117104	0.443571	0.32601181	0.425495536	0.92414224	0.462254464
0.123116	0.459223	0.34350077	0.44165625	0.99505784	0.481366071
0.129941	0.474799	0.36261599	0.457678571	1.04981748	0.501821429
0.136179	0.490433	0.38222442	0.473763393	1.1106556	0.52175
0.142738	0.506027	0.40152626	0.489888393	1.17991828	0.54103125
0.150416	0.52154	0.42386734	0.505723214	1.24791461	0.560459821
0.156907	0.537147	0.44486209	0.521816964	1.31671074	0.579767857
0.163532	0.552741	0.46944261	0.537491071	1.38727976	0.599004464
0.170877	0.568272	0.4898775	0.553348214	3.22687308	0.94846875
0.178102	0.583817	0.50717984	0.569611607	6.87264141	1.300741071
0.186313	0.599277	0.5310672	0.5855625	12.78410984	1.5798125

0.193698	0.614799	0.55383484	0.6015625	19.89967717	1.776008929
0.201989	0.630259	0.57724232	0.617678571	27.06867114	1.892504464
0.210707	0.645665	0.60460881	0.633602679	32.72558989	1.977035714
0.218772	0.661138	0.63202862	0.649392857	40.25658667	2.047848214
0.227783	0.676522	0.65564938	0.66540625	46.32107017	2.111540179
0.236181	0.691973	0.70251766	0.688214286	53.60642171	2.156142857
0.246432	0.707259	0.74449383	0.710102679	60.44967047	2.1981875
0.255296	0.722652	0.78489706	0.731834821	66.58265684	2.235294643
0.2648	0.738018	0.82816624	0.753473214	73.34676539	2.274017857
0.274651	0.753335	0.87395479	0.774825893	79.98594518	2.302379464
0.285782	0.768545	0.92260929	0.795991071	86.60778264	2.328410714
0.296699	0.783777	0.9697575	0.817285714	93.32539615	2.353111607
0.307816	0.799393	1.01777216	0.8385625	100.0060722	2.376102679
0.31896	0.814607	1.06701318	0.859428571	101.4083349	2.386397321
0.330197	0.829808	1.11850697	0.880290179	106.7825377	2.404799107
0.342074	0.844973	1.17629252	0.9005625	113.976832	2.4238125
0.354271	0.860094	1.22803958	0.921424107		
0.366148	0.875263	1.28351904	0.941848214		
0.379478	0.890281	1.34788961	0.961357143		
0.392928	0.905304	3.18864264	1.347075893		
0.406525	0.920299	7.18961548	1.706116071		
0.420455	0.935286	13.03296761	1.947540179		
0.434198	0.950281	20.1636245	2.1135625		
0.450861	0.96642	26.92858617	2.22065625		
0.468403	0.982589	33.2350225	2.293767857		
0.486105	0.998683	39.81587021	2.355919643		
0.503607	1.014857	46.76486586	2.409254464		
0.52183	1.030946	53.49652919	2.450366071		
0.538492	1.047201	60.04717112	2.488794643		
0.558594	1.063228	66.819291	2.521321429		
0.578922	1.079299	73.33388861	2.550401786		
0.60085	1.095286	80.10034324	2.579129464		
0.620885	1.111424	86.66442181	2.603285714		
0.643039	1.127589	93.47106639	2.625772321		
0.682763	1.150973	100.0011001	2.645825893		
0.729524	1.172487	101.4195454	2.654209821		
0.764116	1.194915	106.7628226	2.667040179		
0.806065	1.216772	113.9922415	2.682977679		
0.846682	1.238754				
0.886872	1.260714				
0.93214	1.282429				
0.978222	1.303996				
1.020638	1.325982				

1.069799	1.347201
1.121026	1.368246
1.173733	1.389071
1.229253	1.409906
1.287465	1.430272
1.349089	1.45017
3.244962	1.803848
6.379138	2.058728
13.0181	2.310964
20.41299	2.456237
26.38115	2.538603
33.44874	2.605143
39.85705	2.662518
46.64579	2.703179
53.10244	2.737741
60.01317	2.766844
66.62554	2.795272
73.34463	2.819116
80.09782	2.842313
86.70636	2.865683
93.23637	2.883411
99.99469	2.899897
101.4443	2.90625
106.7415	2.918455
113.9329	2.932719

---

**Appendix C.II: Isotherm Raw Data of CH<sub>4</sub>, C<sub>2</sub>H<sub>6</sub>, C<sub>2</sub>H<sub>4</sub>, and CO<sub>2</sub> on high siliceous ZSM-5 at 303-323-343K**

**Table 5: Isotherm Raw data for CH<sub>4</sub> on high siliceous ZSM-5 at 303-323-343 K**

303K		323K		343K	
P(kPa)	q (mmol/g)	P(kPa)	P(kPa)	q (mmol/g)	P(kPa)
1.349729	0.009929	1.38785295	0.006446429	1.43554769	0.0036875
3.360413	0.024134	3.4432723	0.01575	3.55415124	0.009473214
6.607321	0.046567	6.56758436	0.029674107	6.66044114	0.017928571
13.10178	0.090415	13.17958428	0.058236607	13.37789469	0.036321429
19.88729	0.134701	19.87608307	0.086473214	19.9251508	0.054334821
26.46452	0.176246	26.71088061	0.11478125	26.63540615	0.072232143
33.16748	0.217545	33.20065776	0.141875	33.36463009	0.090022321
39.99212	0.257621	39.95847455	0.169464286	40.15018661	0.109071429
46.68342	0.295321	46.67403524	0.1943125	46.8597488	0.124794643
53.3398	0.331955	53.34063484	0.218410714	54.06294755	0.142361607
59.95766	0.366487	59.96231234	0.243598214	60.72132254	0.159008929
66.59373	0.401487	66.70483962	0.270424107	66.79313754	0.174013393
73.27914	0.435161	73.38214321	0.294946429	74.02232979	0.191607143
79.93896	0.467335	79.94004999	0.315950893	80.68314417	0.208513393
86.58108	0.497978	86.67220653	0.337209821	86.7165821	0.221285714
93.2486	0.527933	93.30116221	0.360276786	94.05750641	0.238035714
99.92536	0.557455	99.99626135	0.383316964	100.8622848	0.252732143
101.3291	0.565438	101.4065087	0.386495536	102.0169161	0.255517857
106.7042	0.586991	107.3080463	0.402191964	107.3783087	0.268321429
113.2301	0.613491	113.3566671	0.42065625	114.0647034	0.281477679

**Table 6: Isotherm Raw data for C<sub>2</sub>H<sub>6</sub> on high siliceous ZSM-5 at 303-323-343 K**

303K		323K		343K	
P(kPa)	q (mmol/g)	P(kPa)	P(kPa)	q (mmol/g)	P(kPa)
0.340555	0.047415	0.61843202	0.041758144	0.29988501	0.007459821
0.725752	0.10008	1.19287504	0.079870593	0.60698155	0.014517857
1.114961	0.151317	1.65126708	0.107563588	0.83523114	0.021441964
1.430589	0.190223	3.25152025	0.202922802	1.16245598	0.031526786
3.22502	0.400321	6.6354074	0.391539491	1.38128126	0.037808036
6.716947	0.725987	13.52536448	0.691958947	3.23328481	0.098160714
14.02589	1.129308	19.65749773	0.887233378	6.79006206	0.207678571
19.82235	1.311201	26.35842208	1.049892905	13.3805207	0.393147321
27.025	1.452018	33.26536158	1.167286925	19.70216656	0.541196429
32.80845	1.529594	39.68078399	1.268027666	26.30064986	0.677017857
39.86487	1.603201	46.81919894	1.335912539	33.18228902	0.794102679
46.75917	1.655094	52.91072901	1.389790272	39.96651254	0.895973214
53.32355	1.694661	59.88686454	1.453253012	46.70649379	0.971075893
60.08426	1.729817	66.79600349	1.49367693	53.13028744	1.04509375
66.54105	1.758777	73.20450763	1.52303436	60.13133674	1.10275
73.36064	1.784272	79.95274015	1.553846497	66.50086396	1.157379464
80.00199	1.806063	86.63226985	1.583386881	73.32565067	1.204861607
86.73119	1.825732	93.40697575	1.611231593	80.06805798	1.245303571
93.32849	1.842719	99.98013205	1.635488621	86.67831167	1.280544643
99.99345	1.859152	101.9467603	1.646233824	93.29708323	1.315290179
101.3416	1.86408	106.7294843	1.660432842	99.99231567	1.347660714
106.7768	1.875161	113.9714334	1.678036591	101.3330204	1.360700893
113.9666	1.888625	0.61843202	0.041758144	106.7122353	1.381611607

**Table 7: Isotherm Raw data for C<sub>2</sub>H<sub>4</sub> on high siliceous ZSM-5 at 303-323-343 K**

303K		323K		343K	
P(kPa)	q (mmol/g)	P(kPa)	q (mmol/g)	P(kPa)	q (mmol/g)
0.606448	0.040964	0.900268	0.029272	0.436864	0.004183
1.183771	0.078531	1.472378	0.048496	0.81361	0.008772
1.632618	0.106938	3.382581	0.109781	1.212857	0.014978
3.270489	0.204362	6.660494	0.211228	1.467753	0.018487
6.629329	0.390625	13.35969	0.404875	3.437847	0.053688
13.45767	0.69571	19.69508	0.548004	6.348786	0.105228
19.63853	0.897848	26.20367	0.690714	13.37191	0.223496
26.44989	1.071804	33.16103	0.818429	19.60552	0.326054
33.28526	1.200317	40.15501	0.910571	26.5966	0.42221
39.96965	1.299473	46.20474	0.998201	33.23665	0.508817
46.73771	1.380857	53.40728	1.075915	39.96273	0.587424
53.38502	1.445647	59.74542	1.145348	46.5227	0.663384
59.978	1.504987	66.80348	1.203835	53.3916	0.724451
66.74056	1.551772	73.37596	1.241911	59.93986	0.782888
73.33076	1.591848	79.77881	1.290763	66.63424	0.839451
79.92007	1.6305	86.68184	1.33654	73.31303	0.891509
86.65924	1.664429	93.25151	1.372089	80.03059	0.934196
93.33253	1.694705	99.95783	1.406473	86.70035	0.976871
100.0063	1.720723	101.372	1.419701	93.41012	1.015259
101.9435	1.731107	106.7798	1.445504	99.85355	1.051513
106.6551	1.748513	113.8733	1.473969	101.399	1.062955
113.2673	1.770598			106.6833	1.088295
				113.8481	1.123304

**Table 8: Isotherm Raw data for CO<sub>2</sub> on high siliceous ZSM-5 at 303-323-343 K**

303K		323K		343K	
P(kPa)	q (mmol/g)	P(kPa)	q (mmol/g)	P(kPa)	q (mmol/g)
0.34826	0.005973	0.50931264	0.002191964	1.05482956	0.000928571
0.68027	0.012098	0.83985665	0.005933036	1.51110213	0.003946429
0.841203	0.015424	1.25851196	0.011290179	3.22856599	0.018044643
1.230306	0.024371	1.51452794	0.014571429	6.51113181	0.046008929
1.456516	0.029719	3.36322565	0.040129464	13.01997086	0.101339286
3.332273	0.074982	6.42063444	0.08190625	19.89650463	0.156892857
6.687981	0.15558	12.81147633	0.166888393	26.60026827	0.206517857
13.38936	0.308893	19.62293304	0.255727679	33.16256062	0.254102679
19.61286	0.440451	26.48500376	0.335441964	39.90667417	0.302808036
26.2501	0.57171	33.02598144	0.410794643	46.6062122	0.347642857
32.93203	0.691045	39.8360385	0.482745536	53.26915938	0.393013393
39.6969	0.797772	46.49758603	0.549535714	59.91992294	0.43728125
46.29604	0.903598	53.23000917	0.609825893	66.62925852	0.476857143
53.21847	0.988799	59.83355787	0.669866071	73.27726277	0.516709821
59.6628	1.076152	66.46745898	0.7305625	79.89262185	0.558821429
66.49389	1.153692	73.22910148	0.784415179	86.6247384	0.5960625
73.10389	1.225585	79.85273849	0.837727679	93.28180705	0.632669643
79.84063	1.288567	86.54549155	0.889504464	99.93868908	0.667254464
86.41109	1.35325	93.22512789	0.9375	101.3325005	0.674147321
93.16978	1.41092	99.79767101	0.990723214	106.6567825	0.698339286
99.86249	1.46267	101.3801153	1.006433036	113.2056249	0.731473214
101.2476	1.477594	106.730604	1.039196429		
106.6364	1.518152	113.0530497	1.078089286		
113.077	1.564634				

**Appendix C.III: Isotherm Raw Data of CH<sub>4</sub>, C<sub>2</sub>H<sub>6</sub>, C<sub>2</sub>H<sub>4</sub>, and CO<sub>2</sub> on 13X at 303-323-343K**

**Table 9: Isotherm Raw data for CH<sub>4</sub> on 13X at 303-323-343 K**

303K		323K		343K	
P(kPa)	q (mmol/g)	P(kPa)	q (mmol/g)	P(kPa)	q (mmol/g)
1.365565	0.010161	1.43088219	0.007214286	1.44213271	0.005165179
3.420651	0.024321	3.4729982	0.016821429	3.50928246	0.0118125
6.632928	0.047138	6.63328793	0.031754464	7.00627466	0.023191964
13.12642	0.091826	13.23331751	0.062428571	13.96622757	0.045839286
19.94928	0.138496	19.92532409	0.093464286	20.72333787	0.06871875
26.5004	0.183027	26.67243689	0.124598214	26.72786303	0.088272321
33.17814	0.227491	33.33301133	0.1544375	34.06836078	0.111580357
39.92146	0.272272	40.00952845	0.184232143	40.80018407	0.132705357
46.60383	0.315866	46.55186579	0.214196429	47.39165579	0.154165179
53.28835	0.359321	53.31082896	0.244727679	53.99967004	0.175013393
59.96442	0.401964	60.00320878	0.273575893	60.69803503	0.195642857
66.62001	0.444165	66.68096559	0.302	67.36598096	0.21596875
73.27417	0.485429	73.35244397	0.330294643	74.06873152	0.234741071
79.94245	0.526098	79.90827127	0.358821429	80.71717566	0.254397321
86.61869	0.565973	86.70646463	0.388	87.43788173	0.276678571
93.24551	0.605304	93.34021911	0.414754464	93.39044655	0.294941964
99.92448	0.645754	99.98575731	0.441799107	100.7196271	0.31484375
101.356	0.656871	101.3405385	0.450607143	102.0633311	0.319723214
106.7092	0.686246	106.7102891	0.471334821	106.728138	0.332950893
113.2432	0.722821	113.966208	0.497013393	114.0677426	0.353455357

Table 10: Isotherm Raw data for C2H6 on 13X at 303-323-343K

303K		323K		343K	
P(kPa)	q (mmol/g)	P(kPa)	q (mmol/g)	P(kPa)	q (mmol/g)
0.896043	0.093196	1.26427052	0.0725625	0.46877611	0.015772321
1.552279	0.159746	2.05568595	0.116540179	0.82060813	0.027709821
3.308253	0.336844	3.20782451	0.178236607	1.29454295	0.0431875
6.526808	0.671281	6.54465676	0.364459821	1.59593425	0.053040179
13.05074	1.294004	13.26562943	0.733464286	3.37570253	0.110758929
20.37598	1.84796	19.41477176	1.047366071	6.72046613	0.217607143
26.78332	2.181304	26.16275101	1.355433036	13.30513955	0.426276786
32.97097	2.417777	32.8324565	1.60690625	19.51897237	0.617303571
39.89429	2.613487	39.59132636	1.829352679	26.158792	0.814919643
46.54253	2.754933	46.55153254	2.015754464	33.1021224	1.000049107
53.34541	2.867446	53.15796052	2.171598214	39.73485047	1.170575893
59.99278	2.957375	60.13570898	2.284861607	46.53693619	1.32440625
66.59517	3.030585	66.16890697	2.394013393	53.12439558	1.461486607
73.27793	3.09454	73.24320462	2.49509375	59.80465843	1.593549107
80.06207	3.148335	79.97128218	2.568941964	66.46556612	1.715348214
86.68322	3.197527	86.61338124	2.635982143	73.33731442	1.816080357
93.31792	3.238045	93.24116388	2.701799107	79.80643007	1.903285714
99.97819	3.274906	99.90957636	2.762875	86.60899567	1.980133929
101.2596	3.289737	101.3440443	2.779142857	93.0968533	2.068700893
106.7015	3.314652	106.8049854	2.809839286	100.058819	2.133584821
113.8927	3.344777	113.763592	2.857098214	101.9045175	2.157263393
				106.7195268	2.201165179
				113.1830038	2.259754464

Table 11: High Resolution Isotherm Raw data for C<sub>2</sub>H<sub>4</sub> on 13X at 303-323-343 K

303K		323K		343K	
P(kPa)	q (mmol/g)	P(kPa)	q (mmol/g)	P(kPa)	q (mmol/g)
0.048881	0.124107	0.12056985	0.12275	0.06573023	0.03015625
0.101015	0.248317	0.25171039	0.245598214	0.13128717	0.060504464
0.15816	0.374308	0.40093974	0.367790179	0.20190951	0.090482143
0.224264	0.500835	0.57087058	0.489227679	0.27385152	0.120517857
0.297619	0.627031	0.76108968	0.604120536	0.34743312	0.150629464
0.379252	0.752777	0.99436468	0.736584821	0.42137463	0.180901786
0.472122	0.877076	1.24547522	0.868120536	0.50242103	0.210803571
0.57507	1.002366	1.51450128	0.974102679	0.58196114	0.241017857
0.714795	1.121799	3.20077294	1.519272321	0.66080809	0.271441964
0.871515	1.258746	7.51502744	2.182700893	0.76426222	0.306816964
1.051924	1.395268	13.63784302	2.627566964	0.8685828	0.34034375
1.267483	1.529728	19.78542574	2.902513393	0.97711566	0.373191964
1.483336	1.641946	26.05480467	3.08184375	1.07714398	0.406754464
3.219248	2.235879	32.80439685	3.232504464	1.19232851	0.438919643
6.818108	2.784696	39.99547863	3.339245536	1.29976831	0.471700893
12.66485	3.192121	46.39078607	3.431513393	1.3959176	0.505584821
19.88992	3.452652	53.42620011	3.504544643	3.18945577	0.928879464
26.4051	3.603612	59.9913984	3.560910714	6.5888857	1.438102679
33.17801	3.714813	66.74934849	3.609232143	13.54463966	2.002758929
40.03299	3.799188	73.35756269	3.6569375	19.64464761	2.302959821
46.5056	3.867406	80.05379488	3.698428571	26.92280095	2.543075893
53.44577	3.922732	86.66812755	3.737535714	32.7130197	2.700142857
59.90802	3.968777	93.3510564	3.771821429	40.21549028	2.8456875
66.75303	4.012308	100.0731355	3.800785714	46.53025786	2.942508929
73.46387	4.048174	101.935883	3.811419643	53.43185203	3.024080357
80.03197	4.081866	106.7423611	3.830522321	59.82398693	3.098071429
86.69048	4.112281	113.9269645	3.858647321	66.7251812	3.167383929
93.28645	4.138353			73.29640465	3.231339286
100.0521	4.164589			80.09985003	3.281370536
101.3226	4.173388			86.62292552	3.325111607
106.7885	4.190357			93.40989502	3.368879464
113.9619	4.210232			99.92730526	3.40603125
				101.9936552	3.422348214
				106.7725802	3.4438125
				114.0091439	3.472415179

**Table 12: High resolution Isotherm Raw data for CO<sub>2</sub> on 13X at 303-323-343 K**

303K		323K		343K	
P(kPa)	q (mmol/g)	P(kPa)	q (mmol/g)	P(kPa)	q (mmol/g)
0.004172	0.032433	0.00895776	0.031888393	0.02323419	0.03246875
0.008225	0.064884	0.02004832	0.063517857	0.05264017	0.064700893
0.012224	0.097353	0.03157877	0.095098214	0.08405898	0.0968125
0.016156	0.129817	0.04340248	0.126633929	0.11577105	0.129040179
0.020342	0.162246	0.05506623	0.158196429	0.14976255	0.161196429
0.024567	0.19467	0.0671832	0.189691964	0.18383403	0.193321429
0.028939	0.227076	0.08019328	0.221075893	0.21938514	0.225616071
0.033285	0.259491	0.09420311	0.252330357	0.25690909	0.257763393
0.037897	0.291853	0.1094393	0.283450893	0.29785885	0.289741071
0.042549	0.324219	0.12315587	0.316678571	0.33854201	0.321767857
0.047348	0.356571	0.14179121	0.349441964	0.3809714	0.353772321
0.052574	0.388875	0.15488127	0.382754464	0.42210778	0.385982143
0.058572	0.421696	0.17506289	0.415558036	0.46942928	0.417727679
0.064477	0.45392	0.19091226	0.448888393	0.51344494	0.450441964
0.071049	0.486054	0.21161375	0.481776786	0.5699908	0.481410714
0.077327	0.518214	0.2318087	0.514834821	0.61513951	0.513575893
0.083486	0.550388	0.25370989	0.547767857	0.6955594	0.551776786
0.090031	0.582513	0.27449136	0.581013393	0.76614175	0.589196429
0.097202	0.614576	0.29973838	0.613861607	0.83457797	0.626678571
0.105974	0.646429	0.32297257	0.647151786	0.91782382	0.662575893
0.114371	0.678335	0.35123217	0.67984375	0.98552689	0.700223214
0.122396	0.710259	0.37809212	0.712821429	1.06468043	0.736607143
0.130941	0.742125	0.40671163	0.745540179	1.14418055	0.772888393
0.140658	0.773848	0.43333164	0.778982143	1.23651746	0.807401786
0.149749	0.805665	0.46613677	0.811736607	1.3142047	0.843566964
0.16052	0.837254	0.49858199	0.844513393	1.40974081	0.877714286
0.171997	0.868772	0.5304007	0.877669643	3.23613743	1.361183036
0.183861	0.902196	0.56751142	0.910379464	6.99285135	1.913580357
0.195964	0.934362	0.60334246	0.943267857	13.43181454	2.444044643
0.208828	0.967813	0.64265263	0.976026786	19.52387781	2.789102679
0.223038	1.001201	0.70107802	1.016517857	26.17876034	3.062549107
0.237487	1.034589	0.76316916	1.054727679	32.85890322	3.29165625
0.253643	1.06792	0.82403394	1.093075893	39.98617429	3.48475
0.270039	1.101339	0.87903352	1.1319375	46.53333709	3.63928125
0.287355	1.134754	0.9454969	1.169625	53.34614013	3.769241071
0.306777	1.168018	1.00532194	1.208017857	59.77929144	3.901415179
0.325425	1.20146	1.07901018	1.2449375	66.78860534	3.99484375
0.346767	1.234714	1.1417145	1.283165179	72.94144008	4.077299107

0.367401	1.268138	1.2095642	1.320772321	79.83544948	4.166196429
0.391342	1.301371	1.28226602	1.357535714	86.64530659	4.249705357
0.415843	1.334603	1.36413888	1.393254464	93.29523036	4.32046875
0.44125	1.367808	3.26687641	1.971	100.0168829	4.380258929
0.468443	1.40079	6.73860826	2.543696429	101.8100211	4.412321429
0.495996	1.433897	13.01263936	3.13846875	106.7483729	4.456299107
0.524189	1.467004	19.48451432	3.520665179	113.8005161	4.505816964
0.551662	1.500304	26.61219862	3.840607143		
0.585027	1.533272	33.34187578	4.05625		
0.621005	1.566049	39.74735401	4.229308036		
0.674018	1.607625	46.57544656	4.388433036		
0.730431	1.647009	53.41406981	4.508308036		
0.783564	1.686629	59.83179831	4.615982143		
0.833752	1.726772	66.60199867	4.694495536		
0.889538	1.766094	73.12084855	4.782129464		
0.942951	1.805531	79.95274015	4.859058036		
1.003149	1.844429	86.67304632	4.933674107		
1.064547	1.882982	93.32619595	4.984375		
1.127251	1.921085	99.81558653	5.038919643		
1.191715	1.959112	101.3314741	5.061147321		
1.258019	1.99692	106.7922553	5.10278125		
1.328161	2.034174	113.8097138	5.1470625		
1.398144	2.071438				
3.174353	2.680897				
6.500015	3.320598				
12.88548	3.983223				
20.23571	4.413879				
26.39591	4.660509				
32.86923	4.856317				
39.7631	5.017585				
46.59214	5.144759				
53.3951	5.254987				
60.10657	5.338951				
66.64452	5.415397				
73.34847	5.483612				
80.06267	5.545344				
86.62546	5.60296				
93.32517	5.651446				
99.95718	5.696799				
101.2726	5.714317				
106.7156	5.744857				
113.7972	5.783777				

